Beam Transport for a Laser-Plasma Driven Free-Electron Laser at the LUX Experiment

Dissertation
zur Erlangung des Doktorgrades
an der Fakultät für Mathematik, Informatik und Naturwissenschaften
Fachbereich Physik
der Universität Hamburg

vorgelegt von Lars Hübner

Hamburg 2025

Gutacher/innen der Dissertation: Dr. Andreas R. Maier

Prof. Dr. Wolfgang Hillert

Zusannensetzung der Prüfungskommission: Dr. Andreas R. Maier

Prof. Dr. Wolfgang Hillert Prof. Dr. Daniela Pfannkuche Prof. Dr. Peter H. Hauschildt Prof. Dr. Peter Schleper

Vorsitzende/r der Prüfungskommission: Prof. Dr. Daniela Pfannkuche

Datum der Disputation: 12.05.2025

Vorsitzender des Fach-Promotionsausschusses PHYSIK: Prof. Dr. Wolfgang J. Parak

Leiter des Fachbereichs PHYSIK: Prof. Dr. Markus Drescher

Dekan der Fakultät MIN: Prof. Dr.-Ing. Norbert Ritter

Eidesstattliche Versicherung

Hiermit versichere ich an Eides statt, die vorliegende Dissertationsschrift selbst verfasst und keine anderen als die angegebenen Hilfsmittel und Quellen benutzt zu haben.

Sofern im Zuge der Erstellung der vorliegenden Dissertationsschrift generative Künstliche Intelligenz (gKI) basierte elektronische Hilfsmittel verwendet wurden, versichere ich, dass meine eigene Leistung im Vordergrund stand und dass eine vollständige Dokumentation aller verwendeten Hilfsmittel gemäß der Guten wissenschaftlichen Praxis vorliegt. Ich trage die Verantwortung für eventuell durch die gKI generierte fehlerhafte oder verzerrte Inhalte, fehlerhafte Referenzen, Verstöße gegen das Datenschutzund Urheberrecht oder Plagiate.

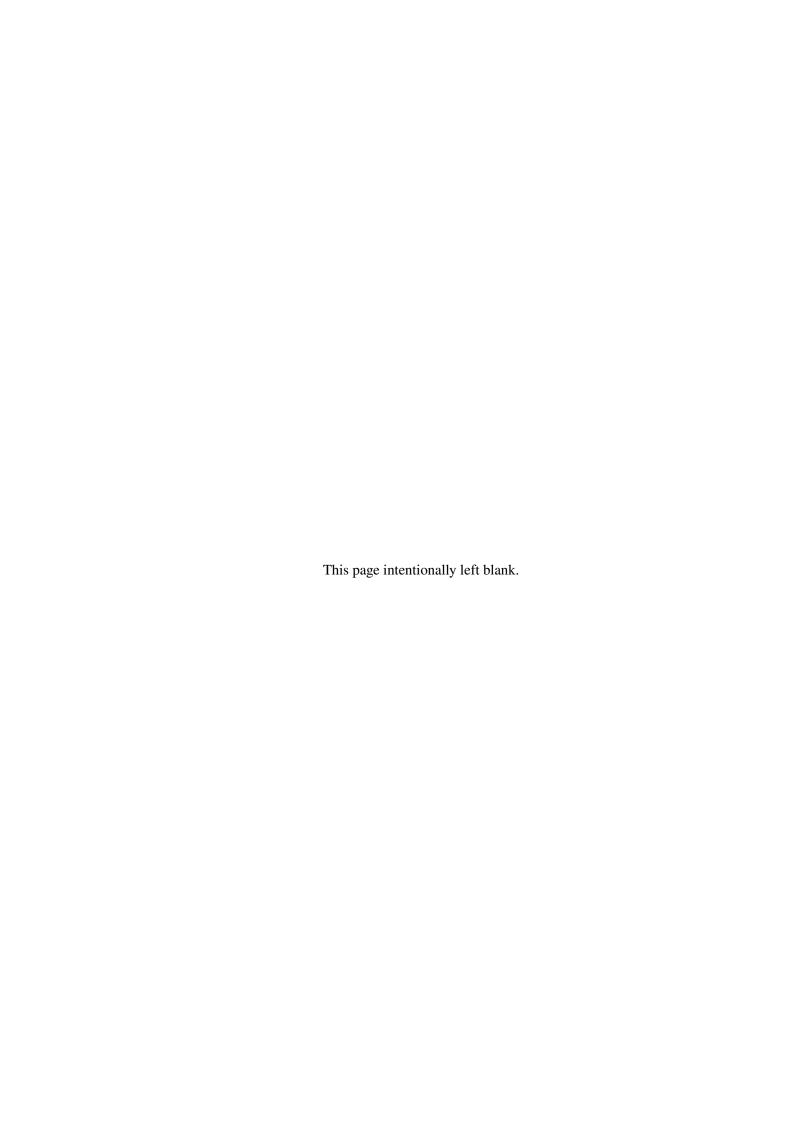
Die Dissertation wurde in der vorgelegten oder einer ähnlichen Form nicht schon einmal in einem früheren Promotionsverfahren angenommen oder als ungenügend beurteilt.

Ich versichere, dass dieses gebundene Exemplar der Dissertation und das in elektronischer Form eingereichte Dissertationsexemplar (über den Docata-Upload) und das bei der Fakultät (zuständiges Studienbüro bzw. Promotionsbüro Physik) zur Archivierung eingereichte gedruckte gebundene Exemplar der Dissertationsschrift identisch sind.

Hamburg, den 25.02.2025,

L. Hube a

(Lars Hübner)

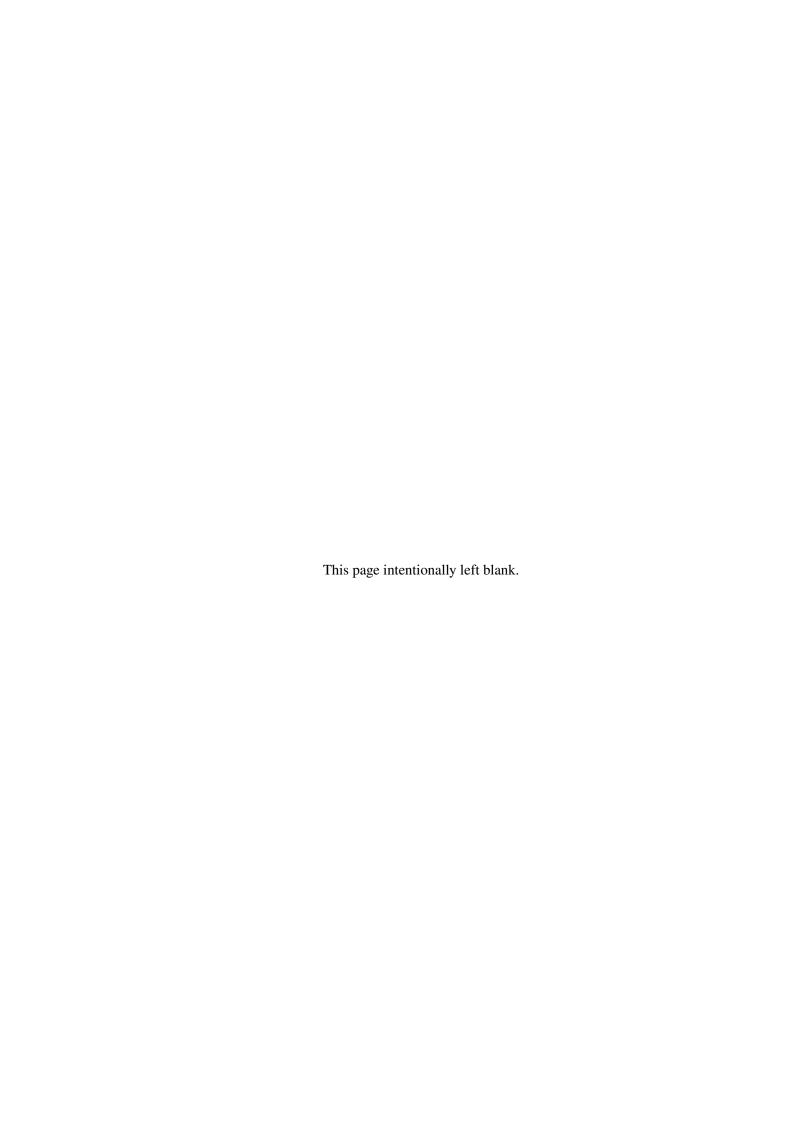


Abstract

Free-electron lasers (FELs) require high-quality electron beams with low energy spread, small emittance, and high peak current to enable coherent amplification of light. Laser-plasma accelerators (LPAs) could offer compact and cost-efficient drivers for FELs. However, the electron beams from state-of-the-art LPAs do not yet meet all FEL beam quality requirements simultaneously as they exit the plasma. Percent-level energy spread, micrometer-scale normalized emittance, and shot-to-shot fluctuations in beam quality pose significant challenges for FEL operation.

In this thesis, a dedicated 25 m-long beamline was designed, constructed, and commissioned to demonstrate free-electron lasing at the *LUX* laser-plasma accelerator. The combination of decompression and chromatic focusing of the electron beams reduces the effective slice energy spread and removes limitations by the beam emittance. Applying both schemes increases the gain in a two meter short ideal undulator from a factor of 5 to a factor of 100 over the spontaneous undulator radiation. FEL simulations with the unaveraged code *Puffin*, suited for ultrashort beams and complex phase-spaces, extended for measured field profiles, predict a factor of 25 in gain in the experiment. Spectrally resolved detection of the FEL pulses increases the contrast by another order of magnitude, which should provide sufficient FEL signal for first lasing experiments at *LUX*.

Beyond numerical validation, experiments were carried out to characterize and refine the beam transport from the plasma-source to the undulator. This included precise quadrupole positioning, determination and correction of strength errors, and undulator alignment to ensure an optimal beam trajectory and matching. These measures provide the necessary beam properties required for future FEL operation at *LUX* and establish a foundation for exploring compact, plasma-based light sources.

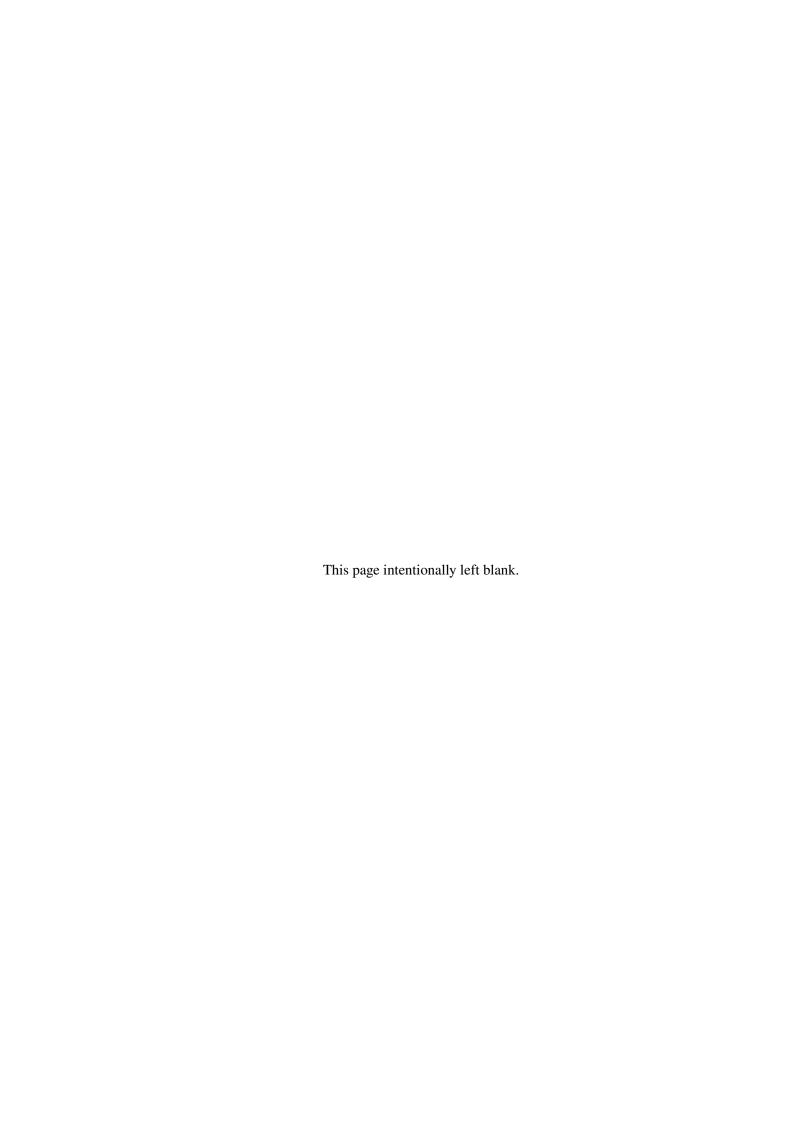


Zusammenfassung

Freie-Elektronen-Laser (FELs) benötigen Elektronenstrahlen hoher Qualität mit geringer Energiebreite, geringer Emittanz und hohen Spitzenströmen. Zukünftig könnten diese durch kompakte und kosteneffiziente Laser-Plasma-Beschleuniger (LPAs) angetrieben werden. Die Stabilität und Qualität der im Plasma erzeugten Strahlen sind mit Energiebreiten im Prozentbereich und gleichzeitigen Emittanzen von Mikrometern nicht ohne weitere Strahlmanipulation zum Treiben eines FELs geeignet.

Im Rahmen dieser Arbeit wurde eine 25 m lange Elektronen-Beamline am *LUX*-Experiment mit dem Ziel der Demonstration eines Plasma-getriebenen FELs entworfen, gebaut und charakterisiert. Die gleichzeitige Verwendung einer Dekompressionsschikane und einer chromatischen Fokussierung in den Undulator reduziert den Slice-Energyspread und erlaubt eine konstante effektive Strahlgröße unterhalb der Emittanzgrenze entlang eines zwei Meter kurzen Undulators. Im Idealfall kann diese Kombination die Verstärkung des Lichtfelds von einem Faktor 5 auf einen Faktor 100 im Vergleich zur spontanen Undulatorstrahlung erhöhen. Realistische Simulationen mit *Puffin*, einem FEL code, der komplexe Strahleigenschaften erlaubt und um die Fähigkeit erweitert wurde, gemessene Felddaten zu verwenden, versprechen eine Verstärkung um den Faktor 25. Der Kontrast zur spontanen Strahlung kann um einen weiteren Faktor 10 erhöht werden, wenn die Messung der FEL Pulse spektral aufgelöst wird. Dies sollte genügend Signal für erste FEL-Experimente bei *LUX* liefern.

Zusätzlich wurden Experimente durchgeführt, um die Elektronen-Beamline feinzujustieren. Die Quadrupol-Magnete wurden zur Elektronenstrahlachse ausgerichtet, ihre Fokussierstärke kalibriert, der Undulator justiert und automatische Strahllagekorrekturen implementiert. Diese Maßnahmen sollten zukünftige FEL-Experimente bei *LUX* ermöglichen.



Contents

1	Intro	duction	1
2	Lase	r-Plasma Acceleration at <i>LUX</i>	5
	2.1	Laser-Plasma Interaction and Acceleration Principle	5
	2.2	Laser System	11
	2.3	Plasma Source	13
	2.4	Electron Beams	13
	2.5	Conclusion	16
3	Elec	ron Beam Dynamics	17
	3.1	Beam Optics	17
		3.1.1 Equations of Motion	17
		3.1.2 First Order Matrix Elements	20
		3.1.3 Internal Bunch Coordinate	23
	3.2	Particle Beams and Beam Envelope	23
	3.3	Phase Space and Emittance	24
	3.4	Bunch Decompression	27
	3.5	Trajectory and Focusing Errors	32
		3.5.1 Quadrupole Offsets	32
		3.5.2 Quadrupole Strength Errors	34
		3.5.3 Magnetic Background Field	35
	3.6	Degrading Effects During Beam Transport	35
		3.6.1 Chromatic Emittance Growth	36
		3.6.2 Slice Energy Spread Degradation	37
		3.6.3 Transverse Space Charge	39
		3.6.4 Longitudinal Space Charge	42
		3.6.5 Synchrotron Radiation	42
	3.7	Transfer Map Calculation for <i>LUX</i> Magnets	46
	3.8	Conclusion	49
4	Free	Electron Lasers	51
	4.1	Electron Motion in the Undulator	52
		4.1.1 Magnetic Field of an Undulator	52
		4.1.2 First Order Motion	53

		4.1.3 Undulator Focusing	
		4.1.4 Beam Size in the Undulator	5
	4.2	Basic Radiation Properties	6
	4.3	High-Gain Theory	1
		4.3.1 Energy Transfer and Microbunching 62	2
		4.3.2 Coupled First Order Equations	3
		4.3.3 Third-Order Equation and Fundamental FEL Scaling 64	4
		4.3.4 Energy Spread and Space Charge in the 1D Limit 68	8
	4.4	3D and Degrading Effects	1
		4.4.1 Limits of the 1 <i>D</i> Theory	1
		4.4.2 Ming Xie Fit	3
		4.4.3 Effects of Short Bunch Length and Superradiance	5
		4.4.4 Undulator and Alignment Errors	9
	4.5	Parameter Optimization	2
		4.5.1 Gain Length Minimization	4
		4.5.2 Undulator Tapering	5
		4.5.3 Phase and Group Velocities	
	4.6	Numerical Estimation	8
	4.7	Conclusion	
5	LUX	Beamline 93	3
	5.1	Design Considerations for the <i>LUX</i> FEL Beamline	4
		5.1.1 Chromatic Matching scheme	
		5.1.2 Requirements to Beam Optics Lattice	6
	5.2	Beam Optics Optimization	7
	5.3	Beamline Components and Diagnostics at <i>LUX</i>	0
		5.3.1 Quadrupoles	3
		5.3.2 Chicane Dipoles	4
		5.3.3 Corrector Dipoles	6
		5.3.4 Spectrometers	7
		5.3.5 Charge and Beam Position Measurement	8
		5.3.6 Undulator	9
		5.3.7 Undulator EUV Radiation Spectrometer	4
		5.3.8 Magnetic Background Field Compensation	5
	5.4	Conclusion	7
õ		-Electron Laser Simulations 119	_
	6.1	Beam Properties	
	6.2	Simulation Setup	
	6.3	Simulation with Idealized Undulator Field	
	6.4	Simulation with Measured Undulator Field	
	6.5	Radiation Pulse Properties	6
	66	Taper Scan	8

	6.7	Conclusion	129
7	Expe		131
	7.1	Quadrupole Positioning	131
	7.2	Quadrupole Strength Calibration	133
	7.3	Trajectory Correction	138
	7.4	Undulator Positioning	138
	7.5	Undulator Radiation	140
	7.6	Conclusion	141
8	Con	clusion and Outlook	143
Bil	oliogr	aphy	147
Lis	st of F	igures	163
Lis	st of T	ables	173
Ac	know	ledgements	175

Introduction

Over the past century, the development of particle accelerators has profoundly influenced numerous fields of science, ranging from materials science, over health, to fundamental physics. A crucial byproduct of particle accelerators, synchrotron radiation, initially considered an unwanted emission, has evolved into a cornerstone technology for studying the structure and dynamics of matter across various scales. This transformation began with the first-generation synchrotron radiation sources in the mid-20th century, which utilized bending magnets within circular accelerators primarily designed for high-energy physics experiments.

As the applications of synchrotron light broadened, subsequent generations of synchrotron sources emerged, increasingly optimized for light production rather than particle physics. By the third generation, facilities were employing advanced insertion devices such as undulators and wigglers to enhance the quality of emitted radiation. These devices manipulate the path of electrons through a periodic magnetic field, allowing for the interference of waves emitted over individual periods. This process significantly increases the emitted radiation's flux and brightness, compared to earlier generations that relied solely on simple bending magnets. The fourth generation of synchrotron radiation sources, including free-electron lasers (FELs) [1], has pushed capabilities further, operating in the ultraviolet and X-ray spectrum to provide unprecedented insights into molecular and atomic structures through coherent and intense light pulses.

Free-electron lasers represent a pinnacle in light source technology, utilizing long undulator sections that allow electrons to interact coherently with their own previously emitted radiation. This interaction results in an energy modulation of the electron beams at the scale of the light wavelength, which translates into a density modulation, while passing through the undulator magnetic field, enhancing the radiation's coherence and intensity dramatically. However, these advanced facilities, such as the *European XFEL* [2], *FLASH* [3], *LCLS* [4], *FERMI* [5], *PAL-XFEL* [6], and *SACLA* [7], embody a significant limitation due to their immense scale and cost, typically stretching over kilometers and costing billions to construct and maintain. This restricts their availability, confining access to a few facilities worldwide.

To enable the coherent amplification and driving a free-electron laser requires an electron beam with exceptionally high beam quality. The key requirements include a low relative energy spread, typically sub-permille, a small normalized emittance, on the order of micrometer, and a high beam current, often exceeding kiloamperes.

Amid these constraints, laser-plasma acceleration (LPA) [8] presents a transformative approach, promising to significantly downscale the physical and financial footprint of accelerator technology. LPA harnesses the intense radiation pressure of a laser pulse to create a charge separation in a plasma medium, forming a wakefield that accelerates electrons to relativistic speeds within a fraction of the distance required by conventional radio-frequency accelerators. This technique, which achieves accelerating gradients on the order of 100 GV/m, three orders of magnitude greater than those possible with radiofrequency accelerators, has marked a pivotal shift towards compact, cost-efficient accelerators. The performance of LPAs was improved over the recent years in terms of energy to multi-GeV [9], percent-level energy spread [10–12], micrometer-level normalized emittance [13] and long-term operation at Hz-rate repetition [14], opening the door to ultra-compact electron accelerators. These properties make LPA beams prime candidates for use as drivers for FELs, although not yet meeting the stringent requirements simultaneously out of the plasma. Further, these developments hint at the possibility of integrating LPA technology with other applications, like novel concepts for light sources [15–17], injectors [18, 19] or linear colliders [20]. Such a combination could potentially overcome the traditional barriers of size and cost of such machines.

Despite these promising advancements, significant challenges remain. Compared to conventional accelerators, state-of-the-art LPAs face difficulties such as the percent-level energy spread and shot-to-shot instabilities in beam quality. Nevertheless, advances in controlling the laser-plasma interaction, particularly the electron injection into the plasma wake [21], pave the way for more stable and reliable electron beams.

The first demonstration of SASE free-electron lasing from an LPA at 27 nm [22] shows that LPAs are able to provide the necessary beam quality to meet the requirements for FEL experiments.

Nevertheless, utilizing LPA beams for FEL applications presents a complex set of challenges. The primary difficulty lies in the transport of an ultra-relativistic electron beam through the beamline without significant degradation of its properties. The unique characteristics of plasma-accelerated beams, such as their broad energy spread and potential for high beam divergence, make this task particularly demanding. In addition to being problematic for driving an FEL itself, the energy variability within plasma-accelerated beams causes significant chromatic aberrations and dispersion, which have to be corrected for. The shot-to-shot jitter in beam quality further complicate the commissioning of the beamline and optimizing the beam transport.

One advanced technique to enhance FEL performance is the decompression scheme [23]. This method involves manipulating the longitudinal phase space of the electron beam, trading increased pulse length for decreased local slice energy spread. A tapered undulator is then used to enhance the coherence of the emitted light, thereby improving the FEL interaction.

In addition to this, advanced focusing schemes can significantly boost the FEL performance. The design and application of a chromatic focusing scheme that makes use of the chirped beams after decompression is content of this thesis. The improvements collectively enable the use of shorter

total undulator lengths on the scale of meters. However, implementing such schemes requires precise control over beam dynamics, has to be supported by diagnostics, and relies on a well-characterized and well-calibrated beamline to ensure that the electron beam is optimally prepared for FEL experiments.

The laser-plasma accelerator *LUX* [24], built at the Deutsches Elektronen-Synchrotron (*DESY*), is dedicated to reliably and reproducibly deliver high-quality electron beams. *LUX* operates at 1 Hz-level repetition rate and generates electron beam with energies of about 300 MeV, emittances on the micrometer-scale and percent-level relative energy spread. It is capable of stable day-long operation, providing high statistics [14].

In the frame of this thesis a 25 m long beamline was designed, built and commissioned, with the goal to demonstrate free-electron lasing from laser-plasma accelerated beams. It features a chicane in combination with a variable-taper undulator and a sophisticated transport beamline with 11 quadrupole magnets for phase space manipulations to bridge the gap to conventional FELs. By utilizing a decompression and a chromatic matching scheme, reducing the impact of energy spread and emittance, it aims to show the startup of FEL amplification within a 2 m short undulator. At *LUX*, several diagnostics are installed to characterize the drive laser, the plasma-source and the electron beams, to tune their individual properties and stabilize crucial parameters.

This work includes theoretical considerations on required beam and longitudinal beam slice properties to enable lasing with the electron beams measured at *LUX*. Potential sources of degradation of beam quality during transport were analyzed and strategies to mitigate these are developed. Simulations of the FEL process with ideal and measured field profiles were performed for the optimized electron beams. Various experiments to characterize and improve the electron beam transport were carried out. Particular attention is given to mitigating beam degradation effects, and to maximize the gain by implementing advanced focusing and decompression schemes.

Thesis Overview

Chapter 2 provides an overview of laser-plasma acceleration, the laser system and plasma source used at *LUX*. The critical beam properties from the accelerator relevant for subsequent beam transport and FEL applications are discussed.

Chapter 3 focuses on the challenges associated with transporting LPA beams. The chapter covers theoretical aspects of beam dynamics, including chromatic effects, emittance growth, and trajectory deviations due to alignment errors. It also presents the beam decompression technique and an analysis of degrading effects such as space charge forces and synchrotron radiation, which influence beam quality during transport.

Chapter 4 discusses the theory of free-electron lasing, outlining the fundamental principles governing FEL interaction, high-gain theory, and microbunching dynamics. The impact of LPA beam properties on FEL performance is analyzed, along with methods to counteract degrading effects such as energy spread and emittance. Strategies for optimizing FEL gain, including undulator tapering and phase-space matching, are examined to assess the feasibility of achieving coherent amplification with plasma-accelerated beams in a short undulator.

Chapter 5 presents the final LUX beamline setup and details its individual components, including the quadrupoles, chicane dipoles, correctors, and diagnostics systems. The design considerations for FEL operation are discussed, particularly the implementation of a chromatic focusing scheme and the requirements necessary to maintain beam quality.

Chapter 6 focuses on FEL simulations to evaluate the expected performance of the LUX beamline. The simulations incorporate realistic beam properties and undulator field errors to predict FEL gain and radiation characteristics at *LUX*. Comparisons between idealized and experimentally measured undulator fields are made to assess their impact on FEL amplification.

Chapter 7 reports on experimental results obtained with the upgraded beamline. The chapter covers the beamline characterization, including quadrupole positioning, strength calibration, and orbit correction. The positioning and alignment of the undulator are discussed, along with measurements of spontaneous undulator radiation. These results represent a crucial step to validating the beam transport and focusing strategies implemented in the LUX beamline.

The thesis closes with a conclusion and outlook in Chapter 8

Laser-Plasma Acceleration at LUX

Laser-plasma acceleration (LPA) utilizes strong electric fields within a plasma generated by high-intensity laser pulses to accelerate electrons to high energies over short distances. This approach provides a viable alternative to conventional particle accelerators, offering the potential for compact, lab-scale setups due to its capability to achieve significantly higher acceleration gradients. This chapter offers an overview of laser-plasma acceleration and its application in the *LUX* experiment. A theoretical introduction to LPA will be provided in section 2.1. Given that the primary focus of this thesis is on the transport and shaping of the electron beam for application in a free-electron laser, only a foundational introduction to LPA is included here. This chapter aims to provide the essential background necessary to comprehend the critical aspects of LPA and their implications for beam transport and beamline design.

The general concept of LPA is divided into two categories: laser-driven and beam-driven plasma acceleration. This chapter will specifically focus on laser-driven acceleration, as used at *LUX*, omitting discussion of beam-driven methods.

Transitioning from the broader context of LPA, the subsequent sections focus on the specific setup at *LUX*, which is divided into three parts: The laser system that generates the high-intensity light pulse is described in section 2.2; the plasma target is discussed in section 2.3; and the properties of the electron beams expected at *LUX* are outlined in section 2.4.

2.1 Laser-Plasma Interaction and Acceleration Principle

A plasma is a state of matter formed by ionized atoms, thus separated into free electrons and ions. This ionization results in a quasi-neutral medium that is electrically conductive and highly responsive to electromagnetic fields. Quasi-neutrality means that despite local fluctuations in charge density, the large-scale balance of charge ensures that plasma behaves as a neutral entity. Introducing an external charge into a plasma distorts the distribution of the surrounding electrons and ions, leading to a concentration of opposite charges that effectively screens the external charge's electric field beyond a certain distance. This phenomenon is known as Debye shielding [25]. The Debye length defines the

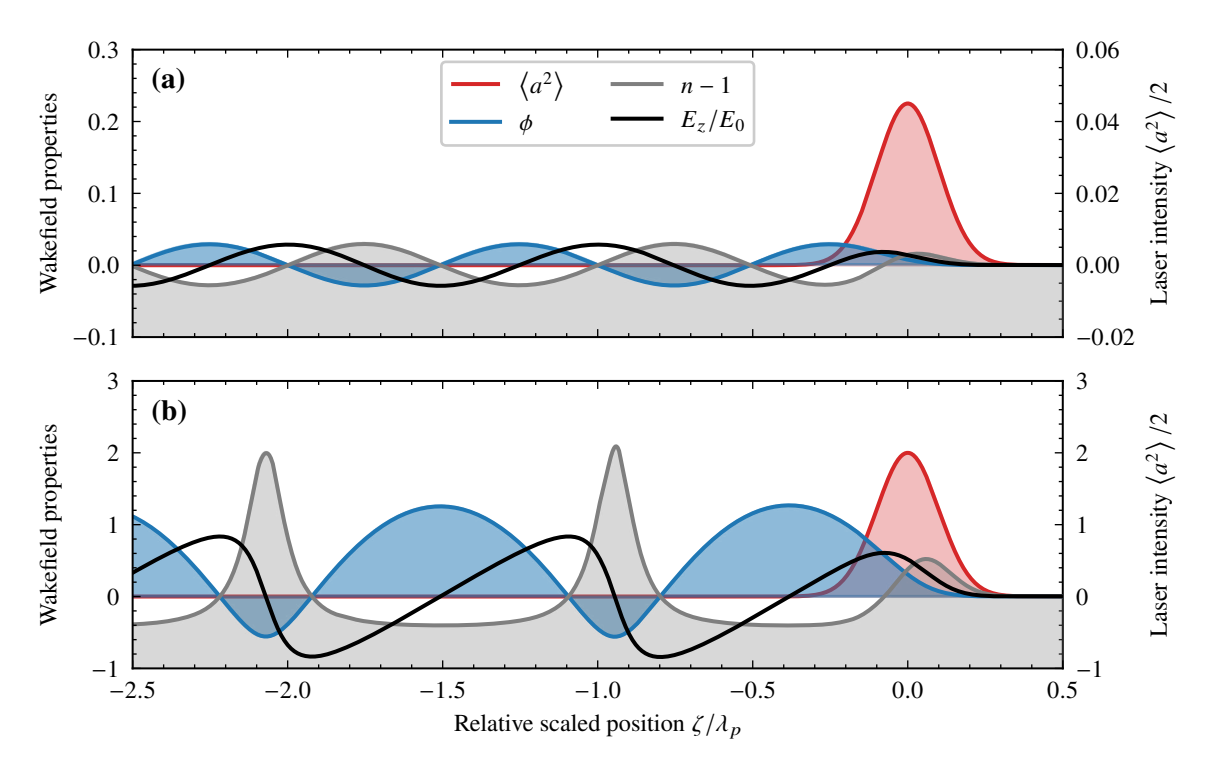


Figure 2.1: Properties of a wakefield generated from a temporally short $(<\lambda_p/c)$ gaussian laser pulse in the 1d limit. The laser pulse propagates to the right and is centered at $\zeta=0$. The spatial scale is normalized to the plasma wavelength λ_p . Displayed are the electric potential ϕ , the electron density modulation n-1, the normalized longitudinal electric field E_z/E_0 and the normalized laser intensity $\left\langle a^2 \right\rangle$ for two cases: (a) Non-relativistic case with laser peak amplitude $a_0=0.3$ (b) Relativistic case with $a_0=2$.

scale over which electric fields significantly influence particle dynamics. It is given by

$$\lambda_D = \sqrt{\frac{\epsilon_0 k_B T_e}{e^2 n_e}} \quad , \tag{2.1}$$

with the vacuum permittivity ϵ_0 , the Boltzmann constant k_B , the electron temperature T_e , the electron number density n_e and the elementary charge e. Further, the neutrality guides how the contributing forces manifest on a macroscopic scale. The behavior of individual particles and collective effects are not independent but are rather dynamically coupled through the plasma's response to perturbations. Therefore, unlike solid, liquid, or gas, plasma often exhibits collective behavior due to the long-range Coulomb forces between charged particles, allowing it to support phenomena such as electric currents, magnetic fields, and waves [26]. Consider a perturbation by some external disturbance, displacing a slice of electrons from its initial position. This creates an electric field with a restoring force causing

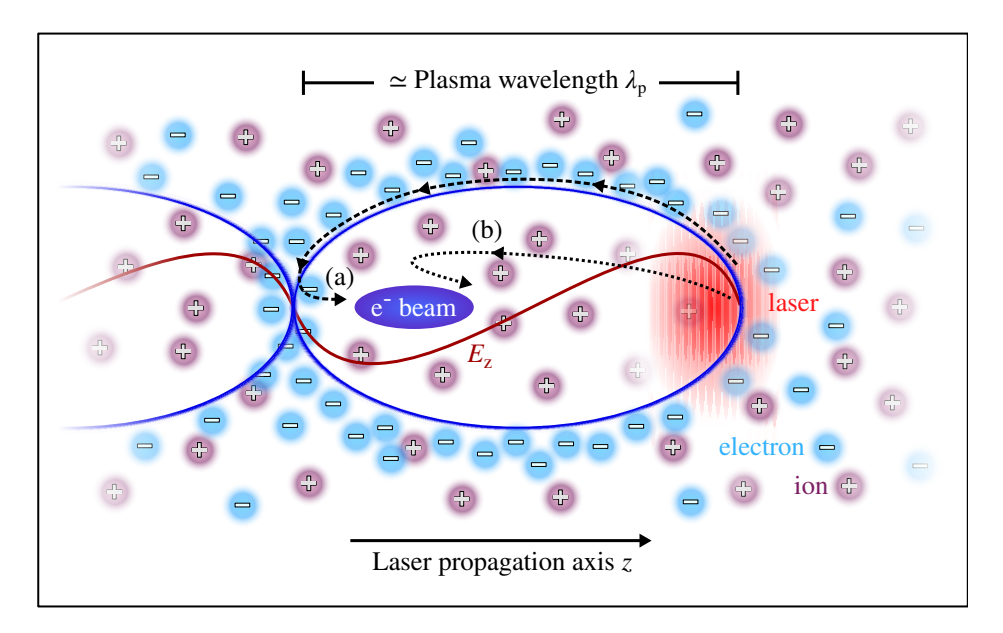


Figure 2.2: Illustration of laser-plasma acceleration. Electrons of the plasma are expelled from high intensity regions of the laser pulse. In response to this expulsion, the electrons oscillate about the propagation axis with a frequency approximately equal to $\sim \omega_p$, generating a density modulation in the plasma with a corresponding electric field trailing the laser pulse. Possible trajectories for electrons getting accelerated in the plasma wake are illustrated for (a) self-injection and (b) ionization injection.

an oscillation with the plasma frequency

$$\omega_p = \sqrt{\frac{e^2 n_e}{\epsilon_0 m_e}} \simeq 56.4 \sqrt{n_e} \,\mathrm{m}^{3/2} \mathrm{s}^{-1} \quad ,$$
 (2.2)

with the electron mass m_e . In the context of Debye shielding, this is also connected to the timescale t_D for the plasma to adjust to a perturbation and recover quasi-neutrality. Comparing the thermal velocity $v_{th} = \sqrt{k_B T_e/m_e}$ to the Debye length shows

$$t_D \simeq \frac{\lambda_D}{v_{th}} = \omega_p^{-1} \quad . \tag{2.3}$$

If an external electromagnetic wave that changes slowly compared to the response of the plasma, i.e. has lower frequency than ω_p , interacts with the plasma, it gets reflected, as the field is effectively shielded from penetrating the plasma. Putting this into context with eq. (2.2), a critical plasma density

$$n_c \simeq 10^{15} \lambda^{-2} \text{m}^{-1} \tag{2.4}$$

is found. Electromagnetic pulses with wavelength λ can pass through the plasma, if it is underdense, i.e., its density is less than the corresponding critical plasma density $n_e < n_c$, which then behaves like a refractive medium. Exciting the plasma with such an electromagnetic field can give rise to

accelerating fields of [27]

$$E_0 = \frac{\omega_p m_e c}{e} \simeq 96 \times 10^{-3} \sqrt{n_e} \text{ Vm}^{1/2} \quad ,$$
 (2.5)

referred to as the cold non-relativistic wave breaking [28]. Using a typical value for a plasma density $n_e \simeq 10^{18} \, \mathrm{cm}^3$ yields an accelerating field of up to $E_0 \simeq 100 \, \mathrm{GV/m}$, about 3 orders of magnitude larger than accelerating radio-frequency cavities which operate at levels of several 10 to 100 MV/m [29]. Thus, maintaining the acceleration process over a short distance on the scale of cm can yield electron beam energies of hundreds of MeV to several GeV.

In order to describe how an external electromagnetic wave interacts with plasma and propagates through it, a starting point is the Lorentz force: $\frac{d\mathbf{p}}{dt} = -e\left(\mathbf{E} + \mathbf{v} \times \mathbf{B}\right)$. For simplicity assume a linearly polarized wave with $\mathbf{E} = E_0 \sin\left(\phi\right) \hat{\mathbf{e}}_\perp$ with the phase $\phi = k_z z - \omega t + \phi_0$. The magnetic field is linked to this via the electromagnetic wave equation and relates to this as $\mathbf{B} = (\mathbf{k} \times \mathbf{E})/\omega$. Here z is the propagation axis, \mathbf{k} the wave vector perpendicular to k, and ω the waves frequency. The magnetic component is suppressed by $\omega k = 1/c$ and therefore only relevant for relativistic particle speeds. In the non-relativistic limit, the dominant motion is oscillatory along the polarization axis of the electromagnetic field with momentum $\mathbf{p} = a m_e c$, referred to as the quiver motion. a is the dimensionless normalized magnetic vector potential $\mathbf{a} = e \mathbf{A}/(m_e c)$ for the corresponding magnetic vector potential \mathbf{A} . The amplitude a_0 , representing the amplitude of this normalized vector potential, is given by

$$a_0 = \frac{eE_0}{m_e\omega c} \simeq 8.5 \times 10^{-6} \sqrt{I_0} \lambda \text{ W}^{-1/2} \quad ,$$
 (2.6)

where the relation $I_0 = \epsilon_0 c \left\langle E^2 \right\rangle = \epsilon_0 c E_0^2 / 2$ was used for the intensity. As a_0 approaches or exceeds unity $(a_0 \gtrsim 1)$, electron velocities can become relativistic. Consequently, interactions with the magnetic field **B** become more significant.

Apart from the quiver motion the electrons experience another acceleration driven by

$$\boldsymbol{F}_{p} = -\frac{m_{e}c^{2}}{2}\nabla\boldsymbol{a}^{2} \quad , \tag{2.7}$$

known as the ponderomotive force. It effectively repels particles from areas of high intensity to areas of lower intensity. This force is fundamental in shaping the behavior of particles under the influence of high-intensity fields, influencing the dynamics in plasma-based acceleration systems. As the ponderomotive force scales with the gradient of the Intensity $F_p \propto \nabla I$, it is most influential for electromagnetic pulses with steep spatial variation. Another thing to note is that the ponderomotive force is proportional to the inverse of a particle's mass. It will therefore primarily act on electrons and not the much heavier ions. This validates the focus on electrons in the above discussion.

From the previous considerations, it becomes evident that for high intensity lasers with $a_0 \gtrsim 1$, the combined effects of E and B result in both transverse and longitudinal acceleration. Due to the plasma's intrinsic restoring forces aiming to restore quasi-neutrality, the electrons are accelerated back to the propagation axis and an oscillatory motion is induced. The frequency of this oscillation is on

the order of the plasma frequency ω_p , resulting in a density modulation trailing the laser pulse, whose periodicity is about the plasma wavelength

$$\lambda_p = \frac{2\pi c}{\omega_p} \simeq \frac{3.3 \times 10^7}{\sqrt{n_e}} \text{m}^{-1/2} \quad .$$
 (2.8)

Those plasma density modulations that follow the laser pulse are commonly referred to as the plasma wakefield, hence the laser-driven interaction also being called laser-wakefield acceleration (LWFA). At an electron density $n_e \simeq 10^{18} {\rm cm}^{-3}$ the length scale of these modulations is approximately $\lambda_p \simeq 33 \, \mu {\rm m}$. Further, the electric potential and associated electric field generated by the density modulation have an axial gradient, which is crucial for particle acceleration. Figure 2.1 shows the interaction of a gaussian laser pulse with plasma under two conditions: a non-relativistic, weak intensity regime $a_0 = 0.3$ shown in (a) and a relativistic, high intensity regime with $a_0 = 2$ depicted in (b), based on a 1d model [30]. In the weak intensity scenario, the resulting density modulation, electric potential, and longitudinal electric field exhibit a sinusoidal pattern. The energy transferred to the electrons' momentum and their displacement are minimal, leading to weak density modulation and low accelerating fields. In contrast, the high-intensity scenario features strong modulation and significant accelerating fields, which trail the laser pulse with a periodicity approximately equal to λ_n . As the electrons return to the axis and accumulate in the high density region, some undergo scattering and eventually end up with just the right amount of forward momentum to get into the accelerating phase of the electric field trailing the laser pulse. A schematic of this laser-plasma interaction is shown in fig. 2.2 with this type of injection, called self-injection, illustrated by a dashed line (a). While this self-injection mechanism is straightforward to implement, requiring only a high a_0 , the inherent randomness of the scattering process results in beams with only moderate properties [31].

In addition to the longitudinal and the ponderomotive forces, radially (de-)focusing forces play a crucial role, arising from the finite transverse profiles of the laser pulse. These forces are shifted in phase by $\pi/2$ relative to the accelerating gradient. Consequently, only those electrons that are in proper phase with both the accelerating and focusing fields can be trapped and accelerated. The region where an electron simultaneously experiences both, acceleration and focusing, spans approximately $\sim \lambda_p/4$ [27]. As a result, particle beams accelerated in such fields are inherently short, typically on a length scale of μ m [32–34]. Moreover, the finite transverse extension of the wakefield and spot size of the laser pulse constrain the spatial distribution of electrons within the accelerating field. With a laser focus size on the order of $100 \, \mu$ m², the expected electron beam cross-section is on a similar scale of $\lesssim (10 \, \mu$ m)².

While the generation of plasma was not previously discussed, note that the intensity threshold required to ionize a material is typically $\leq 3.5 \times 10^{16} \, \text{W/cm}^2 [30]$. Therefore, a laser capable of exciting the plasma will also inevitably ionize the gas prior to this excitation. Modern laser systems can deliver pulse power exceeding > 100 TW. When such a high power laser is focused to a small spot size on the order of $100 \, \mu \text{m}^2$, intensity levels of $10^{20} \, \text{W/cm}^2$ are achievable, sufficient to ionize a gas and accelerate short electron bunches to high energies. At these high intensities, particularly when using gases with higher atomic number Z, multiple ionization can occur. Electrons from inner shells are stripped off at the most intense regions of the laser pulse. These electrons can then be directly trapped

right in the wakefield. This process is known as ionization injection. The mechanism is depicted as a dotted line (b) in fig. 2.2. On one hand, with increased laser intensity, ionization can occur off-peak of the laser electric field. In such cases, electrons may experience undesirable amounts of transverse acceleration. On the other hand, if laser and gas parameters are properly tuned, the ionization of inner-shell electrons occurs just at the peak of the laser pulse, avoiding the gain of transverse momentum [35]. Consequently, electrons accelerated this way can have low transverse momentum, resulting in a beam with reduced divergence and enhanced beam quality in terms of emittance, i.e., occupied phase space volume, when exiting the plasma.

Another aspect to consider is the choice of gases used in laser-plasma acceleration. Utilizing a high atomic number Z for the whole plasma source can result in continuous ionization-injection and acceleration, which often leads to a large energy spread among the accelerated electrons. However, by combining a mixed gas (high and low Z) and a pure gas (low Z), the ionization process can be localized [36]. The benefits of this approach are twofold: Firstly, compared to the self-injection scheme, it offers a highly controllable and tunable method of injection. This control allows for precise adjustments to the ionization dynamics, enhancing the reproducibility and consistency of the acceleration process. Secondly, by transitioning to a lower atomic number along the laser propagation axis, the process of ionization by this method can be intentionally stopped. This action ensures that only the electrons already trapped are available for subsequent acceleration, effectively reducing the energy spread of the accelerated beam.

This might be feasible, as more electrons trail the laser pulse in the wake. Due to their charge the shape of the electric field is modified up to cancellation, at which no more charge is accelerated. This process, called beam loading, sets an upper limit to the number of electrons. As investigated in [37] this limit is given by

$$N_{e,\text{max}} \simeq 31 \times 10^6 \lambda \sqrt{P} \text{W}^{-1} \text{m}^{-1} \quad ,$$
 (2.9)

with the laser power P. For a 100 TW laser at 800 nm, it would be possible to inject up to 400 pC before the accelerating field vanishes. However, it is often more viable to operate at a fraction of the maximum possible charge to ensure that all trapped electrons are accelerated evenly to high energies [21]. Considering electron bunches of length $\sigma_z < \lambda_p/4 \simeq 8 \, \mu m$ and charge $Q \gtrsim 40 \, pC$, or $10 \, \%$ of the maximum, the resulting current can exceed $I > 1.5 \, kA$.

Another consequence of the laser passing through the plasma is the temporary nature of the density modulation, which dissipates some time after the laser has passed. Consequently, the accelerating cavity must be formed anew for every shot. Variations in the laser or plasma parameters lead to inconsistencies in beam properties from shot to shot, resulting in beams of varying quality.

Concluding from this section, electron beams produced by laser-plasma acceleration are expected to reach energies in the range of hundreds of MeV to several GeV. These beams are characterized by their short duration, on the order of μm or fs, resulting in high peak currents of several kA. Additionally, they can exhibit low emittance, typically on the order of nm.

2.2 Laser System

To drive the LPA process outlined above, a high power, short pulse laser is required. At *DESY* the *ANGUS* laser system provides such for the laser-wakefield accelerator *LUX*. *ANGUS* operates on the principle of chirped pulse amplification [38] and utilizes titanium-doped sapphire [39] as gain medium. It has been designed for the generation of 25 fs pulses with high peak powers up to 200 TW level at a repetition rate of up to 5 Hz. When focused down to small spot sizes of $(25 \,\mu\text{m})^2$ FWHM, intensity levels up to $a_0 \simeq 4$ could be achieved.

However, due to limitations from heating related degradation at high pulse energies and intensities [40], typical operation is limited to $\lesssim 100 \, \text{TW}$, i.e. $\sim 3 \, \text{J}$ at 30 fs pulse duration, operating at 1 Hz. Under these reduced conditions compared to its initial design, *ANGUS* can still deliver laser intensities of $a_0 \simeq 2$, sufficient to drive a non-linear wake-field and accelerate electrons to relativistic energies.

The initial seed is provided by the seed laser *MALCOLM*, which works on the principle of optical parametric chirped pulse amplification, providing a pulse of high spatio-temporal quality and stability [41]. It combines a mode-locked oscillator and regenerative amplifier in one device, and replaced individual systems used in *ANGUS* before. It delivers pulses of 40 µJ energy and 200 fs duration.

Before entering the amplifier chain, the pulse is stretched to 400 ps and $4\,\mu J$ after shaping its spectral phase in an acousto-optical programmable dispersive filter (AOPDF) [42], which pre-compensates gain-narrowing and red-shifting in the later amplifier stages [40]. The energy lost in these processes is recovered to $100\,\mu J$ using a two-pass booster amplifier. A pulse picker reduces the repetition rate further to the final value of 1 Hz. Three multi-pass amplifiers are used to raise the energy to 45 mJ, then to $1.3\,J$ and finally up to $6\,J$. The repetition rate of these amplifiers is limited to $5\,Hz$, as their pump lasers, which are driven by gas discharge flash lamps with large heat dissipation, cannot operate at higher rates.

After amplification, the pulse energy can be attenuated to desired energy levels with a motorized waveplate and thin-film polarizers. Before sending the laser to the plasma source, it is magnified to ~ 80 mm in order to reduce the fluence and prevent damage to optical components. Finally, the laser pulse is compressed using gold-coated diffraction gratings to its final length to achieve the desired power. The compressed pulse is then transported over a distance of 35 m to the LUX target chamber, where it is focused into the plasma target using an off-axis parabolic mirror. The pulse is polarized in the horizontal x-plane at the target.

An adjustable lens in the final magnifier telescope is used to tune the laser focus position. Further, a deformable mirror (DM) before the compressor corrects for wavefront aberrations. These aberrations are measured while operating *LUX* by utilizing mirror leakage through the final focusing off-axis parabolic mirror.

Diagnostics are placed after each amplifier to monitor the laser performance, enabling the operation of a feedback loop that stabilizes the input to the subsequent amplifier. This setup ensures stable and reliable day-long operation for driving the *LUX* accelerator [14].

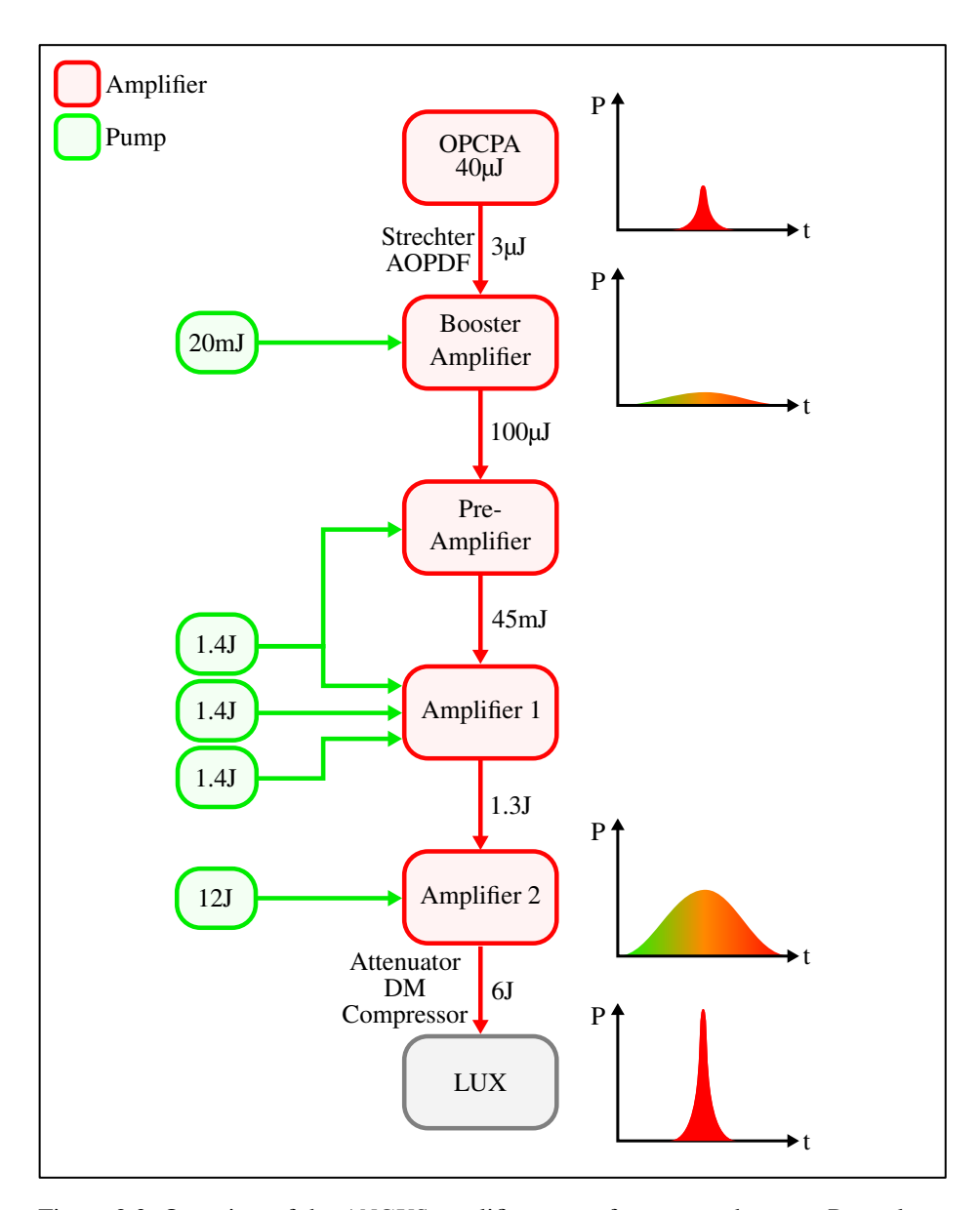


Figure 2.3: Overview of the *ANGUS* amplifier stages from top to bottom. Pump laser energies are indicated in green on the left. The temporal shape of the laser pulse is schematically depicted on the right. The color gradient should illustrate the temporal chirp of the pulse. The pulse is provided by the optical parametric chirped pulse amplification (OPCPA) frontend and stretched in time before being amplified to higher energy levels in the subsequent amplifier stages. Finally, before the beam is sent to *LUX* and the plasma source, it is recompressed to achieve the targeted power levels and short pulse duration.

2.3 Plasma Source

This section describes the basic properties of the plasma source. For a detailed discussion on shaping the density profile at *LUX*, please refer to [36, 43].

The plasma source at *LUX* consists of a capillary milled into a sapphire crystal. Unlike gas jets, which provide short bursts of highly pressurized gas [44], a capillary provides continuous flow of gas through dedicated inlets and outlets. The continuous flow within the capillary prevents rapid changes in pressure or velocity, which benefits the stability of the laser-plasma interaction. Furthermore, this steady state allows for measurement of the pressure, and consequently the plasma density. This is done at *LUX* via pressure gauges attached to the plasma source. The gas mixing and gas flow, and thus the plasma density are controlled by regulation valves and monitored with mass flow meters. A mixture of hydrogen and nitrogen, with typically up to 10 % nitrogen, is supplied to the first gas inlet, while the other inlets are fed with pure hydrogen gas.

The injection method indicated in section 2.1 and employed at LUX is called localized ionization injection [36]. A mixed gas consisting of hydrogen and a small percentage of nitrogen is introduced at that side of the capillary, where the laser pulse enters. Ionization injection is triggered only in this region of high nitrogen concentration. The length of this region controls the duration of ionization injection and the amount of trapped electrons. Beyond this, a longer section contains pure hydrogen gas, where no further ionization injection occurs, allowing the already trapped electrons to be accelerated. The structure of the capillary is illustrated in fig. 2.4 (a). On the lower and upper side of the graphic the gas inlets and an outlet are indicated respectively. The total length of the capillary is 5 mm and features a rectangular channel of $500 \,\mu m \times 500 \,\mu m$. A possible configuration of gas distribution is shown in fig. 2.4 (b). In addition to the previously discussed properties, the dip in plasma density between the mixed gas and pure hydrogen sections causes a change in plasma wavelength according to eq. (2.8). As a result, the wakefield gets elongated and then shortened again during the transition to pure hydrogen. This enhances electron injection in the mixed-gas region while suppressing it in the pure hydrogen region, thereby improving the localization of the ionization injection process. This approach can reduce the energy spread and separate electrons injected via ionization from those self-injected in the pure hydrogen region based on their energy. At the end of the plasma, a smooth transition to the surrounding vacuum is essential. An abrupt change to zero density would cause immediate transverse expansion of the beam. By allowing the plasma density to gradually decrease to zero, the transverse focusing forces also diminish progressively. This gradual transition helps preserve beam quality and provides a lensing effect that reduces the divergence of the beam as it exits the plasma [45]. By fine-tuning the interplay between the laser parameters of the ANGUS system and the plasma properties of the source, high-quality electron beams can be produced.

2.4 Electron Beams

A particle distribution from a particle-in-cell (PIC) simulation [46] is used as a reference for optimizations, estimations and tracking throughout this thesis. The initial beam was generated with FBPIC [47] by S. Jalas, with laser and plasma properties as expected in the experiment [43]. The

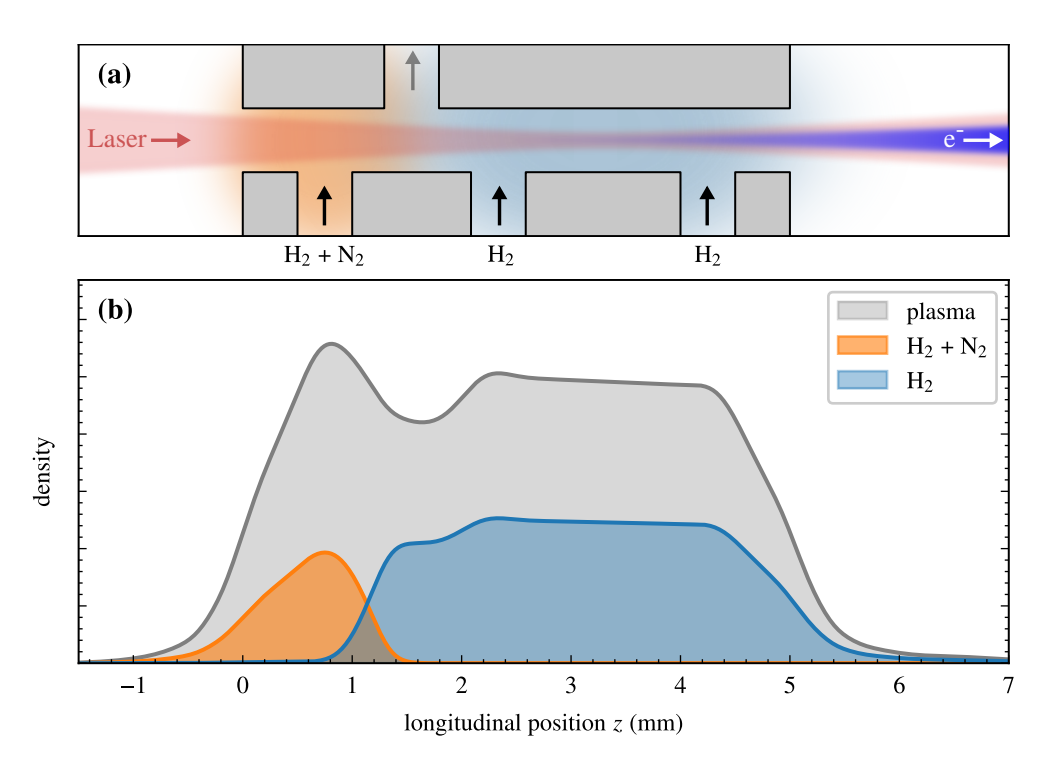


Figure 2.4: Illustration of (a) showing gas inlets at the bottom, an outlet at the top (in the experiment on the side), and the laser envelope propagating to the right, and (b) the longitudinal plasma density profile. Shown are pure hydrogen gas H_2 (blue), mixed gas doped with nitrogen $N_2 + H_2$ (orange) and resulting plasma density (grey).

particle distribution and its corresponding quantities were matched to the experimental data from previous work at LUX [21, 48, 49]. This involved rescaling the projected transverse beam sizes and divergences, charge, energy, and projected energy spread to their observed values. The exact structure of the 6D distribution, particularly the longitudinal profile, bunch length, and current, are not experimentally accessible and are kept as obtained from PIC simulations. Based on the discussion in section 2.1, these values are plausible, and effects related to energy stability, which scale with the bunch length, were observed experimentally and found to align with simulation results [50]. These beam properties represent what is referred to in this thesis as LUX beam reference parameters, summarized in table 2.1. The corresponding distribution is shown in fig. 2.5, with projections onto the horizontal and vertical position and divergence displayed in (a) and (b), and longitudinal position and energy as relativistic gamma factor shown in (c). It is important to note that the usual measure of spread, the second central moment, is sensitive to the presence of tails in the energy distribution. Therefore, to accurately assess the energy spread, the aforementioned rescaling for the energy was performed using robust measures of scale [51], to avoid artificially inflating the energy spread. This method is also used in the experiment to determine the energy spread. Parameters were confirmed with the upgraded setup at LUX, where applicable, and are presented later in chapter 7. The current profile is approximately given by a flat top distribution of about 6.8 µm length with an average current of 2 kA.

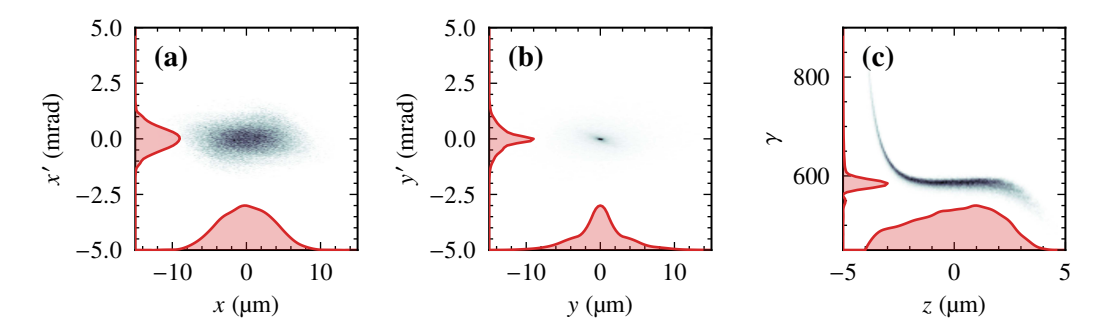


Figure 2.5: Transverse and longitudinal distributions from a particle-in-cell simulation with laser and plasma properties matching those used at *LUX*. (a) Horizontal position and angle, (b) Vertical position and angle, (c) Longitudinal position and total energy. Raw data from simulation was provided by S. Jalas. The beam distribution was rescaled to match experimentally observed parameters. The curves represent the projected 1*D* distributions to each individual coordinate.

Table 2.1: *LUX* beam reference parameters. Values were obtained from measurements, if possible and else taken from simulations.

parameter	symbol	value
	-,	
mean kinetic energy	E_0	300 MeV
relative total energy spread	σ_E/E_0	1.0 %
rms transverse beam sizes	σ_x, σ_y	3.5 µm
rms transverse beam divergences	$\sigma_{x'},\sigma_{y'}$	0.5 mrad
rms transverse normalized emittance	$\epsilon_{n,x}, \epsilon_{n,y}$	1.0 mm mrad
rms bunch length	σ_{ζ}	1.8 µm
rms bunch duration	σ_t	6 fs
charge	Q	45 pC
beam peak current	I_p	2.5 kA

This reference case represents electron beams that are considered to be of good quality from the LUX experiment, characterized by low energy spread, small emittance and high charge (see chapter 3 for definitions of these quantities). Naturally, beams from LPA exhibit fluctuations in their parameters, and not all beams are expected to be suitable for driving an FEL with the setup used at LUX. After tuning the laser system and the plasma source parameters, approximately the best 10% of the beams can deliver such quality [21, 48–50]. These high-quality beams are the primary focus for the beamline setup and FEL estimations. While beams of lesser quality may still be used for FEL applications, they would likely result in lower performance. The objective is not to demonstrate that every beam from LUX can drive an FEL, but rather that the reasonably good beams, which occur frequently, are

suitable for this purpose. Overall, achieving high statistics through stability and long-term operation [14] is a key characteristic of the *LUX* experiment. At an operating rate of 1 Hz, a sufficient number of beams are expected to meet the required parameters.

2.5 Conclusion

This chapter provided an overview of the fundamental principles of Laser-Plasma Acceleration, emphasizing the role of high-power, short-pulse lasers in driving the acceleration process. The *ANGUS* laser system, with its capability to deliver intense pulses, serves as the driver for generating high-quality electron beams at *LUX*. The expected beam properties, including percent-level energy spread, mm mrad emittance, and above-kA current, make these beams promising candidates for applications such as Free-Electron Lasers. While the inherent variability of LPA beams presents challenges, optimizing laser parameters and plasma conditions can produce beams with the desired characteristics. This chapter also highlighted the importance of stability and long-term operation. The insights provided here lay the groundwork for a more detailed exploration of beam manipulation and optimization in subsequent chapters, where the potential of LPA-driven beams and their suitability for FEL applications will be examined.

Electron Beam Dynamics

High-quality electron beams produced by laser-plasma acceleration have potential applications in various fields, including medical imaging, materials science, high-energy physics or light sources. However, these beams cannot be used directly as they emerge from the plasma. They need to be properly shaped and directed to their intended applications while preserving their quality.

The field of beam transport can bridge the gap between the plasma source and the target applications. However, transporting LPA beams presents unique challenges due to their inherent properties, as outlined in the previous chapter. These characteristics complicate the transport process and potentially degrade beam quality. Understanding the potential degrading effects, whether stemming from the beam itself or the beamline, is essential for refining theoretical models and optimizing transport strategies.

This chapter gives an overview about the basic concepts of particle beam transport. It contains a brief introduction to the mathematical approach used to derive the accelerator equations of motion in section 3.1. The basic properties of beams are described in section 3.2 and section 3.3. Given the importance of bunch stretching in the demonstration scheme for an FEL used in this thesis, this concept is explained in detail in section 3.4. Potential effects that may degrade beam quality during transport from the plasma source to the undulator are examined in section 3.5, which describes the impact of beamline components on the beam, and section 3.6, focusing on collective beam effects. Finally, a method for refining the transport model from measured field profiles is presented in section 3.7.

3.1 Beam Optics

The field of beam optics in accelerators addresses a wide range of topics. Here, only aspects relevant to this thesis and transport of laser-plasma accelerated electron beams are covered.

3.1.1 Equations of Motion

In accelerators, a primary interest is the control and transport of particle beams. A fundamental starting point to describe the beam dynamics in an accelerator is the Lorentz force equation. It expresses the behavior of individual charged particles within an accelerator due to electric and magnetic fields \boldsymbol{E}

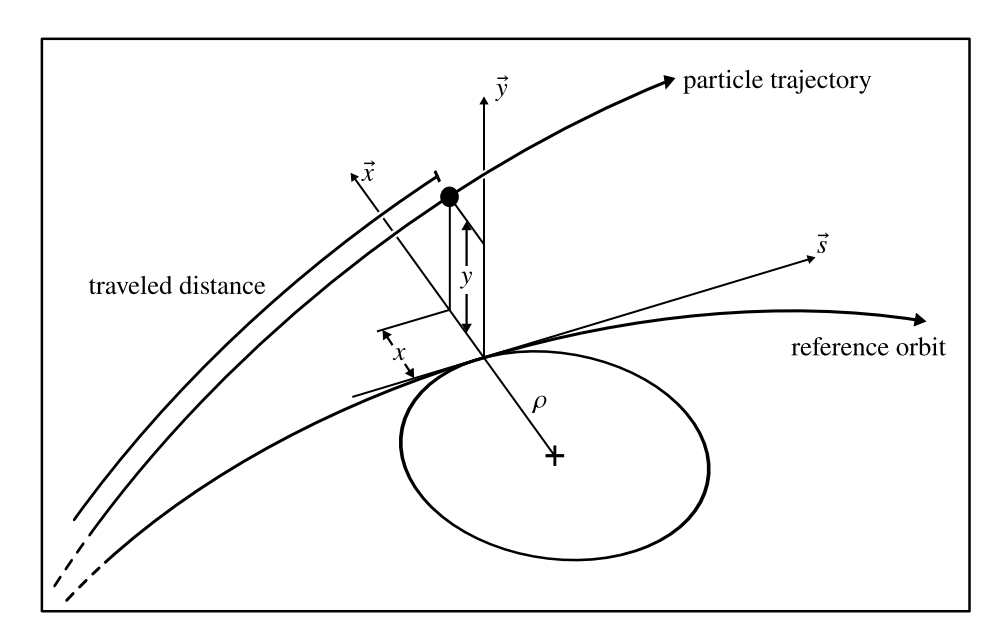


Figure 3.1: Illustration of a curved reference orbit with local bending radius ρ (not to scale for better visualization). The position of a particle is given relative to a local reference frame moving along with the reference orbit.

and \boldsymbol{B} acting upon them by the relation

$$\frac{\mathrm{d}\boldsymbol{p}}{\mathrm{d}t} = q\left(\boldsymbol{E} + \boldsymbol{v} \times \boldsymbol{B}\right) \quad . \tag{3.1}$$

While this equation fully describes the force on and the motion of a single charged particle in an electric field, it cannot be solved analytically for arbitrary fields, but only for specific configurations. Further, solving the equation by numerical integration for a large number of particles is often impracticable and offers limited conceptual insight into how specific components influence a particle beam in an accelerator as a whole. To enhance understanding, it is more practical to find a transformation \mathcal{M} , that describes the propagation through an accelerator component and maps the initial coordinates of a particle to its final coordinates. These transfer maps characterize how each beamline component influences particle trajectories. A common approach to deriving these transformations involves rewriting the Lorentz force into a power series expanded around a reference orbit, a technique well-documented in classical accelerator physics literature [52]. The reference orbit, defined by a local co-moving coordinate system and typically aligned with the local curvature of the motion, traces the path of a reference particle characterized by momentum $p_0 = \beta_0 \gamma_0 m_e c$ with the Lorentz factor γ_0 and the velocity $\beta_0 c$. An illustration for such reference orbit is shown in fig. 3.1, with a local co-moving coordinate system being aligned to it at any position s along this orbit in the accelerator. For a purely magnetic field, the curvature of this orbit is derived by equating eq. (3.1) to the centripetal force, defining the (signed) bending radius ρ as:

$$\frac{1}{\rho} = \frac{qB}{p_0} = -\frac{cB[T]}{p_0[eV/c]} \quad , \tag{3.2}$$

This expression indicates that a curved reference trajectory is inherent whenever the path traverses through a magnetic field. Without loss of generality, the curvature can be assumed to be in one plane only, for example the horizontal direction x, as other configurations only differ from this by rotations. In this frame, positions and momenta of particles may be defined relative to the reference particle with coordinates

$$\mathbf{r}(s) = (x(s), x'(s), y(s), y'(s), l(s), \delta(s))^{\mathsf{T}}$$
 (3.3)

Here, $x' = dx/ds = p_x/p_s$ and $y' = dy/ds = p_y/p_s$ represent the changes in transverse position. The path length difference is denoted by l, and the relative deviation in energy by δ , where $p = p_0(1 + \delta)$ describes the momentum in terms of the reference momentum p_0 .

At *LUX*, *x* and *y* denote the horizontal and vertical position, respectively. Given that *LUX* is a linear accelerator, the coordinate *s* follows a straight trajectory, except when the reference particle takes intended detours from such straight path in a magnetic chicane. To distinguish this path from the longitudinal distance measured from the plasma source in a Cartesian coordinate system, the latter is referred to as *z*.

By assuming that the transverse coordinates and the momentum deviation in eq. (3.3) remain small, i.e. $|x|, |y| \ll |\rho|, |x'|, |y'| \ll 1$, and $|\delta| \ll 1$, the transfer map \mathcal{M} for any beam optical element is approximated using a Taylor series [53]:

$$r_i(s) = C_j(s) + \sum_{j=1}^6 R_{ij}(s)r_j(0) + \sum_{j,k=1}^6 T_{ijk}(s)r_j(0)r_k(0) + \dots$$
 (3.4)

In this expansion C, R and T represent the zeroth, first and second order elements of the Taylor expanded transfer map, respectively. The zeroth order contribution C is often dismissed, as the reference orbit is defined to have $C_j = 0$. It is mentioned here, due to its appearance if the on-axis field does not coincide with the field defining the reference trajectory, such as in cases of misalignment or component errors that introduce an unexpected kick to the trajectory. Similarly, magnetic fields of accelerator components are expanded as a series about the reference axis to provide an analytical form useful for beam dynamics calculations:

$$B_x = B_{x,0} + \left. \frac{\partial B_x}{\partial x} \right|_{x=0} x + \left. \frac{\partial B_x}{\partial y} \right|_{y=0} y + \dots$$
 (3.5)

and the other coordinates accordingly. The constant magnetic field $B_{y,0}$ relates to the horizontal deflection of a particle from a dipole field component and the bending radius according to eq. (3.2). The first derivatives in eq. (3.5) along transverse directions correspond to focusing and defocusing field components associated with magnetic quadrupole fields with gradient $g = \partial B_x/\partial y$. To facilitate a formulation that is independent of the reference momentum, these components are normalized using the ratio $b_i = q/p_0B_i$, analogous to the bending radius.

For electrons with negative charge q = -e, this defines a normalized gradient $K_1 = \partial b_x/\partial y = \partial b_y/\partial x$, also referred to as quadrupole strength. With this notation the equations of motion derived from eq. (3.1), expanded up to first order in the particle coordinates, become the linear ordinary differential equations [54]:

$$x''(s) = -(K_1 + \frac{1}{\rho^2})x(s) + \frac{\delta}{\rho}$$
(3.6)

$$y''(s) = K_1 y(s) (3.7)$$

These differential equations incorporate effects solely from dipole and quadrupole fields, along with energy deviations. Typical magnetic field configurations imply that specific terms in the expansions are negligible, such as the B_z field component, and therefore omitted. The inhomogeneous part δ/ρ of eq. (3.6) introduces a deviation in the motion for particles with energies different from the reference. The deviation to the reference orbit introduced by this term is referred to as the dispersion. It is of particular interest for laser-plasma accelerators like LUX, whose beams commonly show percent-level variations in particle energy.

3.1.2 First Order Matrix Elements

Under the assumptions used, the x and y components do not mix at first order, permitting the independent treatment of the transverse planes (x, x') and (y, y'). First-order solutions to the equations of motion can be concisely represented as a matrix equation with the coordinate vector from eq. (3.3) as $\mathbf{r}(s) = R(s)\mathbf{r}(0)$ [55]. In the following the entries of R will be shown for free drift, quadrupoles, and dipoles of a given length L.

Drift Element

For a free drift, where there is no magnetic field $1/\rho = K_1 = 0$, the first order transfer matrix is

$$R_{\text{drift}} = \begin{pmatrix} 1 & L & 0 & 0 & 0 & 0 \\ 0 & 1 & 0 & 0 & 0 & 0 \\ 0 & 0 & 1 & L & 0 & 0 \\ 0 & 0 & 0 & 1 & 0 & 0 \\ 0 & 0 & 0 & 0 & 1 & 0 \\ 0 & 0 & 0 & 0 & 0 & 1 \end{pmatrix} . \tag{3.8}$$

Quadrupoles and Thin Lenses

For quadrupoles, with $1/\rho = 0$ and no energy dependent terms appearing at first order, the motion is dictated by the normalized gradient K_1 . With the previously chosen sign convention a quadrupole is focusing in the horizontal plane and a defocusing in the vertical plane for $K_1 > 0$. This corresponds to oscillatory and diverging motion respectively. The equations are symmetric in K_1 in that sense, that $K_1 \to -K_1$ switches the behavior in the two planes. The resulting matrix that describes the transport

through a quadrupole is found to be:

$$R_{\text{quad}} = \begin{pmatrix} \cos\left(\sqrt{K_1}L\right) & \frac{\sin\left(\sqrt{K_1}L\right)}{\sqrt{K_1}} & 0 & 0 & 0 & 0\\ -\sqrt{K_1}\sin\left(\sqrt{K_1}L\right) & \cos\left(\sqrt{K_1}L\right) & 0 & 0 & 0 & 0\\ 0 & 0 & \cosh\left(\sqrt{K_1}L\right) & \frac{\sinh\left(\sqrt{K_1}L\right)}{\sqrt{K_1}} & 0 & 0\\ 0 & 0 & \sqrt{K_1}\sinh\left(\sqrt{K_1}L\right) & \cosh\left(\sqrt{K_1}L\right) & 0 & 0\\ 0 & 0 & 0 & 0 & 1 & 0\\ 0 & 0 & 0 & 0 & 0 & 1 \end{pmatrix}$$
(3.9)

By letting $L \to 0$ the matrix for the thin lens approximation with a focal length $1/f = -K_1L$ is obtained:

$$R_{\text{thinlens}} = \begin{pmatrix} 1 & 0 & 0 & 0 & 0 & 0 \\ -\frac{1}{f} & 1 & 0 & 0 & 0 & 0 \\ 0 & 0 & 1 & 0 & 0 & 0 \\ 0 & 0 & \frac{1}{f} & 1 & 0 & 0 \\ 0 & 0 & 0 & 0 & 1 & 0 \\ 0 & 0 & 0 & 0 & 0 & 1 \end{pmatrix}$$

$$(3.10)$$

The thin lens approximation proves especially useful for deriving straightforward analytical estimates.

Dipole and Kick Elements

For a pure dipole field, $\rho \neq 0$ and $K_1 = 0$, the beam is bent depending on its initial position, transverse momentum and energy deviation. A practical quantity for the description of a dipole is its bending or kick angle, which relates to the arc length of the kick $\theta = L_{\rm arc}/\rho$. With this the matrix of a horizontally deflecting (sector) dipole matrix is

$$R_{\text{dipole}} = \begin{pmatrix} \cos(\theta) & \rho \sin(\theta) & 0 & 0 & 0 & \rho(1 - \cos(\theta)) \\ -\frac{\sin(\theta)}{\rho} & \cos(\theta) & 0 & 0 & 0 & \sin(\theta) \\ 0 & 0 & 1 & L_{\text{arc}} & 0 & 0 \\ 0 & 0 & 0 & 1 & 0 & 0 \\ \sin(\theta) & \rho(1 - \cos(\theta)) & 0 & 0 & 1 & \rho(\theta - \sin(\theta)) \\ 0 & 0 & 0 & 0 & 0 & 1 \end{pmatrix}$$
(3.11)

It should be noted here, that a similar matrix for a rectangular dipole in a straight reference frame is given by

$$C_{\rm kick} = \begin{pmatrix} L \tan \left(\frac{\theta}{2}\right) \\ \tan(\theta) \\ 0 \\ 0 \\ 0 \\ 0 \end{pmatrix} \quad R_{\rm kick} = \begin{pmatrix} 1 & L \sec(\theta) & 0 & 0 & 0 & -L \tan \left(\frac{\theta}{2}\right) \sec(\theta) \\ 0 & \sec^3(\theta) & 0 & 0 & 0 & -\sin(\theta) \sec^3(\theta) \\ 0 & 0 & 1 & L & 0 & 0 \\ 0 & 0 & 0 & 1 & 0 & 0 \\ 0 & L \tan \left(\frac{\theta}{2}\right) \sec(\theta) & 0 & 0 & 1 & L \left(\sin^{-1}(\theta) - \sec(\theta)\right) \\ 0 & 0 & 0 & 0 & 0 & 1 \end{pmatrix} \quad . \quad (3.12)$$

Contrary to eq. (3.11), the kick angle is determined from the insertion length L using the relation $\theta = \arcsin(L/\rho)$, with $\theta \simeq L/\rho$ for short dipoles $L \ll |\rho|$. This representation is particularly useful to describe deviations from a straight path. For small angles $\theta \ll 1$ a weak kick element is obtained as

$$C_{\text{corr}} \simeq \begin{pmatrix} \frac{L\theta}{2} \\ \theta \\ 0 \\ 0 \\ 0 \\ 0 \end{pmatrix} \qquad R_{\text{corr}} \simeq \begin{pmatrix} 1 & L & 0 & 0 & 0 & -\frac{L\theta}{2} \\ 0 & 1 & 0 & 0 & 0 & -\theta \\ 0 & 0 & 1 & L & 0 & 0 \\ 0 & 0 & 0 & 1 & 0 & 0 \\ 0 & \frac{L\theta}{2} & 0 & 0 & 1 & 0 \\ 0 & 0 & 0 & 0 & 0 & 1 \end{pmatrix} . \tag{3.13}$$

The constant elements C are explicitly given here, since a deviation from the reference orbit is applied.

Multiple Elements

To understand the behavior of particles as they pass through multiple elements of a beamline, their individual transfer maps are combined into one map describing the transport from its start to its end as

$$\mathcal{M}_{0\to n}\mathbf{r} = \mathcal{M}_{(n-1)\to n} \cdots \mathcal{M}_{0\to 1}\mathbf{r} \tag{3.14}$$

The transformation through two consecutive elements, for instance, is computed by applying the maps in sequence to the particle coordinates

$$r_i(s_2) = C_i + R_{ii}r_i(s_1) (3.15)$$

$$r_i(s_2) = C_i + R_{ij}C_j + R_{ij}R_{jk}r_k(s_0)$$
(3.16)

Summation over repeated indices is implied. For the typically assumed system where the reference particle trajectory coincides with the coordinate system, all constant terms vanish, $C_i=0$. The composition of a first-order transfer matrices from two consecutive elements is expressed through matrix multiplication:

$$R_{0\to 2} = R_{1\to 2} R_{0\to 1} \tag{3.17}$$

Transverse Shift Element

In addition to modeling real transport elements, the framework also describes transformations such as transverse shifts. These are useful for modeling the effects of magnet offsets, or rotations. The map for a transverse shift, representing a translation in the horizontal or vertical plane, is a zeroth-order transformation expressed as

$$C_{\text{shift}} = \begin{pmatrix} \Delta x & 0 & \Delta y & 0 & 0 & 0 \end{pmatrix}^{\mathsf{T}} . \tag{3.18}$$

For this transformation, the linear matrix R and higher order elements are equivalent to the identity map. Consequently, this shift reflects a lateral displacement, horizontally by Δx and vertically by Δy , without otherwise altering the other coordinates. When a component is offset by some value Δx , applying shift operations before and after the transfer map of the component $\mathcal{M}_{\text{shift}}\mathcal{M}_{\text{component}}\mathcal{M}_{-\text{shift}}$ effectively integrates the offset into the transfer matrix.

3.1.3 Internal Bunch Coordinate

Alternatively to using the path length difference l, an internal bunch coordinate ζ is defined as the longitudinal position relative to a reference particle. ζ is derived from the relationship between time, position, and velocity. The time of flight for a particle traveling a distance L is given by $t = L/(\beta c)$. The change in internal bunch coordinate is then obtained from the change in time of flight by $d\zeta = -\beta c dt$. Integrating this equation, keeping again only terms up to first order, yields the internal bunch coordinate

$$\zeta \simeq \zeta_0 - R_{51}x - R_{52}x' - \left(R_{56} - \frac{L}{\gamma_0^2}\right)\delta$$
 , (3.19)

where ζ_0 is the initial coordinate. Here, relativistic motion was assumed with $\beta_0 \simeq 1$ and $\gamma_0 \gg 1$. The additional term $\frac{L}{\gamma_0^2}$ expresses the difference in velocity of the particles with respect to the reference particle.

3.2 Particle Beams and Beam Envelope

The methods discussed in the previous section for single particles are equally applicable to an ensemble of particles, forming a particle bunch. The fundamental properties of such a bunch, including its spatial extent and correlations, are described by the statistical properties of the ensemble. For example, by using the expectation value $\langle \cdot \rangle$, the mean horizontal position is given by $\langle x \rangle$, the mean direction, or beam pointing, by $\langle x' \rangle$ and the bunch length σ_{ζ} . Similarly, the second central moment is a measure

for the transverse size $\sigma_x = \sqrt{\langle x^2 \rangle}$, and defined analogously as the divergence $\sigma_{x'}$, and the absolute and relative energy spread σ_{γ} and $\sigma_{\delta} = \sigma_{\gamma}/\langle \gamma \rangle$. The same applies for the other coordinates. Mixed terms, like $\langle xx' \rangle$ represent a measure of the correlation between the two coordinates. The transverse

plane (x, x') is illustrated in fig. 3.2, indicating the corresponding size σ_x and divergence $\sigma_{x'}$, as well as their correlation $\langle xx' \rangle$. These statistical properties can be determined experimentally and are therefore useful to describe the beam.

By using the expectation value on eq. (3.4), the initial statistical properties $\langle r_i r_j \rangle_0$ evolve accordingly as

$$\langle r_i r_i \rangle = R_{ik} R_{il} \langle r_k r_l \rangle_0 \quad , \tag{3.20}$$

where summation over repeated indices k and l is assumed. The index 0 denotes the initial value, before applying the transfer map. This transformation is concisely expressed in matrix notation as

$$\Sigma_{ij} = (R \cdot \Sigma_0 \cdot R^{\mathsf{T}})_{ij} \quad , \tag{3.21}$$

where Σ is the covariance or sigma matrix with elements $\Sigma_{ij} = \langle r_i r_j \rangle$. The entries of $\Sigma(s)$ describe the beam's extent and correlations in all its coordinates. Therefore eq. (3.21) represents the transformation of the statistical beam properties through a transfer map R. This can be understood as an envelope representing the particle ensemble via its statistical properties. A mathematically equivalent formulation to eq. (3.21) is given by a single matrix-vector product. Assuming no coupling between the planes, this formulation reads

$$\begin{pmatrix}
\sigma_{x}^{2} \\
\langle xx' \rangle \\
\sigma_{x'}^{2}
\end{pmatrix} = \begin{pmatrix}
R_{11}^{2} & 2R_{11}R_{12} & R_{12} \\
R_{11}R_{21} & R_{12}R_{21} + R_{11}R_{22} & R_{12}R_{22} \\
R_{21}^{2} & 2R_{21}R_{22} & R_{22}^{2}
\end{pmatrix} \begin{pmatrix}
\sigma_{x,0}^{2} \\
\langle xx' \rangle_{0} \\
\sigma_{x',0}^{2}
\end{pmatrix}$$
(3.22)

for the horizontal plane and analogous for the other planes. This representation emphasizes the evolution of the horizontal plane's projected size, correlation and divergence, describing the beam envelope for this plane.

3.3 Phase Space and Emittance

An essential characteristic of particle beams in accelerator physics is the emittance, which measures the occupied volume in phase space. The most fundamental definition of emittance derives from Hamiltonian mechanics. In a system that obeys the Hamiltonian equations of motion, the phase-space volume is preserved, as stated by Liouville's theorem. However, this phase space is spanned by the canonical coordinates of the system, which involve the momenta and electromagnetic potentials. Both are usually not accessible in the experiment.

Another definition of emittance is based on the statistical properties of the particle distribution [56]. Similarly to the phase-space emittance, the "trace-space" emittance of a beam is a measure for the occupied volume in the trace space, using x' and y' instead of the momenta. Throughout this thesis, when using the term emittance, it refers to the trace-space emittance unless specified otherwise.

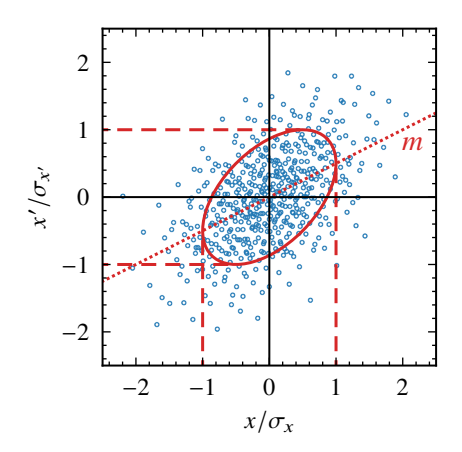


Figure 3.2: Illustration of (red, solid) the equivalent ellipse with area proportional to the emittance $\pi \epsilon_x$ of (blue, circles) a particle distribution in (x-x') space. (Red, dashed) Extent of the ellipse is $\sigma_x = \sqrt{\epsilon_x \check{\beta}}$ and $\sigma_{x'} = \sqrt{\epsilon_x \check{\gamma}}$. (Red, dotted) The slope is given by $m = \langle xx' \rangle / \sigma_x^2$ and connects the points of horizontal extent.

The full six-dimensional emittance ϵ of a bunch is defined by the square root of the determinant of the sigma matrix

$$\epsilon = \sqrt{\det(\Sigma)} \quad . \tag{3.23}$$

This 6D emittance considers the correlations and variations across all trace-space coordinates. However, if the coupling between the planes can be neglected, they may be treated independently. In such scenarios, the cross-plane terms in the sigma matrix are negligible, and the emittance factorizes into the product of 2D emittances for each individual plane $\epsilon = \epsilon_x \epsilon_y \epsilon_\zeta$. While treating each transverse plane as independent is a simplification, it is justified in systems where mixing between the planes is negligible. The emittance for each plane is determined by the determinant of its corresponding 2×2 sub-matrix. For the horizontal plane, the squared emittance is

$$\epsilon_{x}^{2} = \det \begin{pmatrix} \sigma_{x}^{2} & \langle xx' \rangle \\ \langle xx' \rangle & \sigma_{x'}^{2} \end{pmatrix}$$

$$= \sigma_{x}^{2} \sigma_{x'}^{2} - \langle xx' \rangle^{2}$$
(3.24)

If there are correlations between the planes, eq. (3.24) yields the projected emittance, which reflects the behavior of the beam in a specific plane by integrating out the contributions from other planes. However, even though projected emittances are typically used to describe the properties of the beam in these individual planes, they are not inherently conserved properties.

From the previous considerations, the emittance is also a measure of the relation between divergence and beam size. It defines how strong a beam has to be focused to achieve a tight beam waist and of how well it is collimated at a specific size. In cases where there is no coupling between the planes and emittance is conserved, the minimum beam size achievable at a focal point is dictated by $\sigma_x = \epsilon_x/\sigma_{x'}$. This relationship underscores the inherent limitation that the beam's size cannot become indefinitely small and its expansion is inherently governed by the emittance. In summary, a low emittance is beneficial for achieving effective beam transport, enabling smooth focusing and compact beam sizes throughout the accelerator.

Related to the emittance is the normalized emittance. Again, considering only a transverse plane, it is written as [57]

$$\epsilon_{n,x} \simeq \frac{\overline{p_s}}{m_e c} \epsilon_x \simeq \frac{p_0}{m_e c} \epsilon_x \simeq \gamma_0 \epsilon_x$$
 (3.25)

with the average longitudinal momentum $\overline{p_s}$. The normalized emittance remains constant during acceleration processes, which increase the longitudinal momentum p_s and consequently the Lorentz factor γ , while decreasing the transverse divergences x' and y'. Therefore, utilizing the normalized emittance is particularly useful for comparing the quality of beams at different energies. Moreover, for a more granular analysis, one can consider a slice emittance. This refers to the emittance computed for a narrow longitudinal slice of the beam, allowing for a detailed characterization of the beam's properties at different positions within the bunch. This measure is particularly insightful for understanding the dynamics and quality of beams where internal variations along the beam are of interest. Additionally to being a measure volume, the emittance allows for comparisons between differently shaped particle distributions, by representing them through an equivalent area. A practical and common choice for such representation is an ellipse defined by the implicit equation

$$\dot{\gamma}x^2 + 2\dot{\alpha}xx' + \dot{\beta}x'^2 = \epsilon_x \quad . \tag{3.26}$$

By constraining $\check{\beta}\check{\gamma} - \check{\alpha}^2 = 1$, the parameters $\check{\beta}$, $\check{\alpha}$, and $\check{\gamma}$ align with σ_x , $\langle xx' \rangle$, and $\sigma_{x'}$, respectively. With this choice the ellipse encloses an area of $\pi\epsilon_x$. Figure 3.2 illustrates the emittance as such ellipse in the horizontal plane. Although derived differently, $\check{\beta}$, $\check{\alpha}$, and $\check{\gamma}$ match with the ones derived by Courant and Snyder for periodic systems [58], therefore usually called Courant-Snyder parameters ¹. The following relations hold between the statistical properties, the Courant-Snyder parameters and the emittance:

$$\check{\beta}_{x} = \frac{\sigma_{x}^{2}}{\epsilon_{x}} \qquad \check{\alpha}_{x} = -\frac{\langle xx' \rangle}{\epsilon_{x}} \qquad \check{\gamma}_{x} = \frac{\sigma_{x'}^{2}}{\epsilon_{x}} \quad . \tag{3.27}$$

These parameters effectively describe the beam dynamics, encompassing various beam sizes, divergences, and correlations, differing merely by a scaling of the emittance. Therefore, they are interchangeable with the measures used in the discussions on beam envelopes in section 3.2.

¹ Throughout this thesis, the Courant-Snyder parameters are denoted by $\check{\beta}$, $\check{\alpha}$, and $\check{\gamma}$ to distinguish them from the relativistic Lorentz factor γ and the velocity βc .

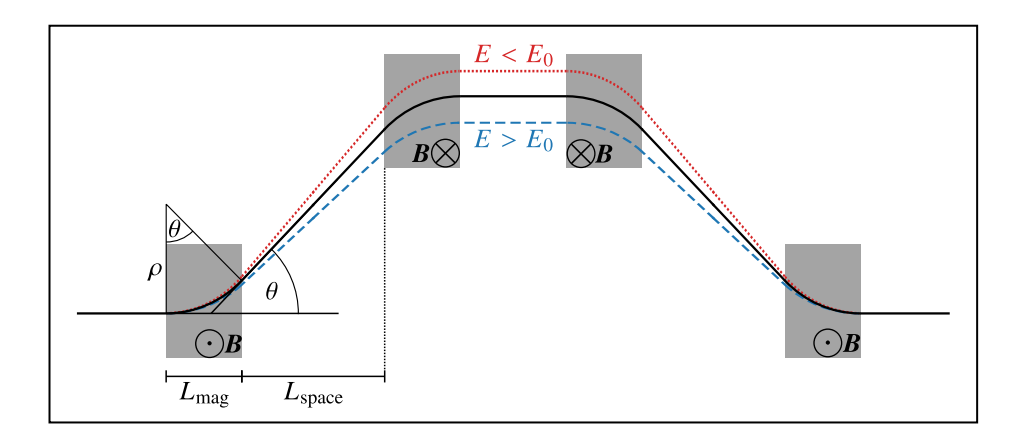


Figure 3.3: Schematic layout of a C-chicane showing trajectories of different energies. Reference energy (black solid) is deflected by an angle θ . Lower energy particles (red, dotted) have a larger detour and higher energy particles (blue, dashed) a shorter one. In the symmetric case, all magnets have same length $L_{\rm mag}$ and kick angle θ , and the spacing from first to second and third to fourth dipole are equal $L_{\rm space}$.

3.4 Bunch Decompression

The percent level energy spreads associated with laser-plasma accelerated electron beams, as outlined in section 2.4, typically exceed the tolerances required for many applications. For free-electron lasers, particularly, a low energy spread is crucial [59], and typically on the order of 10^{-3} to 10^{-4} [60]. The energy spreads from LPA beams are significantly larger, being on the percent-level. Consequently, a reduction of the effective energy spread is essential for the utilization of LPA beams in FEL applications, see section 4.3.4.

One strategy to address this is through use of a magnetic chicane to stretch the bunch. This technique specifically targets the reduction of local energy spread, which pertains to the energy variation within smaller longitudinal segments of the beam [23]. While this method effectively narrows the effective energy spread, it simultaneously results in a decrease in beam current. This reduction in both parameters represents a trade-off that must be balanced to optimize the performance of the FEL, see section 4.3.4.

In its simplest form, the path length a particle travels through the chicane only depends on the matrix element R_{56} , neglecting other and higher order effects of beam transport. Assuming that the path length difference after passing the chicane is independent from the initial position or direction, the corresponding elements in the transfer map reading $R_{51} = R_{52} = 0$, and the internal bunch coordinate from eq. (3.19) simplifies to:

$$\zeta \simeq \zeta_0 + \left(\frac{L}{\gamma_0^2} - R_{56}\right)\delta = \zeta_0 + R_{56}^{\zeta}\delta \tag{3.28}$$

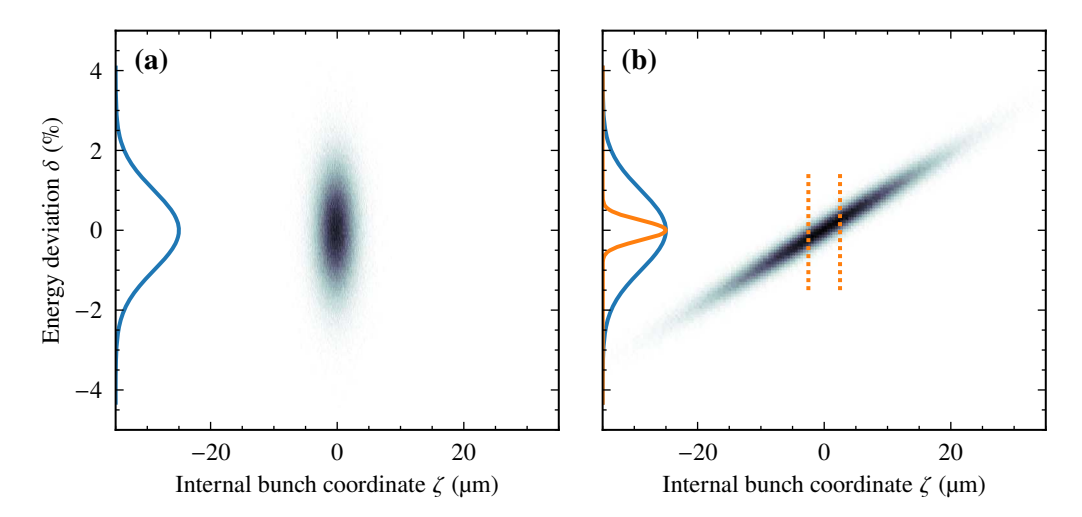


Figure 3.4: Longitudinal ($\zeta - \delta$) space of a bunch with length $\sigma_{\zeta} = 2 \, \mu m$ and energy spread of $\sigma_{\delta} 1 \, \%$. Shown are (a) the initially uncorrelated bunch and (b) after stretching the bunch to $5 \times$ its initial length. The (blue, solid) projected energy distribution and therefore the energy spread do not change, but (orange, dotted) a single slice can have (orange, solid) lower local energy spread.

 R_{56}^{ζ} represents the combined effect of relative position changes due to path length and velocity differences. Note that R_{56} and R_{56}^{ζ} usually have different signs. The superscript ζ is used to distinguish this matrix element for the internal bunch coordinate from that used previously for the path length difference². For LUX, operating at energies $\gamma \simeq 600$, the energy dependent time of flight difference contributes approximately $L/\gamma_0^2 \simeq 3 \, \mu m$ per meter of beam transport to R_{56}^{ζ} . For a short beamline this only slightly modifies the required decompression by the chicane, but has to be considered if the applied stretching is small.

The primary contribution comes from R_{56} , which depends on the detour introduced by the magnetic chicane. An ideal magnetic chicane only increases the path length dependent on energy, and acts like a drift on the other coordinates. In the following, the beam dynamics of a symmetric C-chicane as implemented at LUX will be discussed. A schematic of the C-layout is shown in fig. 3.3, illustrating the varied path lengths traversed by particles of different energies resulting in longitudinal stretching of the beam. This elongation also introduces a correlation between longitudinal position and energy, while simultaneously reducing the local energy spread, as depicted in fig. 3.4. The total bunch length

² Both versions are used in literature about beam optics and commonly referred to as R_{56} , with the specific designation dependent on the choice of the longitudinal coordinate. The distinction here serves to enhance clarity in the context of this discussion.

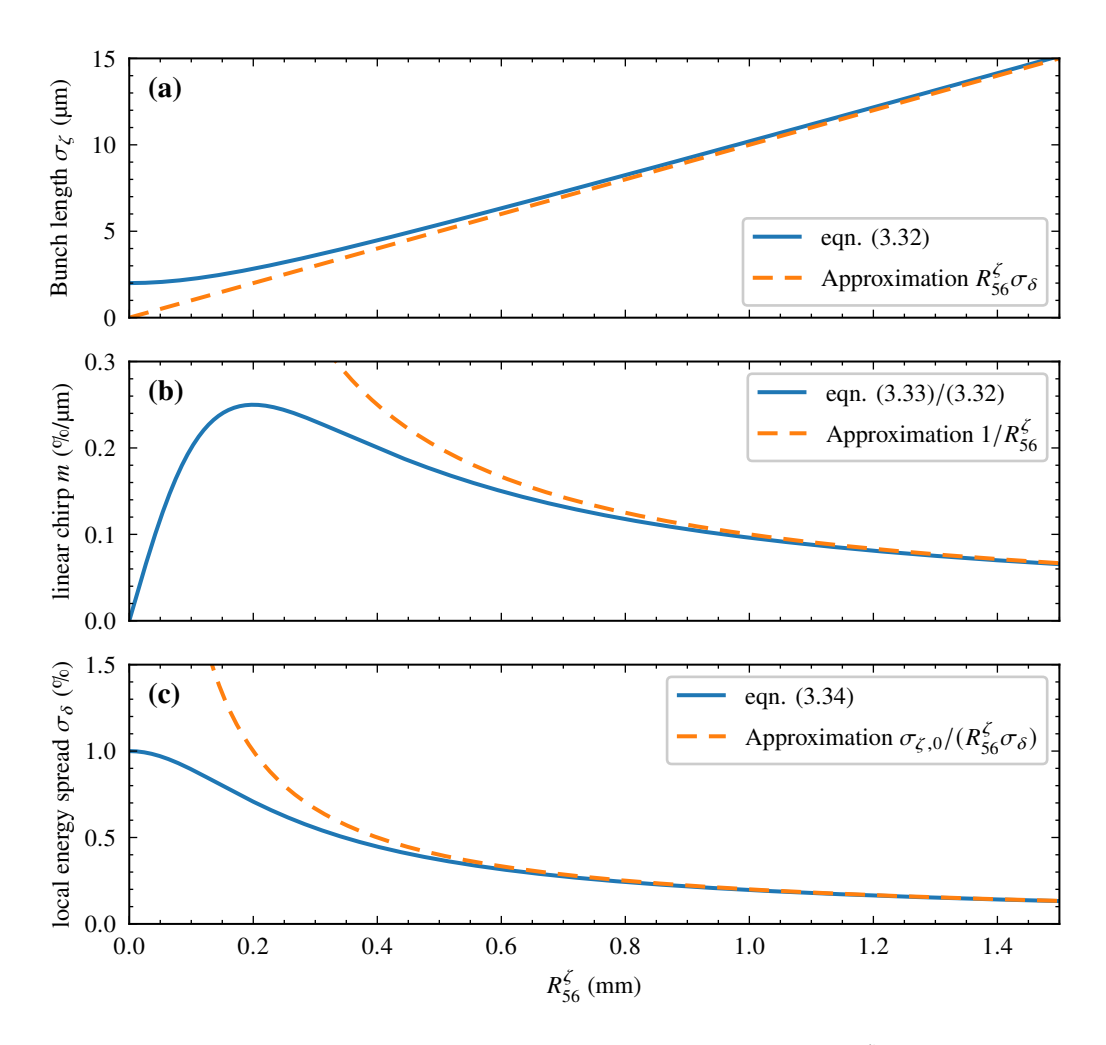


Figure 3.5: Change of longitudinal beam parameters with varying R_{56}^{ζ} for a beam with initially $\sigma_{\zeta}=2\,\mu\mathrm{m}$, $\sigma_{\delta}=1\,\%$, and no chirp $\langle\zeta\delta\rangle=m=0$. Results obtained from (blue, solid) the full formulas eqs. (3.32) to (3.34) and (orange, dashed) approximations for expanding about $R_{56}^{\zeta}\to\infty$ are shown for (a) bunch length, (b) linear energy chirp, and (c) slice energy spread.

and correlation after some transport is then be described by

$$\sigma_{\zeta}^{2} = \sigma_{\zeta,0}^{2} + 2R_{56}^{\zeta} \langle \zeta \delta \rangle_{0} + \left(R_{56}^{\zeta} \right)^{2} \sigma_{\delta,0}^{2}$$
 (3.29)

$$\langle \zeta \delta \rangle = \langle \zeta \delta \rangle_0 + R_{56}^{\zeta} \sigma_{\delta,0}^2 \tag{3.30}$$

$$\sigma_{\delta}^2 = \sigma_{\delta,0}^2 = \text{const} \quad . \tag{3.31}$$

Assuming that the beam initially is longitudinally only linearly correlated is a reasonable approximation, since the beams from LPA only occupy a small region in the accelerating field within the plasma, see section 2.1. Therefore, each particle's energy deviation δ_n is modeled as a linear function of its position as $\delta_n = m\zeta_n + \Delta_n$, where m represents the linear slope crossing the points of maximum extent in σ_{ζ} in the $(\zeta - \delta)$ plane, and Δ is the deviation from this linear relation. In linear beam optics it is uncorrelated with the position, i.e. $\langle \Delta \zeta \rangle = \langle \Delta \rangle \langle \zeta \rangle = 0$. The corresponding local or uncorrelated energy spread is here denoted by σ_{Δ} . The slope m is derived from the statistical properties as $m = \langle \zeta \delta \rangle / \sigma_{\zeta}^2$ and is also indicated in fig. 3.2. Therefore, the total energy spread is expressed by $\sigma_{\delta}^2 = m^2 \sigma_{\zeta}^2 + \sigma_{\Delta}^2$. Although the formulas provide the correlation of position and energy, this slope is typically the quantity of interest, because it characterizes the (linear) energy chirp of the beam in the easily accessible unit %/m. Under this assumption, eqs. (3.29) to (3.31) take the form

$$\sigma_{\zeta}^{2} = \left(1 + m_{0} R_{56}^{\zeta}\right)^{2} \sigma_{\zeta,0}^{2} + \left(R_{56}^{\zeta}\right)^{2} \sigma_{\Delta,0}^{2} \tag{3.32}$$

$$\langle \zeta \delta \rangle = \left(1 + m_0 R_{56}^{\zeta} \right) m_0 \sigma_{\zeta}^2 + R_{56}^{\zeta} \sigma_{\Delta,0}^2 \tag{3.33}$$

$$\sigma_{\Delta}^{2} = \frac{\sigma_{\Delta,0}^{2}}{\left(1 + m_{0}R_{56}^{\zeta}\right)^{2} + \left(R_{56}^{\zeta}\frac{\sigma_{\Delta,0}}{\sigma_{\zeta,0}}\right)^{2}} = \sigma_{\Delta,0}\frac{\sigma_{\zeta,0}}{\sigma_{\zeta}} \quad . \tag{3.34}$$

In contrast to the initial equations, eqs. (3.29) to (3.31), the equations eqs. (3.32) to (3.34) provide insights into the evolution of chirp and the uncorrelated energy spread within the beam.

The following approximations for an initially unchirped bunch hold for cases with large decompression $R_{56}^{\zeta} \gg \sigma_{\zeta}/\sigma_{\delta}$:

$$\sigma_{\zeta} \simeq R_{56}^{\zeta} \sigma_{\delta} \qquad \langle \zeta \delta \rangle \simeq R_{56}^{\zeta} \sigma_{\delta}^{2}$$

$$\sigma_{\Delta} \simeq \frac{\sigma_{\zeta,0}}{R_{56}^{\zeta} \sigma_{\delta}} \qquad m \simeq \frac{1}{R_{56}^{\zeta}} \qquad (3.35)$$

For the beam parameters at LUX, these approximations are applicable for $R_{56}^{\zeta} \gtrsim 500 \, \mu m$. Figure 3.5 shows the change in (a) bunch length, (b) the slope m, and (c) the local energy spread with respect to the applied R_{56}^{ζ} . For an initially uncorrelated and short beam, a significant reduction in local energy spread is already achieved with moderately small R_{56}^{ζ} . For example, in this scenario it decreases to a third of its initial value for $R_{56}^{\zeta} \simeq 500 \, \mu m$. It's noteworthy that the slope m increases from zero until the highest energy particles overtake the former head and the lowest energy particles similarly fall back behind the former tail of the bunch. Another useful metric in this context is a bunch stretching

factor n_B , that is defined as the ratio of the final to initial bunch length

$$n_B = \frac{\sigma_{\zeta}}{\sigma_{\zeta,0}} = \sqrt{1 + \left(\frac{R_{56}^{\zeta}\sigma_{\delta}}{\sigma_{\zeta,0}}\right)^2} \simeq \frac{R_{56}^{\zeta}\sigma_{\delta}}{\sigma_{\zeta,0}} \quad , \tag{3.36}$$

which links initial bunch length, energy spread and R_{56}^{ζ} , and where the second equality is valid for initially uncorrelated bunches.

Using this quantity, the current of a longitudinally gaussian shaped beam changes as $I = I_0/n_B$. However, as shown in fig. 2.5, the initial current distribution is expected to approximately be of flat top shape. As there is no correlation expected between the internal bunch coordinate and the local energy spread at the core of the bunch, the current distribution will change as the beam is stretched. If $R_{56}^{\zeta} \cdot \sigma_{\delta} \gg \sigma_{\zeta,0}$ the shape of the energy spread dominates eq. (3.32). For a short beam and gaussian distributed energy spread, the longitudinal distribution will also converge to a gaussian shape, as high energy particle from the tail catch up and low energy particles at the tail fall back. For the LUX reference beam the left hand side becomes larger than the initial bunch length for $R_{56}^{\zeta} \gtrsim 200 \, \mu \text{m}$, i.e. where high energy particles from the tail overtake the low energy particles from the bunch head, indicating that this scenario is easily achieved. In that case the initial current can be expressed by an equivalent peak current $I_{0,\text{gauss}} = \sqrt{12/(2\pi)}I_{0,\text{flat}} \simeq 1.4I_{0,\text{flat}}$, slightly higher than the provided current in the flat-top beam. The uncorrelated energy spread according to eq. (3.34) then also scales as $\sigma_{\Delta} \simeq \sigma_{\Delta,0}/n_B$.

The transfer map elements contributing to the longitudinal particle position at first order for a symmetric C-chicane can be derived from the elements discussed in section 3.1. Specifically, the R_{56} of the chicane that is relevant to the discussion of decompression is given by [61]

$$R_{56} = -2\left(\frac{L_{\text{mag}}}{\rho_0}\right)^2 \left(\frac{2}{3}L_{\text{mag}} + L_{\text{space}}\right) ,$$
 (3.37)

where ρ_0 is the bending radius of a particle with reference energy. $L_{\rm mag}$ represents the lengths of the individual dipole magnets, and $L_{\rm space}$ the drift between the first and second, as well as the third and fourth dipole magnets. This configuration is also illustrated in fig. 3.3. As indicated by eq. (3.37) a pure magnetic chicane yields a negative $R_{56} < 0$. At conventional accelerators and FELs, the objective is often to compress the beam to increase the beam current. This is typically accomplished by introducing an energy chirp via a cavity before the chicane and with opposite sign to the discussed case, i.e. $\langle \zeta \delta \rangle < 0$. The cumulative effect of the cavity and the chicane results in a positive overall $R_{56} > 0$, which decreases the bunch length and therefore increases the current, in trade for an increase in energy spread. Here, the opposite is intended, thus no cavity is required.

As worked out in this section, instead of compressing the beam, the strategy to reduce the energy spread involves stretching it to achieve parameters comparable to those of conventional accelerators. This stretching is critical for matching the operational characteristics necessary for successful FEL applications.

3.5 Trajectory and Focusing Errors

The beam optics formalism from the previous sections not only describes ideal beam transport, but also quantifies how deviations in accelerator components affect beam dynamics. Any Magnet in the system can be subject to such deviations in position or strength. Especially for quadrupole magnets, discrepancies from the desired parameters can have significant impact on the beam transport. They can affect both the trajectory of the beam through the accelerator and the focusing properties, which is of particular interest when shaping the beam for applications such as an FEL.

3.5.1 Quadrupole Offsets

Transverse offsets δx and δy of a quadrupole are equivalent to an overlap with a dipole field. Considering the reference particle, in the focusing plane it experiences an additional oscillatory motion, while in the defocusing plane it is subjected to a lateral displacement from the beam axis. The introduced changes in position x and pointing x' after passing through the quadrupole are

$$\Delta x = \delta x (1 - \cos\left(\sqrt{K_1}L\right)) \tag{3.38}$$

$$\Delta x' = \delta x \sqrt{K_1} \sin\left(\sqrt{K_1}L\right) \quad , \tag{3.39}$$

and similarly for the defosing plane using sinh and cosh. In the short lens approximation for short quadrupoles, this results in a weak kick originating from the magnet's center

$$\Delta x' \simeq LK_1 \delta x \quad . \tag{3.40}$$

A 10 cm quadrupole magnet operated at $K_1 = 100 \,\mathrm{m}^{-2}$ introduces a kick of approximately 10 µrad per 1 µm of positional offset. Thus, even small transverse offsets will significantly deviate the beam from its intended path.

The effect is more severe if two consecutive quadrupoles kick the beam towards the same direction. Considering two thin quadrupoles of 10 cm length, operating at K_1 of about $100 \, \mathrm{m}^{-2}$ and $-50 \, \mathrm{m}^{-2}$, and spaced by $20 \, \mathrm{cm}$ (center-to-center), the resulting kicks in the horizontal and vertical planes would be approximately $\Delta x_1' \simeq 20\delta x_1 - 5\delta x_2$ and $\Delta y_1' \simeq 2.5\delta y_1 + 4\delta x_2$. The indices denote to which of the two quadrupoles the offset is applied. Following this doublet, the beam's trajectory is mainly influenced by the kick angle, with offsets directly after the doublet being less than 5 μ m. The alignment should be primarily performed in the focusing plane of the first quadrupole due to its more pronounced impact, followed by the vertical alignment of the second quadrupole. If the polarity of the quadrupoles is reversed the procedure has to be adapted accordingly. While the relative position of the plasma source to the first doublet is adjustable during operation, aligning it precisely is challenging. Any residual misalignment has to be corrected using dipole magnets to realign the beam along the desired axis.

For later quadrupoles in the beamline, where the beam is already captured, the focusing strength is typically lower with $K_1 \lesssim 10$. The total impact of offsets by these quadrupoles accumulates if they all kick the beam to the same direction. However, these quadrupoles are not intentionally positioned to maximize the kick, which suggests that the overall effect might be smaller than the sum of individual contributions.

When considering a beamline comprised of quadrupoles with varying polarity and randomly distributed offsets relative to the reference orbit, the particle beam's trajectory will not constantly move away from, but move around the unperturbed reference orbit due to the varying directions of the kicks. To get an estimate on the overall effect of the beamline, the complete transport is here condensed to a single matrix

$$R_{\rm bl} = \begin{pmatrix} m & 0\\ -\frac{1}{f} & \frac{1}{m} \end{pmatrix} \tag{3.41}$$

representing a magnifying system characterized by its magnification m and focusing strength 1/f. To achieve an imaging with focus at the end of the beamline, it is necessary for 1/f to vanish. However, this matrix is particularly chosen considering the initial size and divergence of laser-plasma accelerated beams, being on the order of micrometer and milliradian respectively, thus the focus position being predominantly influenced by the divergence. By setting $R_{12}=0$, the focus will already be close to the desired position.

Applying the same offset $\delta x_{\rm bl}$ to the entire beamline, implying that all quadrupoles share a common axis, results in the position and slope of the beam being $x=(1-m)\delta x_{\rm bl}$ and $x'=-f\delta x_{\rm bl}$. To achieve a magnification of about 10, see section 5.1.2, and limit the positional offset of the beam at the end of the transport beamline to below 100 µm, thereby requiring only a minor kick with a corrector magnet, the beamline offset has to be smaller than $\delta x_{\rm bl} \lesssim 10 \, \mu \rm m$. Simultaneously requiring pointing change of less than x' < 0.01 mrad due to the positional offset, sets a rather relaxed upper limit to the overall focusing strength of the beamline |1/f| < 10. A focus shift due to correlation $\langle xx' \rangle = f\sigma_{x,0}^2 \simeq 10^{-5}$ is negligible.

Combining the thoughts, the impact of quadrupole offsets is kept on a feasible level if the quadrupoles are aligned within $\lesssim 10\,\mu m$ to a common axis. Larger deviations have to be compensated with corrector magnets. The first two quadrupoles, crucial for capturing the beam directly after the plasma source and typically the strongest quadrupole magnets, should be placed with greater precision, ideally within $\sim 1\,\mu m$ to this axis. During operation, the plasma source is adjusted to align with this established axis. However, since these requirements are difficult to meet, steering magnets are utilized to correct any deviations, ensuring the beam remains on course, particularly after passing through the capturing doublet.

Another note has to be made, that the transverse position of beams from the plasma source show shot-to-shot fluctuations. Therefore, the alignment process must be performed to the average position of these fluctuations. To ensure a significant proportion of the beams remain within the desired positional and angular specifications at the final focus, initial positional fluctuations from the source should not exceed a few μm . The stability in source position is primarily dictated by the positional

jitter of the driving laser at the plasma source. The ANGUS laser system, including the laser transport to the plasma source, typically maintains a focus position with shot-to-shot fluctuations of less than $\lesssim 5 \, \mu m$ [36], therefore able to deliver the required properties.

3.5.2 Quadrupole Strength Errors

Variations in the focusing strength of quadrupoles represent another source of error. A measure to quantify the deviation from the desired beam parameters after passing a quadrupole is the mismatch parameter M [62]. It evaluates the discrepancy between the actual and desired trace space ellipses at a given point in the beamline [63]:

$$M = \frac{1}{2} \left(\check{\beta} \check{\gamma}_0 - 2\check{\alpha} \check{\alpha}_0 + \check{\gamma} \check{\beta}_0 \right) \ge 1 \tag{3.42}$$

Here, the Courant-Snyder parameters without subscripts denote the actual conditions resulting from focusing errors, while those with subscript '0' are the design parameters. The mismatch parameter, M, assesses the fit between the actual and the intended focusing properties, with M=1 indicating a perfect match.

An acceptable level of mismatch is determined by the maximum allowed difference in beam size in the undulator. It should be small enough to keep the degrading in FEL performance on a considerably low level. By allowing a maximum deviation in beam size by about 20 % (see section 4.5.1 that this corresponds to a change in beam size by approximately 5 μ m does not significantly impact the gain length), i.e. allow the corresponding $\check{\beta}$ to be about 45 % too large or 30 % too small, the limit on the mismatch parameter is found to be $M-1\simeq 7$ %. Note, that changing $\check{\alpha}$ does neither change M nor the beam size, since the position of interest is a focus with $\check{\alpha}_0$. Distributing this total mismatch evenly across all quadrupoles according to $M_q-1=(M_{\rm total}-1)/\sqrt{N}$ [63], the allowable mismatch for each of a total of N=11 quadrupole magnets (see section 5.2) is $M_q-1\simeq 2$ %.

However, the deviation in mismatch parameter must be translated to an allowed deviation in quadrupole strength for practical interpretation. The latter depends on the targeted quadrupole strength and the beam size within it. Using the same equation eq. (3.42), the mismatch of a single thin lens quadrupole is obtained by substituting the appearing Courant-Snyder parameters by the corresponding transfer maps applied to the parameters before the quadrupole magnet. For the mismatched parameters, the quadrupole strength is altered to $K_1(1 + \Delta K_1)$, where ΔK_1 is the relative deviation in magnet strength. This yields an upper limit for the allowed relative deviation in quadrupole strength [63]:

$$\Delta K_1 < \frac{\sqrt{2(M_q - 1)}}{|K_1| L} \cdot \min\left(\frac{\epsilon_x}{\sigma_x^2}, \frac{\epsilon_y}{\sigma_y^2}\right)$$
(3.43)

For LUX, the expected beam sizes throughout the transport and in the quadrupoles are approximately 200 µm to 400 µm. Further, using a normalized emittance of $\epsilon_n \simeq 1$ mm mrad, i.e. emittance of $\epsilon \simeq 1.7$ µm mrad, and a quadrupole magnet of 10 cm length and strength of about $K_1 \simeq 10 \, \mathrm{m}^{-2}$, the allowed deviation for the quadrupoles can be estimated to be about 0.5 %. Note, that the limit of the first quadrupole is larger, due to the small beam size directly after the target, although its K_1 is larger.

However, the large beam size expected in the second quadrupole, after defocusing the beam in one plane, requires to set its strength on the 0.1 % level. Since this is challenging, after setting up the beamline, the strength of the second quadrupole has to be scanned to obtain a proper focusing size.

3.5.3 Magnetic Background Field

The environmental magnetic fields where the beamline is situated must also be considered, particularly due to their potential effects on beam trajectory. At the *DESY* campus in northern Germany, the Earth's magnetic field is estimated to exert an influence of about $50\,\mu\text{T}$. Specifically, this includes a radial component of approximately $45\,\mu\text{T}$, which points vertically, and an azimuthal component of about $20\,\mu\text{T}$, of which $2\,\mu\text{T}$ is oriented horizontally due to the alignment of the beamline [64]. Natural deviations or the presence of magnetic materials in the accelerator tunnel or its vicinity may alter this field, but the aforementioned values provide a basis for assessing the need for compensatory measures. Assuming a constant transverse field, the displacement x of a beam after traveling a drift distance L is estimated by the bend of a pure dipole field:

$$|x| = \left| \frac{c}{p[\text{eV/c}]} \frac{B_0 L^2}{2} \right| \tag{3.44}$$

For the predominant strength of the radial component of the Earth's magnetic field, this results in a displacement of about 5 mm for a beam freely drifting over 15 m. For shorter distances, such as 3 m between quadrupoles, a displacement of about 200 µm are expected. To mitigate such displacement and the associated dispersion along the beamline, particularly within the quadrupoles inducing position and energy dependent kicks, the background field should be minimized. Helmholtz coils have been installed along the entire distance from the plasma source to the undulator to compensate for the Earth's magnetic field and reduce the reliance on corrector dipoles for beam steering. Furthermore, the quadrupole magnets have to be aligned to this corrected orbit with minimized background field, which can in fact still show deviations from a straight one.

3.6 Degrading Effects During Beam Transport

As pointed out in section 3.3, the projected emittance is only conserved if the planes are decoupled. However, in a real accelerator this condition is rarely met and mixing between the planes occurs. This is particularly pronounced in laser-plasma accelerated electron beams, where high energy spreads and divergences facilitate the coupling of the longitudinal with the transverse planes. Moreover, collective effects, that do not obey Liouville's theorem when considering the electron beam in isolation from radiation processes, can alter the properties of the LPA beams. As a result, neither emittance nor its projected or slice variants are preserved under these processes. First considerations of LPA experiments for FELs assumed beam currents of 10 kA to 100 kA and normalized emittances as low as 0.1 mrad [15, 17]. Such extreme beam properties make the beam highly susceptible to space charge and synchrotron radiation effects, which have the potential to significantly degrade beam quality during transport [65, 66]. Given the beam parameters at *LUX* differ significantly from those estimates, their impact will be reevaluated. Comparing the beam parameters from *LUX*, from section 2.4, with

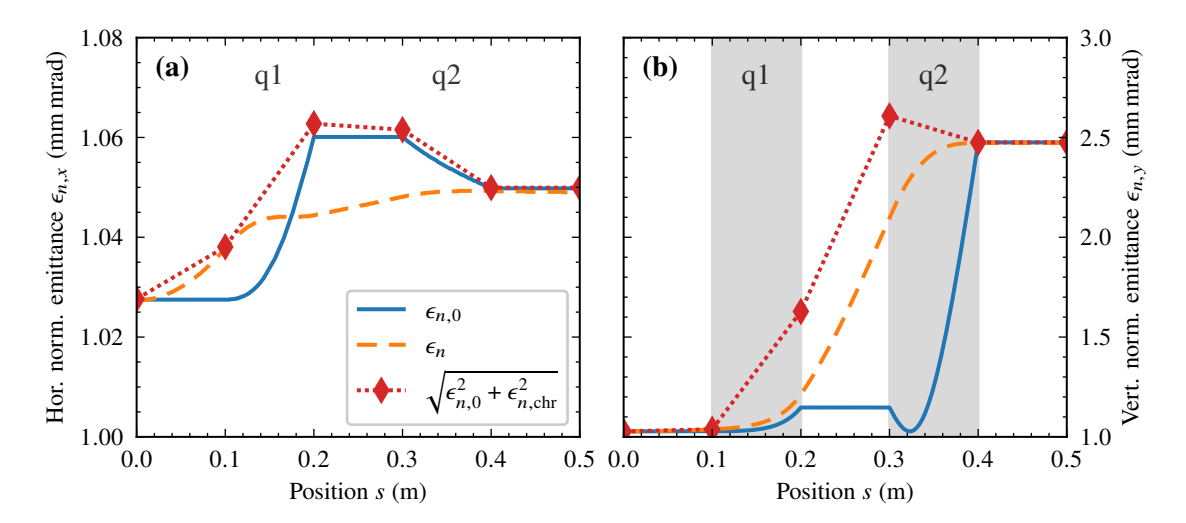


Figure 3.6: Example of emittance increase after the plasma source for (a) horizontal plane and (b) vertical plane. Beam is captured with two quadrupoles of 10 cm length each (grey boxes). The first quadrupole focuses and the second defocuses in the horizontal plane. Shown are the (blue solid) projected normalized emittance without chromatic contribution eq. (3.25), (orange dashed) exact projected normalized emittance eq. (3.45), and (red dotted, diamonds) the approximation including a chromatic contribution eq. (3.46) yielding an upper limit and evaluated before and after drift spaces. Beam simulated with *ASTRA*.

previous assumptions for LPA beams suggests that space charge effects at *LUX* may be an order of magnitude less severe. Nonetheless, given the short bunch lengths and high currents typical for LPA beams, both space charge fields and synchrotron radiation remain critical factors that could undesirably alter the beam quality. Their influence will be discussed in the following sections.

3.6.1 Chromatic Emittance Growth

In the presence of a non-negligible energy spread, the relationship between emittance and normalized emittance becomes more complex. Reevaluating eq. (3.25) under this condition reveals an additional contribution by the longitudinal momentum [67]:

$$\epsilon_{n,x}^2 = \frac{1}{m_e^2 c^4} \left(\left\langle x^2 \right\rangle \left\langle x'^2 p_z^2 \right\rangle - \left\langle x x' p_z \right\rangle^2 \right) \tag{3.45}$$

$$\simeq \gamma_0^2 \left(\epsilon_x^2 + \sigma_x^2 \sigma_{x'}^2 \sigma_\delta^2 \right) \quad , \tag{3.46}$$

where the correlation of δ and the transverse coordinates x and x' was dropped in the second equation, as those correlations between transverse and longitudinal coordinates are usually not accessible in the experiment. However, those terms reduce eq. (3.45), therefore Equation (3.46) offers an upper limit to the normalized emittance in the present of non-negligible energy spread. The additional term can be

considered as a chromatic contribution, extending the previously shown definition of the normalized emittance:

$$\epsilon_{n,x}^2 = \epsilon_{n,x,0}^2 + \epsilon_{n,x,\text{chr}}^2 \quad . \tag{3.47}$$

Both definitions eq. (3.46) and eq. (3.25) have their respective applications. The inclusion of the chromatic term offers a closer alignment with the definition of phase space emittance by acknowledging that there is a mixing between the longitudinal and transverse planes. However, the normalized emittance without chromatic contribution still resembles the projected 2D distribution into the x - x' plane.

If only considering linear beam optics, the chromatic contribution offers to estimate the effects from the chromaticity introduced by quadrupoles without tracking. Equation (3.46) shows the growth in projected normalized emittance for a tracking performed with *ASTRA*. It illustrates the differences between phase space and trace space emittance for a beam that is captured and collimated with a quadrupole doublet within 40 cm behind the plasma source. In the horizontal plane, where the first quadrupole focuses and the second defocuses, the emittance increases to 1.05 mm mrad. In the vertical plane, the increase is more pronounced, reaching approximately 2.5 mm mrad. Additionally, eq. (3.46) was used to estimate the projected normalized phase space emittance using only linear beam optics combined with the energy spread, evaluated at the start and end of the quadrupoles and drift elements. The two definitions of projected emittance agree and in the case of very small divergence $\sigma_{x'} \simeq 0$, i.e. when the beam is close to being collimated, or if the beam is close to a waist where $\langle xx' \rangle \simeq 0$ [57].

While it is possible to reverse the emittance growth with a sufficient number of quadrupoles and adequate drift space [68], this approach increases the length and complexity of the beamline, potentially introducing new sources of error. It is thus preferable to minimize chromatic emittance growth from the beginning.

For applications like an FEL, the emittance within a smaller longitudinal fraction might be more relevant than the projected emittance. Similar to the uncorrelated energy spread, the decompression counteracts the local emittance within such a slice, see section 6.1, hence rendering the effects of chromatic emittance growth less severe if sufficient decompression is applied.

3.6.2 Slice Energy Spread Degradation

In addition to chromatic effects, a possible increase in slice energy spread due to path length differences has to be considered. Except for deliberate detours in a chicane, particles deviating from the reference trajectory by traveling at an angle will inevitably follow a longer path. This leads to a delayed arrival at a subsequent position along the beamline, resulting in their repositioning within the bunch, i.e., they fall back relative to the reference particle. This phenomenon is not apparent at the first order in matrix theory but emerges due to higher order matrix elements such as T_{522} and T_{544} . Particularly, these two elements account for quadratic contributions from the transverse angles relative to the reference trajectory contribute to the increase in path lengths. Consequently, maintaining minimal divergence

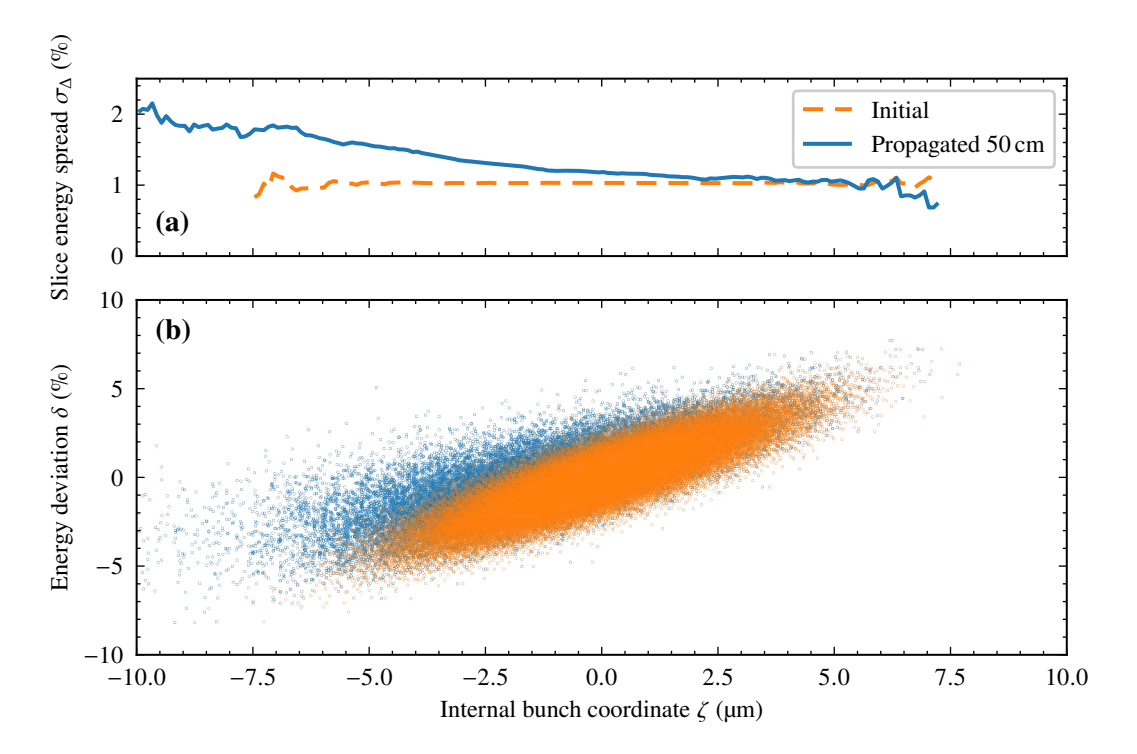


Figure 3.7: Gaussian distributed chirped bunch with 1.5 mrad divergence in both transverse directions, $\sigma_{\delta}=1.5$ % projected energy spread, and an initially $\sigma_{\Delta}=1$ % uncorrelated energy spread. (a) Local energy spread σ_{Δ} of 1 µm long slices for (orange dashed) the initial bunch and (solid blue) the bunch propagated by 50 cm in a free drift. The region for calculating the slice parameters was shifted by 0.1 µm for individual data points. (b) Longitudinal ($\zeta - \delta$) space, overlaid for (orange) the initial position s=0 and (blue) after propagating the beam to s=50 cm.

throughout the beam transport is essential to minimize these differences. This is possible by keeping the first order matrix elements R_{21} , R_{22} , R_{43} , and R_{44} low, that map the initial coordinates to the divergence.

A large contribution to the path length differences originates from the initial drift after the plasma source, where the beam diverges freely before being captured and collimated by the quadrupoles. These effects are more pronounced for a chirped bunch. For example, Figure 3.7 illustrates a gaussian bunch with a large divergence of 1.5 mrad. The normalized emittance is therefore increased to 3 mm mrad. The higher divergence is chosen here for better visualization of the effect and should highlight the significance of keeping the divergence low. This scenario assumes a projected energy spread of 1.5 %, a chirp of m = 0.87 %/µm and a bunch length of 2 µm. This corresponds to an uncorrelated energy spread of $\sigma_{\Delta} = 1$ %, which is the same as the projected energy spread of the reference bunch. Such chirped bunches can be produced from the plasma by beam loading during the acceleration process [21, 50]. Over a drift of 50 cm, such beam lengthens to 2.4 µm and the slice energy spread increases to 1.2 % at the core and reaching up to 2 % at the tail. Although the effect is about ten times smaller for beams with 0.5 mrad divergence, it highlights the necessity of requiring a low divergence at all stages

of the beam transport. Moreover, the effect scales with the length of the beamline, as a comparison with the elements of a free drift $T_{522} = T_{544} = L/2$ reveals. This suggests that sections where the bunch is expected to be chirped or has significant divergence should be as compact as possible.

For an unchirped bunch, these dynamics primarily result in an increase in bunch length rather than slice energy spread. However, addressing increased bunch length and slice energy spread might require more extensive bunch stretching, potentially leading to reduced current, which is undesirable. An initial chirp potentially reduces the required R_{56} , but this advantage holds only when comparing two bunches with the same projected energy spread. In such cases, the chirped beam would exhibit a lower slice energy spread, making it more suitable for certain applications where beam quality is critical.

Ideally, initial beam conditions from the plasma target should feature the lowest divergence possible to mitigate these effects. Since the higher order elements scale quadratically with changes in transverse position, any reduction in divergence can remarkably decrease both the amount of bunch lengthening and the potential increase in slice energy spread. Moreover, capturing the beam earlier would be beneficial, but this would demand higher gradients that are difficult to achieve with electro-quadrupole magnets and not applicable due to space constraints after the plasma source in the current setup.

3.6.3 Transverse Space Charge

The electrons within a bunch exert repulsive Coulomb forces on each other, accelerating them away from the charge center. This force is counteracted by the attractive force between parallel currents, generated by an angular magnetic field component. The repulsive force is stronger, although increasingly compensated when approaching the speed of light. Here, the evaluation of the resulting forces is divided into two parts, beginning with the transverse charge force.

For simplicity, a cylindrically symmetric charge distribution within the bunch, defined as $\rho(r,z)=Q\tilde{\lambda}_r(r)\tilde{\lambda}_\zeta(\zeta)$ is assumed. Here, $\tilde{\lambda}$ represents normalized radial and longitudinal charge density profiles. For an electron inside a bunch moving with $\gamma\gg 1$, the radial space charge force acting on it is derived to be [69]

$$F_r(r,\zeta) = \frac{eQ}{\gamma^2 \varepsilon_0} \frac{\tilde{\lambda}_{\zeta}(\zeta)}{r} \int_0^r r' \tilde{\lambda}_r(r') \, \mathrm{d}r' \quad . \tag{3.48}$$

The radial space charge force scales with the I/γ^2 and depends only on the charges at the same longitudinal position, requiring integration over the radial profile only, but not over the longitudinal profile. For example, if assuming a gaussian distribution for $\tilde{\lambda_r}$ the integral evaluates to $(\exp\left(-r^2/(2\sigma_r^2)\right)-1)/(2\pi)$. To estimate the impact of this force on beam transport, a radially defocusing strength KSC, analogous to the quadrupole strength K_1 , is determined.

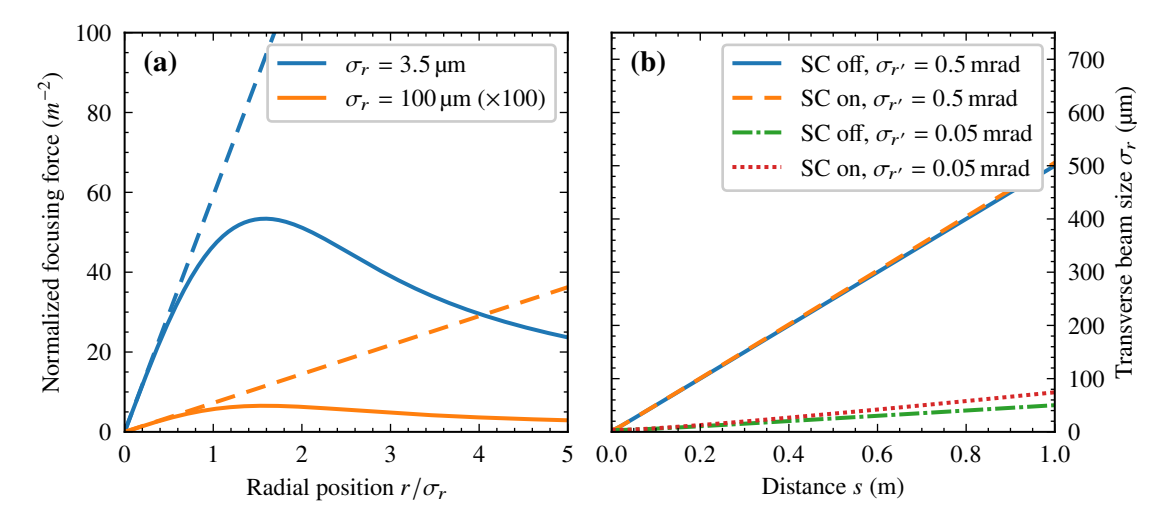


Figure 3.8: Strength and impact of transverse space charge forces expected for a gaussian shaped beam with LUX parameters $I_{\text{peak}} = 2.5 \, \text{kA}$ and $\gamma \approx 600$. Beam radii are $\sigma_r = 3.5 \, \mu \text{m}$ (blue) and $\sigma_r = 100 \, \mu \text{m}$ (orange, scaled ×100 for better visual representation). Dashed lines represent the linear approximations of the force. (a) Normalized space charge force at the bunch center directly after the plasma source, alongside the corresponding linear defocusing strength. The linear model holds for $r/\sigma_r \approx 1$. (b) Evolution of transverse beam size in free drift, assuming linear space charge force. For typical divergences of 0.5 mrad, transverse space charge effects are negligible. An effect becomes visible only if the divergence is reduced by approximately an order of magnitude.

This (first order) defocusing strength is calculated from the force to be

$$K_{\rm SC} \simeq \frac{1}{m_e c^2 \gamma} \left. \frac{\mathrm{d}F_r}{\mathrm{d}r} \right|_{r=0} = -\frac{eQ}{4\pi \varepsilon_0 m_e c^2} \frac{\tilde{\lambda}_{\zeta}(\zeta)}{\gamma^3 \sigma_r^2}$$
 (3.49)

$$K_{\rm SC} \simeq -6 \times 10^{-5} \frac{I}{\sigma_r^2 \gamma^3} \quad {\rm A}^{-1} \quad ,$$
 (3.50)

and using the peak current $I = I_{\rm peak} \simeq cQ\tilde{\lambda}_{\zeta,\rm max}$ to calculate the space charge effects at the core of the bunch. At the source, where the beam is small with a size of approximately $\sigma_r \simeq 3.5\,\mu{\rm m}$ and has a peak current of about 2.5 kA, the radial space charge force imposes a defocusing effect with a strength parameter of $K_{\rm SC} \simeq -50\,{\rm m}^{-2}$.

A comparison between the radial force dependent on the radial position and its linear expansion are illustrated in fig. 3.8(a), where the latter is showing a good agreement up to $\sigma_r/r \simeq 1$, effectively validating this model for the core of the beam. However, at the source, the beam dynamics are predominantly governed by emittance, meaning changes in transverse size due to factors other than space charge play a more significant role in shaping the beam. The transition energy to differentiate between space charge or emittance dominated beams is given by $\gamma_{\rm tr} = \hat{I}\sigma_r^2/(2I_A\gamma\varepsilon_n^2)$ [69], where $\gamma < \gamma_{\rm tr}$ indicates space charge dominated behavior. The initial divergence being $\sigma_{r'} \gtrsim 0.5$ mrad

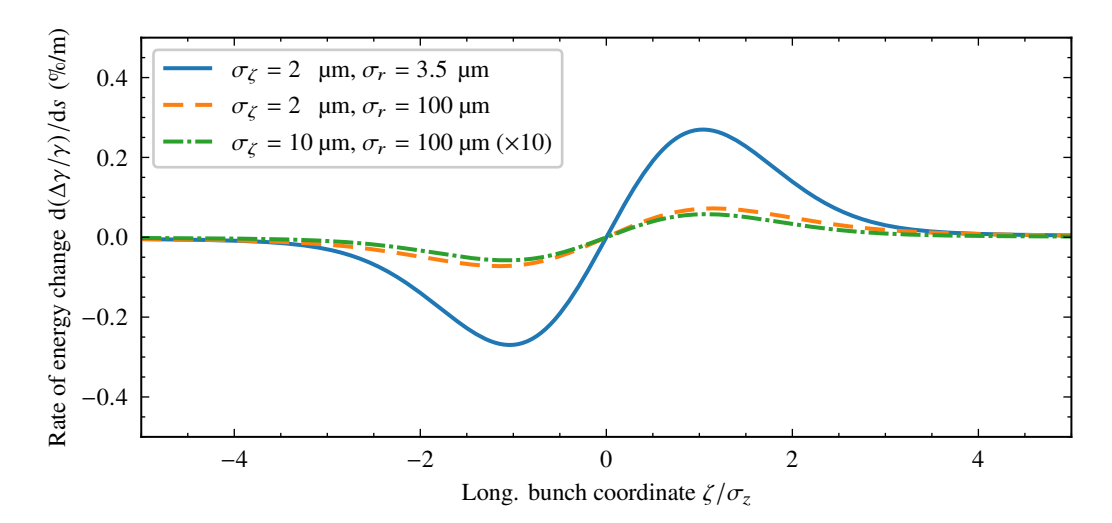


Figure 3.9: Rate of change in energy due to longitudinal space charge forces per unit length propagated in the beam transport. Amplitude depends on a particle's position within the bunch, illustrated for a gaussian beam with LUX parameters: (blue solid) $\gamma \simeq 600$ after the source with $I_{\rm peak} = 2.5$ kA, $\sigma_r = 3.5$ µm, (orange dashed) after transverse expansion $I_{\rm peak} = 2.5$ kA, $\sigma_r = 100$ µm, (green dash-dotted, magnified ×10 for visual representation) and after being stretched with a chicane by a factor of 5 to $I_{\rm peak} = 500$ kA, $\sigma_r = 100$ µm.

causes a much faster expansion than the space charge at $\gamma \simeq 600$. Due to this rapid expansion of the beam, the influence of K_{SC} decreases sharply, and decreases to less than $0.1\,\mathrm{m}^{-2}$ when reaching a transverse size of > 50 µm within the first 10 cm. Figure 3.8(a) illustrates that the effects of transverse space charge would only become significant at the source if the divergence were reduced by an order of magnitude, highlighting the dominance of divergence over transverse space charge effects under conditions expected at LUX.

Furthermore, transverse beam properties are typically measured well after any potential space charge-induced expansions at the source, incorporating their influence into the measurements. Downstream the beamline, where beam sizes are significantly larger than at the plasma source, ranging from 0.1 to 1 mm, space charge effects become markedly less significant, although the beam being considered as space charge dominated with $\gamma < \gamma_{\rm tr} \simeq 10^4$. Here, the space charge strength diminishes to $K_{\rm SC} < 0.01~{\rm m}^{-2}$, rendering it negligible compared to the focusing strengths of the quadrupoles, which range from $K_1 \simeq 1~{\rm m}^{-2}$ to $K_1 \simeq 100~{\rm m}^{-2}$. Only for long drift sections $L_d \gtrsim \sqrt{2/K_{\rm SC}}$, space charge effects remain non-negligible. For the typical beam parameters at LUX, such changes would only be noticeable in drifts exceeding about 10 to 15 m, a scenario that might only occur if all quadrupoles were turned off.

3.6.4 Longitudinal Space Charge

Similarly to the transverse space charge, a longitudinal force acts on the electrons, accelerating those at the head of the bunch and decelerating those at its tail. This difference in acceleration can be crucial because it directly alters the energy distribution along the bunch. The longitudinal force is derived from the electrostatic potential of a three-dimensional charge distribution. However, in this case it is more instructive to calculate the change in energy. In the following gaussian beam profiles in all spatial dimensions are assumed. The momentary energy change along the beam's longitudinal axis, where a particle experiences maximum acceleration, is modeled by [70]:

$$\frac{1}{\gamma} \frac{\mathrm{d}\Delta\gamma(\zeta)}{\mathrm{d}z} = \frac{eQ}{4\pi\epsilon_0 m_e c^2} \sqrt{\frac{2}{\pi}} \frac{\zeta}{\sigma_r^2 \sigma_z^3 \gamma^3} \int_0^\infty \mathrm{d}\lambda \lambda^2 \frac{\exp\left(-\frac{\lambda^2 \gamma^2 \zeta^2}{2\left(\lambda^2 \gamma^2 \sigma_z^2 + 1\right)}\right)}{\sqrt{\left(\lambda^2 + \sigma_r^{-2}\right)^2 \left(\lambda^2 + \gamma^{-2} \sigma_z^{-2}\right)^3}}$$
(3.51)

The relative rate of change due to longitudinal space charge forces is shown in fig. 3.9. Directly after the plasma source, for LUX parameters, see section 2.4, the formulas predict a strong longitudinal space charge force. There, the chirp imprinted onto the beam by this force is approximately $0.25 \%/\sigma_z$ per meter of beamline, which constitutes a substantial portion of the total energy spread of 1%. However, since the beam diverges quickly, the charge density and therefore the longitudinal space charge forces decrease, similar to the transverse space charge case. Nevertheless, they accumulate until the bunch is stretched in the chicane and the charge density is reduced. Therefore, the longitudinal space charge forces were evaluated for conditions after propagation with increased transverse size and after stretching with longer bunch length. Following the initial expansion, these space charge effects rapidly decrease. Once the beam is stretched, the influence of these forces becomes negligible. It is evident that the most substantial space charge effects occur immediately post-plasma source and swiftly diminish.

Moreover, while these forces predominantly modify the total energy spread, they are not expected to significantly alter the local uncorrelated energy spread, as they primarily affect a particle's energy in relation to its longitudinal position. Thus, longitudinal space charge primarily modifies the beam's chirp. The linear contribution by this additionally introduced chirp can be accounted for by adjustments to the chicane strength, thereby compensating for these changes.

3.6.5 Synchrotron Radiation

Charged particles emit electromagnetic radiation, when they are accelerated. For relativistic particles, it is called synchrotron radiation (SR) [55]. The total power emitted via this radiation by an electron bunch scales with the current and energy of an particle beam [55]. Inevitable it occurs in any magnetic component present in the beamline, but particularly when the beam is bent strongly over a short distance at high currents. Although there are dedicated applications for SR [71], a place where it is not desired to generate large amounts of SR are magnetic chicanes and bunch compressors in accelerators [72]. The same is true for the decompression scheme, where the concept is inverted and the beam is initially short. The emitted radiation in return can then interact with the bunch and transfer energy

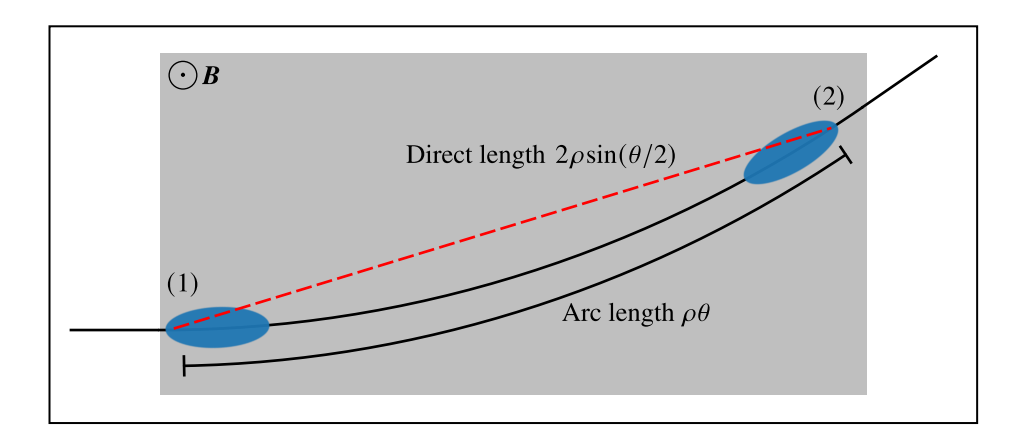


Figure 3.10: Illustration of an (blue ellipses) electron beam following a curved trajectory through a dipole magnet. (Red dashed line) Synchrotron radiation emitted early in the bend from the tail of the bunch (position (1)) overtakes the electron bunch as it progresses along the bend. Parts of this radiation then interact with particles at the head of the bunch at a later position in the bend (position(2)).

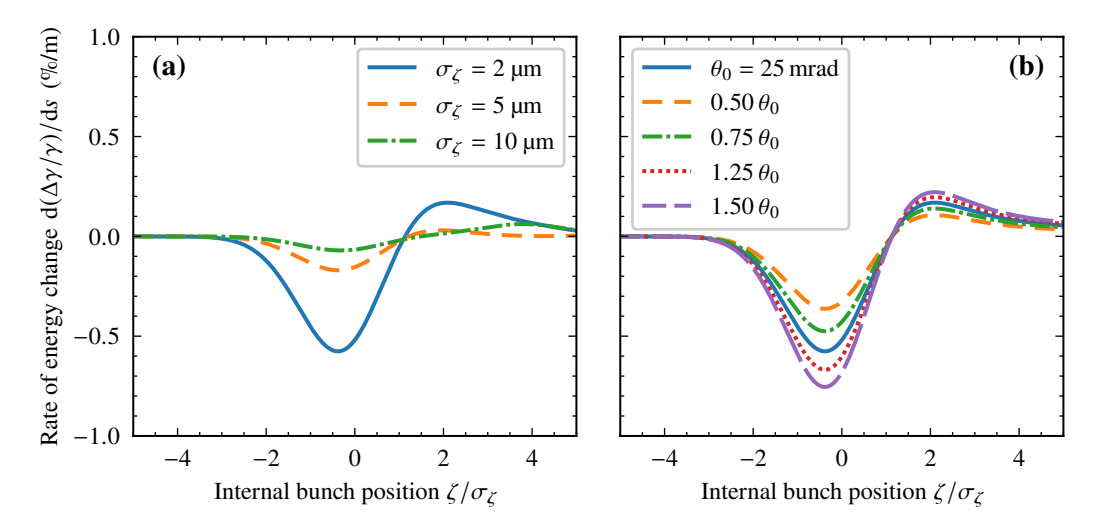


Figure 3.11: Rate of change in energy along the beam due to coherent synchrotron radiation as predicted by eq. (3.53). The beam has a charge of 45 pC. Particles at the bunch tail and center are decelerated and particles at the head accelerated. (a) Influence of bunch length with (blue solid) $\sigma_{\zeta,0}=2\,\mu\mathrm{m}$, (orange dashed) $2.5\times\sigma_{\zeta,0}$, and (green dash-dotted) $5\times\sigma_{\zeta,0}$. The deflection angle $\theta_0=25\,\mathrm{mrad}$ corresponds to a bending radius of 13.7 m for a 35 cm long dipole magnet. (b) Variations in the rate of energy change at different kick angles for an initially short bunch of $\sigma_{\zeta,0}=2\,\mu\mathrm{m}$, ranging from (orange short-dashed) $0.5\theta_0$ to (purple long-dashed) $1.5\theta_0$. The blue solid line represents the same parameters across both plots.

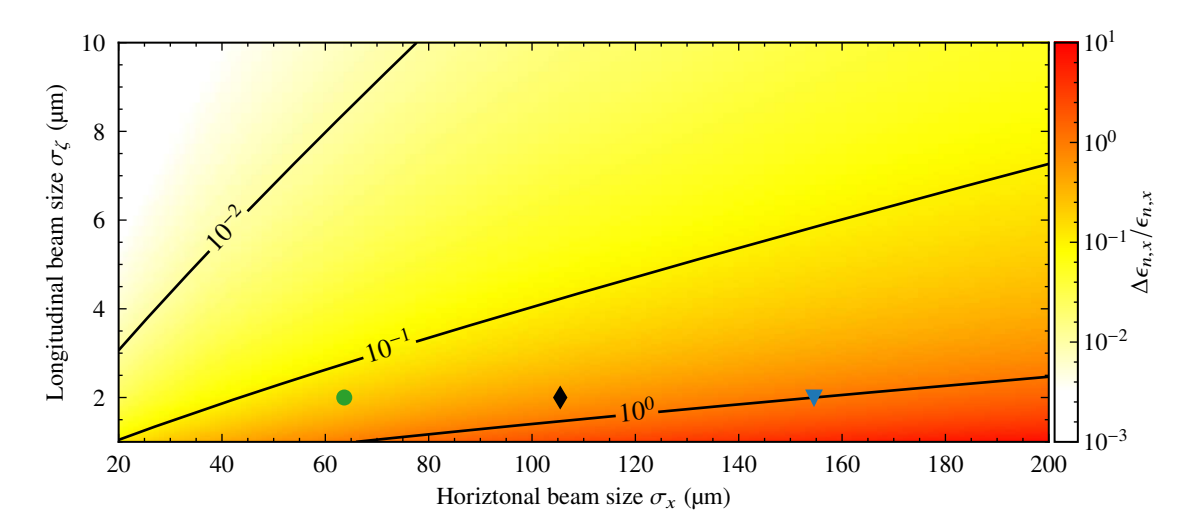


Figure 3.12: Relative increase in horizontal normalized emittance from CSR for a beam with $\gamma_0=587$ and a kick angle of $\theta_0=25$ mrad dependent on horizontal and longitudinal beam size, calculated according to eqs. (3.55) to (3.57). The markers highlight specific transverse beam sizes for a bunch length of $\sigma_\zeta=2\,\mu\text{m}$, where the emittance growth is limited to (green circle) 20 %, (black diamond) 50 %, and to (blue triangle) 100 %.

between its particles. In this process the light is following a straight line of length $2\rho \sin(\theta/2)$, and the electron bunch is traveling on an arc of length $\rho\theta$. As illustrated in fig. 3.10, this path length difference allows radiation emitted from the tail of the bunch to overtake it and act on the head. Parts of this interaction causes coherent emission, therefore called coherent synchrotron radiation (CSR), where the emitted power scales quadratically with the number of electrons in the bunch $P_c \propto N_e^2$ [73]. This phenomenon can imprint significant position-dependent energy variations onto high-current beams as they pass through a magnetic chicane. The maximum fraction of the bunch that is overtaken by the radiation, and hence contribute to this effect, is given by:

$$\Delta z \simeq \rho \theta - 2\rho \sin(\theta/2) \simeq \frac{\rho \theta^3}{24}$$
 (3.52)

The approximation holds true when the magnet length $L_{\rm mag}$ is much smaller than the bending radius ρ . The rate of energy exchange due to synchrotron radiation for electrons in the bunch is calculated in the 1D limit [74]:

$$\frac{\mathrm{d}E_{\mathrm{SR}}(z)}{\mathrm{d}s} \simeq -\frac{1}{4\pi\epsilon_0} \frac{eQ}{3^{1/3}\rho^{2/3}} \left[\frac{\tilde{\lambda}(\zeta - \Delta\zeta) - \tilde{\lambda}(\zeta - 4\Delta\zeta)}{\Delta\zeta^{1/3}} + \int_{\zeta - \Delta\zeta}^{\zeta} \frac{1}{(\zeta - \hat{\zeta})^{1/3}} \frac{\mathrm{d}\tilde{\lambda}(\hat{\zeta})}{\mathrm{d}\hat{\zeta}} \,\mathrm{d}\hat{\zeta} \right] \tag{3.53}$$

The first addend and the integration limits in the formula account for the fact that only a fraction of the bunch is affected by radiation that overtakes and interacts with it.

In cases where the bunch is shorter than the overtaken distance and taking the limit $\Delta z \to \infty$, only the integral remains as a steady-state solution.

For a 35 cm dipole magnet, any kick lower than 12 mrad reduces the path length difference below the initial bunch length of approximately $\simeq 2 \, \mu m$. Therefore, for the setup under consideration with kick angles above this value, the effect of CSR can be estimated from the steady state limit.

The resulting relative change in energy, as per eq. (3.53), is illustrated in fig. 3.11 for a 45 pC bunch at 300 MeV with different bunch lengths. The chosen reference kick angle is $\theta_0 = 25$ mrad in a 35 cm dipole magnet, see section 5.3.2, corresponding to a bending radius of 13.7 m. For the initially short bunch of $\sigma_{\zeta} \simeq 2 \, \mu m$, the rate of change in energy at the center of the bunch is approximately $\frac{dE}{ds} \simeq 0.6 \, \%/m$. As the bunch length increases, such as in later dipole magnets of a chicane used for decompression, the rate of energy change decreases. The corresponding dependence on a particle's position within the bunch is shown in fig. 3.11(a). At the core of the bunch near $\zeta = 0$, the rate of energy change scales near-linear with the kick angle θ , as depicted in fig. 3.11 (b). In the 0.35 m chicane dipoles of LUX, the anticipated energy loss at the bunch's core is estimated to be about 0.2 % from the first dipole. This loss is predominantly at the core and slightly towards the tail of the bunch, thereby imprinting a small additional chirp towards the head. The highest energy loss is expected in the first dipole, significantly reducing in subsequent dipoles due to the increased bunch length.

To compensate this energy loss, later chicane dipoles might require a slight reduction in field strength or the implementation of additional corrector dipoles to adjust for any positional and angular discrepancies after the chicane.

An additional note should be made to the considered 1D limit for the energy exchange. This model assumes that all radiation interacts with every particle within a specific longitudinal distance, disregarding the transverse size, dispersion, or the radiation's opening angle. The underlying assumption for the derivation of these formulas is [75]

$$\sigma_x \ll \left(R\sigma_z^2\right)^{(1/3)} \simeq 350\,\mu\text{m} \quad . \tag{3.54}$$

If this criterion is not met, the 1D model may overestimate the effects of CSR [76]. However, this criterion is likely to be fulfilled in the first and most important dipole, where the bunch is still short. Therefore the 1D estimations are applicable.

The energy exchange induced by synchrotron radiation affects the particles' trajectories, potentially leading to emittance growth. The increase in horizontal normalized emittance due to synchrotron radiation may be quantitatively assessed through [77, 78]

$$\Delta \epsilon_{n,x} = \Delta \epsilon_{n,x}^{(s)} + \Delta \epsilon_{n,x}^{(x)} \tag{3.55}$$

$$\Delta \epsilon_{n,x}^{(s)} \simeq 7.5 \times 10^{-3} \frac{\check{\beta}_x}{\gamma_0} \left(\frac{r_e N_e L_{\text{mag}}^2}{\rho^{5/3} \sigma_{\zeta}^{4/3}} \right)^2$$
 (3.56)

$$\Delta \epsilon_{n,x}^{(x)} \simeq 6.2 \times 10^{-3} \frac{\check{\beta}_x}{\gamma_0} \left(\frac{\Lambda_x r_e N_e L_{\text{mag}}}{\rho \sigma_{\zeta}} \right)^2$$
 (3.57)

with
$$\Lambda_x = \ln \left(\frac{\left(\rho \sigma_{\zeta}^2 \right)^{2/3}}{\sigma_x} \left(1 + \frac{\sigma_x}{\sigma_{\zeta}} \right) \right)$$

with the classical electron radius r_e . $\Delta \epsilon_x^{(s)}$ and $\Delta \epsilon_x^{(x)}$ represent the contributions to the emittance growth from the longitudinal or transverse electric fields acting on the bunch, respectively.

The impact of emittance growth on the bunch, dependent on its length and horizontal beam size, is illustrated in fig. 3.12. For the same bunch and dipole magnet as previously considered, maintaining a horizontal beam size below 155 μ m in the first dipole magnet limits the normalized emittance to double its initial value of 1 mm mrad, while reducing it below 105 μ m and 65 μ m keeps the increase below 50 % and 20 % respectively.

Emittance growth in the vertical plane is significantly less and orders of magnitude smaller [79]. For this case, the relative increase in vertical normalized emittance has been estimated to be only about 10^{-5} , therefore being negligible. Utilizing an S-shaped chicane, as opposed to a C-shaped one, could mitigate emittance growth, since the transverse forces in the two halves of such a setup act in opposing directions [80]. However, this configuration would extend the length of the beamline, presenting its own set of challenges.

3.7 Transfer Map Calculation for LUX Magnets

Not every magnetic field configuration yields equations of motion that can be analytically solved. This often involves addressing the fringe fields of magnets, which naturally occur as the magnetic field does not abruptly drop to zero at a magnet's boundary. Instead, it transitions smoothly to the field-free region, adhering to Maxwell's equations. Further, to accurately describe the motion in more complex field configurations, higher order transfer maps are required. The discussion of fringe field effects and higher orders was intentionally omitted in the analytical discussions in section 3.1 for clarity of the basic concept, and should be briefly addressed here.

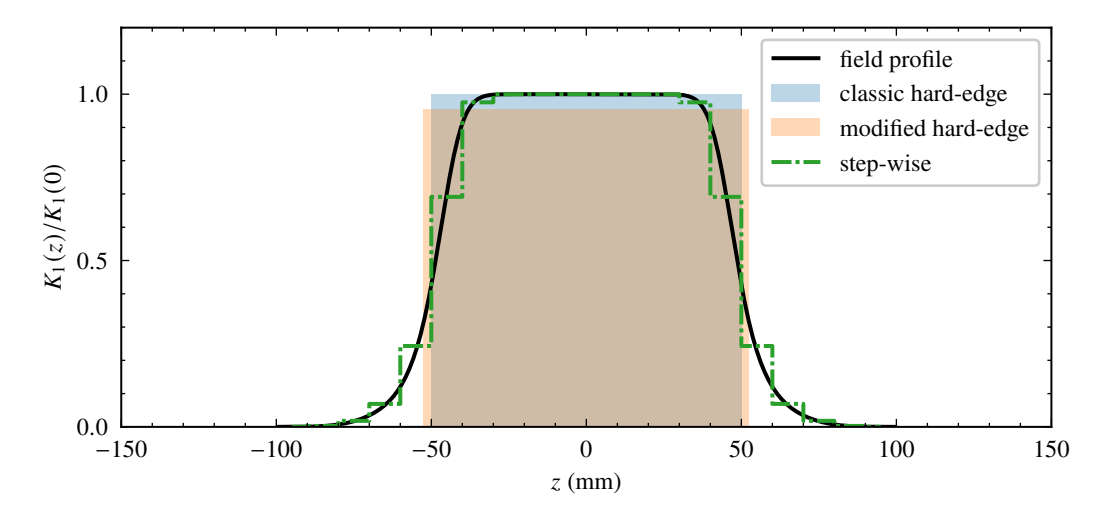


Figure 3.13: Comparison of (black solid) a realistic quadrupole field profile with models for simplification, which include (blue box) the usual hard-edge model, (orange box) a modified hard-edge-model to improve accuracy of the matrix elements, and (green dotted) a step-wise approximation with 20 subdivisions.

Fringe Fields and Non-Analytical Models

A way to find the transfer matrix elements for arbitrary field profiles is by solving the equations of motion numerically, i.e. by tracking a substantial number of particles through the magnetic field, and fit the matrix elements to the final coordinates [81–83]. However, this requires the exact 3D field to be known.

A simpler approach, that is applicable to many beam optics elements, is the use of an equivalent field with the same integrated field. For this purpose consider the matrix eq. (3.9) for a pure quadrupole field. The commonly used "hard-edge" model [84] simplifies the field profile to a constant gradient, determined by the peak gradient at the center of the magnet g_0 , and an effective length obtained by dividing the integrated field by this gradient

$$L_{\text{eff}} = \frac{\int g(z) \, \mathrm{d}z}{g_0} \quad , \tag{3.58}$$

where the integration is performed over the full field profile.

The peak gradient g_0 and the effective length are then used in eq. (3.9) to describe the transport though the quadrupole. The use of the peak field is justified by the fact that it is the most influential part of the magnet onto the beam dynamics. This model gives a reasonable approximation for the transfer matrices and can be used as a first educated guess for the beam optical properties when designing a beamline.

While the peak field provides a approximation for transfer matrices and aids in initial beamline design, its accuracy reduces with shorter magnet lengths $L \leq d$ [85],where d is the bore diameter, and large quadrupole strengths $K_1 \gg 1$ [86]. As LUX targets to be a compact accelerator, the used components were chosen to be of short length. However, this results in the requirement of high gradients to transport the beam at the expected energies. Such high gradient electromagnet quadrupoles with a yoke length of 10 cm are used at LUX. With typical K_1 values on the order of 10 to $100 \, \mathrm{m}^{-2}$, a more precise calculation of matrix elements, including fringe fields and their impact on the beam transport, has to be considered.

Enhancing the accuracy of matrix elements can be approached in several ways. One method is to rescale the peak field and effective length in the hard-edge model to better match the true matrix elements [84]. Alternatively, the field profile could be divided into smaller segments, each characterized by its own field strength and shape [87], or the fringes could be parametrized using integrals to incorporate their influence more accurately [88, 89].

For an improved hard-edge model a modified effective length and a corresponding effective field strength is calculated as [84, 90]

$$L_{\text{eff,S}} = \left(\frac{12}{L_{\text{eff}}} \int z^2 \frac{g(z)}{g_0} dz\right)^{1/2} , \qquad K_{1,S} = \frac{L_{\text{eff}}}{L_{\text{eff,S}}} K_1 .$$
 (3.59)

The increased effective length at lower peak field better reflects the impact of the fringes and improves the accuracy of the used matrices [86]. Therefore, using this modified effective length ensures that both routine operations and detailed studies benefit from enhanced modeling precision of fringes. For optimizations and simulations conducted with the accelerator code *Elegant* [83], the modified hard-edge model was utilized.

Additionally to this approach, an in-house matrix code is used, that either uses a hard-edge model with the values obtained by eq. (3.58) and eq. (3.59), or matrices from the numerical integration of the equations of motion, including the measured fringe fields. The latter is used to increase the accuracy further.

For the two electron spectrometers at *LUX*, addressing the challenges posed by the large deflection angles, energy-dependent path lengths through fringe regions, and screen rotation relative to the beam axis requires tracking and cannot be described by a normal dipole model [48, 91]. To accurately model these transfer maps, particle trajectories were numerically tracked through measured 3*D* field maps of the magnets using *ASTRA*[92]. Subsequently, the relationship between initial coordinates of particles entering the spectrometers and their final positions on the spectrometer screens were determined by fitting the matrix elements that describe the transformation from the input to the output states. These matrices are incorporated into the in-house code to accurately describe the imaging into the electron spectrometers, while taking into account their geometry and the specifics of their magnetic field.

Energy Deviations

The equations of motion handle particles that deviate in energy from the reference particle by their relative energy offset δ . To increase the accuracy of the beam transport calculations, especially when dealing with larger energy deviations, the utilization of higher-order elements is necessary. While a first-order transport model suffices for basic understanding, most accelerator simulation codes incorporate higher-order contributions for increased accuracy in particle tracking and lattice optimization. However, this approach lacks the ability to easily address and optimize the properties of individual energies within the beam other than the reference energy.

An approach to extend the formalism to more accurately describe such deviating energies, is to use individual matrices with exact momentum p for each energy of interest. Every energy considered this way then has its individual set of transport matrices with the normalized field components b_i adjusted accordingly.

This approach becomes particularly useful when dealing with changes in the beam size at energies different from the reference energy, as these variations are not readily available from standard transport matrices. Further, it allows to optimize the beamline for multiple energies simultaneously in an easy and direct way. An algorithm to utilize this property was developed and used in section 5.2, to focus different energies contained in the beam at different positions in the beam line.

3.8 Conclusion

The properties of laser-plasma accelerated beams can pose a challenge to their transport and therefore their utilization in an FEL experiment. Degrading effects have to be limited and beam quality preserved during transport. This chapter explored various effects that can impact beam quality during transport and decompression, including collective phenomena like longitudinal space charge and coherent synchrotron radiation. However, their impact depends on the actual beam parameters and has to be mitigated by proper beam manipulation. Consequently, the beamline design has to account for this. Within the beamline, the quadrupoles have to be well aligned and their strengths accurately known, to properly focus the beam at the proper position, longitudinally and transversely.

For successful integration into an FEL setup, the beamline must adhere to some requirements to control and minimize adverse influences:

- Capturing the beam early is essential to reduce initial divergence, thereby preventing a growth of emittance and potentially slice energy spread.
- Maintaining a small divergence on the level of 0.1 mrad divergence throughout transport avoids reintroducing those detrimental effects.
- A shorter beamline reduces cumulative adverse effects, enhancing overall beam quality.
- While maintaining small transverse beam sizes increases tolerance for magnet errors, overly small sizes should be avoided to prevent significant space charge effects.

- Achieving a minimal horizontal beam size in the decompression chicane, particularly in the first dipole, limits emittance growth due to coherent synchrotron radiation.
- Transverse positioning of beam optical elements within 10 µm relative to a common axis ensures
 that transverse offsets within the undulator are kept below 100 µm, reducing the need of corrector
 dipoles.
- Reducing external magnetic fields minimizes unwanted kicks and dispersion.
- Installation of corrector dipoles can effectively compensate for residual misalignments and external field influences.

These considerations are incorporated in optimizing the beam transport and have to be balanced with the needs and space requirements of diagnostics.

Free-Electron Lasers

A free-electron laser is a source of intense, coherent synchrotron radiation, able to generate wavelengths over a wide range from the microwave regime down to sub-nanometer hard X-rays of short pulse duration. Following previously available synchrotron radiation sources, such as parasitic or dedicated generation in bends of storage rings, or wigglers, FELs are referred to as 4th generation light sources [1]. Several FELs are currently operational worldwide, with more under construction or proposed [93, 94].

Early theoretical considerations of generating intense light pulses at below cm to sub-mm wavelength in a periodic electromagnetic oscillator structure [95] were followed by the description [96] and first operation of an undulator [97]. The free-electron lasing process, based on the stimulated emission in undulators, was predicted [98, 99] and later experimentally demonstrated [100, 101]. Originally, FELs utilized optical cavities for amplification of the radiation over multiple passes. However, subsequent theoretical developments showed that saturation could be reached from spontaneous emission alone, leading to the concept of self-amplified spontaneous emission (SASE) for single-pass FELs, eliminating the need for optical cavities [102, 103]. Dropping the requirement to reflect the radiation and achieving high intensities in a single pass is especially important for developing X-ray FELs due to the lack of mirror materials for nm-scale wavelengths. The formulation of the high-gain theory [104] further enhanced the understanding of the FEL process, laying the groundwork for the modern understanding, design and operation of FELs.

This chapter summarizes the fundamental concepts important to the understanding of an undulator and a free-electron laser, and their application to the *LUX* experiment. The basic motion in the undulator is described in section 4.1, followed by properties of the undulator radiation in section 4.2 and the 1*D* FEL theory in section 4.3. Implications by 3*D* and degrading effects relevant to *LUX* are treated separately in section 4.4. The optimization of the beam properties and interaction of the beam with the FEL pulse is discussed in section 4.5. Finally, simulations with the obtained parameters to estimate the expected performance are presented in section 4.6.

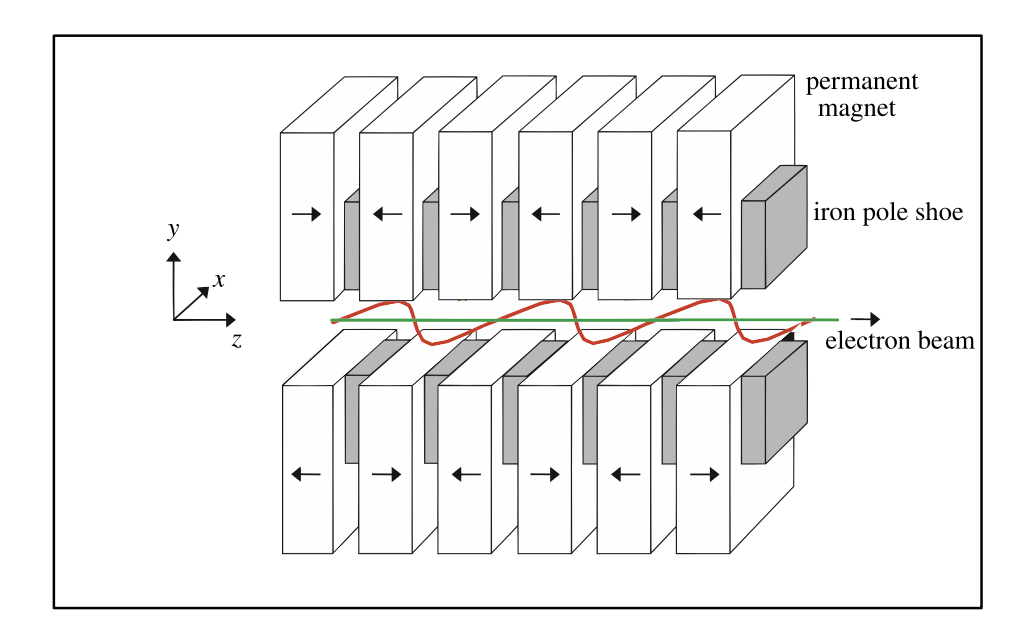


Figure 4.1: Schematic view of an undulator structure with alternating polarity of the magnets, guided by iron pole shoes towards the gap and creating a periodic vertical magnetic field along (green line) the central axis. The electron beam moves on a (red line) sine trajectory in the horizontal plane about this central axis. Figure adapted from [105].

4.1 Electron Motion in the Undulator

An undulator is a device, which produces an alternating magnetic field, to accelerate the electrons perpendicular to their axis of motion, causing them to emit radiation. Due to its periodicity an increasing amount of radiation is generated, which eventually in return can interact with the electrons. A schematic illustration of this motion is shown in fig. 4.1 and will be briefly presented in the following.

4.1.1 Magnetic Field of an Undulator

A magnetic field that represents a perfect undulator structure and satisfies Maxwell's equations can be found by solving the Laplace equation $\Delta \phi_B = 0$ for a scalar potential ϕ_B in absence of electric fields and currents. At LUX a plane pole undulator is used, that has the main field component in vertical y direction. For the discussion of the motion of the particles in the field, it is sufficient to consider an horizontally infinitely wide magnetic structure, neglecting the influence of finite pole width. The

solution for the corresponding magnetic field $\mathbf{B} = \nabla \phi_B$ in cartesian coordinates x, y, z is [106]:

$$B_x = 0$$

$$B_y = B_0 \cosh(k_u y) \cos(k_u z)$$

$$B_z = -B_0 \sinh(k_u y) \sin(k_u z)$$
(4.1)

with k_u being the undulator wave number of the field and linked to the period length $\lambda_u = 2\pi/k_u$. Here, the field is chosen such that the main component points in the y-direction and the periodic structure goes along the z-axis.

As trajectories of interest are close to the central axis, where $|k_u y| \ll 1$, the field is expanded about small vertical offsets to first order:

$$B_x = 0$$

$$B_y \simeq B_0 \cos(k_u z)$$

$$B_z \simeq -B_0 k_u y \sin(k_u z) . \tag{4.2}$$

4.1.2 First Order Motion

Plugging the vertical field component into eq. (3.6) yields an equation of motion for a particle without energy deviation in the horizontal plane

$$x'' = \frac{eB_0}{\gamma m_e c} \cos(k_u z) \quad , \tag{4.3}$$

where relativistic motion $\beta \approx 1$ is assumed. Integration with respect to the longitudinal position z in the undulator gives the horizontal position and its change

$$x' = \int x'' dz = \frac{K}{\gamma} \sin(k_u z) + x'_0$$
 (4.4)

$$x = \int x' dz = -\frac{K}{\gamma k_{u}} \cos(k_{u}z) + x'_{0}z + x_{0} \quad , \tag{4.5}$$

where the undulator strength parameter $K = \frac{eB_0}{m_e c k_u} \simeq 0.934 B [T] \lambda_u [cm]$ is introduced. It defines the maximum change in horizontal position $x' \leq K/\gamma$ and also the angular width of the radiation cone of the radiation emitted along one undulator period $\theta_{\rm max} \simeq K/\gamma$ as the electron sweeps over this angular region [106]. The magnetic structure and the oscillatory motion in the horizontal plane are depicted in fig. 4.1.

Similarly the transverse velocity $\beta_x(z) = (K/\gamma) \sin(k_u z) + \beta_{x,0}$ is directly computed by rewriting the Lorentz force eq. (3.1) in terms of the velocity and integrating β_x' , having the same form as eq. (4.4). Using this the momentary (for $\beta_{x,0} = 0$) and average longitudinal velocities are given by

$$\beta_z = \sqrt{\beta^2 - \beta_x^2} \stackrel{\gamma \gg 1}{\simeq} 1 - \frac{1}{2\gamma^2} \left(1 + K^2 \sin^2(k_u z) \right)$$
 (4.6)

$$= \overline{\beta_z} + \frac{K^2}{4\gamma^2} \cos(2k_u z) \tag{4.7}$$

$$\overline{\beta_z} = \frac{1}{\lambda_u} \int_0^{\lambda_u} \beta_z \, \mathrm{d}z \simeq 1 - \frac{1}{2\gamma^2} \left(1 + \frac{K^2}{2} \right) \quad . \tag{4.8}$$

The longitudinal motion is slowed down by $(K/2\gamma)^2$ on average due to the detour and performs small oscillations with the same amplitude. This longitudinal oscillation is twice as fast as the transverse oscillation.

4.1.3 Undulator Focusing

In addition to the average movement in the undulator, the methods presented in chapter 3 can be utilized to calculate the transport elements for the undulator. Although the wiggling motion at any longitudinal position z is important to describe the emission of and interaction with radiation, as explored in the next sections, the focusing properties of an undulator are well described by a smooth period-averaged motion, considering only slow changes [107]. Following this approach using the above result for x' in the undulator and averaging the right hand side over one period, the equation of motion to first order for the y component becomes [106]

$$y''(z) = -\frac{eK^2k_u^2}{2\gamma_0^2}y \quad . \tag{4.9}$$

The corresponding first order transport matrix in this smoothed sense, neglecting the influence of the oscillations over individual undulator periods, is given by

$$R_{\text{und},y} = \begin{pmatrix} \cos\left(\omega_{y}L\right) & \frac{1}{\omega_{y}}\sin\left(\omega_{y}L\right) \\ -\omega_{y}\sin\left(\omega_{y}L\right) & \cos\left(\omega_{y}L\right) \end{pmatrix} \quad \text{with} \quad \omega_{y}^{2} = \frac{K^{2}k_{u}^{2}}{2\gamma_{0}^{2}}$$
(4.10)

In the averaged motion, variations in the horizontal plane vanish and the undulator only focuses the beam in the non-wiggling plane, similar to a magnetic quadrupole with focusing strength ω_y^2 . This is due to particles that are vertically offset see a longitudinal field component between the poles that couples to the horizontal wiggling motion. For the infinitely wide undulator model, no change from a free drift is obtained at first order, except for the oscillatory motion with no influence on the averaged horizontal envelope.

4.1.4 Beam Size in the Undulator

The obtained matrix and the formalism shown in section 3.1 is used to calculate the transport through the undulator. Focusing effects are taken into account to still achieve the desired beam focus position and size for non-negligible ratios $(Kk_uL_u)/\gamma_0$. Further it allows to determine the smallest achievable minimum and average beam sizes. This is done to maximize the current density available throughout the undulator and additionally keep all particles close to the center to avoid off-axis field deviations.

First, the average beam size in the horizontal plane without focusing and neglecting any field imperfections is minimized. The beam envelope is expected to behave like in a free drift. Therefore, the beta function inside the undulator is given by

$$\hat{\beta}_{x}(z) = \hat{\beta}_{x,\text{in}} - 2\hat{\alpha}_{x,\text{in}}z + \frac{1 + \hat{\alpha}_{x,\text{in}}^{2}}{\hat{\beta}_{x,\text{in}}}z^{2}$$
(4.11)

with the average beta function

$$\hat{\beta}_{x,\text{avg}} = \hat{\beta}_{x,\text{in}} - \hat{\alpha}_{x,\text{in}} L_u + \frac{1 + \hat{\alpha}_{x,\text{in}}^2}{\hat{\beta}_{x,\text{in}}} \frac{L_u^2}{3}$$
(4.12)

In the symmetric case with a waist at the undulator center, i.e. $\hat{\alpha}_{x,\text{min}} = 0$ at that position, the beta function along the undulator is expressed as

$$\hat{\beta}_x(z) = \hat{\beta}_{x,\min} + \frac{1}{\hat{\beta}_{x,\min}} z^2$$
 , (4.13)

and the average value reformulated as

$$\hat{\beta}_{x,\text{avg}} = \hat{\beta}_{x,\text{min}} + \frac{1}{\hat{\beta}_{x,\text{min}}} \frac{L_u^2}{3}$$
 (4.14)

Minimizing the average beta function shows that indeed the symmetric case yields the smallest average beam size. In that case the beam size is matched at the undulator entrance with

$$\hat{\alpha}_{x,\text{in}} = \sqrt{3}$$
 and $\hat{\beta}_{x,\text{in}} = \sqrt{4/3}L_u$. (4.15)

The average and minimum beta-function for a 2 m undulator follows from this as

$$\hat{\beta}_{x,\text{avg}} = L_u / \sqrt{3} \simeq 1.15 \,\text{m}$$
 (4.16)

and

$$\hat{\beta}_{x,\text{min}} = L_u/(2\sqrt{3}) \simeq 0.58 \,\text{m}$$
 (4.17)

The average beam size for *LUX* parameters with a geometric emittance of $\epsilon_x \simeq 1.75$ nm is then found by averaging over $\sigma_x(z) = \sqrt{\epsilon_x \beta_x(z)}$ to be $\sigma_{x,\text{avg}} \simeq 45 \, \mu\text{m}$.

For the LUX reference beam and an undulator K=2, the focusing strength $\omega_y\simeq 1$ which corresponds to the beam covering about a third of the focusing oscillation over $2\,\mathrm{m}$ undulator length. In a similar fashion to the horizontal beam size, the vertical average beta function is optimized including the oscillatory behavior with a minimum beta function at the undulator center $\hat{\beta}_{y,\mathrm{min}}=\sqrt{(1-\mathrm{sinc}(L_u\omega_y)/(1+\mathrm{sinc}(L_u\omega_y))/\omega_y}$. The resulting average beta function is

$$\hat{\beta}_{y,\text{avg}} = \frac{1}{\omega_y} \sqrt{1 - \text{sinc}^2 \left(L_u \omega_y \right)} \quad , \tag{4.18}$$

which gives a similar average vertical beam size of $\sigma_{y,avg} \simeq 40 \, \mu m$. Again, minimizing the beam size directly instead of the beta function, also does not significantly alter the average beam size for the assumed K and ω_y .

Another useful solution appears when matching into the undulator with $\hat{\beta}_{y,\text{in}} = 1/\omega_y$ and $\hat{\alpha}_{y,\text{in}} = 0$, which balances the divergence and the focusing force of the undulator, such that the beam size stays constant and $\hat{\beta}_{y,\text{avg}} = \hat{\beta}_{y,\text{in}}$. For the *LUX* reference beam and undulator parameters both these solutions yield similar beam.

The average beam sizes cannot be reduced further than those values. Typically, they are larger either due to degrading effects during transport or chromatic aberration from the quadrupoles' combined imaging into the undulator, if not compensated. Therefore, the beam size and in consequence the current density may change along the bunch. On the other hand proper beam manipulation might utilize this to improve the FEL output [108]. However, the obtained parameters for the beam sizes provide a reference for the typical values available in the undulator.

4.2 Basic Radiation Properties

During the electrons' motion through the undulator spontaneous undulator radiation is emitted. Since it is part of the startup of a SASE FEL, both share some properties like the fundamental wavelength, and they have to be differentiated from each other at low FEL amplification. During the sinusoidal motion of the relativistic electrons, with $\gamma \gg 1$, in the magnetic field of the undulator, they constantly emit synchrotron radiation into a cone with opening half-angle of about $1/\gamma$ [106]. This can be understood from the distribution of emitted power in a moving frame with the instantaneous velocity at the position of a bend. In that frame the radiation is emitted in a dipole pattern according to the Larmor equation. By Lorentz-transforming the radiation to the laboratory frame, causing relativistic aberration, the forward cone is contained within $\theta = \pm \arcsin(1/\gamma) \simeq \pm 1/\gamma$. Therefore a common distinction between an undulator and a wiggler is made if $K \gg 1$, as the opening angle of the radiation is then dominated by the previously found radiation cone due to the electrons' instantaneous direction of movement. However, the exact value of K where this distinction is made is arbitrary and different values of K can be found in literature, also in combination with device length or energy [106, 109]. The main distinction criterion is their different spectra in the observed frequency range.

In the following the observable properties of the radiation from electrons in the undulator are described.

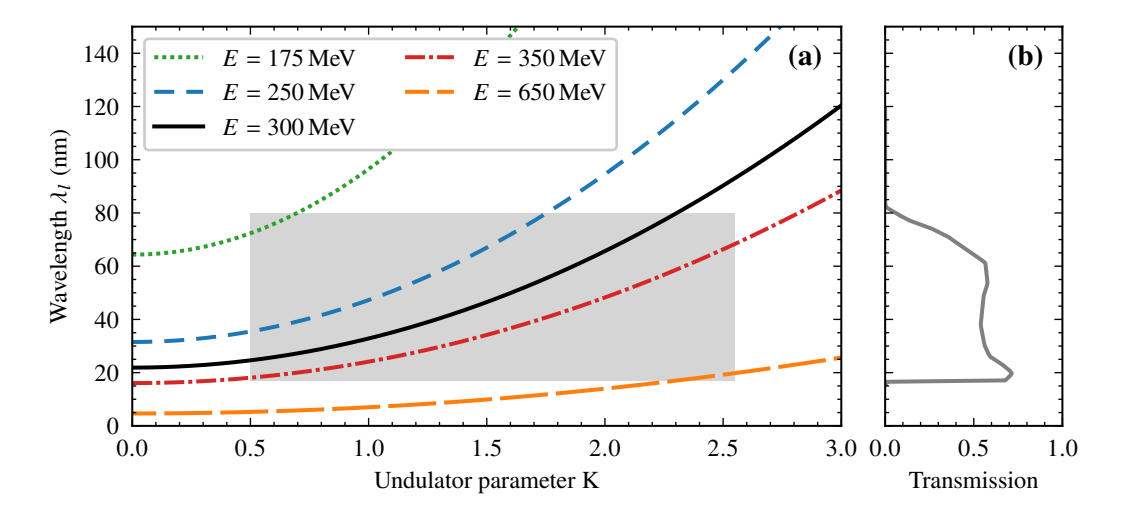


Figure 4.2: (a) Fundamental wavelength of undulator radiation for different electron energies dependent on undulator strength given by eq. (4.20). Gray shaded area indicates transmission window of an aluminum filter ≈ 17 to 80 nm in the reasonably accessible range for the undulator strength of 0.5 < K < 2.55. (b) Transmission of a 250 nm aluminum filter.

Wavelength

To obtain the fundamental wavelength, the electrons' motion in a frame moving along with the bunch with $\overline{\beta_z}c$ from eq. (4.8) is considered. The magnetic structure is Lorentz-contracted by $\overline{\gamma_z}$, acting like a traveling electromagnetic wave, with an electric field pushing the electron transversely. In that frame the transverse velocity of the electrons oscillates with a frequency $\omega^* = 2\pi c \overline{\beta_z} \overline{\gamma_z}/\lambda_u$ and they emit dipole radiation as mentioned before. Looking at the radiation in the laboratory frame from an angle θ to the longitudinal axis, another Lorentz transformation can be applied to get a relation between the observed photon energy $E_{\rm ph} = h\omega_l = 2\pi c/\lambda_l$ and the photon energy in the moving frame $E_{\rm ph}^* = h\omega^*$. From these relations, the observable radiated wavelength λ_l from the undulator is calculated as as

$$\omega^* = \overline{\gamma_z} \omega_l \left(1 - \overline{\beta_z} \cos \theta \right) \qquad \Leftrightarrow \qquad \lambda_l = \frac{\lambda_u}{\overline{\beta_z}} \left(1 - \overline{\beta_z} \cos \theta \right) \quad . \tag{4.19}$$

Substituting $\overline{\beta_z}$ from eq. (4.8) and approximating for small angles $\cos\theta \simeq 1 - \theta^2/2$ the fundamental wavelength of undulator radiation is given by

$$\lambda_l \simeq \frac{\lambda_u}{2\gamma^2} \left(1 + \frac{K^2}{2} + \gamma^2 \theta^2 \right) \quad , \tag{4.20}$$

where terms containing θ^2/γ^2 were dropped. The θ^2 dependence indicates the red shift of photons with an angle to the longitudinal undulator axis in the observer frame. This is due to less momentum towards the forward direction in the moving frame. Due to the apparent transverse motion not being

sinusoidal in time due to the oscillating longitudinal velocity eq. (4.6), higher harmonics appear naturally in the emitted radiation. Although not being sinusoidal, the motion is symmetric about a half period. Therefore a Fourier expansion only yields odd harmonics towards the forward direction [110]. This distortion from a sinusoidal motion and therefore higher harmonics are suppressed for $K \ll 1$. Increasing $K \gg 1$ leads to stronger higher harmonics in the spectrum, reasoning the above mentioned distinction between undulators and wigglers. Further, when looking at the motion from non-forward direction moving away from the axis, the symmetry is broken and even harmonics are observable.

The fundamental wavelengths for different electron energies γ with respect to the undulator parameter K are shown in fig. 4.2. The electron beam energies at LUX generate wavelengths in the range of the extreme ultraviolet [111] when passing through an undulator with typical values of K on the order of 1. In this wavelength range, an aluminum filter with transmission window of approximately ≈ 17 to 80 nm [112, 113] is used to block the laser that drives the laser-plasma acceleration, which could otherwise mask the FEL signal.

For the LUX reference beam with an energy $E = 300 \,\text{MeV}$, staying within the observable wavelength range requires a K < 2.3 for an undulator period length of $\lambda_u \simeq 15 \,\text{mm}$. Conversely, considering a reasonable range of undulator strengths from K > 0.5 to the maximum K < 2.55 at room temperature [114] in principle allows for a wide accepted energy range of the electron beam from 175 MeV to 650 MeV.

Interference and Opening Angle

As indicated in fig. 4.3, constructive interference requires that the radiation emitted by an electron at different positions along the undulator has the same phase, which is dependent on the angle of emission. To have the phase matched, the traveled time of the bunch along the undulator and that of a wavefront from previously emitted radiation must only differ by a multiple of the wavelength per speed of light

$$\frac{\lambda_u \cos \theta + n\lambda_l}{c} = \frac{\lambda_u}{\overline{\beta_z}c} \quad , \tag{4.21}$$

which is the same as eq. (4.19) to eq. (4.20) if re-arranged for $n\lambda_l$ and expanded about $1/\gamma \approx 0$. Higher harmonics with wavelength λ_l/n also interfere constructively, which is the coherence condition for undulator radiation. Similarly the opening angle of the radiation of a given wavelength from the undulator is obtained by finding the angle θ^* where full destructive interference first occurs. This is when the advance of the light wave compared to the electron beam is one wavelength over the full undulator [106]. From the picture shown in fig. 4.3 the condition for destructive interference at the fundamental wavelength is deduced to be

$$N_u \lambda_u \cos \theta^* + (N_u + 1)\lambda_l = \frac{N_u \lambda_u}{\beta_z} \quad . \tag{4.22}$$

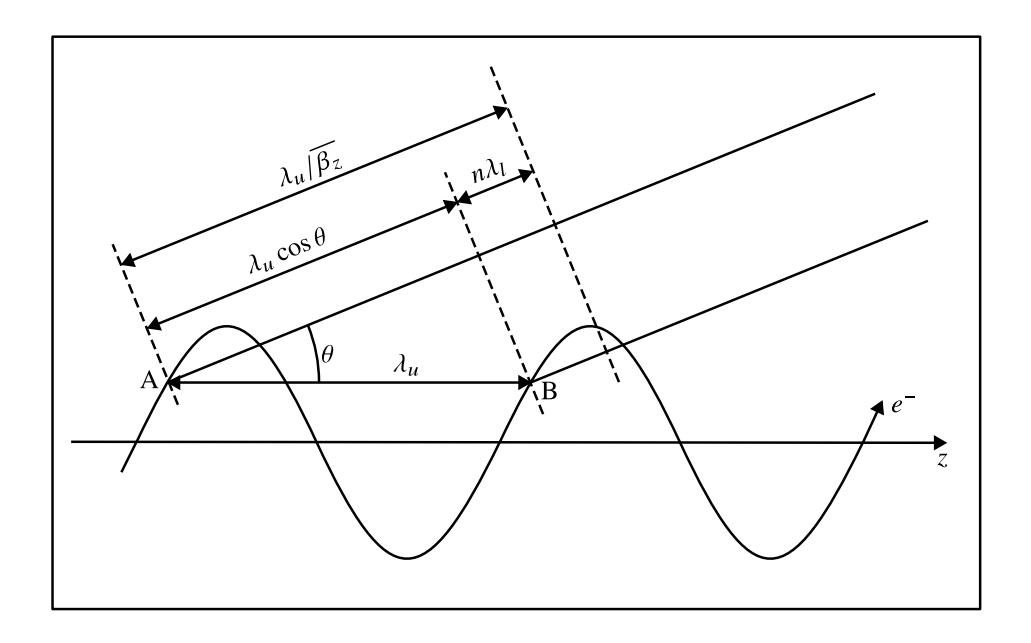


Figure 4.3: Illustration of the coherence condition for undulator radiation. An electron travels one undulator period λ_u from A to B in $t = \lambda_u/(\overline{\beta_z}c)$, therefore radiation of wavelength λ_l emitted at A under an angle θ is traveling a distance $\lambda_u/(\overline{\beta_z}$ in the same time. Radiation emitted at B in the same direction interferes constructively if the wavefront is shifted by an integer multiple of λ_l . Figure adapted from [106].

Equating this with the constructive interference, the opening angle of the cone about the central axis $\theta = 0$ containing the fundamental radiation is

$$\theta^* \simeq \sqrt{\frac{2\lambda_l}{N_u \lambda_u}} = \frac{1}{\gamma} \sqrt{\frac{1 + \frac{K^2}{2}}{N_u}} \quad , \tag{4.23}$$

where $\cos \theta^* \simeq 1 - {\theta^*}^2/2$ was expanded. It should be noted that an undulator parameter $K \ge 1$ broadens the radiation cone, while for values $K \ll 1$ the approximation $\theta^* \simeq 1/(\gamma \sqrt{N_u})$ is commonly used. For LUX at 300 MeV and K = 2, this corresponds to an approximate half-angle of $\theta^* = 0.25$ mrad of the on-axis radiation cone for the fundamental wavelength. The angular distribution can be approximated by a Gaussian with standard deviation [106]

$$\sigma_{r'}^* = \frac{\theta^*}{\sqrt{2}} = \sqrt{\frac{\lambda_l}{L_u}} \quad . \tag{4.24}$$

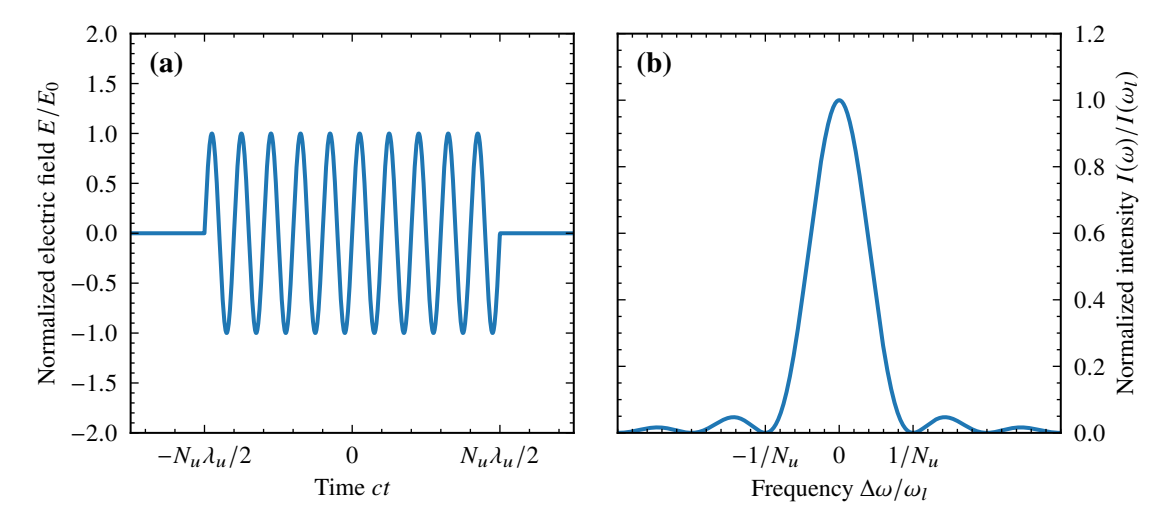


Figure 4.4: (a) Finite wave train of $N_u = 10$ cycles and (b) corresponding spectrum with minima at $\Delta\omega/\omega_l = \pm 1/N_u$.

Further assuming the radiation from the undulator behaves as the fundamental mode of an optical resonator, the source size is obtained from the relation of the phase space volume $\lambda_l/2 = 2\pi\sigma_r^*\sigma_{r'}^*$ to be [115]

$$\sigma_r^* = \frac{1}{4\pi} \sqrt{\lambda_l L_u} \quad . \tag{4.25}$$

Bandwidth

To estimate the spectrum of the (single particle) on-axis radiation, a finite light pulse consisting of a sinusoidal wave train is considered, neglecting higher harmonics. During the motion in the undulator one oscillation of the wave train is emitted per undulator period, yielding N_u cycles and a pulse duration of $T = N_u \lambda_l / c = N_u 2\pi/\omega_l$. The (intensity) spectrum is obtained as the squared Fourier transform of the light pulse

$$\frac{I(\omega)}{I(\omega_l)} = \operatorname{sinc}^2\left(\frac{\pi N_u \Delta \omega}{\omega_l}\right) \tag{4.26}$$

with $\Delta\omega = \omega - \omega_l$. The wave train and the spectral shape is shown in fig. 4.4. The position of the first zeros of the sinc^2 -function appear at an argument of $\pm\pi$, resulting in a spectral half-width of $\Delta\omega/\omega_l = 1/N_u$ of the central peak. The FWHM can be (numerically) determined to be $(\Delta\omega/\omega_l)_{\mathrm{FWHM}} \simeq 0.89/N_u$. It should be noted that this derivation only considers the on-axis radiation at the fundamental wavelength. Collecting the radiation from a wide range of angles shows a broader spectrum due to the angle dependent Doppler frequency shift in eq. (4.20).

Emitted Power

The energy loss of a single electron passing through a magnetic structure is given by [106]

$$\Delta E = \frac{e^4 E^2}{6\pi \epsilon_0 m_e^4 c^6} \int_0^{L_u} B(z)^2 dz \quad . \tag{4.27}$$

Assuming a purely sinusoidal magnetic field the total emitted instantaneous power from an electron beam follows from the product of the energy loss and the beam current [116]

$$P_{\rm sp} = \frac{\Delta \gamma m_e c^2}{e} I \tag{4.28}$$

$$= \frac{\pi e}{3\epsilon_0} \gamma^2 I L_u \left(\frac{K}{\lambda_u}\right)^2 \quad . \tag{4.29}$$

For LUX, a 300 MeV beam with a current of 1 kA passing through a 2 m undulator of $K \simeq 2$ therefore emits spontaneous radiation with a power level of about $P_{\rm sp} \simeq 230$ kW. However, this characterizes the power over all angles and frequencies. Considering only the power emitted at the fundamental within the opening angle eq. (4.23) and relative spectral bandwidth $1/N_u$ [116]

$$P_{\text{sp,cen}} = \frac{\pi e}{\epsilon_0} \frac{\gamma^2 I}{\lambda_u} \frac{K^2 [JJ]^2}{\left(1 + \frac{K^2}{2}\right)^2} \simeq 0.5 \text{ kW} \quad . \tag{4.30}$$

The modification [JJ] to the undulator parameter K has its origin in the longitudinal velocity of the electrons following eq. (4.6). For planar undulators this "Bessel JJ-Factor" is given by

$$[JJ] = J_0(\xi) - J_1(\xi)$$
 with $\xi = \frac{K^2}{4 + 2K^2}$, (4.31)

where J_0 and J_1 are Bessel functions of the first kind. The values from eq. (4.29) and eq. (4.30) were compared to a numerical calculation using the synchrotron radiation tool *SPECTRA* [117]. The opening angle was chosen slightly larger than eq. (4.23) to be $\theta=\pm 2.5$ mrad to collect all the radiation that would fit through the beam pipes available at LUX. Within this angle the total emitted radiation is expected to have a power of about 150 kW. Again considering only the frequencies about the fundamental, as would be available from a spectrally resolved measurement, the power drops to a value close to eq. (4.30) of $P_{\rm sp}$, $\theta \simeq 1$ kW. This power level has to be exceeded by the FEL radiation to outperform the spontaneous radiation and is in the following considered as the lower threshold.

4.3 High-Gain Theory

The methods and formulas described in the previous section only considered the emission from the electrons, but not the interaction between the radiated light and the electrons. However, due to energy transfer from the electrons to an electric field, either the spontaneous emission by the electron bunch or generated from an external source to seed the process, the field amplitude can grow by large factors.

4.3.1 Energy Transfer and Microbunching

The energy transferred between the electric field and an electron (indexed n) is given by the zeroth component of the covariant form of the Lorentz force

$$\frac{\mathrm{d}\gamma_n}{\mathrm{d}t} = \frac{-e}{m_e c} \, \boldsymbol{\beta}_n \cdot \boldsymbol{E} \quad . \tag{4.32}$$

An electron loses energy to the field when its velocity points in the same direction as the electric field, and otherwise gains energy from the field. This energy exchange occurs depending on the relative position of an electron to the light field. Assuming that the bunch is longer than the electric wave train $\lambda_l < \sigma_z$, longitudinal energy modulations will be imprinted onto the bunch. Depending on their energy, the particles then follow a longer or shorter detour in the undulator field, scaling with γ^{-1} according to eq. (4.4). Therefore, particles gaining energy catch up to preceding ones, while those losing energy fall back, causing a density modulation.

Utilizing the transverse and longitudinal velocities obtained in the previous section and the Ansatz of an oscillating electric field E_x into eq. (4.32), the energy transfer is described by [105]

$$\frac{\mathrm{d}\gamma_n}{\mathrm{d}t} = -\frac{eK[JJ]E_x}{2\gamma_0 mc^2} \left(\cos(\psi) - \cos(\chi)\right) \tag{4.33}$$

with the arguments $\chi = (k_l - k_u)z - \omega_l t$, a fast oscillation, and $\psi = (k_l + k_u)z - \omega_l t$. ψ , called ponderomotive phase. The latter describes the position of a particle relative to the electric field.

Here, [JJ], as defined in eq. (4.31), accounts for the reduction of the interaction of the electrons with the light field due to their longitudinal velocity, see eq. (4.6). To obtain an energy transfer to the field that (on average) grows, either of the phases must be constant in time, i.e. $d\chi/dt = 0$ or $d\psi/dt = 0$, therefore

$$\overline{\beta_z} \stackrel{!}{=} \frac{k_l}{k_l \pm k_u} \quad , \tag{4.34}$$

where $\omega_l = k_l c$ and the average longitudinal electron velocity $\mathrm{d}z/\mathrm{d}t = c\overline{\beta_z}$ were used. The minus solution is ignored due to requiring superluminal speed, keeping only the one obtained from the ponderomotive phase. This condition is fulfilled if $k_l = 2\pi/\lambda_l$ and is the same as eq. (4.19). This means that the radiation wavelength required to induce a resonant energy modulation with unidirectional energy transfer on average is identical to the wavelength of the spontaneous undulator radiation emitted by the electrons. The cause is again attributed to the requirement of the light wave "slipping" over the electron beam by one wavelength λ_l per undulator period λ_u .

The resulting density and current profiles form a periodic structure with high particle counts separated by one wavelength of the electric field, called microbunches. During their formation they develop the proper spacing to increasingly emit at the same phase, therefore interfering constructively.

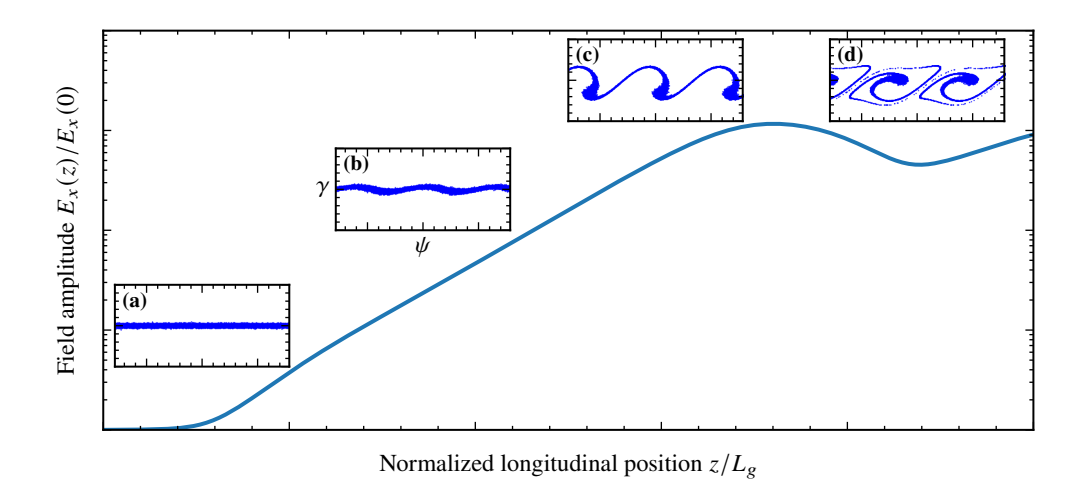


Figure 4.5: Gain curve obtained from eqs. (4.37a) to (4.37c) starting from a small initial field. Insets (a)-(d) show the microbunching process at different stages of the amplification process up to saturation, where the average energy transfer between electrons balances and the power level starts to oscillate.

To describe this process, the change in phase for a single electron along the undulator is further expressed via the longitudinal velocity from eq. (4.8) as

$$\frac{\mathrm{d}\psi_n}{\mathrm{d}z} = \left(k_l + k_u\right) - \frac{\omega_l}{c\overline{\beta}_{z,n}} \simeq \left(\frac{\gamma_n^2 - \gamma_0^2}{\gamma_n^2}\right) k_u \quad , \tag{4.35}$$

If the distribution of the electrons over the phases ψ is exactly uniform, all particles having the exact same energy with no spread, and there is no initial (external) field, there will be no energy transfer on average. If all three conditions apply simultaneously, all contributions cancel out exactly in eqs. (4.33) and (4.35) due to the conservation of energy. Thus, there must be some initial driver, such as statistical noise in the spread of ψ or γ , or radiation to seed the FEL process, for amplification to happen.

4.3.2 Coupled First Order Equations

In addition to the change in electron energy, the next step is to also account for a change of the electric field and the resulting effects of the microbunching process. These effects are incorporated through the inhomogeneous wave equation

$$\left(\nabla^2 - \frac{1}{c^2} \frac{\partial}{\partial t}\right) \tilde{\mathbf{E}} = \mu_0 \frac{\partial \mathbf{j}}{\partial t} + \frac{1}{\epsilon_0} \nabla \rho \quad , \tag{4.36}$$

with the current density j and the charge density ρ . The \tilde{E} denotes that the field is described as a complex valued wave. The fundamental aspects of the FEL theory are covered by 1D theory, dropping variations in the charge density, $\partial \rho / \partial x = 0$, and transverse dependencies of the electric field,

 $\tilde{E}_x = \tilde{E}_x(z,t)$. The highest order derivatives in \tilde{E}_x are dropped, assuming that the amplitude and phase change slowly, therefore called the slowly varying envelope approximation (SVEA). In this case the second order derivatives are neglected while advancing one light wavelength in the undulator, i.e. $\left|\partial^2 \tilde{E}_x/\partial z^2\right| \ll \left|\partial \tilde{E}_x/\partial z\right|/\lambda_l \ll \left|\tilde{E}_x\right|/\lambda_l^2$ and $\left|\partial^2 \tilde{E}_x/\partial t^2\right| \ll \left|\partial \tilde{E}_x/\partial t\right|\omega_l \ll \left|\tilde{E}_x\right|\omega_l^2$. Further, fast oscillations shorter than the undulator period are replaced by their respective average contribution over that range. Together with the found equations for the change in phase and electron energy, the set of coupled first order differential equations describing the FEL interaction is [105]:

$$\frac{\mathrm{d}\tilde{E}_x}{\mathrm{d}z} = -\frac{\mu_0 c K[JJ]}{4\gamma_0} \tilde{J}_1 \tag{4.37a}$$

$$\frac{\mathrm{d}\eta_n}{\mathrm{d}z} = \frac{-e}{\gamma_0 m_e c^2} \operatorname{Re} \left(\left(\frac{K[J]\tilde{E}_x}{2\gamma_0} - \frac{ic^2 \mu_0}{\omega_l} \tilde{j}_1 \right) \exp\left(i\psi_n\right) \right)$$
(4.37b)

$$\frac{\mathrm{d}\psi_n}{\mathrm{d}z} = 2k_u \eta_n \tag{4.37c}$$

$$\tilde{j}_1 = j_0 \frac{2}{N_e} \sum_{n=1}^{N} \exp\left(-i\psi_n\right) \quad ,$$

with the modulated current density \tilde{j}_1 . Instead of the absolute energy the deviation from the resonant energy $\eta_n = (\gamma_n - \gamma_0)/\gamma_0$ is used after an expansion about $\gamma_n \simeq \gamma_0$ to first order. The additional term in eq. (4.37b) is the repelling space charge force between the electrons.

The set of equations describes the repeating and self-enhancing process fundamental to the FEL:

Equation (4.37a): Density modulations and bunching produce coherent radiation

Equation (4.37b): Coherent radiation induces energy modulations

Equation (4.37c): Energy modulations cause density modulations

A solution to the coupled first order equations is shown in fig. 4.5. During the FEL process the electric field amplitude and the microbunching increase as energy is transferred from the electrons. In return the energy spread increases and their phase changes. At some point energy is extracted back from the light field and transferred to the electrons, when their phases do not align anymore. The process comes to a saturation after amplifying the electric field by several orders of magnitude.

For self-amplified spontaneous emission (SASE) without an externally applied field, as it is the case for *LUX*, the initial field is provided by the spontaneous undulator radiation, produced over the first few undulator periods. The non-vanishing statistical noise of the finite particle distribution further allows for a non-zero energy transfer to the field, as not all contributions to the bi-directional energy transfer cancel.

4.3.3 Third-Order Equation and Fundamental FEL Scaling

A drawback of the coupled first order equations is, that for a system of N_e electrons $2N_e + 1$ equations have to be solved. This restricts their analytical treatment and limits their applicability to numerical calculations. By replacing the individual electrons by a distribution function, eq. (4.37a) may be

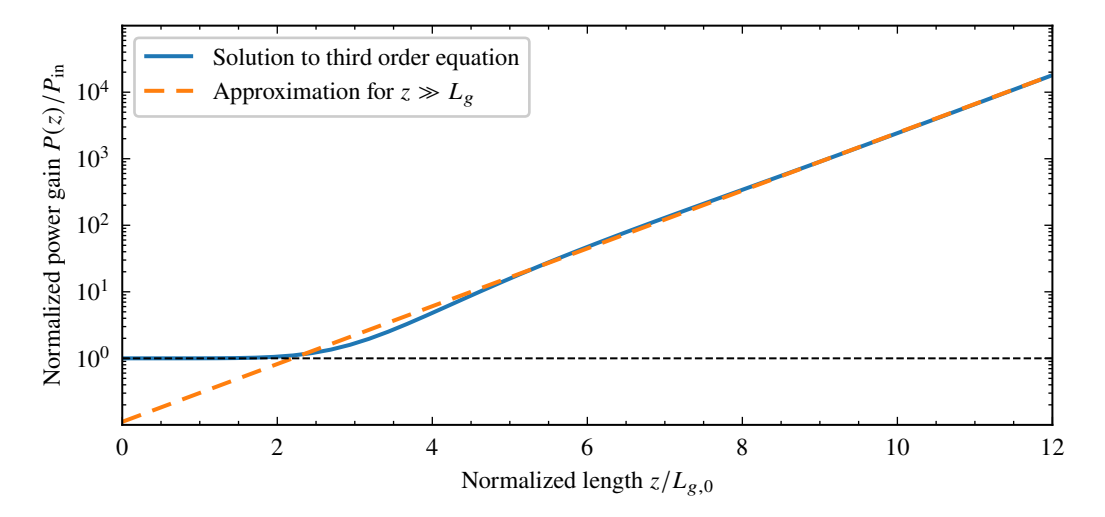


Figure 4.6: Gain power curve according to (blue solid) eq. (4.43) and (orange dashed) the approximation for $z\gg L_g$ for the first 12 gain lengths.

rewritten to a single integro-differential equation describing the increase in electric field amplitude depending solely on the initial conditions [118]. For a mono-energetic beam with deviation η_0 from the resonance energy and assuming only small periodic density modulations, it reduces to a third order differential equation in \tilde{E}_x [105]

$$\frac{\tilde{E}_{x}^{\prime\prime\prime}}{\Gamma^{3}} + 2i\frac{\eta_{0}}{\rho_{\text{FEL}}}\frac{\tilde{E}_{x}^{\prime\prime}}{\Gamma^{2}} + \left(\frac{k_{p}^{2}}{\Gamma^{2}} - \left(\frac{\eta_{0}}{\rho_{\text{FEL}}}\right)^{2}\right)\frac{\tilde{E}_{x}^{\prime}}{\Gamma} - i\tilde{E}_{x} = 0 \quad , \tag{4.38}$$

with the gain parameter $\Gamma = \left(\mu_0 K^2 [JJ]^2 e^2 k_u n_e / \left(4\gamma_0^3 m_e\right)\right)^{1/3}$ and the space charge parameter $k_p = \sqrt{2e^2\mu_0 n_e \lambda_l / (\gamma_0 m_e \lambda_u)}$, and the FEL scaling parameter (also called pierce parameter) $\rho_{\rm FEL} = \Gamma/(2k_u)$. n_e denotes the electron number density. Due to the restriction to small modulations, eq. (4.38) describes only the build-up and amplification process of the FEL, but not saturation.

The FEL parameter may be written in the more convenient form [104, 118]

$$\rho_{\text{FEL}} = \frac{1}{4\gamma_r} \left(\frac{I_{\text{peak}}}{I_A} \frac{K^2 [JJ]^2 \lambda_u^2}{\pi^2 \sigma_r^2} \right)^{1/3}$$
(4.39)

with the non-relativistic Alfvén-current $I_A = 4\pi m_e c/(\mu_0 e) \simeq 17$ kA. The FEL parameter is a useful quantity as it appears as a scaling in many quantities related to the high-gain FEL process. The most obvious one from eq. (4.38) is the relation to the electron energy deviation, since if all energy deviations $\eta \ll \rho_{\rm FEL}$ the contribution of the respective terms to the FEL process are strongly reduced.

For the initial current of the *LUX* reference beam from section 2.4, an average beam size of $\sigma_r \simeq 45 \, \mu \text{m}$, as determined in section 4.1.4, and for an undulator strength of K=2 the FEL parameter is $\rho_{\text{FEL}} \simeq 0.7 \, \%$. This value is at least one order of magnitude larger than for conventional FELs, where $\rho_{\text{FEL}} \simeq 0.01 \, \% - 0.1 \, \%$ [2, 4, 5, 119].

By scaling the quantities in the differential equation eq. (4.38) by ρ_{FEL} and using the Ansatz $\tilde{E}_x \sim \exp(-i\alpha z)$, a cubic polynomial equation

$$\hat{\alpha}^3 - 2\hat{\eta}_0 \hat{\alpha}^2 - \left(\hat{k}_p^2 - \hat{\eta}_0^2\right) \hat{\alpha} - 1 = 0 \tag{4.40}$$

is obtained that can be solved analytically. The scaled quantities are given $\hat{\eta} = \eta/\rho_{\rm FEL} = (\gamma - \gamma_0)/(\gamma_0\rho_{\rm FEL})$, $\hat{\alpha} = \alpha/\Gamma$ and $\hat{k}_p = k_p/\Gamma$. To describe the basic process of increase in the electric field due to the FEL process, the case of negligible space charge $\hat{k}_p \to 0$ and operation at resonance $\hat{\eta} \to 0$ are considered. Then eq. (4.40) simplifies to

$$\hat{\alpha}^3 - 1 = 0 \Leftrightarrow \frac{\tilde{E}_x^{"'}}{\Gamma^3} - i\tilde{E}_x = 0 \quad . \tag{4.41}$$

The three complex roots correspond to a growing (Im(α_1) < 0), a decaying (Im(α_2) > 0) and an oscillating mode (Im(α_3) = 0). For some initial conditions $\tilde{E}_x(0) = E_{\rm in}$ and $\tilde{E}_x^{(n)}(0) = 0$ the electric field is given by

$$\tilde{E}_{x}(z) = \frac{E_{in}}{3} \left(\exp\left(\frac{\left(i + \sqrt{3}\right)\Gamma z}{2}\right) + \exp\left(\frac{\left(i - \sqrt{3}\right)\Gamma z}{2}\right) + \exp\left(-i\Gamma z\right) \right) , \qquad (4.42)$$

The radiated power is then given by

$$P(z) \propto \left| \tilde{E}_x(z) \right|^2 = \frac{E_{in}^2}{9} \left(3 + 4 \cos \left(\frac{3}{2} \Gamma z \right) \cosh \left(\frac{\sqrt{3}}{2} \Gamma z \right) + 2 \cosh \left(\sqrt{3} \Gamma z \right) \right) \quad . \tag{4.43}$$

For large $\Gamma z \to \infty$, the growing mode dominates and the power increases as

$$P(z) \propto \exp\left(\sqrt{3}\Gamma z\right) = \exp\left(\frac{z}{L_{g,1D}}\right)$$
 (4.44)

Here the (power) gain length was introduced:

$$L_g = \frac{P(z)}{P'(z)} \tag{4.45}$$

$$L_{g,1D} = \frac{1}{\sqrt{3}\Gamma} = \frac{\lambda_u}{4\pi\sqrt{3}\rho_{\text{FEL}}}$$
, (4.46)

with the latter being the 1D gain length for the ideal conditions in which the power e-folds³, i.e. small density modulation; no energy spread; no space charge, and being on resonance. Comparing to eq. (4.42), the field gain length in \tilde{E}_x , which is important for estimation of coherence properties of the radiation, is half of the power gain length.

Further, the power gain is defined as [120]

$$G(z) = \frac{P(z)}{P_{\rm in}} = \frac{\left|\tilde{E}_x\right|^2}{E_{\rm in}^2}$$
 (4.47)

Expanding the power gain about small $z \approx 0$ using eq. (4.43) yields the power gain during the startup $G(z) \approx 1 + (z/(3.2L_{g,1D}))^6$. This indicates the lethargy regime, where the gain stays about unity over the first $\approx 3.2L_g$. The power gain curve according to the solution to the third order equation is shown in fig. 4.6 for 12 gain lengths.

For SASE FELs, including LUX, there is no initial or external electromagnetic wave to amplify. However, since the spontaneous undulator radiation satisfies the resonant condition it can serve as a seed radiation for the FEL process. The input power can be understood as the power of the spontaneous undulator radiation emitted over the first few undulator periods, where no exponential FEL amplification is expected, and which is emitted within the appropriate solid angle and couples into the exponentially growing mode [121, 122]. This "shot noise" is used to estimate an equivalent input power as [120] $P_{\rm sn} \simeq \rho_{\rm FEL} \gamma m_e c^2/(N_c e \sqrt{\pi \ln N_c})$, with $N_c = I/(\rho_{\rm FEL} e \omega_l)$ the number of interacting electrons, and being on the level of about $P_{\rm sn} \simeq 10\,{\rm W}$ for LUX parameters. The exact position of startup may vary due to statistical fluctuations in the distribution of the finite number of electrons in the beam. The initial radiation consists of discrete spikes at the electrons' locations, creating a white noisy spectrum, from which a narrow portion is amplified. It should be noted here, that due to the averaging in the SVEA the initial radiation is uniformly small, in contrast to those stronger radiation spikes that occur in the spontaneous emission and increase the interaction with the light field early in the undulator. Consequently, the SVEA overestimates the length of the lethargy regime and the startup process [123]. However, to exceed the power levels determined for the undulator radiation in section 4.2, the required number of gain lengths to fit into the undulator has to be larger than $\ln(9 \cdot P_{\text{sp},\theta}/P_{\text{sn}}) \simeq 6$, where the factor 9 is the fraction of the shot noise that couples into the growing mode in eq. (4.43).

The bandwidth of a SASE FEL in the exponential gain regime following the startup decreases as [105]

$$\sigma_{\omega}(z) = 3\sqrt{2}\omega_{l}\rho_{\text{FEL}}\sqrt{\frac{L_{g,1D}}{z}}$$
(4.48)

along the undulator. Comparing with spontaneous radiation in section 4.2 which decreases as $1/N_u \propto 1/z$, the bandwidth of a SASE FEL scales slower with $1/\sqrt{z}$. It is estimated to drop from about 2.5 % at the start of the exponential gain regime to 1 % relative bandwidth at the end of the 2 m undulator.

³ Some authors define $L_{g,1D} = \Gamma^{-1}$ corresponding to an additional factor of $\sqrt{3}$ in the definitions of and relations to other quantities.

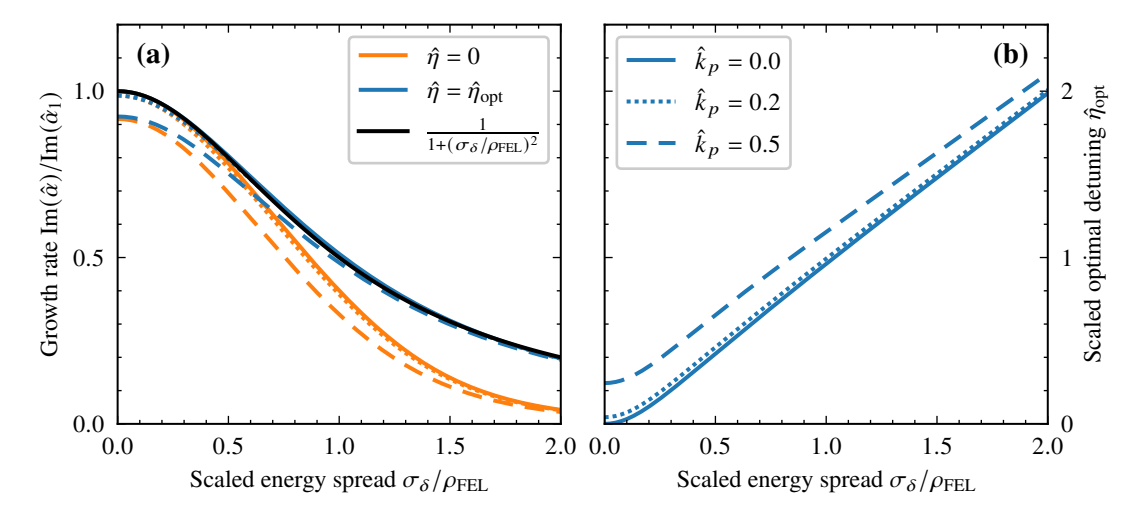


Figure 4.7: (a) Change of growth parameter $-\text{Im}(\hat{\alpha})$ for Gaussian distributed energy spread, obtained from eq. (4.49). Only the root that corresponds to an increase in \tilde{E}_x is shown for (orange) being on resonance and (blue) at optimal energy detuning. Different space charge parameter \hat{k}_p are (solid) 0.0, (dotted) 0.2, and (dashed) 0.5. Values are normalized to the growth rate of a monoenergetic beam and no space charge. An approximation for the growth rate at optimum detuning is also shown (black, solid). (b) Optimal detuning at which largest growth rate is achieved.

Concluding from the 1D theory, for LUX the estimated 1D power gain length is $L_{g,1D} \simeq 10$ cm, therefore fitting $L_u/L_{g,1D} \simeq 20$ gain length into the 2 m undulator. Nevertheless, the 1D theory does not cover all aspects, and the true gain length might be higher. Those effects are discussed in the next sections.

4.3.4 Energy Spread and Space Charge in the 1D Limit

Before considering more effects, the energy and space charge terms in eq. (4.38) are further investigated, as they appear already in the 1D theory. Keeping the distribution of energy deviation of eq. (4.40) the electrons in the derivation of shows that this equation can be written in a more general form [105, 118, 124] as

$$\hat{\alpha} = \left(1 + \hat{k}_p^2 \hat{\alpha}\right) \int \frac{V(\overline{\eta})}{(\hat{\alpha} - \overline{\eta})^2} d\overline{\eta} \quad . \tag{4.49}$$

with V being the distribution function of the electron energies with $\int V d\overline{\eta} = 1$. Setting $V(\hat{\eta}) = \delta(\hat{\eta} - \hat{\eta}_0)$ again yields eq. (4.40) as the limit of no energy spread.

The increase of the gain length $L_g \propto -\mathrm{Im}(\hat{\alpha})$ in the 1D case can be obtained analytically for some energy distributions, like an uniform or Cauchy distribution. However, the growth rate for a Gaussian distribution, which is better suited to describe spread in energy of real electron beams, can only be obtained numerically. The relative decrease in growth rate due to Gaussian distributed energy

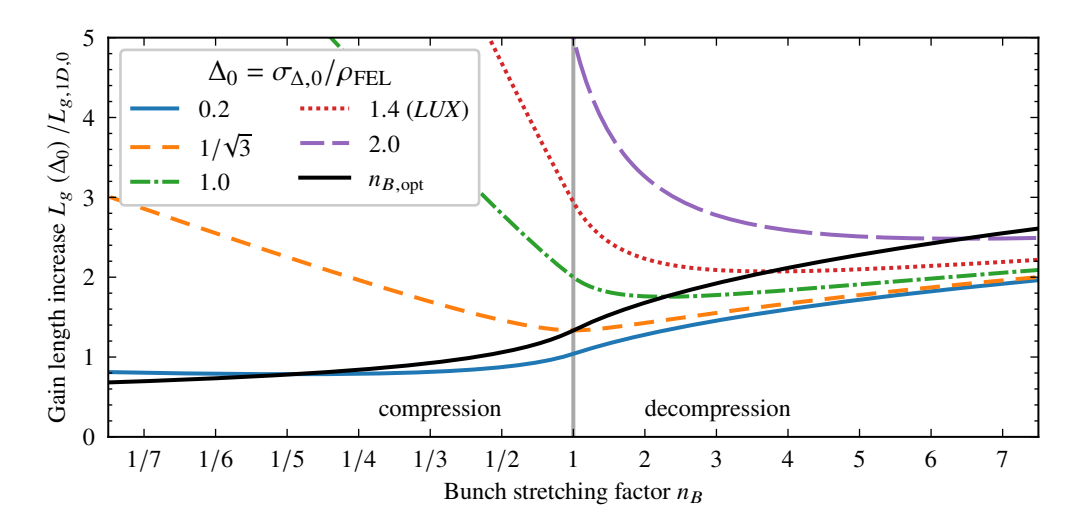


Figure 4.8: Increase in gain length relative to the initial 1D gain length as a function of applied (de)compression, considering different initial scaled uncorrelated energy spreads: $\Delta_0 = \sigma_{\Delta,0}/\rho_{\rm FEL}$ (blue, solid) 0.2, (green, dash-dotted) 1.0, and (purple, long dashed) 2.0. The case where neither compression nor decompression improves the gain length is indicated by (orange, dashed) $1/\sqrt{3} \simeq 0.6$. The *LUX* parameters (red, dotted) correspond to $\Delta_0 \simeq 1.4$, suggesting a benefit from decompression. Additionally, (black, solid) the locations of minima is indicated, representing the optimal stretching factor $n_{B,\rm opt}$. Note that the scaling of the n_B -axis changes depending on whether n_B is greater or smaller than 1, reflecting that compression and decompression are reciprocal operations.

spread and finite space charge parameter is shown in fig. 4.7(a) for operating at the resonance energy $\hat{\eta} = 0$ and a detuned beam with $\hat{\eta} = \hat{\eta}_{\text{opt}}$ to maximize the growth rate for $\hat{k}_p \in \{0, 0.2, 0.5\}$. The corresponding optimum energy detuning is shown in fig. 4.7(b).

The space charge parameter has only minor influence if either $\hat{k}_p \ll 1$ or $\hat{k}_p \ll \sigma_\delta/\rho_{\rm FEL}$. The assumption $k_p \to 0$ is typically justified by low electron density or large γ . Specifically, for typical beam and undulator parameters at LUX $\hat{k}_p \simeq 0.25$. It is close to the value of $\hat{k}_p \simeq 0.19$ for the XUV and soft X-Ray FEL *FLASH*, where space charge forces are negligible [105]. As indicated in fig. 4.7(a), the expected increase in gain length for LUX is on the order of 2%. Also a larger value of $\hat{k}_p = 0.5$ would only cause an increase by 10%. Therefore, space charge effects will not be considered in the following discussion, but might be relevant for future LPA based FELs.

Note that in the case of a mono-energetic beam and no space charge, being on resonance $\hat{\eta}_{\rm opt}=0$ yields the fastest growth rate. For increased energy spread $\sigma_{\delta}\gtrsim \rho_{\rm FEL}/3$, the optimum detuning scales approximately linear. With finite energy spread a slightly off-resonant wavelength contained in the spectrum of the spontaneous emission will be amplified more than the resonant one. Therefore with increased energy spread a shift of the central wavelength is observed.

Considering a beam with only Gaussian distributed energy spread as a degrading influence on FEL performance, an approximation for the increase in gain length at optimum detuning is given by [120]

$$L_{g,\delta} = L_{g,1D} \left(1 + \left(\frac{\sigma_{\delta}}{\rho_{\text{FEL}}} \right)^2 \right) \quad . \tag{4.50}$$

Optimizing at the initial value of LUX with $\sigma_{\delta}/\rho_{\rm FEL} \simeq 1.4$ and a Gaussian energy spread, shows a maximum growth rate of ${\rm Im}(\hat{\alpha})/{\rm Im}(\hat{\alpha}_1) \simeq 0.3$ at a detuning of $\hat{\eta}_{\rm opt} \simeq 1.5$ compared to ${\rm Im}(\hat{\alpha})/{\rm Im}(\hat{\alpha}_1) \simeq 0.1$ at resonance. Thus, at this energy spread a slightly detuned energy shows a gain length that is a factor of 3 shorter than the resonant one. This also translates to a wavelength shift of about 2.1% at $\rho_{\rm FEL} \simeq 0.7\%$. However, when reducing the gain length by improving the effective energy spread, for example with the decompression scheme as considered in [23] and discussed in section 3.4, the optimal detuning is closer to resonance and the wavelength shift is reduced.

If the energy spread should not reduce the growth rate significantly, e.g. less than a factor of 2, an upper limit to the energy spread can be justified to be

$$\sigma_{\delta} < \rho_{\text{FEL}}$$
 , (4.51)

defining an energy acceptance for a FEL. Depending on the energy spread distribution shape or less acceptable reduction in growth rate, a stronger limit, e.g. $\sigma_{\delta} \lesssim \rho_{\rm FEL}/2$, might be used. This condition is obviously not fulfilled in the initial LUX case with $\sigma_{\delta}/\rho_{\rm FEL} \simeq 1.4$. This does not mean, that such large energy spread prevents FEL interaction to happen at all, but strongly suppresses it. In addition, the achievable gain might be reduced. Further, the SASE startup process might be obstructed for $\sigma_{\delta}/\rho_{\rm FEL} \gtrsim 1$ as no proper density modulation and microbunching can build up [125]. In such cases only seeded FELs might operate in the high gain regime.

Therefore, the ratio $\sigma_{\delta}/\rho_{\rm FEL}$ has to be significantly reduced, to trigger the SASE startup and achieve sufficient FEL gain within the 2 m undulator.

Using these first estimations, an optimum decompression for an energy spread dominated beam can be found by comparing the scaling of the 1D and the gain length with energy spread contributions [126, 127]. As decompression reduces the uncorrelated (slice) energy spread σ_{Δ} , it will be used instead of the total energy spread in eq. (4.50). Plugging in the above scalings for the current and energy spread, i.e. $L_{g,1D} = L_{g,1D,0} \cdot n_B^{1/3}$ and $\Delta = \sigma_{\Delta,0} n_B^{-1/3}/(\rho_{\rm FEL} n_B^{-1/3}) = \Delta_0 n_B^{-2/3}$, into this formula gives a scaling for the gain length with only energy spread contributions after decompression compared to the 1D gain length without decompression

$$\frac{L_g\left(\Delta_0\right)}{L_{g,1D,0}} = n_B^{1/3} \left(1 + n_B^{-4/3} \Delta_0^2\right) \quad , \tag{4.52}$$

where $L_{g,1D,0}$ is the 1D gain length before decompression at the equivalent current $I_{0,gauss}$, see section 3.4. Minimizing for smallest gain length gives an estimate on the optimum (de)compression of

$$n_{B,\text{opt}} = 3^{3/4} \Delta_0^{3/2}$$
 (4.53)

The threshold of $n_{B,\rm opt} > 1$, where bunch decompression is favorable over compression, as used by conventional radio-frequency accelerator based free-electron lasers, is achieved at initial values of normalized energy spread $\Delta_0 > 1/\sqrt{3} \simeq 0.6$. This is also compatible with the previous considerations of $\sigma_\delta \lesssim \rho_{\rm FEL}/2$ for having only a small increase of the gain length. The increase in gain length for different normalized initial energy spreads dependent on the bunch stretching factor is depicted in fig. 4.8. For LUX beam parameters with $\Delta_0 \simeq 1.4$ the optimum decompression can be estimated to be $n_B \simeq 3.9$ or $R_{56} \simeq 700\,\mu{\rm m}$.

4.4 3D and Degrading Effects

Previously, only 1D effects were considered to highlight the physics of an FEL and describe its underlying process. However, 3D effects impact the FEL performance and lead to an increase in the gain length. These effects include beam-related factors such as energy spread, transverse size, and emittance, as well as radiation properties like diffraction. Additionally, interactions between the electron beam and radiation, such as their spatial overlap, further influence FEL dynamics. The 1D theory is still approximately applicable, if the beam satisfies some conditions concerning its quality [59]. In the following the limiting factors for the 1D theory will be discussed.

4.4.1 Limits of the 1D Theory

First constraints on the beam properties and the conditions under which the 1D theory remains applicable are directly derived from the emitted wavelength eq. (4.20). The deviations in γ , θ and K should induce wavelength shifts smaller than the (approximate) FWHM natural line half-width $(\Delta \lambda/\lambda_l)_{\rm FWHM}/2 \simeq 1/(2N_u)$ of the forward radiation $\theta=0$, as obtained from eq. (4.26) [128]. This means that any radiation contributing to the FEL has to be close to the resonant wavelength to avoid a degradation in performance. Expanding eq. (4.20) to the lowest order of appearance about small relative deviations in energy, angle and undulator strength, the maximum allowed broadening is estimated to be

$$\left(\frac{\Delta\lambda}{\lambda_l}\right)_{\rm br} \simeq \frac{-2\Delta\gamma}{\gamma} + \frac{K\Delta K}{1 + K^2/2} + \frac{\gamma^2 (\Delta\theta)^2}{1 + K^2/2} \lesssim \frac{1}{2N_u} \quad . \tag{4.54}$$

By rewriting the term for the undulator strength deviation by the field expansion eq. (4.2) as $\Delta K/K \simeq \Delta B_y/B_y \simeq k_u^2 r^2/2$, neglecting errors in the undulator period, and wanting the beam size σ_r to be contained in this region, a constraint on the latter is obtained. Further $\Delta\theta$ sets the limit for the beam divergence $\sigma_{r'}$ in the same way. Also not holding strictly on their own, the constraints on each of

those parameters is individually formulated to the following set, with the numbers for the LUX case, as

$$\sigma_{\delta} \lesssim \frac{1}{4N_u} \simeq 0.2 \,\% \tag{4.55}$$

$$\sigma_r \lesssim \sqrt{\frac{1}{k_u^2 N_u} \frac{1 + K^2/2}{K^2}} \simeq 180 \,\mu\text{m}$$
 (4.56)

$$\sigma_{r'} \lesssim \sqrt{\frac{1 + K^2/2}{2\gamma^2 N_u}} = \sqrt{\frac{\lambda_l}{L_u}} \simeq 180 \,\mu\text{rad}$$
 (4.57)

$$\frac{\Delta K}{K} \lesssim \frac{1}{2N_{\mu}} \frac{1 + K^2/2}{K^2} \simeq 0.3 \%$$
 (4.58)

The strongest limitation for the applicability of the 1D theory obtained from this consideration is the energy spread, which causes a broadening beyond the natural line width. The other equations put a rather weak constraint on the beam size and divergence for LUX parameters, which are easily fulfilled when focusing into the undulator as found in section 4.1.4. In addition, eq. (4.58) sets a limit on the (global) undulator field quality before possibly degrading the FEL performance. As found in [114], for the used undulator $\Delta B/B \simeq 0.5$ %, mainly caused by local field deviations only weakly affecting the absolute line broadening on the order of 0.01% and corresponding to $\simeq 1$ % relative line broadening. However, as this value is violating the condition eq. (4.58), the influence of the field should be checked in simulations.

Additionally to emitting at the same wavelength, the radiation has to be transversely coherent, to interfere constructively while propagating through the electron beam. As the amplified radiation follows the electron beam size, to not spoil the coherence by electron beam properties it has to satisfy the diffraction limited criteria [110]

$$\sigma_r \lesssim \frac{\sqrt{2\lambda_l L_u}}{4\pi} \simeq 40 \,\mu\text{m}$$
 (4.59)

$$\sigma_{r'} \lesssim \sqrt{\frac{\lambda_l}{2L_u}} \simeq 130 \,\mu\text{rad}$$
 (4.60)

$$\epsilon_n \lesssim \frac{\gamma \lambda_l}{4\pi} \simeq 3 \,\text{mm mrad}$$
 (4.61)

However, this criteria are not strict and especially for SASE FELs, where the fundamental mode is expected to dominate over higher order modes, those values can be exceeded and the FEL operated in an intermediate regime with contributions from diffraction and emittance effects [129]. However, the limits should not be exceeded drastically. In addition, to keep diffraction losses on a low level, the expansion of the radiation per gain length due to diffraction should be smaller than the beam area, giving a lower limit for the beam size [118, 130]

$$\sigma_r > \sqrt{\frac{\lambda_l L_g}{2\pi}} \simeq 30 \,\mu\text{m}$$
 (4.62)

corresponding to the gain guiding condition of a Rayleigh range greater than the field gain length, i.e. twice the power gain length, $Z_R > 2L_g$ [131]. Here the 1D gain length was used to estimate of the minimum beam size to fulfill the guiding condition. However, eq. (4.62) increases with a longer gain length caused by effects not covered by the 1D theory. Consequently, eq. (4.62) and eq. (4.59) are two competing conditions that cannot be generally fulfilled. Usually this means that contributions from emittance and diffraction effects can not be completely suppressed and 3D effects should be considered when either of the two is not satisfied.

Another thing to consider is the distribution of a particle's momentum into the longitudinal and transverse components. Particles of same energy entering the undulator under different angles do have a different longitudinal momentum. Therefore a spread in incident angle is equivalent to a smear out in energy and adds to an effective energy spread. Due to the relation between transverse size, divergence and emittance, this effective energy spread is therefore linked to the former, and a limit on the emittance can be formulated. Depending on the upper tolerable contribution of this effect on the energy spread, which is here chosen to be $< \rho_{\rm FEL}/2$ to not dominate the natural energy spread of the beam, the normalized emittance has to fulfill [105]

$$\epsilon_n < \sigma_r \sqrt{\frac{\rho_{\rm FEL}}{2\sqrt{2}}} \simeq 2.2 \,\mathrm{mm \, mrad}$$
 , (4.63)

where LUX parameters of $\rho_{FEL}=0.7$ % and $\sigma_r=45\,\mu\mathrm{m}$ from above considerations where used, and putting a slightly stronger condition on the allowed emittance. The spread in transverse momentum and therefore the demands on the emittance could be reduced by increasing the beam size, due to the weaker scaling on the beam size in ρ_{FEL} . However, this counteracts the need for small current densities to obtain a high ρ_{FEL} and at some point violate the above criteria for small spectral broadening and diffraction to not decrease the FEL performance.

For *LUX*, this discussion highlights that the consideration of 3D effects is relevant in almost all aspects, since it operates at most limits for beam size, emittance and energy spread, even when considering the decompression scheme.

4.4.2 Ming Xie Fit

To include the discussed effects and estimate the increase in gain length, their contributions are written as an additional factor to the idealized 1D gain length as

$$L_g = (1 + \Lambda)L_{g,1D}$$
 (4.64)

Since Λ is a general factor combining all effects that increase the gain length, there is no exact analytical form for arbitrary beams. It is convenient to write it as a combination of scaling parameters to include the relevant effects. A common choice are contributions of radiation diffraction, emittance and energy spread. A parametrization with the respective parameters η_d , η_ϵ and η_γ was formulated

Table 4.1: Xie fitting parameters for formula eq. (4.66)

$a_1 = 0.45$	$a_5 = 3$	$a_9 = 2.4$	a_{13} = 5.4	a_{17} = 2.2
$a_2 = 0.57$	$a_6 = 2$	a_{10} = 51	a_{14} = 0.7	a_{18} = 2.9
$a_3 = 0.55$	$a_7 = 0.35$	a_{11} = 0.95	a_{15} = 1.9	a_{19} = 3.2
$a_4 = 1.6$	$a_8 = 2.9$	$a_{12} = 3$	a_{16} = 1140	

by Ming Xie [132]. Those scaling parameters are given by

$$\eta_{d} = \frac{L_{g,1D}}{Z_{R}} = \frac{L_{g,1D}\lambda_{l}}{4\pi\sigma_{r}^{2}}$$

$$\eta_{\epsilon} = \left(\frac{L_{g,1D}}{\hat{\beta}}\right) \left(\frac{4\pi\epsilon}{\lambda_{l}}\right) = 4\pi \left(\frac{L_{g,1D}}{\lambda_{l}}\right) \left(\frac{\epsilon^{2}}{\sigma_{r}^{2}}\right)$$

$$\eta_{\gamma} = 4\pi \left(\frac{L_{g,1D}}{\lambda_{u}}\right) \left(\frac{\sigma_{\gamma}}{\gamma_{0}}\right) = \frac{\sigma_{\delta}}{\sqrt{3}\rho_{\text{FFL}}},$$
(4.65)

and define similar conditions as stated above, under which 3D effects become important, i.e. gain guiding and diffraction limitation, transverse coherence and beam size, and energy spread relative to the FEL parameter. One can identify the scaling parameters from eqs. (4.51), (4.62) and (4.63), and their values should be well below unity to fulfill the requirements formulated for the corresponding effects to not significantly spoil the FEL process.

Further, the parametrization is used to estimate the 3D gain length. For this purpose Xie [133] gave a fit for Λ with 19 parameters and under the assumption of no space charge $\hat{k}_p = 0$. The function to be fitted is

$$\begin{split} \Lambda_{\text{Xie}}(\eta_{d},\eta_{\epsilon},\eta_{\gamma}) = & a_{1}\eta_{d}^{a_{2}} + a_{3}\eta_{\epsilon}^{a_{4}} + a_{5}\eta_{\gamma}^{a_{6}} \\ & + a_{7}\eta_{\epsilon}^{a_{8}}\eta_{\gamma}^{a_{9}} + a_{10}\eta_{d}^{a_{11}}\eta_{\gamma}^{a_{12}} + a_{13}\eta_{d}^{a_{14}}\eta_{\epsilon}^{a_{15}} \\ & + a_{16}\eta_{d}^{a_{17}}\eta_{\epsilon}^{a_{18}}\eta_{\gamma}^{a_{19}} \end{split} \tag{4.66}$$

and the fit parameters found by Xie are listed in table 4.1. Each term is positive and corresponds to a contribution deviating from the optimum 1D case, increasing the gain length. Therefore the gain length is shortest when there are no 3D contributions at all.

The fit was performed at the ideal detuning $\hat{\eta}_{\rm opt}$ to obtain the highest growth rate. If $\eta_{\epsilon} < 1$, $\eta_{\gamma} < 1$ and $\eta_d \ll 1$ the fit gives a good approximation to the exact solution, whereas an increasing $\eta_d \gg 0$ has the largest influence on its inaccuracy. For the LUX case, all parameters stay within the parameter range well below unity, therefore the fitting formula should give a reasonable estimate on the 3D gain length.

In the case of only energy spread being relevant, i.e. $\eta_{\epsilon} = \eta_d = 0$, eq. (4.64) matches the previously considered approximation eq. (4.50).

Again using LUX parameters from table 2.1 and the previously found values for the beam size in the undulator in section 4.1, the expected 3D gain length for the initially uncompressed beam with LUX parameter according to eq. (4.66) results in

$$L_{g,\text{Xie}} \simeq 1 \,\text{m}$$
 (4.67)

Since this is too long with respect to the experimental setup, the gain length has to be reduced, such that $L_g \ll L_u$. This can be done in the context of the decompression scheme, where the uncorrelated energy spread σ_{Δ} is used instead of the total σ_{δ} , because it represents the local contribution to the gain length from the interacting electrons [23]. The initially uncompressed beam parameters yield $\eta_d \simeq 0.25, \eta_{\epsilon} \simeq 0.03, \eta_{\gamma} \simeq 0.8$ and a well decompressed beam with $n_B = 10$ yields $\eta_d \simeq 0.55, \eta_{\epsilon} \simeq 0.06, \eta_{\gamma} \simeq 0.2$. The evolution of the scaling parameters with respect to the decompression is shown in fig. 4.9(a). The slice energy spread and therefore η_{γ} reduces significantly as the bunch is stretched. The increase in the other parameters comes from the reduced current and therefore an increasing $L_{g,1D}$ contributing to their magnitude. The resulting evolution of the scaling parameter $\Lambda_{\rm Xie}$ is shown in fig. 4.9(b). It drops rapidly for moderate decompressions, but only shows small improvements for larger values of n_B .

The resulting gain length and the impact of the individual scaling parameters is shown in fig. 4.10. For a beam with LUX parameters 3D effects mainly arise from a combination of energy spread and diffraction. The individual contributions on their own only show a small increase compared to the 1D gain length. Especially emittance effects have a minor contribution to the 3D gain length for the used parameters. An increased emittance mainly limits the achievable average beam size, therefore also having an impact on the other parameters via $L_{g,1D}$. Consequently, a moderate increase of η_{ϵ} while fixing η_d and η_{γ} would only have a minor impact. For example, an increase of the gain length by a factor of two is obtained when increasing the emittance, and the corresponding achievable average beam sizes accordingly, to the values marking the transition from the diffraction to emittance limited regime from eq. (4.61).

Summing up the effects, on the one hand, decreasing the (slice) energy spread by decompressing the beam the 3D gain length decreases due to reduction of the scaling parameters, but on the other hand, the 1D gain length increases, due to the reduction in current. This has to be balanced to obtain the lowest total gain length and highest growth rate.

For LUX beams the gain length is reduced to 30 cm with a stretching factor of $n_B \gtrsim 5$, having about 6.5 gain length in the undulator and consequently an expected power gain of about 100 when following eq. (4.43). Thus, this might be on par or just above the power level of spontaneous undulator radiation. In the following sections more aspects will be considered that further influence the gain length.

4.4.3 Effects of Short Bunch Length and Superradiance

Presented formulas are valid for the steady-state regime, which assumes the electron beam to be infinitely long and of uniform current density in the region where the radiation interacts with the electrons. However, for short bunches, as expected from LPA, those assumptions might not hold.

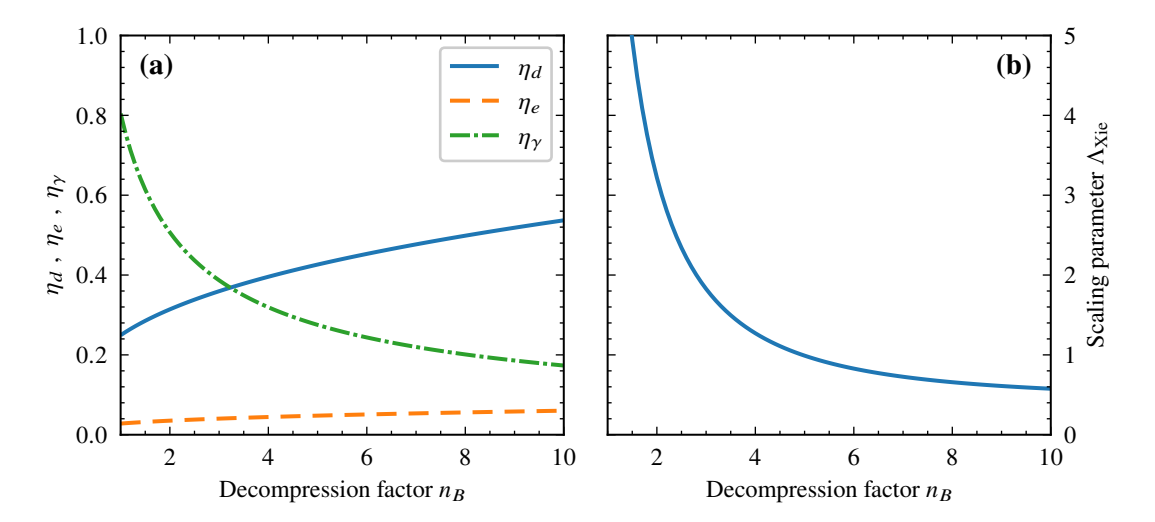


Figure 4.9: Change of scaling parameters for 3D gain length at LUX parameters with varying decompression n_B . (a) Values of (blue, solid) η_d , (orange, dashed) η_ϵ , and (green, dash dotted) η_γ related to the change in $L_{g,1D}$ and slice energy spread σ_Δ . (b) Total change of $\Lambda_{\rm Xie}$.

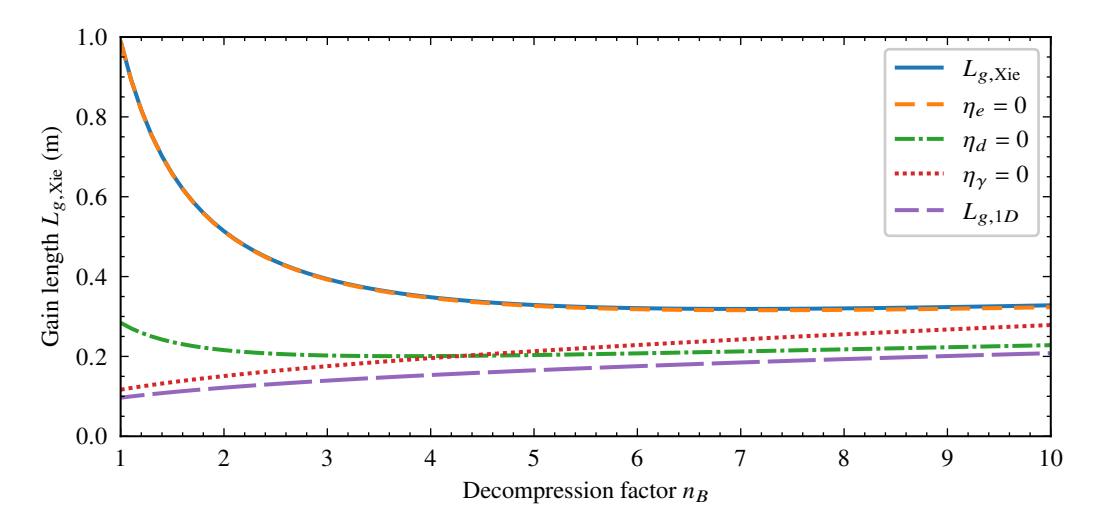


Figure 4.10: Scaling of 3D gain length for LUX parameters at varying decompression n_B . The 1D gain length (purple, long dashed) increases due to 3D effects (blue, solid). Neglecting either contributions from emittance (orange dashed), diffraction (green, dash dotted), or energy spread (red, dotted) reveals, that a combination of the latter two have largest impact.

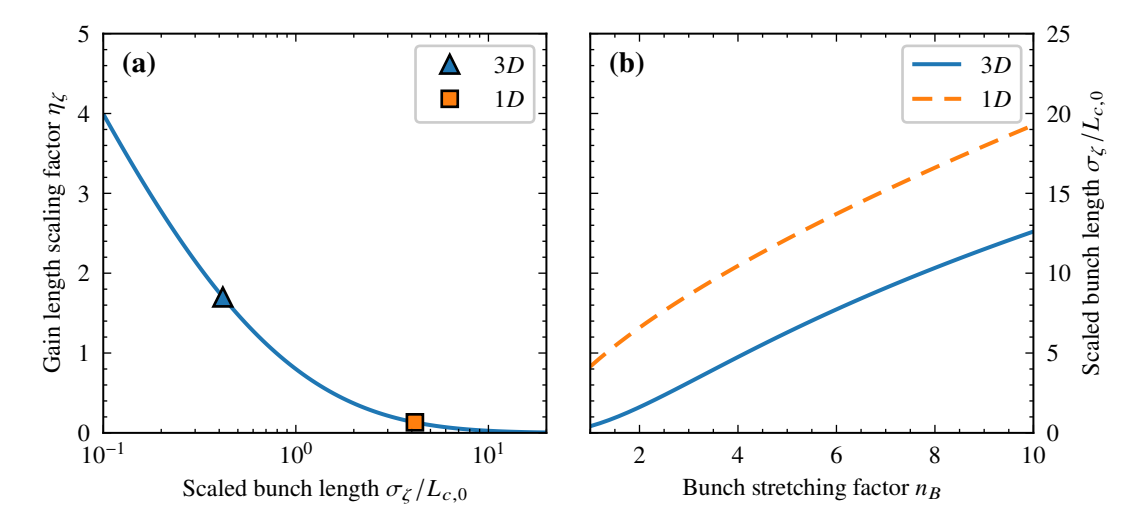


Figure 4.11: (a) Increase in gain length due to short electron bunch lengths σ_{ζ} compared to the steady state cooperation length $L_{c,0}$. (Blue triangle) In the 3D case the gain length is expected to be almost increased by $200\,\%$ while (orange square) in the 1D case the influence of the short bunch would be insignificant for LUX parameters. (b) With decompression the ratio $\sigma_{\zeta}/L_{c,0}$ is shifted to more favorable values and therefore reducing the impact from short bunches on the gain length.

A length scale to quantify a bunch as long or short is the cooperation length [134]

$$L_c = \frac{\lambda_l}{\lambda_u} L_g \quad . \tag{4.68}$$

It is the slippage of the radiation relative to the bunch within one gain length. The electrons can self-organize within this distance to radiate cooperatively, meaning the radiation emitted from these electrons can coherently interact within this range. Therefore, it defines a scale of longitudinal coherence. This is seen as growing spikes that develop in the longitudinal structure of a SASE FEL pulse built up from noise with distances on the order of $2\pi L_c$ [135, 136]. Typically for FELs operating at nm-scale wavelengths and few m gain lengths, therefore having $L_c \ll 1~\mu\text{m}$, the electron bunch is long compared to the cooperation length $\sigma_\zeta \gg L_c$. For such beams with $\sigma_\zeta \gtrsim 10L_c$ radiation pulses originating at the bunch tail can reach saturation before completely slipping over the whole electron bunch. Then no significant influence from the bunch length is expected.

However, if the electron bunch is on the scale of only a few or shorter than the cooperation length L_c , a radiation pulse slips over the whole electron bunch before achieving full amplification. In that case, photons can escape the beam before interacting with electrons and any radiation that overtakes the whole bunch already within the undulator does not contribute to the exponential amplification process anymore. This leads to a decrease in interaction time of electrons and light wave, partially suppressing the FEL process. Consequently, the growth rate is reduced and therefore the gain length is increased.

This regime is referred to as "weak" superradiance⁴. It is called weak, since the emitted power is lower than the steady-state FEL regime [137]. This short bunch regime could be present, since the bunches from laser plasma acceleration are intrinsically short. Indeed, using the initial LUX parameters and the previously obtained gain length of 1 m from the M. Xie fit formula, a cooperation length of $L_c \simeq 4.3 \, \mu m \simeq 2.4 \, \sigma_{C,0}$ is obtained.

For short bunches the increase in power of the growing mode can be estimated analytically by assuming a rectangular bunch shape with length $L_b \lesssim 2\pi L_c$ in the 1D limit to be [138]

$$P_{\text{short}}(z) \propto \exp\left(\frac{3}{2^{2/3}} \left(\frac{z}{L_{g,0}}\right)^{2/3} \left(\frac{L_b}{L_{c,0}}\right)^{1/3}\right)$$
 (4.69)

where $L_{g,0}$ and $L_{c,0}$ are the values of the steady-state solution. The growth rate reduces with smaller L_b and does not follow an exponential scaling with z, but slower with $z^{2/3}$. Since the growth rate is smaller and the power level is lower it could be favorable to operate at bunch lengths significantly larger than $L_{c,0}$.

Considering more realistic longitudinal bunch shapes, changes in the current possibly dropping to values significantly below I_{peak} can occur within the range of a few L_c . Similar to eq. (4.64), the gain length can be modified to take this into account and model the reduced growth rate under these conditions. A heuristic formula obtained for a Gaussian current distribution is given by [139]

$$L_{g,\zeta} = L_{g,1D} \left(1 + \eta_{\zeta} \right)$$

$$\eta_{\zeta} = b_1 \exp \left(b_2 \left(\frac{\sigma_{\zeta}}{L_{c,0}} \right)^{b_3} \right)$$
(4.70)

with the fit parameters $b_1 = 16.7512$, $b_2 = -3.0420$ and $b_3 = 0.3267$. Note that in return the total cooperation length is again defined as eq. (4.68).

For example, the estimated increase in the gain length from eq. (4.70) is less than 10 % for $\sigma_{\zeta}/L_{c,0} > 5$. The increase of the corresponding scaling factor to the gain length with respect to the ratio of bunch length to the cooperation length is shown in fig. 4.11(a). For LUX parameters a significant increase in the bunch length scaling is expected when considering 3D effects and their influence on the gain and cooperation lengths. For cases, where 3D effects would be negligible, e.g. by improved beam properties and especially very small energy spread, also the effects from short bunch lengths are reduced, as indicated by the 1D case in fig. 4.11. By decompressing the beam, $\sigma_{\zeta}/L_{c,0} = 5$ is already achieved for a moderate value of $n_B \simeq 4$. Further, the ratio of bunch length to cooperation length scales almost linearly increasing for LUX parameters with the bunch stretching factor as shown in fig. 4.11(b). This takes into account the changes in 3D gain length and cooperation length due to reduction in beam current and uncorrelated energy spread while the bunch length is increased. Under the assumption, that the bunch length effects solely depend on the ratio of bunch length to cooperation

⁴ In contrast to the "weak" superradiance a "strong" superradiance can occur for long bunches, where a radiation spike originating from the tail of the bunch continuously extracts energy while slipping over the electron bunch end eventually exceeds the power of the FEL after saturation.

length, a combined scaling with the previously found contribution from 3D effects is given by [139]

$$L_{g,\zeta} = \left(1 + \eta_{\zeta}\right) \left(1 + \Lambda\right) L_{g,0} \quad , \tag{4.71}$$

where in η_z the cooperation length with respect to the 3D scaling $L_c = (1 + \Lambda)L_{c,0}$ has to be used. Therefore Λ has to be determined first from the Xie scaling. Using initial parameters for LUX including the short bunch length, the 3D gain length is further increased from the previously determined 1 m to about 2.5 m. If using a decompression of $n_B \gtrsim 5$, the ratio $\sigma_\zeta/L_{c,0}$ increases to values above 7. The impact of the bunch length on the gain length is consequently reduced to below 5 % and becoming negligible.

Nevertheless, another effect should be discussed related to superradiance when considering the LUX case, where the FEL gain within the short undulator is crucial. For longer bunches exceeding L_{α} , dynamics exhibit characteristics of both steady-state and superradiant instabilities: superradiance still manifests near the bunch's trailing edge, while steady-state behavior dominates towards the leading edge⁵. The absence of forward-propagating radiation from behind means electrons emit spontaneously without the influence of an accumulating radiation field. Its generation is less affected by energy spread or beam detuning and essentially represents coherent spontaneous emission, resonant with the electrons emitting at the bunch tail [141, 142]. It can emerge under conditions beyond those supporting the FEL instability as derived in the steady-state regime [143]. Therefore, it can already grow before the usual SASE startup allowing for an early startup. Especially at the bunch tail when entering the undulator, this might be further supported by either a large gradient in the current density or features on the scale of the emitted wavelength [144, 145]. However, amplification of such a pulse primarily occurs when interacting with unperturbed electrons [146] and it stops growing when slipping over electrons that have already interacted with previous radiation spikes that have left them micro-bunched and with a large amount of energy spread [135]. Consequently, after the initial phase, steady-state dynamics and exponential growth predominate. It's important to note that typical FEL simulation codes, applying the slowly varying envelope approximation, might not accurately represent the influence of coherent radiation at the bunch tail on the startup phase [123, 147].

The discussion highlights, that the effects due to the initially short bunch length on the gain length are reduced by decompressing the beam and only a minor increase in gain length, but on the other hand possibly lead to earlier startup.

4.4.4 Undulator and Alignment Errors

Any variation in undulator peak strength and period length cause the beam to deviate from its design orbit. This causes the beam to either leave the radiation cone partially or completely. Further, due to detours and path length differences, the electrons lose their phase relation to the light field. Both can cause severe reduction of the amount of energy they can gain from the field.

⁵ The presence of a superradiant contribution in the radiation is not to be confused with the superradiant regime, increasing the FEL power output beyond the exponential regime [140].

If the electron beam is being kicked away from the axis due to a local error in K, the gain length will be reduced. In that case the direction of the electrons does not coincide with the orientation of the longitudinal microbunching and the wavefront normals of the radiation. Similarly, this is the case if the beam enters the undulator under an analle. The reduction in gain length of a beam traveling with an angle with respect to the undulator axis is given by the formula [148]

$$L_{g,\theta} = \frac{L_g}{1 - \left(\theta/\theta_c\right)^2} \quad , \tag{4.72}$$

with the critical angle $\theta_c = \sqrt{\lambda_l/L_g}$, at which no amplification happens anymore. For *LUX* parameters with a wavelength at about 65 nm and 3D gain length of 30 cm the critical angle is rather large $\theta_c \simeq 0.5$ mrad. To limit the influence to a 10% increase in gain length to still have enough gain lengths fit into the undulator, any local kicks in the undulator as well as the alignment of the beam through the undulator must be smaller than $0.3\theta_c \simeq 0.15$ mrad.

If microbunching has already built up, a kick potentially leads to debunching due to spoiled coherence, which has more impact on the gain length increase given by eq. (4.72). The latter can be reformulated to [148]

$$L_{g,\theta} = \frac{L_g}{1 - \pi \left(\theta/\theta_c\right)^2} \quad , \tag{4.73}$$

thus the kick must be smaller than about 0.1 mrad to keep the gain length increase below 10 %. Further, due to the quadratic dependence on θ_c in the denominator the gain length quickly grows, and a kick of 0.15 mrad would already increase the gain length by 50 %.

In contrast to a single kick, the orbit within the undulator can be distorted by the accumulating effects of variations in K. This includes longitudinal misalignment of the undulator magnet poles, thus changing λ_u , peak field errors in B, and polarization or field orientation errors [149]. One effect of these errors is their impact on the proper slippage between radiation and electron beam and therefore the resonance condition, thus reducing the energy transfer. Assuming a random distribution of these errors over the whole undulator, a measure for combined amplitude of errors is given by the root mean square phase shake introduced by the undulator [150]

$$\sigma_{\Phi} = \sqrt{\frac{1}{2N_u} \sum_{n=1}^{2N_u} \Phi_n^2} \quad , \tag{4.74}$$

where the $\Phi_n = k_l \Delta z_n$ give the deviation of the phase from the resonance up to each of the $2N_u$ half periods from the cumulated path length difference Δz_n , i.e. the slippage error. The deviation in phase has a similar effect as a path length difference due to energy detuning of an electron. To estimate whether the phase spread from the electron beam's energy spread dominates over undulator errors both values are compared against each other. In that case the gain length remains well described by the electron beam parameters only. According to eq. (4.37c) an electron with an energy deviation

from the design energy has a change in phase ψ relative to the resonant phase of

$$\Delta \Psi_n = \frac{\mathrm{d}\psi_n}{\mathrm{d}z} L_g = 2k_u \eta L_g \tag{4.75}$$

over one gain length L_g . Consequently, the resulting phase spread for an ensemble of particles is given by the energy spread

$$\sigma_{\Delta\Psi} = \frac{4\pi}{\lambda_{\mu}} \sigma_{\delta} L_g \quad . \tag{4.76}$$

Using the expected uncorrelated energy spread $\sigma_{\Delta} = \sigma_{\delta}/n_B \simeq 0.3$ % after decompression with $n_B = 3$ results in a phase spread of $\sigma_{\Delta\Psi} \simeq 48^\circ$, therefore being significantly larger than the undulator phase shake. Both values would be only at the same level after decompressing the beam by $n_B > 10$ to less than 0.1% uncorrelated energy spread. Thus, the contribution from phase shake is not the dominant factor, if $\sigma_{\Psi} < \sigma_{\Delta\Psi}$. For cases where the 1D theory describes the interaction and gain length well, this is more conveniently written as $\sigma_{\Phi} < \sigma_{\delta}/(\sqrt{3}\rho_{\rm FEL})$ [149]. Nevertheless, any contribution from the undulator phase shake should be kept low.

The expected increase in gain length for the high-gain FEL by only the phase shake eq. (4.74) is given by [151]

$$L_{g,\Psi} \simeq \left(1 + \frac{\sigma_{\Psi}^2}{\sqrt{3}}\right) L_g$$
 (4.77)

To limit the increase in the gain length from only the phase shake of the undulator to less than 10 %, it has to stay below $\sigma_{\Psi} \simeq 23^{\circ}$. Note that to this point, only the effect of phase shake on the phase of the electrons to the light field was considered.

In addition, field errors cause a transverse motion of the beam away from the design trajectory. This beam wander reduces the overlap of electron beam and the radiation field. Therefore the interaction between the two is also decreased and consequently the gain length increased. Similar to eq. (4.74) the root mean square beam wander is given by [150]

$$\sigma_{x,w} = \sqrt{\frac{1}{2N_u} \sum_{n=1}^{2N_u} x_n^2} \quad , \tag{4.78}$$

where $x_n = \int x'(z) dz$ is the second field integral of the motion up to the n^{th} half-period. Note, that x_n is evaluated at the poles and therefore includes the extent of the wiggling motion of the electrons.

An estimate on the increase in gain length from the beam wander in relation to the beam size is given by [149]

$$L_g \simeq \frac{L_g}{1 - R^2} \tag{4.79}$$

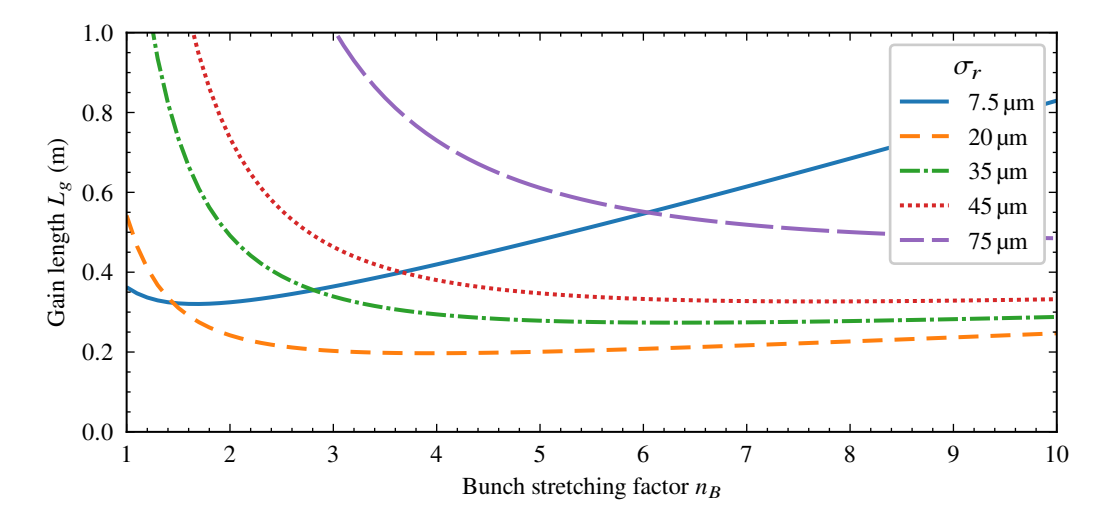


Figure 4.12: Scaling of the gain length L_g from Xie fit and including bunch length effects dependent on the bunch stretching factor n_B for LUX beam parameters. Different lines represent different spot sizes σ_r in the undulator from (blue, solid) 7.5 μ m to (purple, long dashed) 75 μ m. The average achievable beam size in the undulator coincides with the curve for (red, dotted) 45 μ m and is the same as given before in fig. 4.10.

with

$$R = \sigma_{\Psi} + \frac{1}{2} \left[\left(\frac{\Delta x}{\sigma_x} \right)^2 + \left(\frac{\Delta y}{\sigma_y} \right)^2 \right] \qquad (4.80)$$

As seen from this, the beam wander has to be smaller than the beam size, due to their ratio contributing to the increase in gain length with the fourth power. Therefore, a small beam size sets stricter limits to the field quality of the undulator. If the contribution from the beam wander in one plane is dominant over the contribution of the other plane and the phase shake, for example due to the main magnetic field component being much larger than the other components and errors form there having larger impact, the increase in gain length is limited to 10% if the beam wander stays below $\Delta x \approx 0.8 \sigma_x$.

4.5 Parameter Optimization

In order to achieve substantial gain in the short undulator, the beam parameters at the undulator's position have to be optimized, including 3D and short bunch effects. Further, the undulator strength has to be adapted to the electron beam chirp to keep the radiation resonant by changing K along the propagation axis.

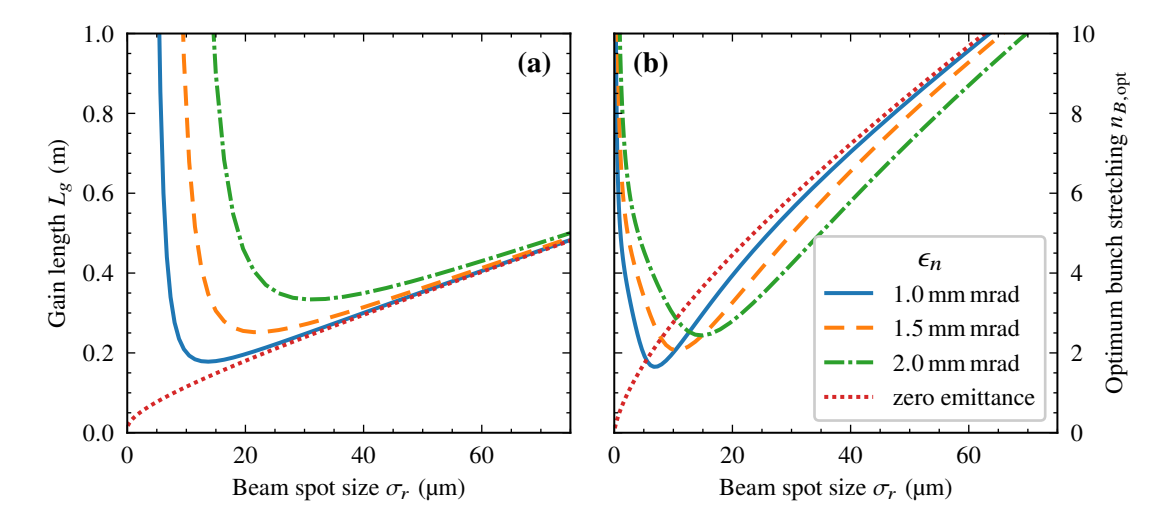


Figure 4.13: Scaling of (a) the gain length L_g from Xie fit and including bunch length effects, and (b) the corresponding optimum bunch stretching $n_{B,\text{opt}}$ dependent on the transverse beam spot size σ_r for LUX beam parameters. Different lines represent differences in the normalized emittance ϵ_n in the undulator for (blue, solid) 1 mm mrad, (orange, dashed) 1.5 mm mrad, and (green, dash dotted) 2 mm mrad. Additionally the gain length for (red, dotted) zero emittance is shown, corresponding to a beam of constant size.

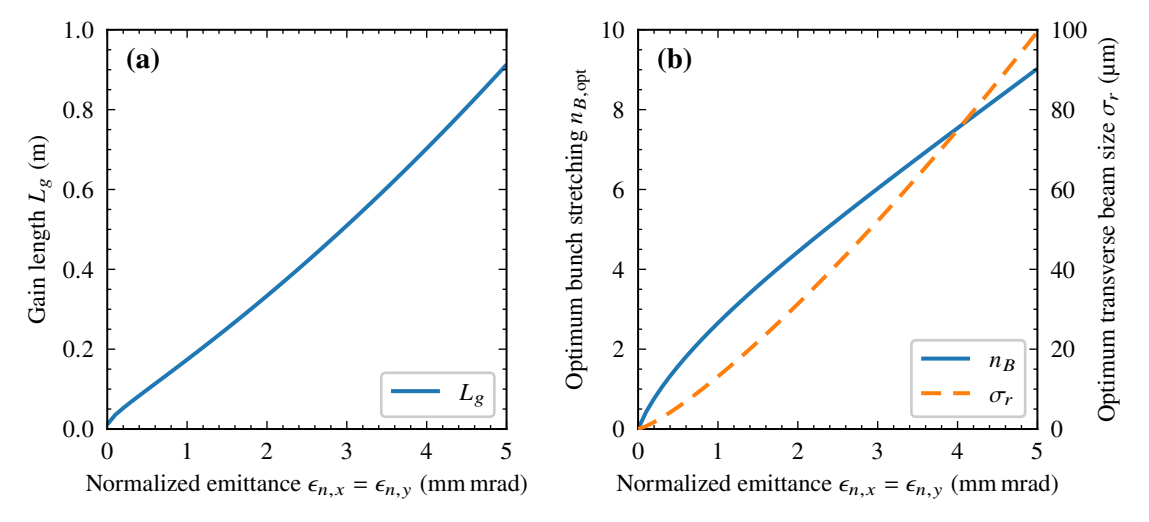


Figure 4.14: (a) Minimum gain length L_g from Xie fit and including bunch length effects. (b) The corresponding (blue, solid) optimum bunch stretching $n_{B, \mathrm{opt}}$ and (orange, dashed) beam spot size σ_r dependent on the normalized emittance ϵ_n for LUX beam parameters.

4.5.1 Gain Length Minimization

Based on the previous considerations, the beam parameters at the position of the undulator are optimized. This is done by numerically minimizing eq. (4.71) for the shortest gain length, including the 3D and bunch length scalings. It is performed by varying the bunch stretching from R_{56}^{ζ} , as the rest is determined by the undulator or initial parameters of the beam. In a first step, the beam size is assumed to be matched to the undulator according to section 4.1 with all energies being focused at the undulator center and following the same envelope, thus using the average beam size with $\sigma_{r,\text{avg}} = 45\,\mu\text{m}$. The optimized decompression is obtained to be $n_B \simeq 7.7$ or equivalently $R_{56}^{\zeta} \simeq 1.5\,\text{mm}$ and yields a gain length of $L_g \simeq 32\,\text{cm}$. However, the 3D gain length does not drastically increase if going away from the optimum decompression and still yields a gain lengths below 35 cm for any $n_B \simeq 5$ to 13.5 or a $R_{56}^{\zeta} \simeq 0.9$ to $2.6\,\text{mm}$.

A parameter that was kept fixed for optimization is the beam size, since the average size inside the undulator is limited by its length, see section 4.1.4. However, in a chirped bunch after decompression, properly matching the optics to focus the energies in the bunch that deviate from the design energy, i.e. synchronize the focused part of the beam with the position of a FEL pulse as it travels though the electron beam, allows for the scaling of the gain length with the focused instead of the average beam size [108]. The focus spot size achieved by the different energies throughout the undulator can be tuned to balance emittance, diffractive and energy spread effects. In the following only the impact of varying the beam's transverse spot size is discussed and the actual realization with beam optics will be presented in section 5.2.

Figure 4.12 shows the comparison of several beam sizes and stretching factors according to eq. (4.71) and the achievable 3D gain length. The main contribution from reducing the transverse beam size is the increase in current density and therefore a decrease in $L_{g,1D}$. In return this affects the scaling parameters in the Xie fit and a reduction in the 3D gain length. Additionally, the cooperation length and therefore the impact of a short bunch length and requirement for large stretching factors reduces. If reducing the beam size too much, the impact of diffraction and emittance effects start to dominate over the improvement from the higher current density and the gain length increases again. This limits the benefit of further decreasing the beam focus size in the undulator. However, if operating at a beam size above this threshold, a wide range of bunch stretching can be used without significant impact on the gain length. Further, variations on the order of 20% in transverse size have an impact on the gain length of less than $5\,\mathrm{cm}$. With LUX parameters, slightly decreasing the focus size and operating at smaller values than $45\,\mathrm{\mu m}$ is expected to improve the FEL performance and reduce the gain length below $30\,\mathrm{cm}$.

In addition to the LUX reference beam with initially 1 mm mrad normalized emittance, the gain length for beams with larger emittance are also of interest, because of the possible increase of its value during beam transport caused by the effects discussed in chapter 3. Further, as pointed out in section 2.4, the reference beam represents only the 10 % best beams at LUX, but could be slightly worse from day to day operation and also fluctuate from shot to shot. The gain lengths for normalized emittances of 1, 1.5, and 2 mm mrad are shown in fig. 4.13(a) for varying transverse beam sizes. It was obtained for optimum decompression at each beam size, which is shown in fig. 4.13(b). At higher emittances the minimum achievable gain length increases and the lower limit of acceptable beam sizes is shifted to

higher values. As the impact of slightly increased focus size on the gain length is less severe than a too small one, it might be favorable to operate at slightly larger beam sizes, if the exact emittance is not known.

The minimum achievable gain length is shown in fig. 4.14(a) from zero normalized emittance up to 5 mm mrad. The corresponding optimum transverse beam size and bunch stretching are given in fig. 4.14(b). The gain length can be kept below 30 cm, or equivalently having > 6.5 gain length in the undulator for sufficient amplification, if the normalized emittances in both planes are at or below $\epsilon_n \lesssim 2$ mm mrad. Furthermore, the emittance has to remain below this value only within a longitudinal slice, i.e. the fraction of the bunch that interacts with the FEL pulse, which can be achieved with the LUX beams in the presence of chromatic effects and possible influence of CSR in the decompression chicane.

Another interesting effect appears if the initial emittance would be about a factor of 5 smaller at 0.2 mm mrad, which is in principle achievable from laser plasma accelerators [13], but otherwise unchanged parameters from LUX. In that case, reducing the focus size to $\sigma_r < 10\,\mu m$ with an appropriate beam optics increases the FEL parameter ρ_{FEL} to a level surpassing the initial energy spread. For compact LPA based FELs, where such focusing schemes are applicable, improving the transverse beam properties from the plasma source would similarly reduce the strong requirement for decompression as a reduction in initial energy spread.

Concluding from the above, at 1 to 2 mm mrad normalized emittance and a spot size of 30 to 35 μ m, although being slightly above the optimum, a gain length of just below 30 cm can be achieved with a moderate decompression of $n_B > 3$ or $R_{56}^{\zeta} > 500 \,\mu$ m. Note, that this beam size is still larger than the expected beam wander from the undulator presented in section 4.4.4.

4.5.2 Undulator Tapering

A linear change in the undulator strength K along the longitudinal axis, known as tapering, can be utilized for several use cases [152]. For example, standard tapering, which is a decrease in K, can increase the power output as post-saturation taper [153] or compensate beam energy loss due to radiating [154], and reverse tapering, for afterburners to control polarization [155]. Here, it is employed in combination with the decompression to keep the radiation at resonance as it travels through the electron beam [23, 156]. The concept is illustrated in fig. 4.15. After a R_{56} is applied the beam is chirped in the longitudinal phase space. The wavelength emitted at each longitudinal position inside the bunch differs dependent on the energy and scales as $1/\gamma^2$ according to eq. (4.20). Therefore, as the radiation slips over the bunch, the resonant wavelength decreases towards the bunch head if K is constant. Consequently, to compensate this, the undulator strength K has to be increased along the undulator and keep λ_I constant.

To vary K either the undulator period λ_u or the magnetic B-field has to be changed. However, the latter is simpler to implement, since the B-field depends on the undulator gap, which is motorized. Requiring a constant wavelength to be emitted along the bunch while passing the undulator $\frac{\mathrm{d}\lambda_l}{\mathrm{d}\zeta}=0$

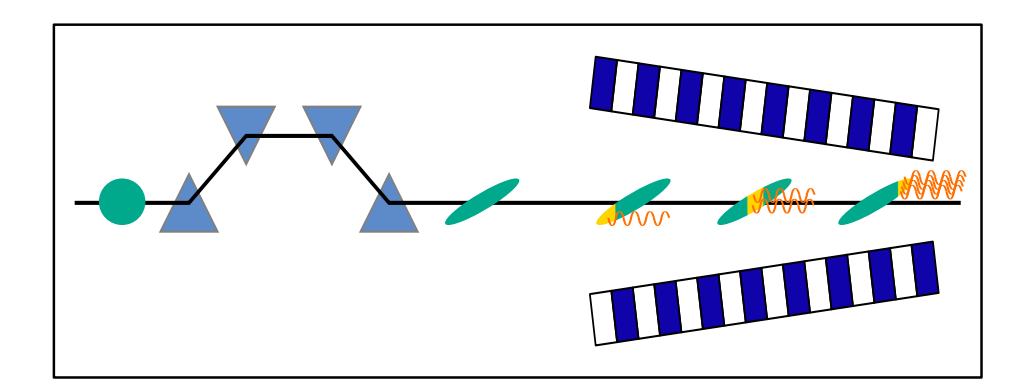


Figure 4.15: Schematic illustration for the use of a tapered undulator to keep the radiation resonant. From left to right: The (green, circle) initially short and unchirped bunch passes a (blue, triangles) decompression chicane and is stretched and chirped afterwards. The taper of the (white and blue) undulator is set to have (yellow parts) different fractions of the electron bunch emit at the same wavelength. As the (orange, waves) radiation passes through the bunch it is amplified.

and solving for $\frac{dK}{dz}$ yields [156]

$$\frac{\mathrm{d}K}{\mathrm{d}z} = \frac{\left(1 + \frac{K^2}{2}\right)^2}{K\gamma^3} \frac{\mathrm{d}\gamma}{\mathrm{d}\zeta} \quad . \tag{4.81}$$

Note that $\frac{\mathrm{d}K}{\mathrm{d}\zeta} = \frac{\mathrm{d}K}{\mathrm{d}z} \frac{\lambda_l}{\lambda_u}$ was used, which reflects that the bunch and radiation travel along the undulator and slip by one radiation wavelength per undulator period relative to each other. In the limit of a small relative energy chirp $\left|\frac{\sigma_z}{\gamma_0}\frac{\mathrm{d}\gamma}{\mathrm{d}\zeta}\right| \ll 1$ and small relative taper $\left|\frac{L_u}{K_0}\frac{\mathrm{d}K}{\mathrm{d}z}\right| \ll 1$ over the respective length scales, the values $\gamma(\zeta)$ and K(z) on the right hand side can be replaced by the mean values γ_0 and γ_0 and γ_0 and linear energy chirp γ_0 of the bunch. For γ_0 this criterion is fulfilled as the changes are typically on the order of percent.

Using the expected values at LUX with 300 MeV, a $K_0=2$, and a linear energy chirp from a $R_{56}^{\zeta}=500\,\mu\mathrm{m}$ of $m=\mathrm{d}(\gamma/\gamma_0)/\mathrm{d}\zeta\simeq 1/R_{56}^{\zeta}\simeq 2\,000/\mathrm{m}=0.2\,\%/\mu\mathrm{m}$ the required taper to compensate the chirp is estimated to be

$$\frac{1}{K_0} \frac{dK}{dz} = \frac{\left(1 + \frac{K_0^2}{2}\right)^2}{K_0^2 \gamma_0^2} \ m \simeq 1.3 \frac{\%}{m} \quad . \tag{4.82}$$

Although the optimum taper is non-linear, the linear taper approximation deviates by less than 0.01 %/m at the undulator entrance and exit. Additionally a detuning of the electrons from energy loss to the gaining field occurs. However, this becomes only relevant close to saturation, as it is much smaller than ρ_{FEL} in the exponential gain regime [158]. Since both effects are expected to be small, applying a linear taper is sufficient for LUX.

Note, that either a slightly chirped bunch or a small undulator taper already decrease gain length on their own [159]. Therefore chirp and taper might be slightly compensated against each other and the optimum value might be different, but close to the obtained value. When applying more decompression and therefore decreasing the chirp, the required taper also decreases. As seen previously, applying slightly more decompression than required might be favored, and therefore a taper of about 1 %/m is reasonable. Previous estimations for the decompression scheme assumed a much shorter initial bunch length, which suggested a stronger chirp of the electron beam and consequently a taper of over 5 %/m [23].

The Frosty Undulator at LUX can therefore go up to a taper of 5.7 %/m at maximum K, which gives enough room to adjust the taper to the required value.

4.5.3 Phase and Group Velocities

The velocities of the electromagnetic waves constituting the radiation during amplification. They propagate with less than c, since the electrons act as a medium, and determine which part of the electron beam the radiation interacts with as they move through the undulator together.

In the exponential gain regime, the fundamental wave travels at a phase velocity of [105]

$$\frac{v_{ph}}{c} = 1 - \frac{\lambda_l}{\lambda_u} \rho_{\text{FEL}} \quad , \tag{4.83}$$

which is just barely smaller than c. Note, that this causes just a small slippage of the radiation field (relative to an electromagnetic wave in vacuum) of about λ_l until saturation, allowing for the extraction of energy when operating a high-gain FEL at resonance.

More important for the LUX case is the group velocity v_g , describing the envelope and the corresponding amplitude of the growing FEL pulse and is relevant to slippage effects in short bunches. At the beginning of the interaction, the spontaneous radiation dominates and $v_g \simeq c$. When reaching the regime of exponential grow after a few gain lengths and a FEL pulse develops, the group velocity, i.e. velocity of the emerging spikes, reduces to [105]

$$\frac{v_g}{c} = 1 - \frac{1}{3\gamma_0^2} \left(1 + \frac{K^2}{2} \right) \quad . \tag{4.84}$$

Comparing this with the average longitudinal velocity of the electrons due to their detour from a straight line in the undulator eq. (4.8) yields [105]

$$\frac{v_g}{c} - \overline{\beta_z} = \frac{1}{6\gamma_0^2} \left(1 + \frac{K^2}{2} \right) \tag{4.85}$$

or similarly [120, 136]

$$\frac{v_g/c - \overline{\beta}_z}{1 - \overline{\beta}_z} = \frac{1}{3} \quad . \tag{4.86}$$

This shows that also the wave packet moves faster than the electron beam, but their difference and the slippage of the pulse relative to the beam are reduced to a third in the exponential regime.

Methods to increase the FEL gain that are linked to the propagation of the wave packet, like the previously mentioned focusing schemes to locally increase the current density [108], have to be matched to this reduced pulse slippage per undulator period of $\lambda_l/(3\lambda_u)$. However, note that this only applies to the exponential gain regime and not during the startup, where $v_g \simeq c$ [105]. An intermediate value between the two might be favorable for an experiment like LUX, where the exponential gain regime is expected to just begin halfway through the single undulator used.

4.6 Numerical Estimation

To investigate if the optimized parameters show improvement over the initial values and are in principle sufficient to grow beyond spontaneous undulator radiation, some simplified FEL simulations were performed with the time-dependent SVEA code *SIMPLEX* [160]. Although not covering all aspects from laser-plasma accelerated beams and the decompression scheme, and their impacts on FEL operation, it gives an estimation on whether the beam properties are sufficient to drive an FEL at all.

The considered cases are:

- 1. Initial beam parameters for LUX with the average beam size in the undulator of $\sigma_r \simeq 45 \, \mu m$. The horizontal focus is at the center of the undulator and the vertical beam size is matched to the natural focusing of the undulator and therefore constant.
- 2. Bunch length, current and (uncorrelated) energy spread are set to values expected after decompression with $n_B = 3$, but electron beam chirp and undulator taper are set to zero. Focusing is the same as for 1.
- 3. Same as 2, except for fixing the beam size to a constant value of $\sigma_r = 35 \, \mu m$.
- 4. Same as 3, but added a chirp of 2 000/m and an undulator taper of 1.3 %/m.

In all cases the beams were assumed to be Gaussian shaped in all dimensions.

The last two were realized by using a continuous focusing along the undulator to keep the beam of non-zero emittance from diverging. This simplified setup closely resembles an energy dependent focusing scheme to that sense, that in both cases the propagating light pulse sees an electron beam of

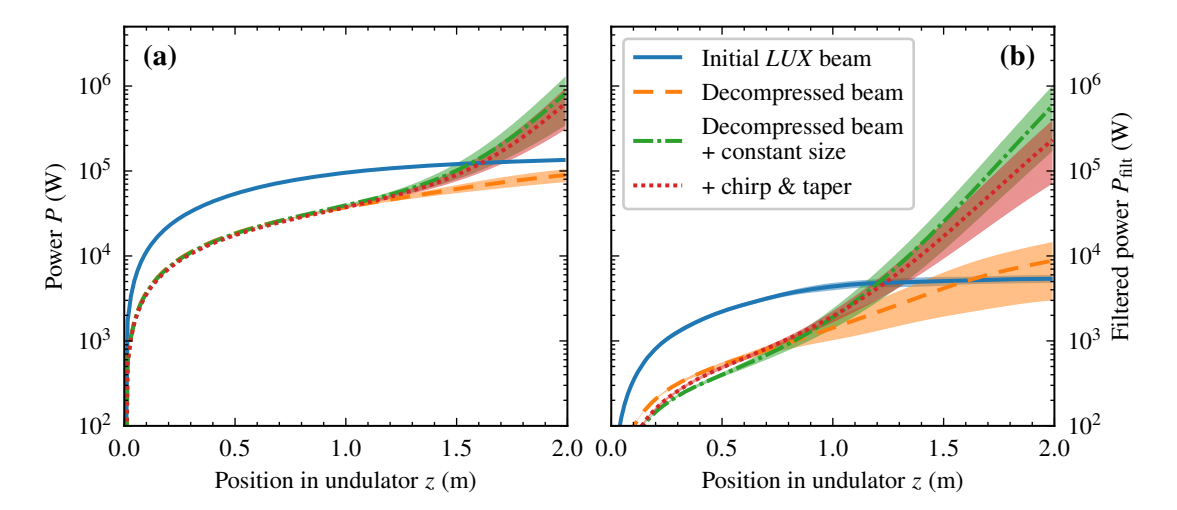


Figure 4.16: Emitted power from SVEA FEL simulations for (a) the power emitted to all frequencies and (b) the power filtered about $\pm 2\,\%$ relative bandwidth about the fundamental. Power is shown for (blue, solid) initial *LUX* parameters, focus at the undulator center in the horizontal and matched to natural focusing in the vertical plane, (orange, dashed) energyspread as after decompression with $R_{56}^{\zeta} = 500\,\mu\text{m}$, but no chirp or taper, (green, dash-dotted) same as before, but with constant beam size of 35 μ m, and (red, dotted), constant beam size, but with chirp and taper included.

finite emittance, but constant beam size throughout the undulator. The idea is, that gain length then scales with the effective size given by the focus spot size in such a scheme. Therefore, if a radiating pulse only encounters fractions of the beam with constant size while it propagates through the bunch, a gain length lower than achievable with the lowest average beam size limited by the emittance can be reached.

The simulations were performed for 5 random seeds in the beam generation. Two power curves were calculated for all four cases. The first includes the full radiation collected over all angles and frequencies available from the simulation. The second is filtered about the opening angle of ± 2.5 mrad from available beam pipe apertures at LUX and about $\pm 2.5(\sigma_{\omega}/\omega_{l})$ times the SASE bandwidth eq. (4.48) at the end of the undulator or about $\pm 2\%$ about the fundamental. This corresponds to a window of about ± 1 nm, which on one hand covers the full FEL pulse, and on the other hand is also assumed to be reasonably above the resolution limit for a spectrally resolved measurement.

Note that the power levels of the spontaneous radiation for the initial bunch are larger than for the other cases due to the shorter bunch length without decompression, or equivalently a higher current.

The total power emitted into all frequencies is shown Figure 4.16(a). As expected, for the initial *LUX* beam the energy spread is too large to drive an FEL. Just applying decompression is not enough to grow beyond the spontaneous radiation, although the hint of growth is visible. In the filtered power

about the opening angle and frequency range, the decompressed beam shows some power above spontaneous undulator radiation. However, the power gain is still small in this case. At these levels any degrading effects would likely suppress the small signal.

Only the constant beam size cases show a visible increase in power of about 1 order of magnitude above the spontaneous radiation already in the unfiltered case seen in fig. 4.16(a). This might be just enough to detect the FEL pulse. Using the last 20 cm where exponential growth is visible, the gain length is estimated to be about $L_g \simeq 23$ cm, which is lower than expected from the Xie fit for a beam with 1 mm mrad normalized emittance and 35 µm beam size. However, it is compatible with the considered scenario of a zero emittance beam in section 4.5.1. Further, if applying the filters in opening angle and frequency in fig. 4.16(b), the spontaneous undulator radiation is decreased by more than 1 order of magnitude. A focusing scheme, that is able to provide a constant beam size at the position of the FEL pulse, combined with a spectrally resolved measurement of the radiation, should provide sufficient growth beyond the undulator radiation to be detectable in an experiment.

4.7 Conclusion

The electron beams right from the plasma are not of sufficient quality, especially in terms of energy spread, to generate FEL gain and power levels beyond spontaneous undulator radiation. However, through proper beam manipulation, the expected gain length can be reduced. The power from an FEL pulse from such a beam should then grow sufficiently beyond the power levels of the spontaneous radiation within the 2 m undulator to be observable in an experiment.

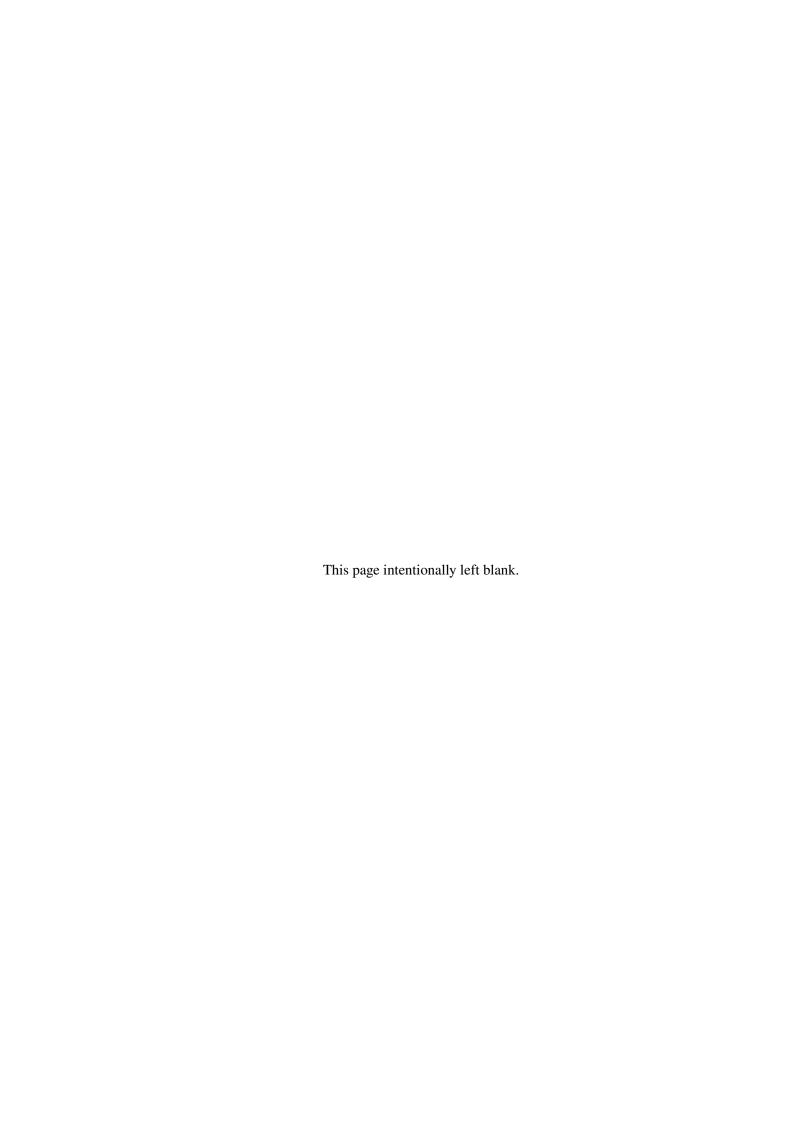
The following points should all be implemented at LUX to achieve this

- Stretching the beam with a decompression chicane with a $R_{56} \gtrsim 500 \, \mu \text{m}$ to reduce the uncorrelated energy spread and weaken effects of short bunch length.
- Taper the undulator to compensate the chirp introduced during bunch stretching to match the change in energy and the undulator strength, therefore keep the radiation at resonance.
- Implement a focusing scheme that matches the beam size along the undulator to the propagation of the radiation pulse to increase the current density and mitigate emittance effects.
- Measure the radiation spectrally resolved to isolate the FEL pulse from spontaneous undulator radiation and enhance the signal.

Including a focusing scheme with constant beam size at the position of the radiation pulse is expected to decrease the gain length by approximately 10 cm and consequently increase the power in the FEL pulse at the exit of a 2 m undulator by about one order of magnitude compared to only using decompression and a tapered undulator. The expected achievable gain length from such an optimized setup is $L_{\varphi} \simeq 20$ to 30 cm, fitting 6.5 to 10 gain lengths into the 2 m undulator.

Isolating the signal in a small window about the fundamental wavelength further improves the signal over the spontaneous undulator by another order of magnitude. Therefore, detecting FEL amplification over the spontaneous radiation should be possible, at least in such a spectrally resolved measurement.

Based on these considerations the LUX beamline was designed. FEL simulations including effects that were not considered here, such as the full 6D distribution after beam transport, are presented after explaining the LUX beamline setup in the next chapter.



LUX Beamline

During the period of this thesis, and based on the methods presented in the previous chapter to improve the FEL signal, the *LUX* beamline was upgraded from an existing setup, as described in [24]. Both the previous and the upgraded setups described in this chapter were used for several experiments and studies [36, 48, 49, 114, 161, 162]. The laser system was independently modified [41, 163].

Laser-plasma acceleration, with its high accelerating gradients, allows for the construction of short accelerator beamlines. As discussed in chapter 2, such high accelerating gradients remove the need for long accelerating structures. In combination with a short-period, high-K undulator, a Free-Electron Laser beamline could be scaled down from hundreds of meters to only a few tens of meters. Other emerging technologies could further shorten the beamline, for example high-gradient permanent magnet quadrupoles [164, 165] or plasma lenses [166, 167]. However, these elements add complexity and could make it more difficult to understand and tune the accelerator for a given goal. Therefore, at LUX, the beam transport of the laser-plasma accelerated electron beams is performed using only well-understood and well-established transport elements, namely electromagnetic quadrupoles and dipoles of the type used in conventional accelerators. Transport through these components is described by linear elements, such as the matrices shown in section 3.1. Higher-order nonlinear elements like sextupoles or octupoles are avoided to keep the setup simple.

From the previous beamline setup, the plasma source area for the generation and acceleration of the electron beam, as well as the post-plasma-target laser diagnostics, were retained, because they had been tested and used extensively before the upgrade. The first quadrupole doublet was replaced by revised models, maintaining the same geometry and available gradients as in the previously installed prototypes. The new 25 m FEL beamline components were then installed after the plasma source and the first meters of electron beam capture.

The following chapter provides an overview of the design considerations derived from the FEL estimations in the previous chapter section 4.5. The procedure to optimize the beam optics and the resulting transport are presented in section 5.2. The final setup and the actual components used therein are described in section 5.3.

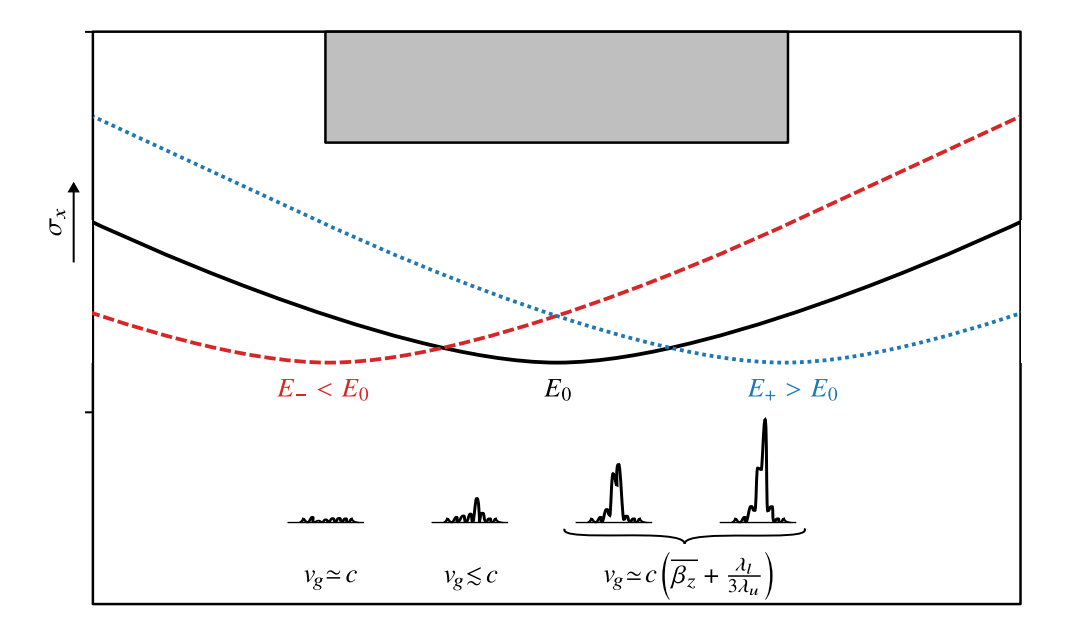


Figure 5.1: Schematic illustration of chromatic matching scheme showing transverse beam sizes σ_x for (red, dashed) a lower energy E_- than (black, solid) the central energy E_0 focused in the front, and (blue, dotted) a higher energy E_+ focused in the back of (position indicated by grey box) the undulator. A radiation pulse is shown below, starting with an initial group velocity $v_g \simeq c$. It slows down in the exponential gain regime at later positions in the undulator, slipping by $\lambda_l/(3\lambda_u)$ relative to the electron bunch.

5.1 Design Considerations for the LUX FEL Beamline

The beamline upgrade is intended to provide the beam properties to gain enough FEL power in the undulator to be detectable. To provide the parameters described in section 4.5, several components are required. This included a magnetic chicane to stretch the beam and reduce the local energy spread, and a set of magnetic quadrupoles to transport the electron beam and match it into the undulator. At the same time, diagnostics are needed to measure the beam properties and provide feedback for accelerator tuning.

5.1.1 Chromatic Matching scheme

As discussed in the previous chapter, the FEL growth rate in the undulator is high when the radiation pulse interacts with an electron beam of high current density throughout the whole undulator. However, focusing the beam to the center of the undulator to minimize the average beam size is constrained by the beam emittance and the undulator length. Matching a beam to the natural undulator focusing, for a planar undulator in its non-wiggling plane, can keep the transverse size constant, but this is also limited by the emittance and the undulator strength.

Basic Concept

A scheme that only focuses the fraction of the beam interacting with a FEL radiation pulse is not bound by the same restrictions. The focus spot size, focus position and focus slip, i.e. the shift of a longitudinal focus position within the bunch, are tuned independently of the undulator length and can be adapted to the undulator's strength and focusing properties. The main limitations are geometric, such as apertures or regions of good field quality.

A key difficulty in implementing such a scheme is deliberately focusing only a part of the beam longitudinally. For beams where all particles behave (nearly) independently of their longitudinal position during transport through static elements, this would normally require time-dependent structures. However, the energy spread in laser-plasma accelerated electron beams are exploited to focus just the desired energy slice at a given position, using the energy-dependent focusing properties of magnetic quadrupole lenses.

In a chirped bunch, for example, a bunch after passing through a magnetic chicane, the longitudinal position of an electron is correlated with its energy. Consequently, the concept of "focus slippage" is realized by combining beam decompression with a suitable chromatic dependence from the quadrupole focusing. A scheme that utilizes the latter to impose a focus slippage matched to the FEL pulse is called a "chromatic matching scheme". This is illustrated in fig. 5.1. Here, a positive focus slippage is defined by a beam waist moving forward through the bunch as it propagates, and a negative one if the waist moves backward.

A partially similar approach was presented in [108], relating the focus slippage to energy-dependent beam expansion in a free drift. However, that particular strategy is limited to the wiggling plane of a planar undulator, or any undulator with weak natural focusing, $(Kk_{\mu}L_{\mu})/\gamma_0 \ll 1$.

In contrast, for *LUX* a different approach was explored that makes use of the anticipated focus slip, includes the undulator's focusing, and requires only linear beam optics (though it is not restricted to linear optics). The key idea is to address the properties of each relevant energy component within the bunch and tune its parameters individually, i.e., to optimize multiple beamline lattices simultaneously, all sharing the same geometry.

Focus Slippage for a Chirped Bunch in an FEL

Synchronizing focus slippage with an FEL pulse in the exponential gain regime requires matching it to the pulse's group velocity eq. (4.84). The pulse slips through the bunch at a rate of 1/3 that of the single-photon slippage (see section 4.5.3). The mean energy of electrons located at the pulse position is set by the beam's chirp m. Hence, the rate at which the focused energy has to change along the undulator depends on the chirp and the pulse slippage [108]

$$\frac{\mathrm{d}\delta_f}{\mathrm{d}z} = m \frac{\lambda_u}{3\lambda_l} \simeq \frac{1}{R_{56}^{\zeta}} \frac{\lambda_u}{3\lambda_l} \quad . \tag{5.1}$$

After the chicane, the beam is chirped with lower energies at the tail and high energies at the head, m > 0. Consequently, lower-energy electrons should be focused at the undulator entrance, and higher-energy electrons at the exit. For *LUX* parameters with $m \approx 2000/m$, this implies an optimum

focus slippage of $\delta_f \simeq 0.3 \,\%/\mathrm{m}$ in the exponential gain regime. Early in the undulator, before exponential gain sets in, $v_g \simeq c$ [105]. Thus, the optimum focus slippage is three times larger, around 0.9 %/m, over the first few gain lengths.

Increasing the focus slippage broadens the range of energies brought to a waist within the undulator. This can be achieved, for instance, by chromatic correction with sextupoles or in a suitably designed apochromatic drift-quadrupole beamline [68]. However, such correction eventually focuses all energies at a single point, e.g., at the center of the undulator, reverting to a situation where the FEL scaling depends on the average beam size.

Reducing the focus slippage, in turn, keeps the waist close to the peak current region, but only focuses a smaller fraction of the beam's energy spread, leaving the rest with a larger size.

Moreover, for a fixed chicane R_{56} and therefore beam chirp, aiming for a tighter waist implies an increase in the lowest achievable focus slippage [108].

It is also worth recalling that rapid changes in the current density, particularly at the tail, can support an early startup [144, 145], see section 4.4.3. For a Guassian distributed current profile, the steepest slope is located at $\pm \sigma_{\zeta}$, corresponding to electrons whose energies deviate by about the projected relative spread σ_{δ} from the central energy. Consequently, a focus slippage near $2\sigma_{\delta}/L_u \simeq 1\,\%/\mathrm{m}$ could boost startup.

In summary, once the R_{56} and the magnification from plasma source to the undulator haven been chosen based on section 4.5, a focus slippage value in or close to the range $\frac{\mathrm{d}\delta_f}{\mathrm{d}z} = 0.3 \,\%/\mathrm{m}$ to 0.9 %/m is applied. For *LUX* parameters, FEL amplification emerges from lethargy roughly one-third to halfway along the undulator, see section 4.6. For a longer undulator operating primarily in the exponential regime, a value closer to eq. (5.1) might be favored.

5.1.2 Requirements to Beam Optics Lattice

Implementing the above focusing scheme requires enough degrees of freedom in the lattice to shape the beam's phase space appropriately to match the parameters for a FEL. Consider first a monoenergetic slice of the beam in the horizontal plane (the same principle applies in the vertical). The condition for bringing the beam to a waist is to have the beam-envelope correlation term $\langle xx' \rangle$ vanish

$$\langle xx' \rangle \stackrel{!}{=} 0 = R_{11}R_{21}\sigma_{x,0}^2 + R_{22}R_{12}\sigma_{x',0}^2$$
 (5.2)

Because initial beam parameters in laser-plasma acceleration can fluctuate, it helps to have either $R_{11} = R_{22} = 0$ or $R_{12} = R_{21} = 0$. This way, the focus position is independent from the initial beam parameters. This ensures the waist location does not depend on the initial beam parameters. Other combinations of two zero elements conflict with the det(R) = 1 constraint for linear transport to preserve the phase space volume [55]. To magnify the transverse beam size by a factor of 10 from initially 3.5 µm to 35 µm, see section 4.5, a $|R_{11}| = 10$ is targeted, with then $|R_{22}| = 1/10$. This requires three parameters per transverse plane to set the focus for the reference energy at the undulator center.

Since the initial beam size is on the order of $5 \,\mu m$ and the divergence of 1 mrad, having $R_{12} = 0$ is important so that any change in the initial divergence does not significantly shift the waist position or size. Further, beam pointing could displace the beam from the undulator's good-field region or cause vertical offset and therefore oscillations of the beam's centroid due to natural undulator focusing.

Applying focus slippage adds two more constraints per plane [108]. The first sets the rate of focus slippage, and the second governs how the beam size evolves for off-crest energies during the slip. Here, we fix it to remain constant, although it can in principle grow or shrink. In practice, additional focal points are imposed at the undulator entrance and exit for the respective energies.

These constraints translate into at least ten adjustable parameters. Since LUX does not always operate at a fixed 300 MeV but rather in the 250 to 350 MeV range, the lattice has to contain sufficient quadrupole magnets to focus the beam over that range. The optimization thus focuses primarily on tuning quadrupole gradients, not drift lengths. Once determined, the latter are fixed and any changes in the transport have to be achieved by adjusting the quadrupole strengths. However, the drift between quadrupoles has to be sufficient to provide the focusing, but avoid excessive beam size and divergence, and keep required magnet strengths within feasible limits.

At the very start, the beam is captured within 40 cm behind the plasma target with a quadrupole doublet, thus reducing the divergence to $\lesssim 0.1$ mrad and minimizing slice degradation from chromatic effects, see sections 3.6.1 and 3.6.2. In total, 11 quadrupoles are used from the plasma source to the undulator.

In addition to quadrupoles, the beamline has to include a chicane providing sufficient R_{56} to decompress the bunch. The chicane's length and dipole angles are chosen carefully so that it does not exceed the limited tunnel space or induce excessive coherent synchrotron radiation (CSR). For the anticipated kick angles, a small horizontal beam size $\sigma_x \leq 100 \, \mu \text{m}$ in the first dipole of the chicane is also important for limiting CSR-induced emittance growth to about 0.5 mm mrad, see section 3.6.5. Although larger emittance may be partly mitigated by the chromatic focusing scheme, it is still desirable to keep it small enough for the downstream transport after the chicane. Finally, an undulator with a taper matched to the beam's chirp maintains the resonance condition and enhances the output power. A variable-gap, variable-taper undulator was designed and built at LUX for this purpose [114].

5.2 Beam Optics Optimization

Based on the requirements found before, an optics lattice with 11 quadrupoles up to the undulator was set up. It includes the initial two quadrupole magnets to capture the beam, followed by drift space for laser diagnostics inherited from the pre-upgrade beamline. The remaining quadrupoles are arranged as two doublets before the chicane and a quintet between the chicane and the undulator. Their effective lengths are 113 mm for the first magnet, 121 mm for the second, and 135 mm for the rest, reflecting the available magnet types for LUX, see section 5.3.1.

The intent of the second and third doublets is to keep the beam sufficiently small throughout the chicane and provide the right transport matrix elements for the quintet to implement the chromatic focusing into the undulator. Further, this setup allows for installing additional diagnostics and the

U	UI.					
	Quadrupole No.	$K_1 (1/\text{m}^2)$	Quadrupole No.	$K_1 (1/\text{m}^2)$		
	1	107.10	7	-12.60		
	2	-40.15	8	12.60		
	3	10.25	9	-11.35		
	4	-14.67	10	11.27		
	5	4.92	11	-12.57		
	6	-6.90				

Table 5.1: Magnet strength for optimized *LUX* lattice with chromatic focusing into the undulator.

decompression chicane in the drift between the quadrupole magnets. This arrangement also leaves room for additional diagnostics and the decompression chicane. For instance, an electron spectrometer is installed early in the line, which can be matched using the first or second doublet (or both). The lattice incorporates the magnets and undulator positions as they are physically installed at LUX. In the optimization, the undulator has a fixed parameter K = 2, providing vertical focusing. A small taper in the range of a few %/m is neglected here.

Because of the large number of quadrupoles involved and the desire to avoid beam degradation, a systematic search was performed to find suitable sets of quadrupole gradients. To avoid local minima caused by poor initial guesses, the 11-dimensional space of quadrupole gradients was sampled with a large number of points from a Halton sequence, a low-discrepancy sequence that evenly explores parameter space. Each quadrupole's gradient was limited by its technical maximum: about 180 T/m for the first quadrupole, 70 T/m for the second, and 23 T/m for the others. At each sample point, a minimization was performed against a cost function measuring deviation from the target matrix elements.

The matrix elements at the undulator center were evaluated for a reference energy of 300 MeV, as well as for ± 1 % energy deviations at the undulator entrance and exit, aiming for a focus slippage of 1 %/m. Off-energy beam sizes were assigned a lower weight so that the central energy waist is prioritized, while still permitting some variation in the slippage and waist size, close to the goals in section 4.5.1.

Optimized Lattice

The resulting lattice solution is listed in table 5.1. As expected, the first two quadrupoles require high gradients, while the following transport is realized with quadrupole magnets with strengthw about $K_1 \simeq 10\,/\text{m}^2$. The best matching was obtained when the quadrupoles of the second and third doublets, as well as those in the quintet, were spaced at the maximum allowed center-to-center distance of 50 cm, giving the largest possible drift between them. fig. 5.2(a) and (b) show the horizontal and vertical beam sizes, respectively, through the beamline for the reference energy and $\pm 1\,\%$ energy deviation from that. The initial size is 3.5 µm size and 0.5 mrad divergence in both planes, see section 2.4 for comparison. These plots show the individual mono-energetic energy slices rather than the full projection, highlighting how the chromatic matching yields smaller spot sizes only in the relevant slices that are expected to interact with the FEL pulse.

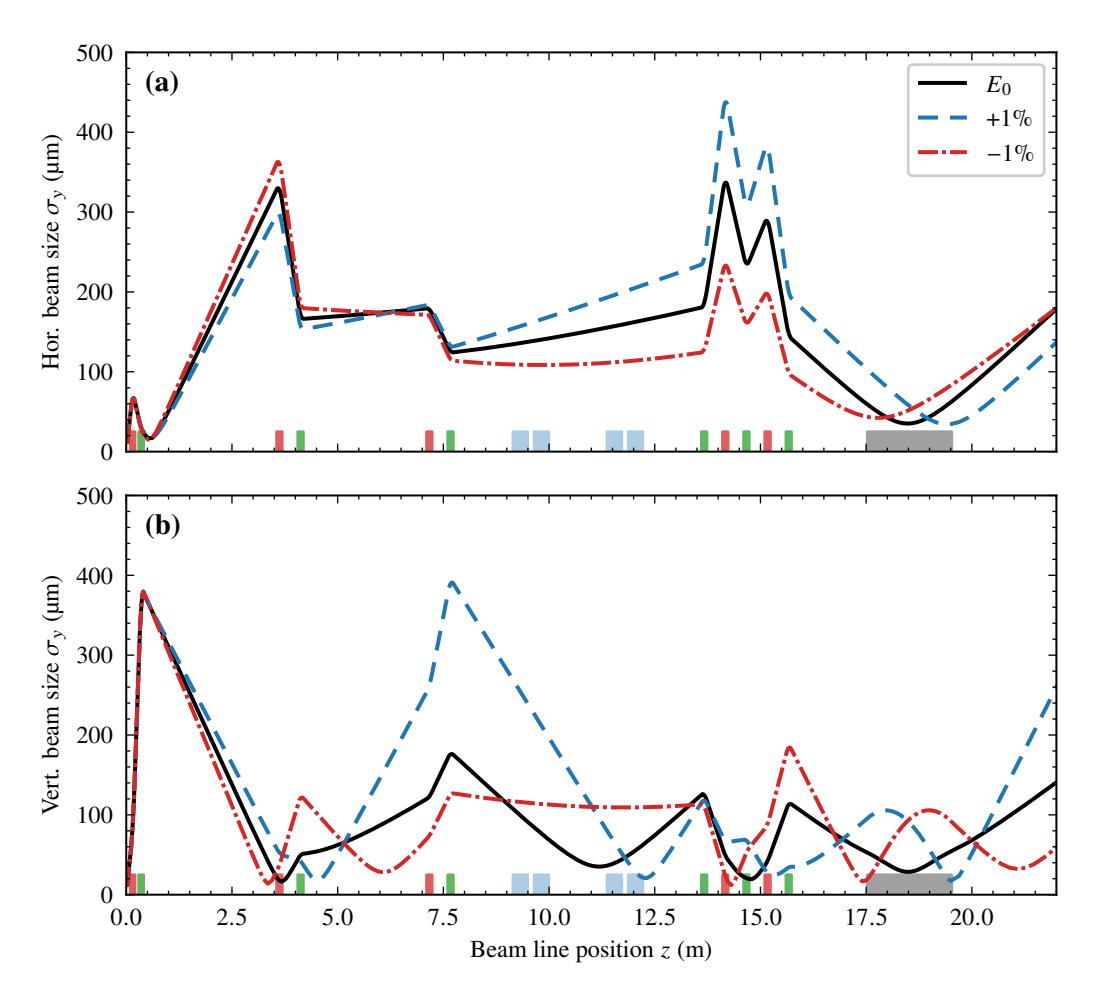


Figure 5.2: Optimized beamline layout for LUX with beam sizes for the (a) horizontal plane and (b) vertical plane. Energies are focused along the undulator according to a chromatic matching with about 1 %/m focus slippage over the undulator. The reference energy (black, solid) is focused at the center of the undulator, whereas (red, dash-dotted) -1 % lower energies are focused at the undulator entrance and (blue, dashed) 1 % higher energies are focused at its exit. Initial beam size and divergence are 3.5 μ m and 0.5 mrad in both planes. Colored boxes indicate (red) quadrupole magnets with K > 0, (green) quadrupole magnets with K < 0, (blue) chicane dipole magnets, and (grey) the undulator.

At the undulator center, the horizontal and vertical magnifications are about 10 and 8, respectively. The vertical plane's magnification decreases to about 5 near the undulator ends, having beam sizes of roughly 35 µm horizontally and 15 µm to 30 µm in the vertical plane. The resulting focus slippage for this optics is about 0.8 %/m in the horizontal and 1.0 %/m in the vertical plane, close to the target range. These slightly different values in size and focus slippage to the targeted ones are mainly attributed to the set constraints in the optimization, like the length or maximum divergence. However, the parameters are in the parameter range that was aimed for. The slightly smaller size in the vertical plane is not expected to have a negative impact on the FEL performance, see section 4.5.1.

Overall, the beam remains at about $200\,\mu m$ on average in transverse size with a divergence near 0.1 mrad in the longer drift sections, and up to 0.3 mrad in the shorter drifts between the closely spaced quadrupoles of the individual doublets and the quintet. The beam size in the first dipole magnet of the chicane is kept at about $120\,\mu m$, mitigating the effects of CSR-induced emittance growth, see section 3.6.5.

Hence, this optimized setup fulfills the main requirements: low divergence during transport, sufficiently small beam size in the chicane's first dipole, and implementation of chromatic focusing in the undulator. It is therefore adopted as the baseline layout of the *LUX* beamline.

5.3 Beamline Components and Diagnostics at LUX

Building on the optimized layout, the *LUX* beamline has to accommodate the components discussed above, as well as correction elements for beam alignment and diagnostics to characterize both the electron beam and the undulator radiation. The full setup is shown in fig. 5.3. It contains a total of 13 quadrupoles. Two additional quadrupoles after the undulator refocus the beam into a permanent-magnet electron spectrometer at the beamline end. Another electromagnetic spectrometer is installed earlier, after only a few meters of transport. A dark-current and charge monitor is placed upstream of this first spectrometer. A total of 10 corrector dipoles are used. 4 are located after the initial doublet and allow to steer beams exiting the plasma at an angle back onto the nominal axis, 4 more are placed after the chicane to correct any residual dispersion or kick due to chicane magnet errors, and 2 are installed directly before the undulator to steer the beam through the undulator. The chicane is a 4-dipole C-chicane, as considered in section 3.4, with a collimator at its center to possibly remove particles at large transverse offsets or with large energy deviations.

To measure transverse beam profiles, 6 screens are distributed along the beamline. 4 of them are preceded by beam-position monitors (BPMs) that measure the charge and the beam's centroid position. 2 BPMs are installed immediately before and after the *FROSTY* undulator to track the beam's position and angle. Finally, a radiation spectrometer for the extreme ultraviolet (EUV) range is mounted at the end of the beamline to measure the undulator radiation. An overview of these components is given in table 5.2, and their individual properties are detailed in the following subsections.

Table 5.2: Installed components at LUX and their center positions in the beamline. Based on their position the components are categorized in one of three sections: The capturing section from the plasma target to the first electron spectrometer, the chicane section from the quadrupoles after the first spectrometer to the profile screen behind the chicane, and the undulator section from the quintet to the end of the beamline. Used abbreviations: Quad. = quadrupole, Cor. H. = horizontal corrector, Cor. V. = vertical corrector, e^- -Spec. = Electron Spectrometer, Dip. = Chicane Dipole.

Capturing Section		Chican	ne Section	Undulator Section	
Component	Position (mm)	Component	Position (mm)	Component	Position (mm)
Source	0	Quad. 5	7169	Quad. 7	13669
Quad. 1	151	Quad. 6	7670	Quad. 8	14169
Quad. 2	352	BPM2	8187	Quad. 9	14668
Cor. H. 1	552	Screen2	8611	Quad. 10	15169
Cor. V. 1	739	Dip. 1	9320	Quad. 11	15668
Cor. H. 2	2109	Dip. 2	9820	BPM 3	16191
Cor. V. 2	2307	Collimator	10500	Cor. V. 5	16464
BPM 1	2655	Screen3	10796	Screen 4	16609
Screen 1	3160	Dip. 3	11546	Cor. H. 5	16919
Quad. 3	3623	Dip. 4	12046	Undulator	18526
Quad. 4	4122	Cor. H. 3	13206	BPM 4	20417
DCM	4472	Cor. V. 3	12660	Quad. 12	20908
e^- -Spec. 1	4990	Cor. H. 4	12756	Quad. 13	21259
		Cor. V. 4	12855	Screen 6	21598
		Screen 4	12955	e^- -Spec. 2	22317

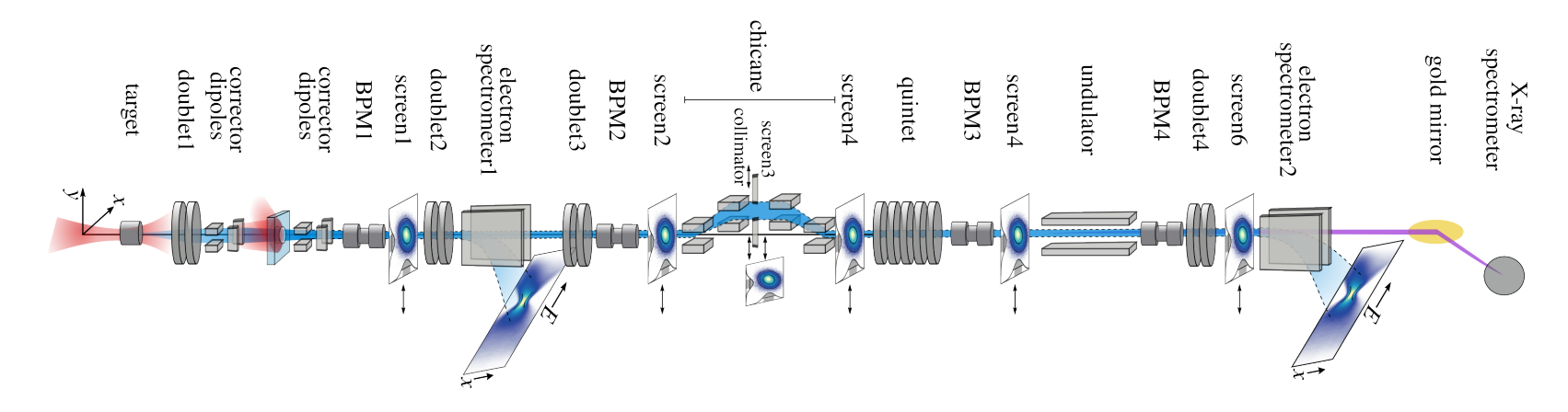
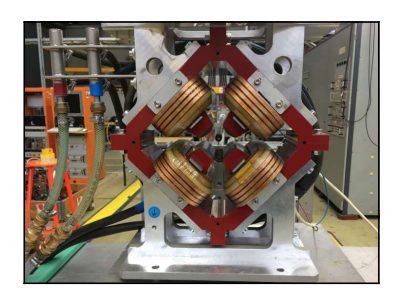


Figure 5.3: Schematic *LUX* beamline layout with all components and diagnostics shown. Modified figure, original by P. Winkler.

5.3.1 Quadrupoles



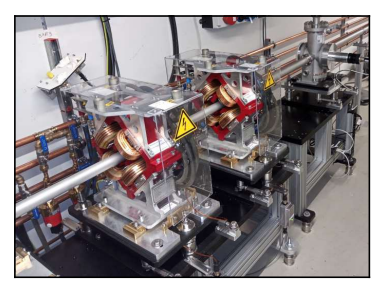


Figure 5.4: Photos of quadrupoles of the type installed as third to eleventh magnet for the beam transport. Left: Measurement setup with Hall Probe Right: Third doublet installed before the chicane.

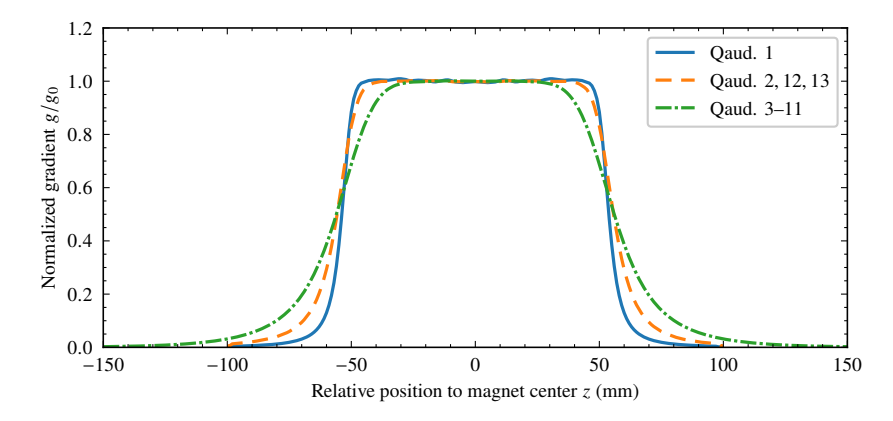


Figure 5.5: Measured profiles for the (blue, solid) quadrupole magnet 1 (orange, dashed) quadrupole magnets 2, 12, 13, and (green, dash-dotted) quadrupole magnets 5–11 used at *LUX*.

To provide beam capture, transport, and transverse shaping of the beams at *LUX*, three types of quadrupole magnets are used. In the region immediately following the plasma target, where the beam is initially small but highly divergent, high field gradients are necessary. Because adverse effects on emittance and slice properties can accumulate over longer drifts, see section 3.6, this initial capture has to happen as early as possible in the beamline.

For this purpose, two magnet types are used, each with a geometric length of 10 cm and small bore radii of 6 mm and 11 mm, respectively, providing gradients up to 180 T/m and 70 T/m. The remaining quadrupoles, also of only 10 cm length, have a larger 20 mm radius to accommodate wider beam pipes for improved transmission.

Measured field profiles for all three magnet types, obtained using a Hall probe, are shown in fig. 5.5. From these measurements, the classical and modified effective lengths, eqs. (3.58) and (3.59), are determined for use in tracking and optimization. The achievable peak gradients per applied current

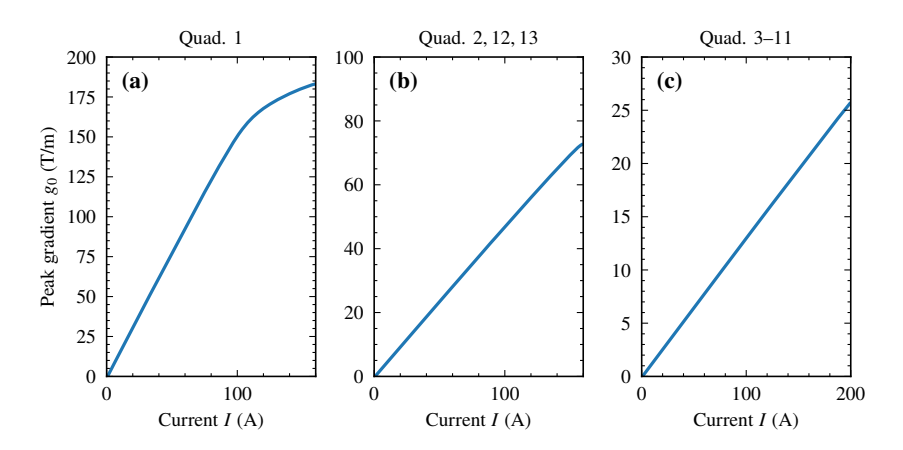


Figure 5.6: Measured relation between applied current I and peak gradient g_0 for the (a) first, (b) second and last two, and (c) first, all other quadrupole magnets used at LUX.

	Quad. 1	Quad. 2, 12, 13	Quad. 3–11
Yoke length (mm)	102	102	100
Bore radius (mm)	6	11	20
Max. current (A)	160	160	200
Max. peak gradient g_{max} (T/m)	180	70	23
Effective length L_{eff} (mm)	110.5	115.6	118.3
Mod. effective length $L_{\text{eff,S}}$ (mm)	112.8	121.1	134.7

Table 5.3: Properties of quadrupole magnets used at *LUX*.

set in the experiment are depicted in fig. 5.6 (a)-(c). Because of technical limits, the current in the first two quadrupoles is restricted to 160 A, which is sufficient to capture electron energies up to approximately 500 MeV. In principle, the remaining quadrupoles can be driven up to 300 A, but the available power supplies provide only 200 A. Consequently, the same energy limit applies throughout. In this range, only the first quadrupole shows saturation above 100 A or 160 T/m. A summary of these magnet properties is given in table 5.3.

5.3.2 Chicane Dipoles

The chicane dipole magnets were designed to provide a large tunable range of R_{56} over the expected energies at LUX, while maintaining a compact overall length of the chicane. At least a $R_{56} \simeq -1$ mm was targeted for energies that can be transported by the available quadrupoles, with additional margin towards higher values. Existing HERA CV/CH dipole magnets were modified for this purpose. After reducing their gap to 20 mm, their effective field length is approximately 350 mm. With a minimum center-to-center distance of 500 mm between dipoles, the overlap of their fringe fields occurs only where the field amplitude falls to less than 5 % of its peak, making the resulting cross-talk negligible

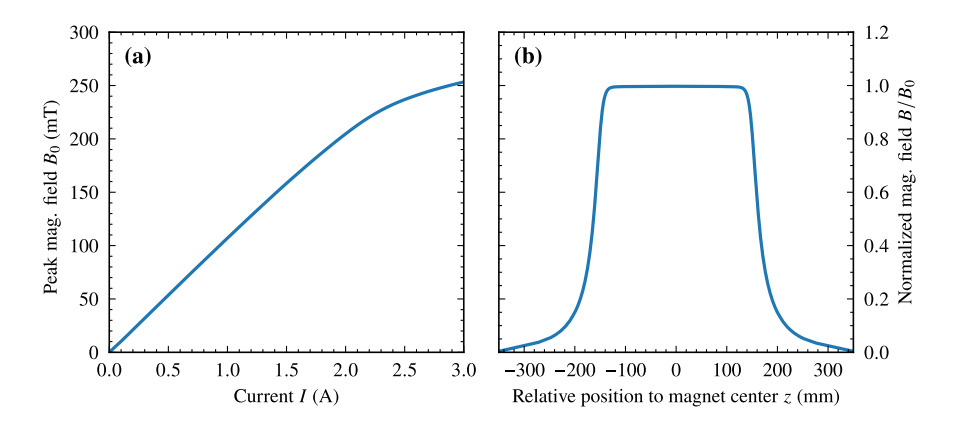


Figure 5.7: (a) Peak magnetic field g_0 of chicane dipole magnets dependent on the applied current and (b) field profile of chicane dipole magnets.

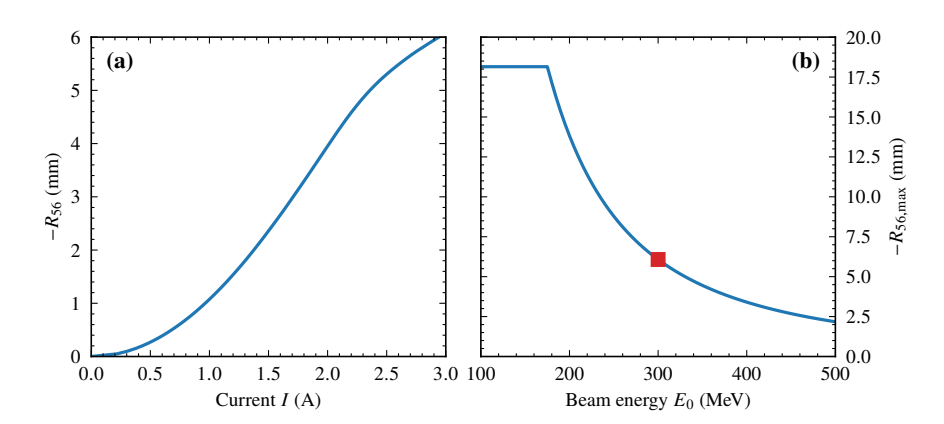


Figure 5.8: (a) R_{56} dependent on the applied current for a 300 MeV beam. The quadratic increase is reduced by saturation effects in the magnets toward higher currents. (b) Maximum (absolute) R_{56} in the chicane. Magnet pole width and apertures limit the value at energies below 180 MeV. Maximum value of the left plot is indicated by a red square.

for the intended purpose. Magnet dimensions and spacing considerations show that a kick angle of about 50 mrad, corresponding to 240 mT peak field at 500 MeV, is required to achieve the desired range of R_{56} . This field is reached by reducing the magnet gap to 30 mm.

Figure 5.7(a) displays the peak field dependence on the applied current, while fig. 5.7(b) shows the measured field profile. Saturation effects set in starting at approximately 2 A. For the reference energy of 300 MeV , a theoretical maximum kick angle of 90 mrad is thus possible, providing $R_{56} \simeq -6$ mm. This corresponds to a maximum decompression factor of $n_B \simeq 30$ for an initially 2 µm long beam. The resulting relationship between R_{56} and the magnet current at 300 MeV is plotted in fig. 5.8(a). At the maximum setting, the horizontal beam displacement at the chicane center is about 45 mm. The pole width and vacuum chamber are dimensioned to accommodate offsets up to 80 mm.

Table 5.4: Properties of chicane dipole magnets used at *LUX*.

Yoke length (mm)	Effective length (mm)	Full gap (mm)	Max. peak B_0 (mT)
300	350	30	255

For the anticipated decompression of about $n_B \gtrsim 3$, corresponding to $R_{56} \simeq -500\,\mu\text{m}$, a kick angle of approximately 25.5 mrad is required, which corresponds to the value used for CSR estimations in section 3.6.5. The maximum achievable (absolute) R_{56} for given energies is shown in fig. 5.8(b). At energies below 180 MeV the limit arises from the maximum allowable horizontal displacement, whereas at higher energies the limitation is set by the available magnet current.

A summary of the dipole parameters and their performance is provided in table 5.4.

5.3.3 Corrector Dipoles

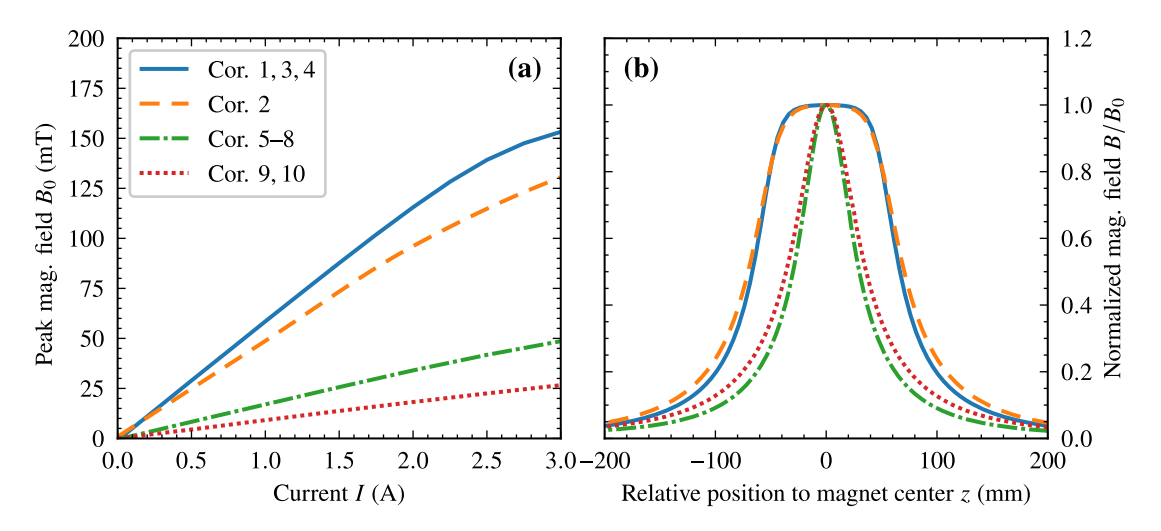


Figure 5.9: (a) Measured dependence of peak field on applied current and (b) field profiles for the corrector dipole magnets: (blue, solid) correctors 1, 3, 4, (orange dashed) corrector 2, (green dash-dotted) correctors 5–8, and (red dotted) 10 and 11.

Corrector dipoles are installed to steer the beam back to the nominal axis when offsets arise from factors such as initial beam pointing, magnet misalignment, or ambient fields. 4 correctors are placed after the capturing quadrupole to compensate horizontal position and angle, 4 are positioned behind the chicane to correct any residual dispersion or misalignment, and 4 are located just upstream of the undulator to fine-tune the beam trajectory through it.

The peak fields as functions of the current and the field profiles were measured and shown in fig. 5.9(a)–(b). In standard operation, the beamline should be configured such that these correctors are rarely needed. A summary of their properties is provided in table 5.5.

	Yoke length (mm)	Effective length (mm)	Full gap (mm)	Max. peak B_0 (mT)
Cor. 1, 3, 4	100	165	40	160
Cor. 2	100	175	50	130
Cor. 5 – 8	20	90	40	40
Cor. 9, 10	20	110	50	25

Table 5.5: Properties of corrector dipoles at LUX.

5.3.4 Spectrometers

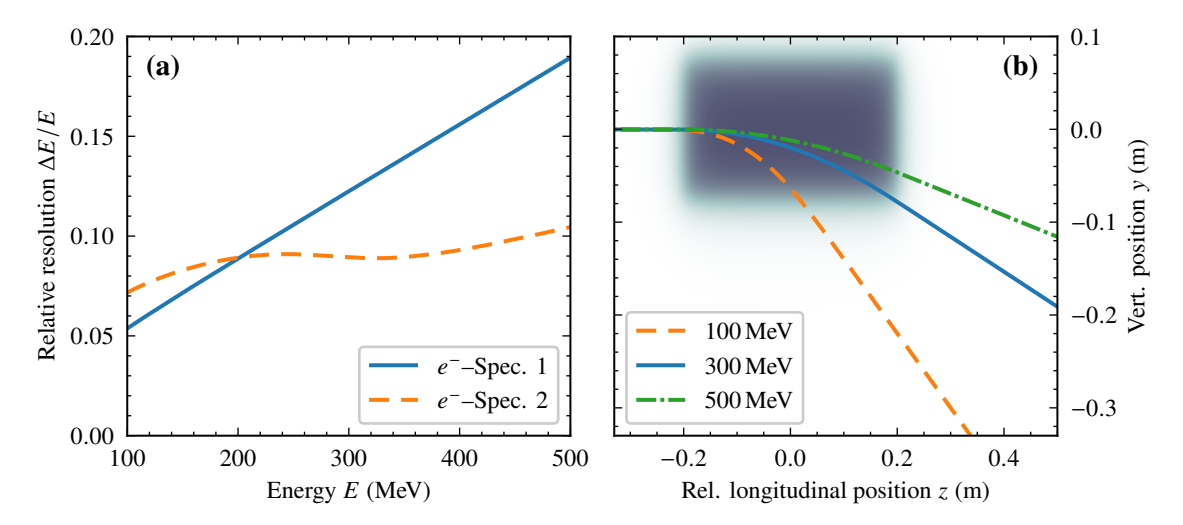


Figure 5.10: (a) Relative resolution dependent on the electron energy for (blue, solid) the first spectrometer and (orange, dashed) the second spectrometer. (b) 2D field map of central (y-z)-plane for the second spectrometer with trajectories of (orange, dashed) 100 MeV, (blue, solid) 300 MeV, and (green, dash-dotted) 500 MeV leaving the spectrometer magnet through the fringe field at the bottom or rear edge.

To measure the energy and the energy spread of the electron beams, 2 electron spectrometers are installed in the *LUX* beamline. The first spectrometer, using an electromagnetic dipole, is located about 5 m behind the plasma source for measurements without utilizing the full beam transport. It is used to optimize the electron beams from the plasma targeting low energy spread, small mean energy jitter, and high charge. After tuning the laser to achieve the desired electron beam properties, this spectrometer is switched off to transport the beam further downstream the beamline to the undulator and finally to the second spectrometer at the end of the electron beamline. The second spectrometer allows to correlate the properties of the radiation emitted from the undulator to the electron properties on a shot-to-shot basis. Both spectrometers deflect and disperse the beam vertically, mapping the energy onto a positional offset on a scintillating screen, which is then recorded by a camera. They

Table 5.6: Properties of spectrometer dipoles at *LUX*.

	Yoke length (mm)	Full gap (mm)	Max. peak B_0 (mT)
e^- -Spec. 1	500	55	245
e^- -Spec. 2	400	40	950

provide relative resolutions of about 0.1 % at the typical beam energy of 300 MeV, determined by the amount of dispersion, the granularity of the screen material and the camera resolution. The dependence of the resolution on the beam energy is shown in fig. 5.10(a).

Basic properties of the spectrometer dipoles are listed in table 5.6. Dependent on their energy, electrons take different paths through the spectrometer and either exit the spectrometers at the rear or bottom edge, passing through extended regions of fringe fields. This is illustrated in fig. 5.10(b). Along these paths, the respective fractions of the beam experience either focusing or defocusing effects, therefore a normal dipole transport matrix is not sufficient to describe the orbit. Instead, matrices for each energy are derived by fitting tracked particle distributions. A detailed description of the spectrometers and the calculation of their matrix elements is provided in previous work [48, 91].

5.3.5 Charge and Beam Position Measurement

In the LUX beamline the beam position can be measured in two different ways. The first is by means of transverse profile screens, which additionally offer the ability to measure the transverse extent and shape of the beam at a resolution of about 30 µm per pixel. However, such a screen blocks the electron beam and therefore cannot be used as diagnostics simultaneously to operating the undulator. The second method is the use of cavity beam position monitors (BPMs) [168], which provide a non-invasive measurement. As the beam traverses the cavity, the TM_{01} and TM_{11} modes are measured, providing a signal proportional to the bunch charge and transverse positions. However, they cannot measure the beam size or profile. Therefore, both are used in combination to measure the charge and transverse beam properties along the beamline. In addition, a charge monitor is installed in front of the first spectrometer.

The BPMs and profile screens are positioned along the beamline to measure position and charge of the beams at crucial positions. Most importantly they are placed in front and behind the undulator, to be able to measure and correct the trajectory through the undulator. The other two are installed behind the first doublet and correctors, to measure the charge from the plasma source after capturing the beam, and in front of the chicane, to be able to correct the trajectory through the chicane and detect charge losses during the beam transport.

Four of the six screens are positioned behind the four BPMs, to also be able to measure the transverse beam size and calibrate both devices against each other. With the known pixel size of the screen, the linear response of the TM_{01} and TM_{11} signals of the BPM and hence the position measurement is calibrated, and the zero reading of the BPM is used to locate the center position of the screen.

⁶ A dark current monitor with integrated charge measurement.

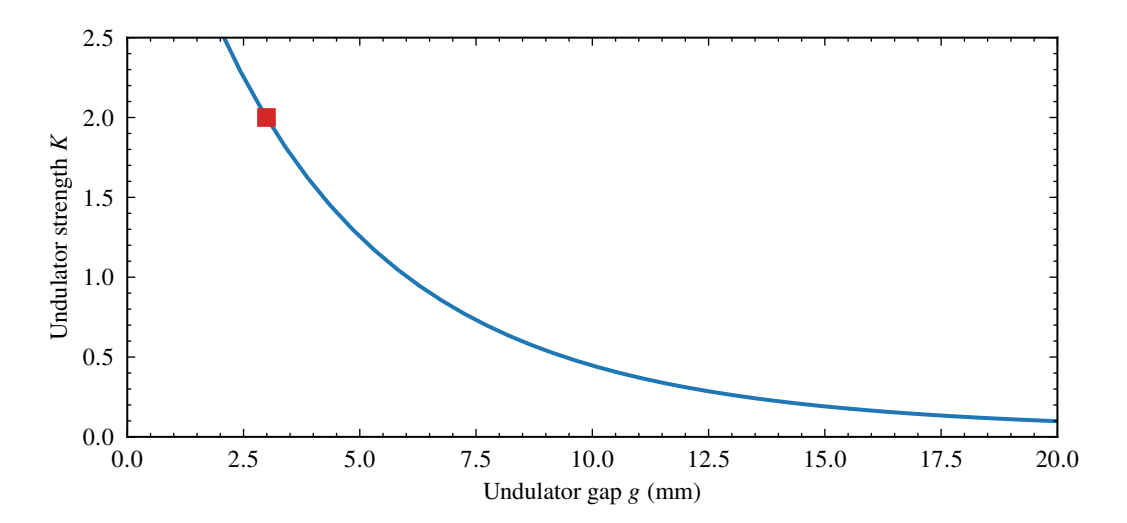


Figure 5.11: Strength parameter K for the FROSTY undulator dependent on the gap. (red, square) A K of 2 is achieved with a gap of 3 mm.

5.3.6 Undulator

Design and construction of the *FROSTY* undulator was done by M. Trunk. Only a few aspects relevant to the FEL are addressed here and detailed information is given in [114].

FROSTY, initially designed as a cryogenic undulator, has a period length of $\lambda_u \simeq 15.08$ mm with variable gap and taper. At room temperature, it can reach a magnetic peak field of $B \simeq 1.81$ T, corresponding to a K of 2.55, at a gap of 2 mm. The magnetic good field region, with relative peak field deviation less than 10^{-3} , was found to be of size of about ± 900 µm horizontally and ± 140 µm vertically [114].

Undulator Peak Field

The on-axis peak field of a planar undulator is described by an exponential function of the form [106]

$$B_0(g) = a \exp\left(b\left(\frac{g}{\lambda_u}\right) + c\left(\frac{g}{\lambda_u}\right)^2\right) \quad , \tag{5.3}$$

where g is the undulator gap and a, b, c are parameters dependent on the undulator that have to be determined. They were obtained from a fit to data taken at various gaps to be [114]

$$a = 3.007$$
 $b = -3.944$ $c = 0.833$. (5.4)

The corresponding undulator strength is shown in fig. 5.11. For a targeted value of K=2, the undulator gap has to be set to $g \simeq 3$ mm. There, a change in K of 1% corresponds to a difference in gap of 26 µm. In principle the gap can be increased or decreased in steps of 0.13 µm, which is the resolution

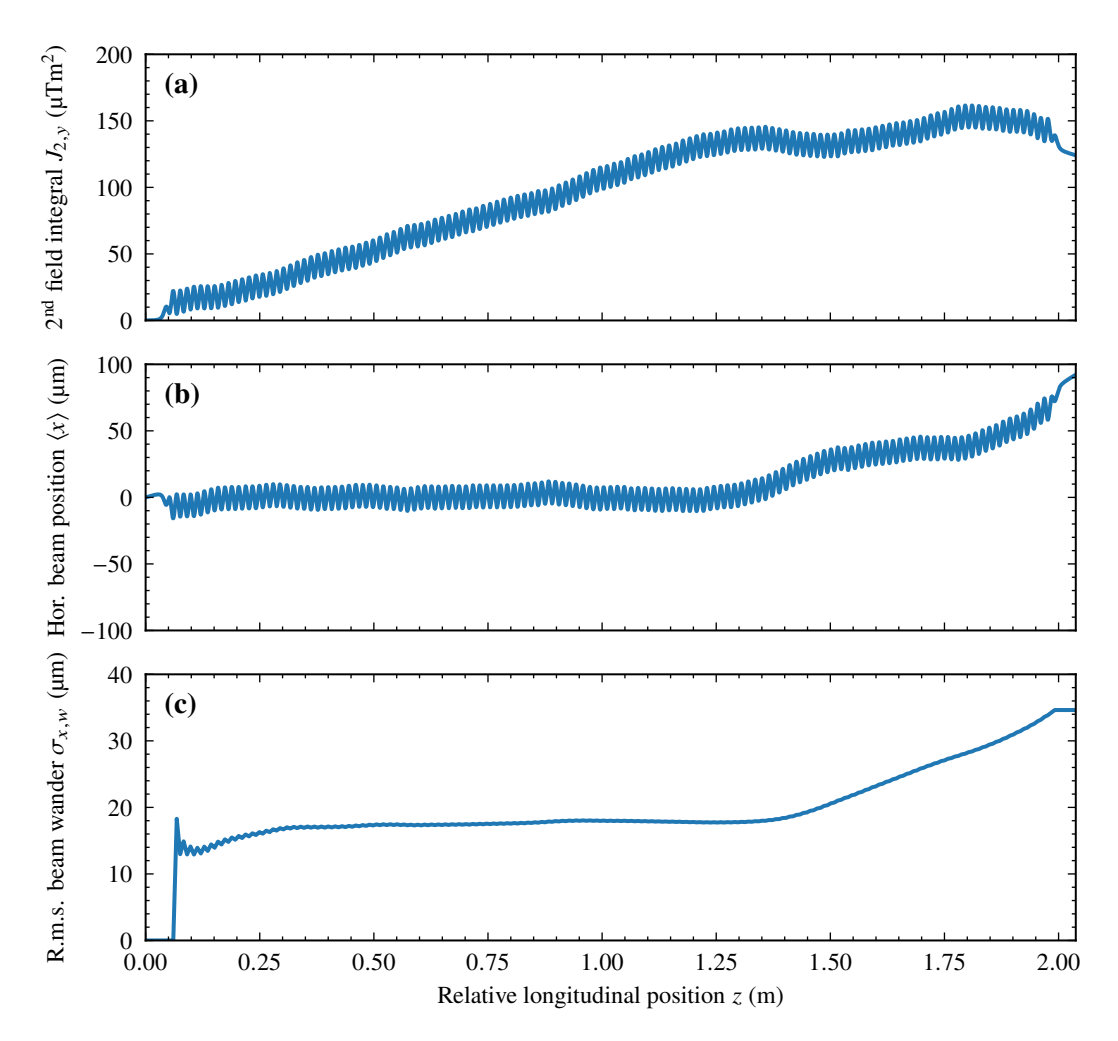


Figure 5.12: (a) Second field integral of the measured horizontal magnetic field of the *FROSTY* undulator. (b) Corresponding average horizontal electron movement for an energy of 300 MeV. A pointing of $-80\,\mu\text{rad}$ at the undulator entrance was chosen such that the average motion up to the local kick at 1.3 m is about the central axis of the undulator. (c) Root mean square beam wander along the undulator.

of the step motors driving the gap. However, the accuracy is limited by the gap measurement systems [169] and was determined to be approximately $3.2 \,\mu m$ [114]. Therefore, the undulator strength can be set to approximately $0.13 \,\%$ accuracy. The gap measurement systems are mounted $1.87 \,m$ apart, close to the entrance and exit of the undulator. Therefore, changing the gap at only one side of the undulator, the taper can be set in steps smaller than $0.1 \,\%/m$. Consequently, both the targeted K and taper can be set precisely to the targeted values of 2 and $1.3 \,\%/m$ respectively, as used in the previous chapter. Further it is possible to scan the taper about this value to tune it to an optimum value in the experiment.

Transverse Field Quality

After having determined the accuracy of K and taper, the field profile and connected to that the field quality is of main interest. As outlined in section 4.4.4 it can be used to estimate the influence of the real field properties on the FEL process. The field was tuned for low field errors at a K=2 and the corresponding field measurements were performed and reported in [114]. A constant offset in the field magnitude, originating from the amplification of background fields in the poles, is compensated by a Helmholtz coil built around the undulator chamber. It removes a quadratic contribution to the second field integral and therefore reduces the corresponding beam wander. The second field integral of the vertical field component, i.e. the main component, of FROSTY, measured in the accelerator tunnel, is shown in fig. 5.12(a). The change in the slope in the second field integral at about 1.3 m appeared after installing the periodic magnetic structure into the vacuum chamber after the field was tuned. The corresponding horizontal motion of the electrons with an energy of 300 MeV is shown in fig. 5.12(b). An entrance angle of 80 μ rad was used to keep the electron motion about the design axis at the center of the undulator.

For *FROSTY*, the phase shake was determined to be about $\sigma_{\Phi} \simeq 11^{\circ}$ [114]. This results in an estimated increase in gain length of about 2 % from the phase mismatch to the light field according to eq. (4.77), and is therefore negligible compared to the phase spread contributed by the energy spread of the electron beam. However, the local kick at 1.3 m imprints an average transverse motion onto the electron beam, then moving at an angle of about 80 µrad to the central axis and being displaced by about 60 µm at the end of the undulator. The corresponding root mean square beam wander, plotted in fig. 5.12(c), increases from about 15 µm, originating from the wiggling motion, to 35 µm at the end of the undulator. Considering the beam wander limit from eq. (4.79) and the debunching effect from eq. (4.73) for the optimized FEL case, the gain length is expected to double. To the end of the undulator, the horizontal displacement is about one beam radius $\sigma_x \simeq 35 \,\mu\text{m}$. Nevertheless, this only happens at the end of the undulator, losing only about one gain length over the whole 2 m length of the undulator compared to an ideal undulator. To account for these effects, the measured undulator field profile is compared to an ideal field for the FEL simulations in chapter 6.

Note, that the beam wander limit requires the horizontal beam size in *FROSTY* to be at least $\sigma_x \simeq 10 \, \mu m$ up to the local kick at 1.3 m and at least $\sigma_x \simeq 20 \, \mu m$ for the remaining undulator length. For smaller beam sizes the beam and radiation would not sufficiently overlap and the FEL process stops.

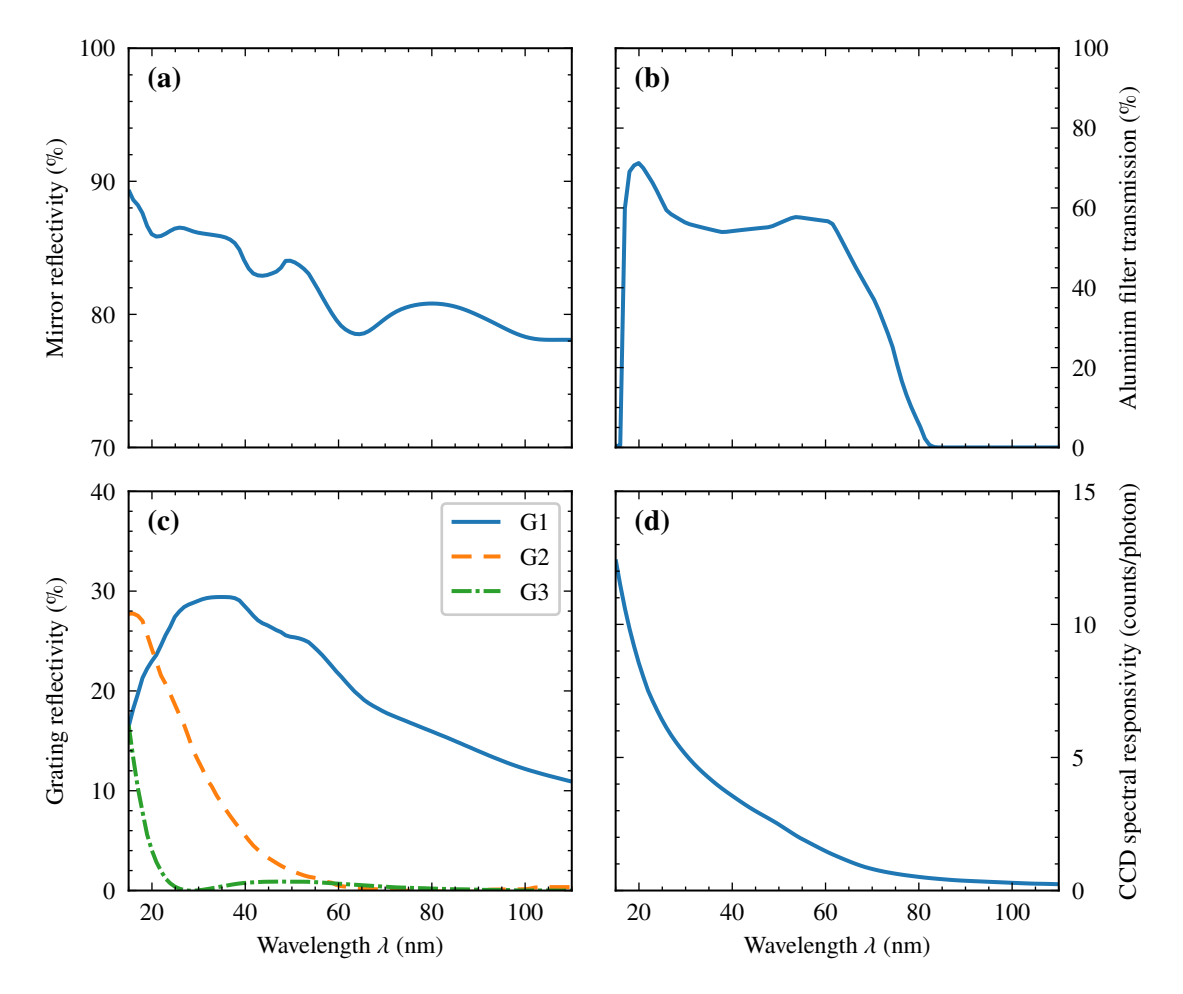


Figure 5.13: Efficiencies of the EUV spectrometer components dependent on the wavelength. (a) Reflectivity of the gold mirror. (b) Transmission of $250 \, \mathrm{nm}$ aluminum filter [112]. (c) Grating reflectivity to the (blue, solid) first, (orange, dashed) second, and (green, dash-dotted) third diffraction order G1-G3. (d) CCD camera spectral responsivity. Figures (a),(b),(d) adapted from [114].

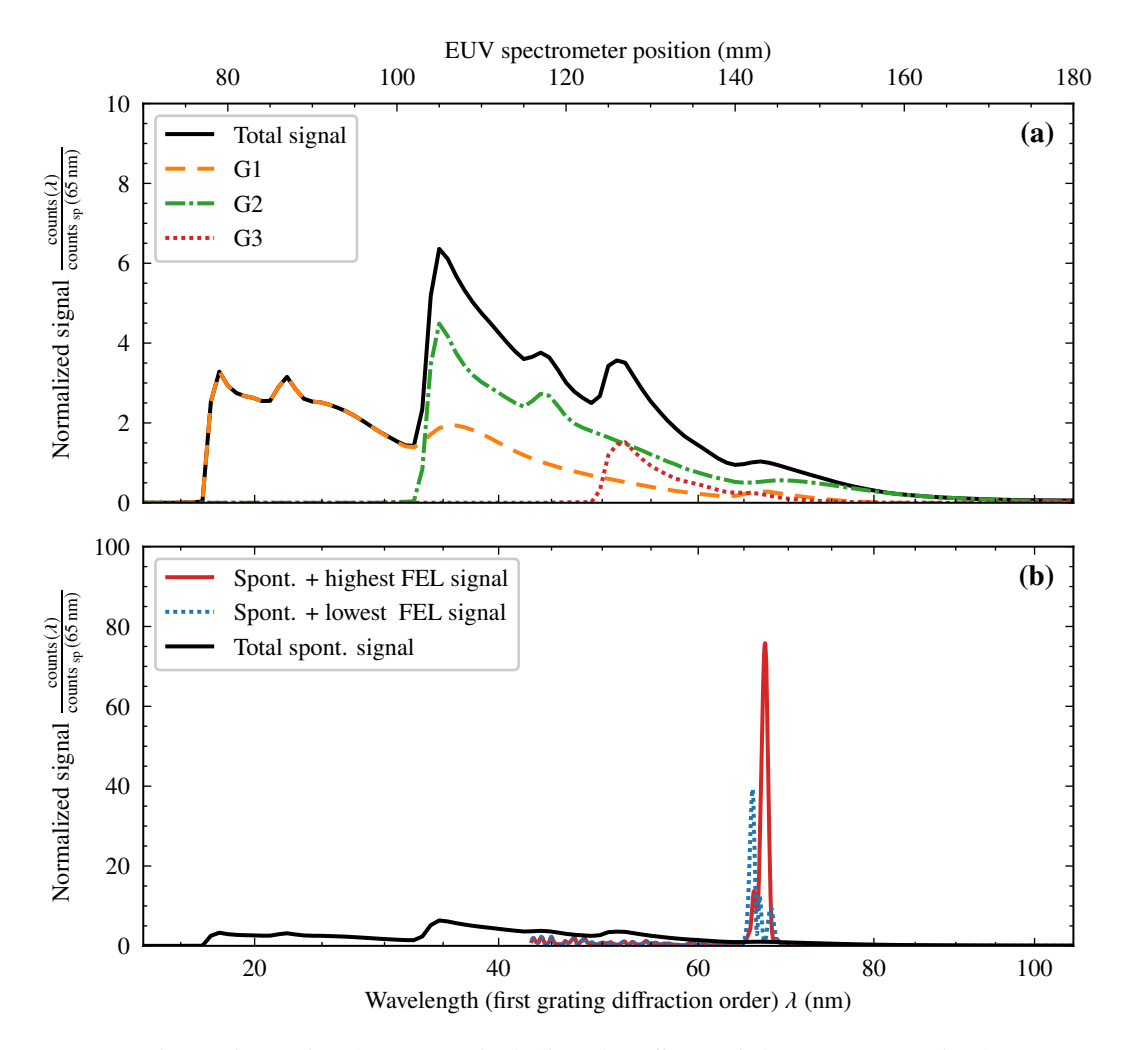


Figure 5.14: Signal on CCD including the effects of the components in the EUV spectrometer at LUX. Wavelength corresponds to the position in the image plane of the first diffraction order of the grating. Signal is normalized to the counts of the total spontaneous radiation in the first three diffraction orders of the grating at 65 nm (a) Spontaneous undulator radiation for (orange, dashed) first, (green, dash-dotted) second, and (red, dotted) third diffraction order G1-G3. (Black, solid) their combined signal. (b) Total signal for undulator radiation (same is in (a)) and FEL signal for the (red, solid) highest signal and (blue, dotted) lowest signal from 5 simulations. Raw spectrum shows same photon count for wavelength ranges of only spontaneous undulator radiation. Lower signal level in the FEL case comes from the absence of lower wavelengths in the simulation and their higher diffraction orders.

5.3.7 Undulator EUV Radiation Spectrometer

The beamline and the *FROSTY* undulator are designed to show the startup of an FEL, but not saturation. Therefore, the FEL signal is expected to be only a small factor larger than the spontaneous undulator radiation. As already seen from the estimations in section 4.6 (and shown later with the full transport in section 6.4), the FEL signal, considering all wavelengths, is expected to be only about one order of magnitude larger than the background. To improve this ratio to about two orders of magnitude, a spectrally resolved measurement about the fundamental wavelength with resolution better than the FEL bandwidth after the 2 m undulator (see eq. (4.48)) is required. The wavelengths expected at LUX are in the extreme ultraviolet (EUV) range. They range from about 20 nm, for electron energies of $350 \, \text{MeV}$ at a undulator K = 0.5, to $130 \, \text{nm}$, for $250 \, \text{MeV}$ at the maximum K = 2.55. At the tuned $K = 2 \, \text{and}$ typical beam energy of $300 \, \text{MeV}$ the fundamental wavelength is $65 \, \text{nm}$.

Efficiencies

To detect the FEL signal within this range, a EUV radiation spectrometer is installed at LUX. The radiation from the undulator is collected by a toroidal gold mirror onto a diffraction grating and from there dispersed onto a CCD camera. For best resolution, the setup images the exit of the undulator, where most FEL radiation is generated, onto the camera chip. In this setup, the CCD chip of $13 \times 13 \text{ mm}^2$ at 1024×1024 pixel can cover a range of 11.7 nm at a resolution of 0.01 nm [114]. To cover the full wavelength range, the camera can be moved from the on axis position to 120 mm, where 120 nm are still detectable. However, to block any signal from the LPA drive laser while being able to detect the EUV radiation, a 250 nm aluminum foil is installed, which limits the transmission window to the range from 17 nm to 80 nm.

The efficiency curve for the gold mirror, the transmission of the aluminum filter, the grating reflectivity for the first three diffraction orders, and the CCD spectral responsivity are shown in fig. 5.13(a)–(d) respectively. The camera signal including all the above contributions for a spontaneous undulator radiation spectrum, obtained with the synchrotron radiation code *SPECTRA*, was calculated and is shown in fig. 5.14(a) for all three diffraction orders and their combined signal. Note, that the individual diffraction orders are reflected at different angles and are therefore mapped to different positions in the image plane. Therefore, the diffraction orders overlap at the same position for different wavelengths. All signals are normalized to the total signal at the position of the fundamental wavelength at about 65 nm. Due to the broad spectrum and the higher spectral responsivity and the higher efficiency of the higher diffraction orders at lower wavelengths, peaks larger than the signal of the fundamental can be seen at 17 nm, 34 nm and 51 nm. Further, the signal from the higher diffraction orders is expected to overlay the signal at 65 nm.

Detection of FEL Signal

In addition the signal from the SVEA FEL simulations performed with *SIMPLEX* in section 4.6 is shown in fig. 5.14(b). The used beam, stretched by $n_B \simeq 3$, a constant beam size of 35 µm, and a undulator with K = 2 and taper of 1.3 %/m, showed a power level of one order of magnitude over the

spontaneous undulator radiation for the full spectrum, and two orders of magnitude within a spectral window of $\pm 2\%$ of the fundamental. Here, the signal level will be compared including the effects of the LUX EUV spectrometer.

It was checked that the number of photons obtained for the spontaneous undulator spectrum is the same in *SPECTRA* and *SIMPLEX*, i.e. for all simulated wavelengths except the FEL signal, before applying the effects of the mirror, aluminum filter, grating, and CCD. Both spectra are normalized to the same value, the signal of the spontaneous undulator radiation at 65 nm. Note, that the higher diffraction orders from lower wavelengths are not included in the FEL simulation, due to only simulating a 50 % frequency window, i.e. the wavelength range of 45 nm to 130 nm. However, this does not impact the FEL signal level.

About the fundamental wavelength the signal on the CCD is about 40–80 times larger for the FEL cases than from the spontaneous undulator radiation alone.

Since the spontaneous undulator signal scales linearly with the charge, if the changes, the signal on the CCD changes by the same factor. Charge fluctuations therefore cause a charge fluctuation in the camera signal. Further the signal is subject to camera noise, for example thermal, shot, and read noise. Combined fluctuations from these in the signal from spontaneous undulator radiation of an electron beam in this setup were found to be on the order of a factor of 2 [114].

Consequently, a beam, that is properly stretched and focused into the 2 m undulator, and reaches FEL power levels of one order of magnitude over the spontaneous undulator radiation over all wavelengths, will show about a factor of ≥ 20 signal over the undulator radiation background in the spectrally resolved measurement with the EUV spectrometer at LUX.

5.3.8 Magnetic Background Field Compensation

Additionally to the desired magnetic fields from the dipole and quadrupole magnets, that were placed on purpose, the beam is influenced by any magnetic fields along beam path. Due to the percent-level energy spread of the laser-plasma accelerated electron beams and the 300 MeV beam energy, compensating those fields is relevant for *LUX*. The magnetic fields cause energy-dependent detours of the electron beam, which lead to undesired dispersion and potentially lower the performance of the chromatic matching scheme.

A major contribution has been identified to be the earth magnetic field with about $50\,\mu\text{T}$, see section 3.5.3, bending the beam trajectory over the whole transport. Further, the field can be influenced by material in the accelerator tunnel or its surroundings, therefore not being constant along the beam transport.

As possible local influences on the trajectory the magnetic holders for alignment devices were identified. They are used along the beamline for proper positioning of the components and their field amplitude follows a r^{-3} dipole law [170]. For those closest to the beam pipe, a local variation in the magnetic field of about $100\,\mu\text{T}$ to $200\,\mu\text{T}$ at the position of the beam pipe was measured, which would cause a kick of about $30\,\mu\text{rad}$. Consequently all magnetic holders close to the beam pipe were removed.

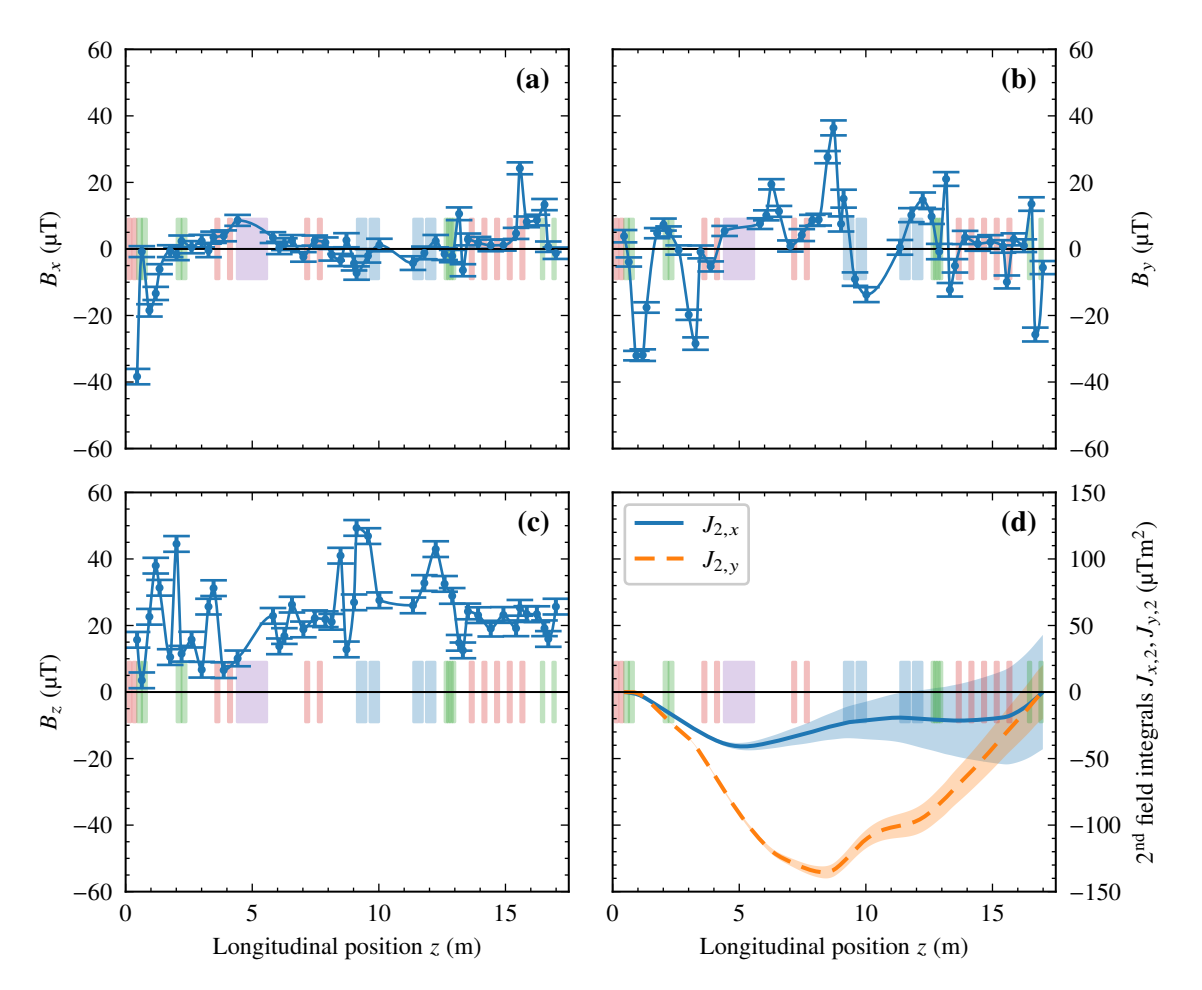


Figure 5.15: Magnetic background field along the accelerator for (a) the horizontal, (b) vertical, and (c) longitudinal field components. The horizontal and vertical field component are compensated with correction coils spanning the range 0.5 m to 17 m to minimize the (d) (blue, solid) horizontal and (orange, dashed) vertical second field integral at the last corrector before the undulator. Beamline lattice shown for (red) quadrupole magnets, (green) corrector magnets, (purple) electron spectrometer, and (blue) chicane dipoles.

To compensate the remaining magnetic background field in the accelerator tunnel, pairs of large rectangular Helmholtz coils were installed. One for each, the horizontal and the vertical field component. The longitudinal field component is not corrected, since its effect on the beam transport is small. The magnetic background field along the beam pipe was measured at 48 longitudinal positions for different currents applied to the compensation coils. The individual field components at the optimum coil current are shown in fig. 5.15(a)–(c). The remaining background field is not constant over the accelerator and also shows different compensation for the applied coil currents at some positions. This can be due to magnetizable material guiding the field. For example, the beam dump behind the first spectrometer at 5 m is known to contain such material.

The compensation coils are set such that the mean transverse beam positions are on axis in front of the undulator for a freely drifting beam after the initial capture with the first doublet. A residual mean beam pointing is compensated by the correctors installed directly in front of the undulator.

The second field integrals at the optimum compensation, which are proportional to the beam displacement, are shown in fig. 5.15(d). The trajectory of particles with an energy of 300 MeV defines the reference trajectory.

5.4 Conclusion

To shorten the gain length and increase the FEL signal, the initially percent-level energy spread beam is stretched in a decompression chicane, thus decreasing the uncorrelated energy spread. However, the expected gain with LUX parameters would not be sufficient to show significant signal above the spontaneous undulator radiation level. Therefore a chromatic focusing scheme is implemented, that uses the longitudinal sorting of the electrons by their energy to allow for a constant beam size at the position of the FEL radiation pulse. A setup that realizes such a focusing scheme has been designed and optimized. Further, the used focus slippage should benefit the startup of the FEL process in the short undulator.

The beamline setup features a total of 13 magnetic quadrupole lenses, of which 11 are used to transport the electron beam at a low divergence towards and to apply the focusing scheme into the undulator. A magnetic chicane allows for a decompression of a beam with an energy of 300 MeV up to $R_{56} \simeq -6$ mm. For a targeted decompression of about -0.5 mm in the chicane, the CSR effects are expected to be on a tolerable level, which is achieved by keeping the beam size small with the optics provided by the quadrupoles. Compensation coils to reduce the average magnetic background field are installed along the accelerator tunnel and 10 corrector dipole magnets provide the capability to tweak the trajectory, if required.

The beamline was built with additional diagnostics, including 6 screen stations, 4 non-invasive beam position monitors, 1 non-invasive charge measurement, 2 electron spectrometers, to characterize and control the electron beam, and an EUV spectrometer to measure radiation from the *FROSTY* undulator. Using beam parameters from *LUX*, the decompression and chromatic focusing scheme, power levels of one order of magnitude above the undulator radiation over all frequencies can be achieved. These pulses result in signal levels in the spectrally resolved measurement of 20–40 times larger than the undulator background and noise.

Consequently, the beamline setup is capable to demonstrate the startup of an FEL from the 2 m FROSTY undulator for the electron beam properties as provided by LUX.

Free-Electron Laser Simulations

For the correct simulation of the FEL interaction in the undulator the time-dependent 3D FEL code *Puffin* [171, 172] is used. Unlike many other codes, it does not apply the slowly varying envelope approximation, period-averaging of electron motion, or periodic slicing of the electron bunch. While codes incorporating some or all of these approximations describe most FELs accurately and agree well with experimental results from existing facilities [173, 174], they impose constraints on resolving sub-wavelength scale and short-bunch effects.

In contrast, *Puffin* can accurately model broadband radiation, the spontaneous background, coherent spontaneous emission potentially present at the bunch tail, and shot-noise effects over a broad frequency range. It self-consistently models the longitudinal dynamics of beams with large energy spread, enabling electron redistribution within the bunch over regions larger than the resonant wavelength. These capabilities are particularly important for laser-plasma accelerators like *LUX* and its decompression scheme, where the total energy spread is large and the mean energy changes rapidly along the bunch due to the energy chirp. Effects related to these properties are not captured by SVEA-based codes, making them less suitable for accurately simulating the FEL process with laser-plasma accelerated electron beams [156, 175].

The general setup and the preparation of the input beam are outlined in section 6.1. Simulation results are discussed in section 6.3 for an undulator without errors using the original *Puffin* code, and in section 6.4 for the measured *FROSTY* undulator field, employing a modified version of *Puffin* that allows for user-defined field profiles.

6.1 Beam Properties

The setup and beam optics described in the previous chapter was used to track the *LUX* reference beam to the undulator, accounting for decompression and the implemented focusing scheme. The tracking was performed with the particle tracking code *elegant* [83] with 1D CSR effects in the chicane (see section 3.6.5 for comparison). The beam was decompressed with a total R_{56}^{ζ} of 550 µm. The chicane was set for a kick angle of $\theta \simeq 25.5$ mrad contributing 500 µm to this value, and the

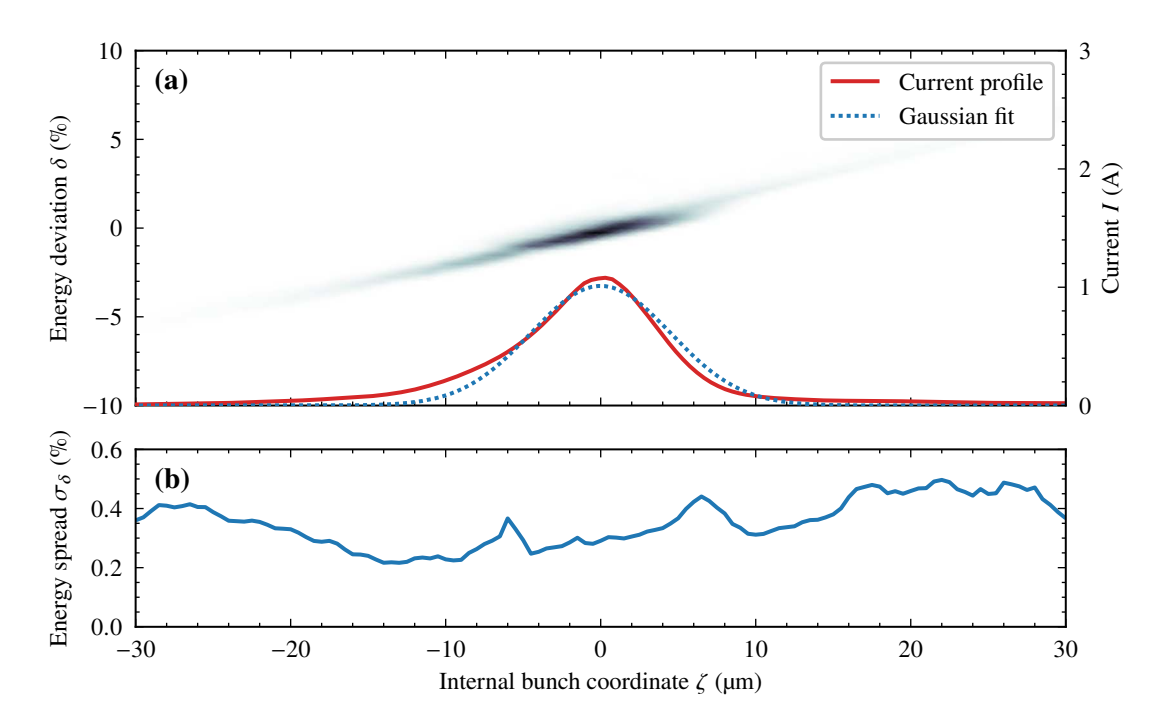


Figure 6.1: (a) Longitudinal phase space of the LUX reference beam after transport to the undulator entrance with a bunch stretching of $R_{56}^{\zeta}=550\,\mu\mathrm{m}$. The bunch is stretched to a bunch length of 5.3 $\mu\mathrm{m}$. The (red line) current profile peaks at about 1.1 kA and shows a slight asymmetry with higher currents towards the bunch tail compared to (blue, dotted) a gaussian fit. (b) Slice energy spread along the beam evaluated over a slice length of 1 $\mu\mathrm{m}$, matching the estimated cooperation length.

beamline itself contributes $L/\gamma_0^2 \simeq 50\,\mu\mathrm{m}$ due to time of flight differences. The resulting bunch length is $\sigma_{\zeta} \simeq 5.3\,\mu\mathrm{m}$ with a peak current of about $I_{\mathrm{peak}} \simeq 1.1\,\mathrm{kA}$, close to the estimations obtained from an equivalent gaussian shaped beam.

The longitudinal phase space and current distribution of the resulting beam are shown in fig. 6.1(a). The distribution is stretched with long tails towards the front and back of the bunch, which arises mainly from the path length difference of high and low energy particles in the chicane. Note that those high and low energy particles were initially located at the other sides of the bunch and overtook the bunch or fell back. Further, the beam shows a slight asymmetry with larger current towards the tail.

The slice energy spread along the bunch, presented in fig. 6.1(b), varies in the range of 0.25 % to 0.5 %. Here, a slice corresponds to the expected cooperation length of $L_c \simeq 1 \, \mu m$, assuming a gain length of 23 cm as estimated from the simplified SVEA simulations section 4.6. The slice energy spread at the core of the bunch matches the estimated 0.3 % from decompression of an equivalent gaussian beam. It is not spoiled in the process of decompression, since leading and trailing particles with large energy deviations passed through this region and are now located far to the head and tail. However, note that the initially large slice energy spread in the leading and trailing regions also causes two spikes in the slice energy spread of the transported beams at about $\zeta \simeq \pm 6 \, \mu m$.

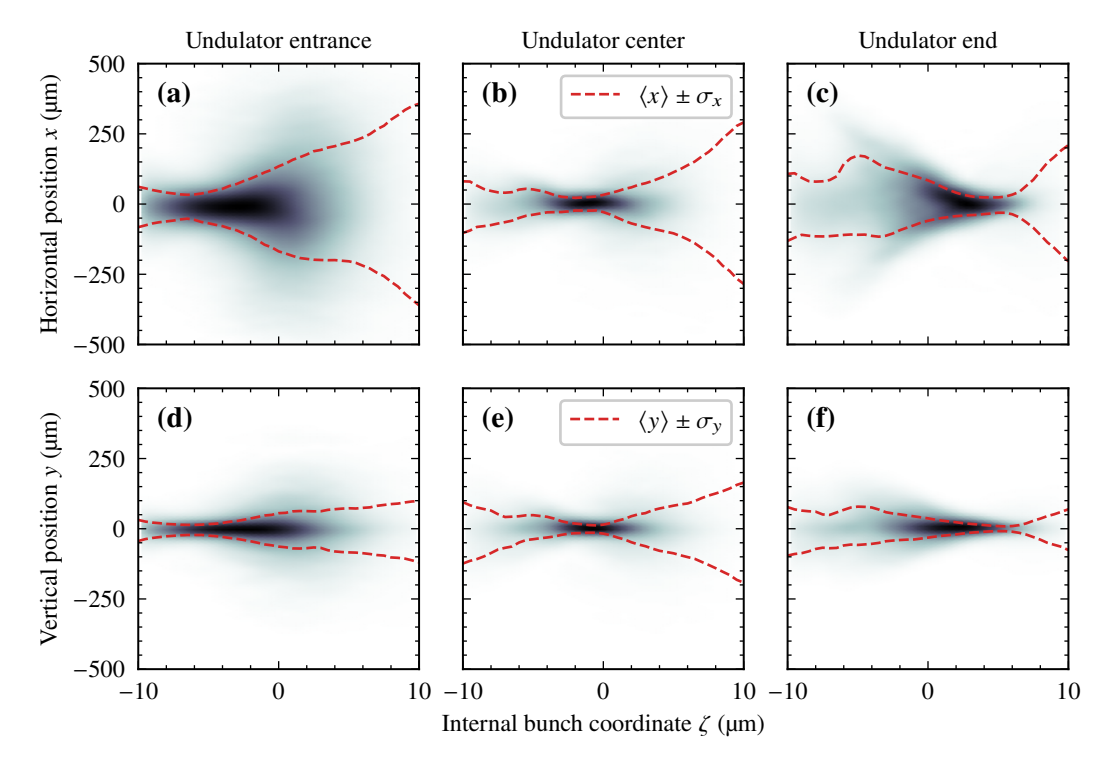


Figure 6.2: Transverse particle distribution along the bunch for (a)-(c) the horizontal plane and (d)-(f) the vertical plane. The focus position shifts towards the head in both planes from (a)+(d) undulator entrance, via the (b)+(e) undulator center to (c)+(f) undulator end. Additionally, the (red dashed) $\pm 1\sigma$ beam sizes about the mean values $\langle \cdot \rangle$ are shown. Asymmetries that originate from the initial beam and effects in tracking primarily affect particles at the head and tail $|\sigma_{\mathcal{L}}| \gtrsim 6 \, \mu \text{m}$, outside the core region.

The chirp over the whole bunch matches the estimated value of 2 000/m. However, at the core of the bunch it is slightly reduced to about 1 700/m, lowering the ideal estimated taper to about 1.1 %/m. This is also due to the redistribution of the particles within the bunch.

Still looking at longitudinal slices, the effect of the focusing scheme can be evaluated for the LUX reference beam. The transverse beam sizes along the bunch are shown in fig. 6.2(a)-(c) for the horizontal and in fig. 6.2(d)-(f) for the vertical plane at the undulator entrance, center and exit. The part of the beam, that has a deviation of about -1% from the design energy and is located at about $\zeta \simeq -\sigma_{\zeta}$, is focused at the undulator entrance and shows small transverse sizes. Similarly, the core and tail of the bunch are focused at the undulator center and end respectively. The spot sizes are about 31 µm in the horizontal and 15 µm in the vertical plane, again close to what was estimated from an equivalent Gaussian beam and in the region that is aimed for.

Due to the chromatic contributions to the emittance, which only vanish at a waist, see section 3.6.1 and [57], and minor contributions from CSR in the horizontal plane, the slice emittance along the bunch is also increased. Again, the width of slices is chosen to be of length L_c . In the horizontal plane, shown in fig. 6.3(a), it follows closely to the focusing scheme along the undulator, where the focused fraction

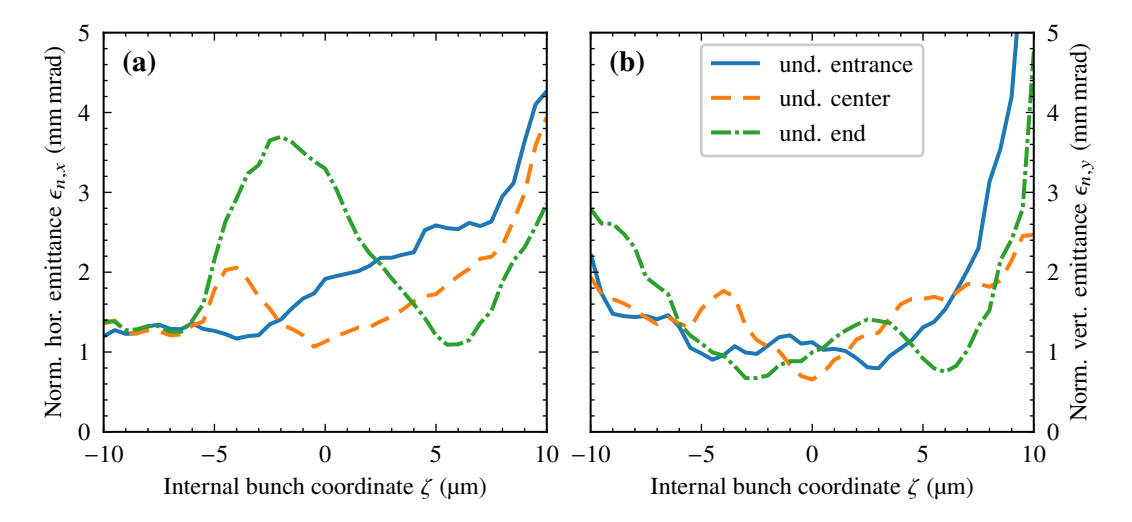


Figure 6.3: Normalized slice emittances along the bunch for the (a) horizontal and (b) vertical plane. It changes from (blue, solid) the undulator entrance, via (orange, dashed) the undulator center to (green, dash-dotted) the undulator end. Each slice is about the estimated cooperation length of $1 \, \mu m$.

of the bunch goes down to 1.1 mm mrad. In the vertical plane, shown in fig. 6.3(b), the situation is slightly more complex due to the natural focusing of the undulator. However, at the core of the bunch the normalized slice emittance stays at about 1 to 2 mm mrad over the whole undulator. Especially, the fractions that are intended to be focused at the very front or back of the undulator undergo a partial oscillation and show two minima. Note that the slice emittance can be smaller than the initial projected value of 1 mm mrad due to variations in the bunch.

For completeness, the projected normalized emittances of the full beam are

$$\epsilon_{x,\text{tot}} = 3.8 \text{ mm mrad}$$
 $\epsilon_{y,\text{tot}} = 1.2 \text{ mm mrad}$ (6.1)

As pointed out, this is expected and can be explained by the different energies in the beam intentionally not focused close together, but stretched and distributed over the whole undulator range with the focusing scheme. However, as the electrons only cooperatively interact within L_c , the slice quantities evaluated before are of more interest for the FEL interaction.

6.2 Simulation Setup

The beam that is obtained this way is not yet suitable to be used by an FEL code. The number of macroparticles in the initial beam is about 65000 and they conceivably fill the phase space unevenly. This is suitable for particle tracking, but the proper simulation of a FEL requires higher macroparticle counts. With low macroparticle number, there might be spurious coherent contribution to the radiation, resulting in an overestimation of spontaneous undulator radiation, shot noise and FEL signal [176].

Therefore, the distribution must be resampled to a higher macroparticle count and the electron shot-noise has to be properly modeled for the correct simulation of the startup of a SASE FEL. There exist different algorithms and realizations to achieve this [177–179], and is done here with the *Puffin* companion tool *JDF* [180], which implements the method described in [179]. Here, within each radiation wavelength, 20 slices of 800 macroparticles each, i.e. 16000 per λ_l , were placed and proper Poissonian shot-noise statistics and particle weights are added. The method consequently removes artificial shot-noise that is contained in the initial beam.

The processed beam has an increased macroparticle number that obeys the same statistical properties as the beam from particle tracking. For this case, each macroparticle in the resulting beam represents about 15 electrons on average. The resampling was performed with 10 different seeds for the random number generator in *JDF* to obtain beams with the same properties, but different shot noise. All simulations were performed for all 10 seeds and then averaged.

To avoid issues in the pre-processing and the simulation, for example a poor resolution, i.e. a too coarse grid, or a too large bounding box, the outer 0.1% of the charge was removed in all projections of the 6D distribution. These are typically macroparticles with low weight that increase the simulation volume without contributing to the simulation.

Note that Puffin does not employ any data reduction of the radiation field, but stores and calculates the electric field amplitude and orientation on a 3D grid. For the calculation of the power when writing the output, integration is performed with a trapezoidal rule. This can lead to a slight reduction in the calculated power, but affects all radiation equivalently. It was verified that this only results in the power value being scaled, but does not affect the simulation by any other means. Particularly, the ratio of the power from simulations with FEL interaction turned on and off is unaffected, therefore yielding the correct gain.

Further, *Puffin* has absorbing boundaries in the outer 8 grid nodes on each side implemented [181] to remove artificial reflections in the diffraction step [175]. This removes the fraction of the radiation that would travel outside the bounding box and decreases the energy in the simulation volume. This means that the simulation domain must be large enough to only affect the fraction of spontaneous undulator radiation that is emitted under a large angle and would not be detected in the experiment anyway, for example due to beam pipe apertures.

The simulations were consequently set up to have a reasonably large bounding box and a sufficient number of grid nodes to resolve the radiation field and the electron beam.

6.3 Simulation with Idealized Undulator Field

As a first step, to get the maximum possible gain, the FEL simulations were performed for an ideal sinusoidal undulator field. For this case, the undulator strength is K=2, has a period length of 15 mm and a taper of 1 %/m. It contains 130 undulator periods, and therefore the simulation stops at 1.95 m. The power curve is shown in fig. 6.4 and shows a clear increase in power above the spontaneous undulator radiation and growth beyond that level at about 1 m. The total power reaches values of about 2.5 GW. This is about 2 orders of magnitude larger than that obtained from the spontaneous undulator

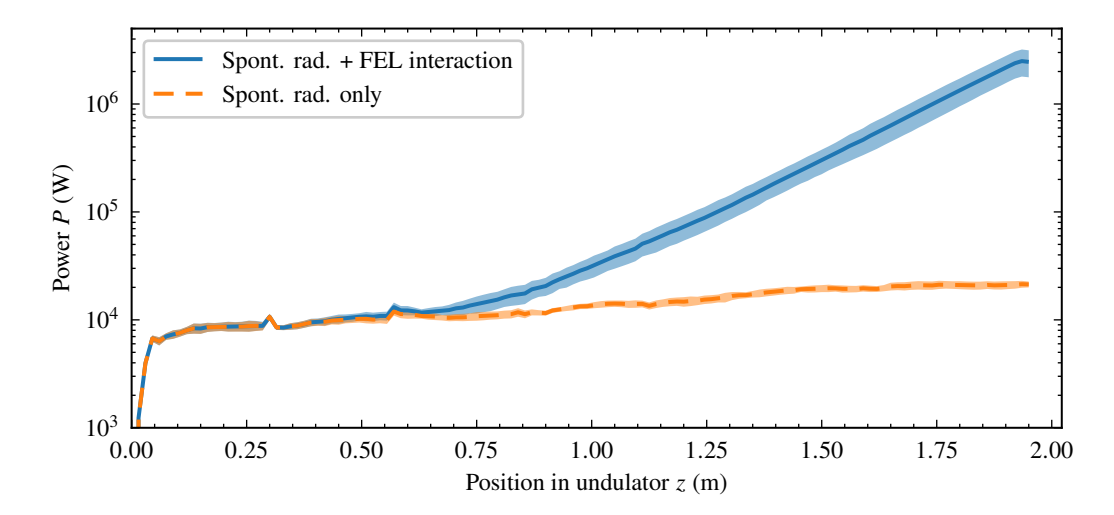


Figure 6.4: Emitted Power from simulation with LUX beam parameters after transport and perfect undulator field with K=2 and a taper of 1 %/m. It is shown for (blue, solid) mean value with (blue, filled) 1σ standard deviation calculated over 10 simulations with different shot noise seed values. In comparison (orange, dashed and filled) the spontaneous undulator radiation is shown for the same seed values. The power level reaches about 2.5 GW at the end of the undulator.

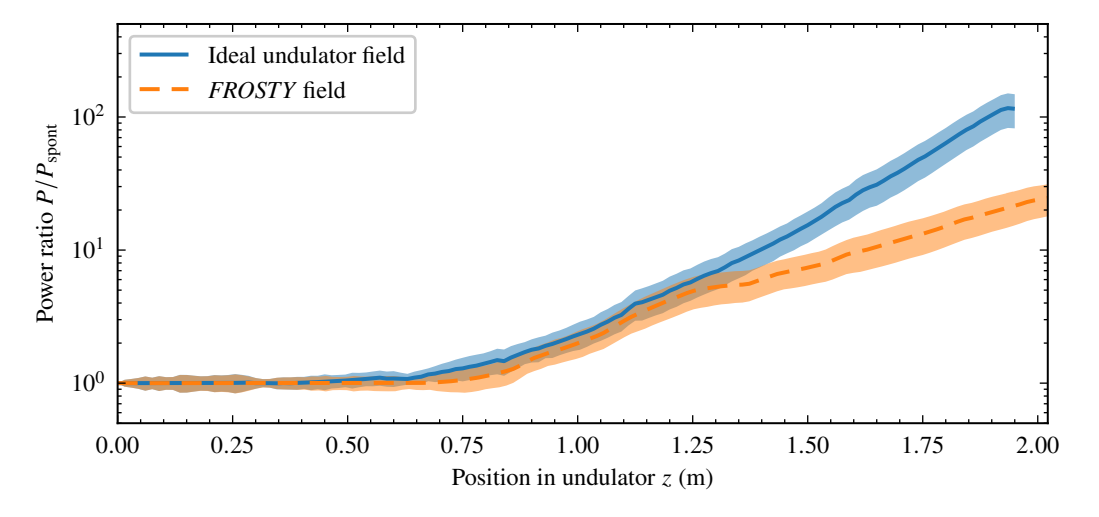


Figure 6.5: Ratio of total emitted power to spontaneous undulator radiation only, averaged over 10 simulations with different shot-noise seeds for (blue, solid) an ideal sinusoidal undulator field and (orange, dashed) the measured FROSTY field profile with (filled) 1σ standard deviation calculated over 10 simulations. To cover the the extent of the full FROSTY field, the z axis is slightly longer and the undulator centered within this range.

radiation. As expected when including all aspects for the FEL interaction for the parameters at *LUX* by using a non-SVEA code, the startup and consequently the growth beyond undulator radiation happens earlier.

In both, the simulation and the experiment the pure FEL signal is not available but overlapped with the spontaneous undulator radiation. However, it is possible to switch off the FEL interaction in the simulation to simulate spontaneous radiation only. In the experiment the FEL interaction could be suppressed by detuning the undulator taper, or changing the focusing or trajectory through the undulator such that no FEL interaction can occur. Therefore, different from section 4.3.3, here the power gain is not given as a ratio to some initial power level. Instead the ratio of the full signal to the spontaneous undulator background. It is shown in fig. 6.5.

The gain length obtained from a fit to the last 50 cm of this power ratio, averaged over all 10 simulations with different seeds, is

$$L_g = (21.3 \pm 0.7) \,\text{cm}$$
 , (6.2)

similar to the value found before from the SVEA estimations in section 4.6. Further, the gain length is lower than normally achievable by a beam of 1 mm mrad normalized emittance, which would be limited by the average beam size in the undulator. Here, the gain length scales with the effective size of the electron beam as seen by the radiation pulse, i.e. the size of the slipping focus.

6.4 Simulation with Measured Undulator Field

To capture the influences of field imperfections, *Puffin* was modified to allow the use of user-defined undulator field profiles. The measured and tuned *FROSTY* undulator field section 5.3.6 was used for the simulations in this section. To cover the whole region of the field, a few centimeters were added in front and at the back of the simulation, totaling slightly more than 2 m. The beam enters the undulator such that it oscillates about the central axis at the center of the undulator, thus respecting the incoupling periods and a small kick at the beginning of the undulator. However, the later local kick at about 1.3 m is already in the exponential gain regime. Here, the 0.1 mrad kick is expected to increase the gain length more significantly due to smearing out the micro-bunching.

The gain curve for the measured undulator field at K = 2 and with 1 %/m taper is shown in fig. 6.5. Its initial behavior is similar to the perfect undulator field. After the kick the gain length for the last 60 cm of the undulator increases to

$$L_{\varrho} = (41.8 \pm 0.7) \,\text{cm}$$
 (6.3)

Therefore, after the initial growth only 2 more gain lengths fit into the undulator after the kick. The ratio of FEL power to spontaneous undulator radiation is reduced to a factor of about 20. Nevertheless, this would still be significant power gain, considering that this is the unfiltered power and not spectrally resolved.

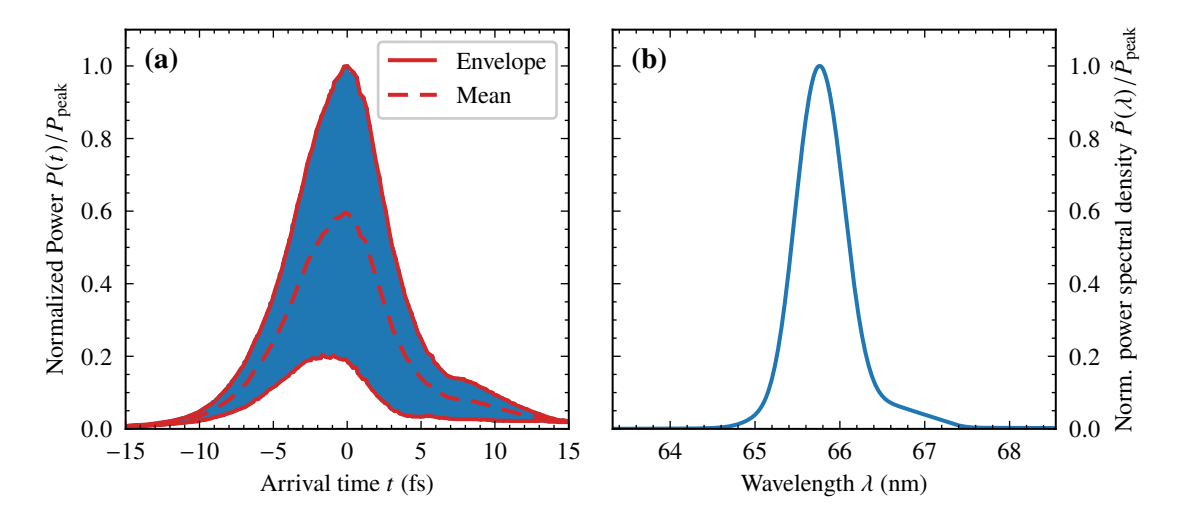


Figure 6.6: (a) Temporal profile of normalized power of one simulation. (Red, solid) Envelope of the maximum and minimum instantaneous power and (Red, Dashed) the average power. (Blue) The instantaneous power shows oscillations twice as fast as the electric field with frequency $f = 2c/\lambda_l$. (b) Corresponding normalized power spectral density.

6.5 Radiation Pulse Properties

The radiation emitted from an electron beam in the SASE FEL has a noisy structure in the time domain from the discrete nature of the single electrons. From this noise a fraction is amplified in the FEL process. However, the noisy structure is kept within the amplified envelope. As mentioned in section 4.4.3, during the FEL process these envelopes emerge as spikes of high amplitude in the electric field. They are separated by about $2\pi L_c \simeq 6 \, \mu m$ or $\tau_c = (2\pi L_c)/c \simeq 20 \, fs$. Since the electron bunch is rather short with $\sigma_{\zeta} \simeq 5.3 \, \mu m \simeq 15 \, fs$, here only a single intense spike is amplified.

The emitted radiation power of one of the simulations is shown in fig. 6.6(a). The pulse length is about $\sigma_{\tau} \simeq 3.5$ fs or in terms of FWHM $\tau_{\rm FWHM} \simeq 7.1$ fs. The corresponding power spectral density is obtained from the Fourier transform of the electric field and shown in fig. 6.6(b). The central wavelength is $\lambda_l \simeq 65$ nm and the FWHM bandwidth is $(\Delta \lambda/\lambda_l)_{\rm FWHM} \simeq 0.7$ %.

A transverse radiation profile at the end of the undulator is shown in fig. 6.7(a) and its corresponding projections to the transverse axes in fig. 6.7(b). It has a transverse horizontal size of $\sigma_{x,rad} \simeq 51 \,\mu m$ and vertical size of $\sigma_{y,rad} \simeq 39 \,\mu m$. This is consistent with the extent of the focused fraction of the electron beam in the sense that the recently emitted radiation over the last gain length already increased in size due to the Rayleigh range being on the same length scale as L_g .

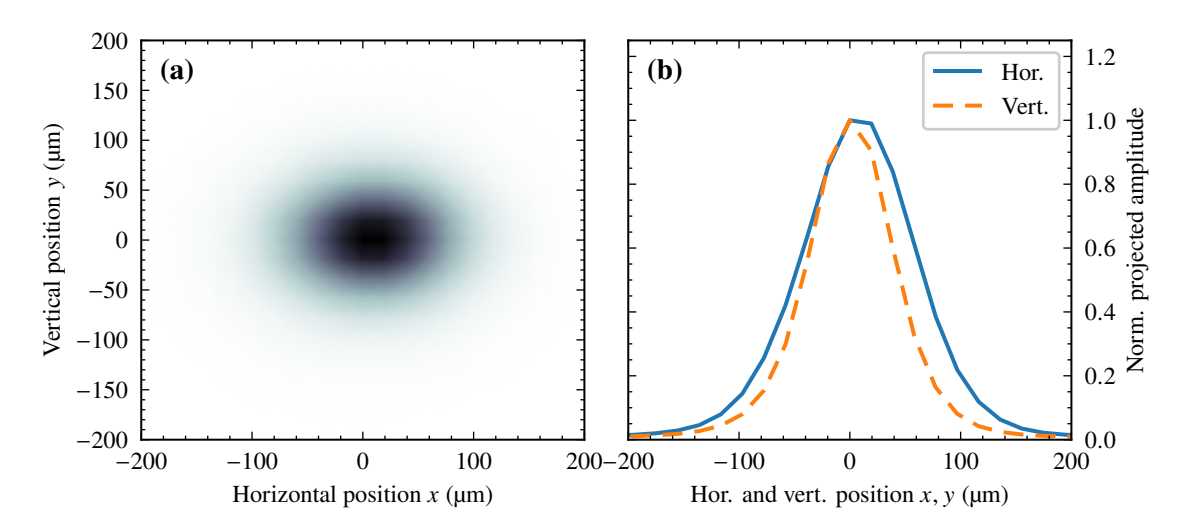


Figure 6.7: (a) Radiation intensity profile. (b) Projected transverse profiles to the horizontal and vertical axes.

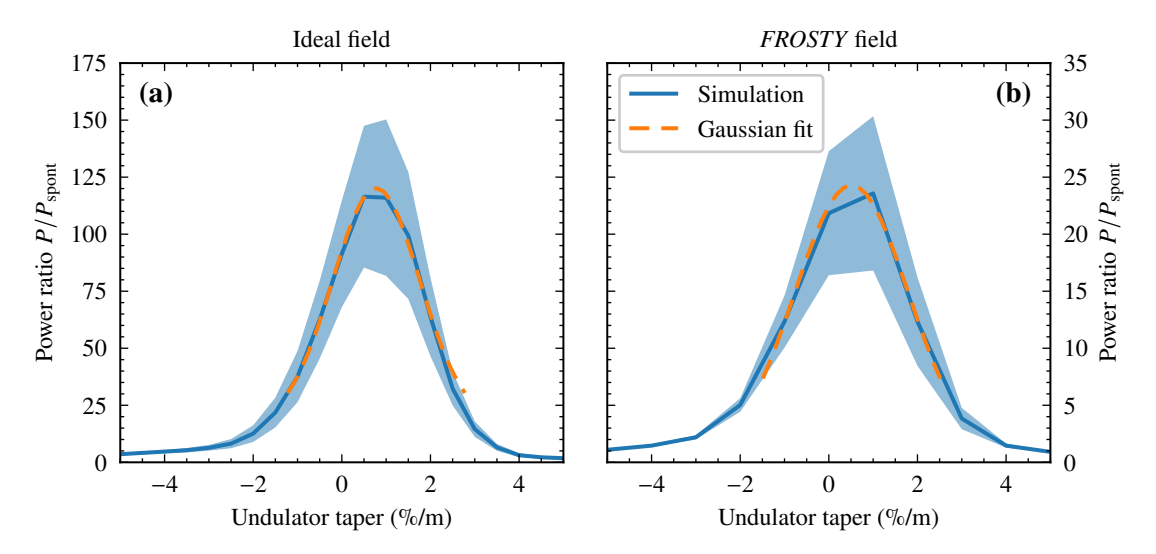


Figure 6.8: Ratio of total emitted power to spontaneous undulator radiation only, (blue solid) averaged over 10 simulations with different shot-noise seeds for (a) an ideal sinusoidal undulator field and (b) the measured *FROSTY* field profile. (solid) represents 1σ standard deviation. Additionally, (orange, dashed) a Gaussian fit is applied to the central region to estimate the best taper.

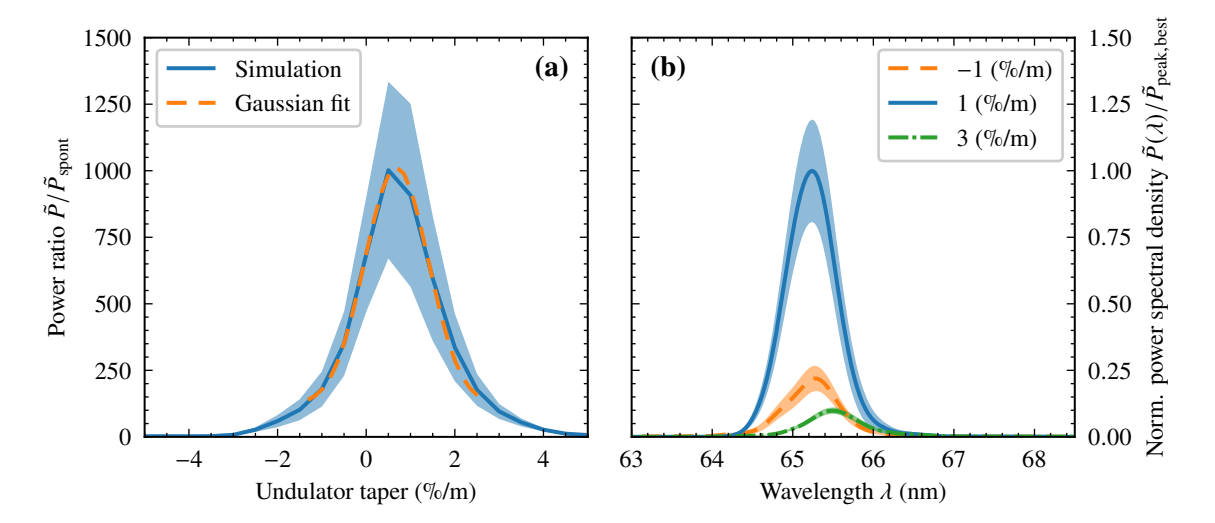


Figure 6.9: (a) Ratio of total emitted power to spontaneous undulator radiation only filtered within a window about $\pm 2\,\%$ of the fundamental, (blue solid) averaged over 10 simulations with different shot-noise seeds and (orange, dashed) a gaussian fit applied of the central region to estimate the best taper. (b) Averaged spectra about the fundamental for (blue, solid) a taper of 1 %/m, close to the optimum, and detuned tapers of (orange, dashed) $-1\,\%$ /m and (green, dash dotted) $3\,\%$ /m

6.6 Taper Scan

To validate the optimum taper, it was scanned in the region $\pm 5 \%/m$. For the ideal field the scan was performed in steps of 0.5 %/m. For the *FROSTY* field the step size was increased to 1 %/m, since the evaluation of the interpolated field data at runtime is computationally more expensive than evaluating the hard coded and compiled ideal field profile. The results for both, the ideal case and the measured frosty field, are shown in fig. 6.8 respectively. Both curves are qualitatively similar, and are mainly scaled by the previously found reduction in gain.

To find the optimum taper, a gaussian fit is applied to the highest power ratio in a window of $\pm 2 \%/m$. For the ideal field it is found to be about 0.8 %/m, slightly lower than estimated. For the *FROSTY* field a slight asymmetry is found, with less decrease in power to negative tapers. Consequently, the ideal taper is slightly shifted to a lower value of 0.6 %/m, which, however, can also be attributed to the lower sampling about the optimum.

For both considered cases, a detuning of the taper by about 0.5 %/m decreases the FEL gain by less than 10 %. Considering this to be acceptable in the experiment, the taper has to be met within this range. This is possible with *FROSTY*, whose taper can be set with high accuracy and precision and allows for fine scans [114].

Finally, the radiation is filtered within a range of $\pm 2\%$ about the fundamental to estimate the improvement from a spectrally resolved measurement in the non-SVEA code, here done for the ideal undulator field. The taper scan for the filtered signal is shown in fig. 6.9(a). Some individual spectra

for different taper settings are shown in fig. 6.9(b) for comparison. Although the peak position slightly shifts with the taper setting, the same range about the fundamental is amplified. Further, the signal drops faster with detuned taper, dropping by 10 % of its peak value when going away from the optimum of 0.7 %/m by 0.3 %. Nevertheless, about the same ratio of FEL power to spontaneous radiation seen in the signal collected over all wavelengths can be achieved with a highly detuned undulator of 3 %/m. The improvement to the unfiltered signal is about one order of magnitude, highlighting once again the importance of the spectrally resolved measurement for possibly showing FEL gain with the *LUX* setup.

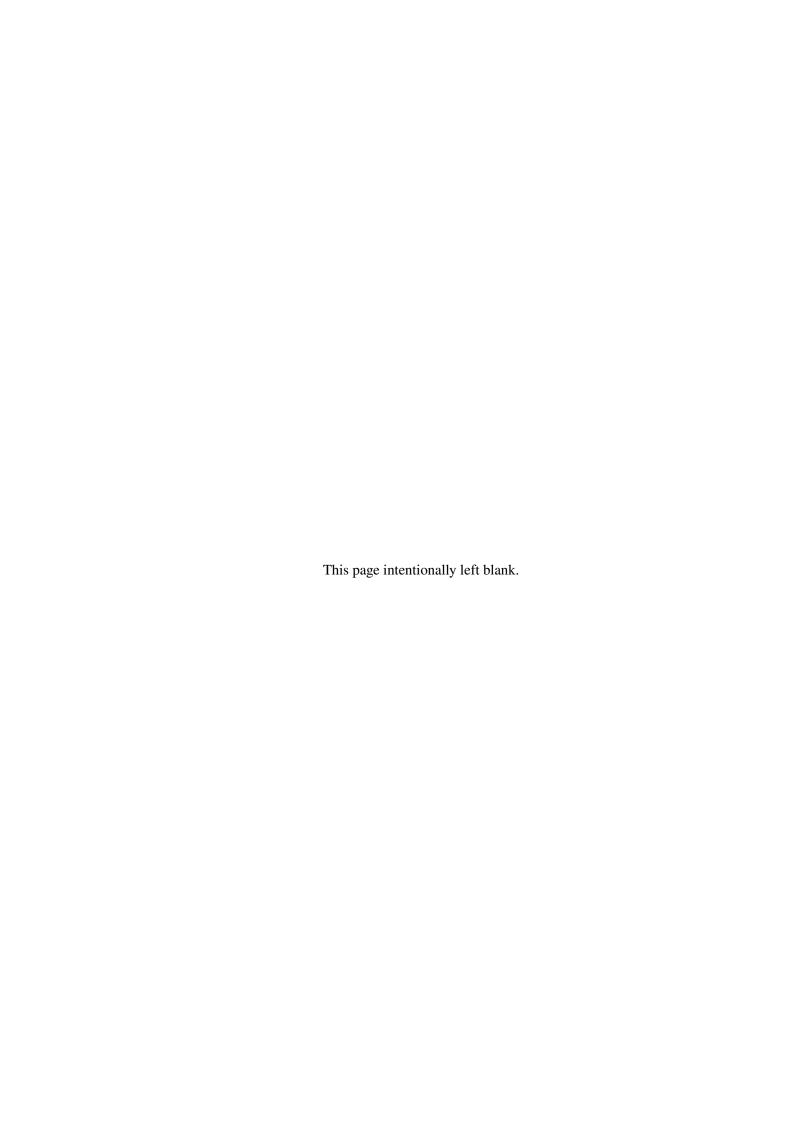
6.7 Conclusion

Comparing to the basic simulations with SVEA approximation section 4.6, the gain length is similar, but an earlier startup is encountered. As pointed out before in this chapter and in section 4.4.3, this is expected for three reasons: Firstly, the non-averaged code respects the individual spikes from the electrons in the current density, causing a slightly higher initial bandwidth, and therefore shot-noise, for beams with energy spread [123, 147]. Secondly, the pulse building up in the bunch tail is only weakly disturbed by trailing radiation [146], compare section 4.4.3, benefiting the startup. Thirdly, a slightly stronger focus at the bunch tail in the vertical plane at the undulator start increases the current density to levels similar to those at the bunch center, see section 5.2.

The simulations suggest that an FEL signal two orders of magnitude above spontaneous undulator radiation is in principle achievable in spectrally resolved measurements with the 2 m undulator at *LUX*, if utilizing bunch decompression, a tapered undulator, and the implemented focusing scheme. Although field imperfections of the undulator are expected to degrade the gain length and the FEL performance, the simulations suggest still one order of magnitude difference between FEL and spontaneous radiation at the end of the undulator. If measuring the signal spectrally resolved, the increase in signal about the fundamental should be clearly visible.

Further, applying an undulator taper to an optimum value of approximately 0.7 %/m increases the FEL signal by about a factor of 2 in the spectrally resolved measurement compared to the untapered measurement. However, the signal is not sensitive to a small taper mismatch of up to 0.3 %/m.

The next steps to show FEL gain are the proper setup and control of the beamline. For this, the beamline itself and the electron beam have to be characterized, to be able to tune the machine towards the desired parameters. This includes the proper transport to and through the undulator by means of the focusing properties and the beam pointing.



Experimental Results

After construction and commissioning of the beam line, the beam transport was characterized in terms of trajectory errors and focusing errors. To stay in the good field region of the undulator and not degrade the FEL process by beam pointing, the quadrupole magnets have to be well aligned to the design axis. On the one hand, they steer the beam if misaligned, and, on the other hand, detours are to be avoided to not disperse the percent level energy spread beams unintentionally and spoil their phase space. Further, the actual quadrupole strengths for a given applied current and their focusing properties have to be well known. Finally, it has to be made sure that the beam travels centered through the undulator.

In this chapter, the results of beam based measurements are presented. Section 7.1 and section 7.2 cover the measurements of transverse positional offsets and the deviation in focusing strength for the quadrupole magnets. This is followed by the recorded position in the BPMs with an algorithm running to correct the trajectory along the beamline and through the undulator in section 7.3. A method used to determine the vertical undulator position and rotation with data recorded from BPMs is presented in section 7.4. Lastly, a recorded undulator spectrum is shown in section 7.5.

7.1 Quadrupole Positioning

In principle, the goal is to position the magnets as accurately as possible to this axis to avoid the use of the corrector dipoles. A threshold for this was estimated in section 3.5.1 to be on the level of 10 μ m Since residual offsets can be compensated with corrector dipole magnets by steering the beam back on the design axis, the required positioning accuracy might be slightly less strict. However, corrector magnets are not installed between all individual quadrupole magnets. With the determined level of quadrupole strengths $K_1 \simeq 10 \, / \text{m}^2$ for all of the quadrupole magnets between the first capturing doublet and the undulator, and an effective field length of 135 mm, a displacement by 1 μ m results in a kick of 1.35 μ rad according to eq. (3.40). For a displacement of a magnet by 10 μ m, the offset in the following magnet in a doublet or the quintet is 7 μ m, which is on the same order of magnitude as the offset itself. Consequently, two consecutive magnets without corrector magnets in between should still be positioned to a common axis.

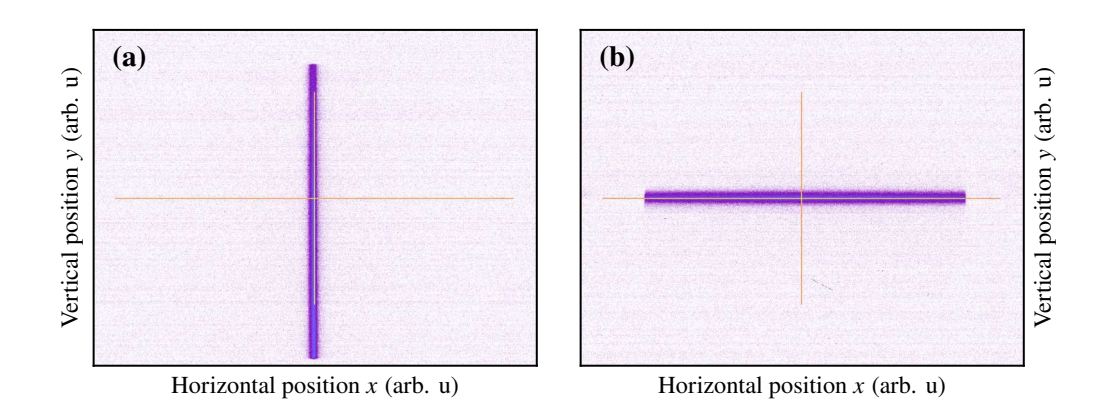


Figure 7.1: Line foci with single quadrupole magnet. Unprocessed camera image. (a) Focus in the horizontal axis and (b) focus in the vertical axis only.

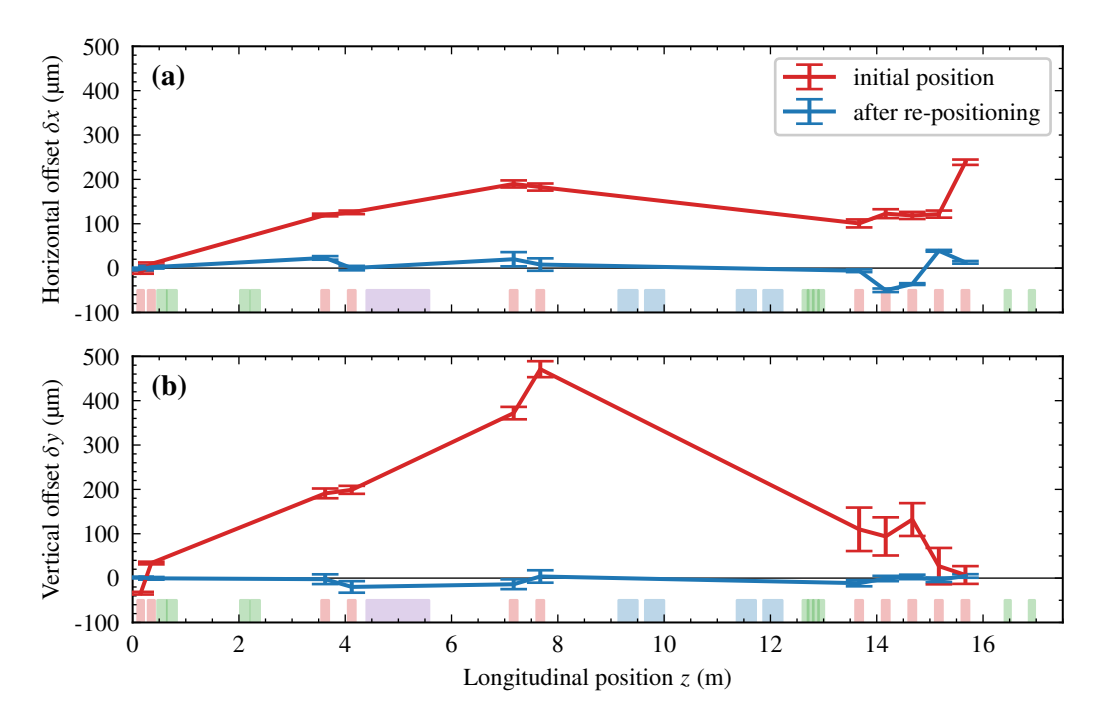


Figure 7.2: Transverse positions of quadrupole magnets at LUX for (a) the horizontal and (b) the vertical axis. (Red) Initial position after commissioning and (blue) after measuring the magnetic axes and re-positioning. Lines between the measured data points for the offset positions are added for better visualization.

Initially, the quadrupole magnets were positioned according to their geometric center with about $100\,\mu m$ to $200\,\mu m$ accuracy. This neither has to coincide with their magnetic center nor does it fulfill the positioning requirements. Therefore, a beam based measurement to determine the discrepancy between the magnetic axes and the reference trajectory was conducted, and the magnets were re-positioned accordingly.

To obtain the position, the electron beams are allowed to freely drift up to the magnet of interest. This is set to focus the beam in just one plane onto a profile screen further downstream. Here, the screen directly in front of the *FROSTY* undulator was chosen, since it is downstream of all quadrupole magnets in the transport. The signal on the screen is a thin line, since the electron beams are defocused in the other plane. Examples are shown for both polarizations of a quadrupole magnet in fig. 7.1 with (a) showing a horizontal focus and (b) a vertical focus. The misalignment is calculated from the displacement of the line, i.e. the peak position of its projection along the dispersed axis, to the corresponding central axis of the screen. By using the quadrupole strength, and the spacing between quadrupole magnet and profile screen, the offset is

$$\delta x \simeq \frac{x_{\rm sp}}{L_{\rm drift} L_{\rm mag} K_1} \tag{7.1}$$

for the horizontal axis, and for the vertical axis equivalently. Here, the subscript "sp" denotes the position on the screen. Since the screen has a resolution of about $30\,\mu\text{m}$, the quadrupole offsets can be determined to an accuracy of about $0.5\,\mu\text{m}$ for the quadrupole magnets early in the beamline and about $3\,\mu\text{m}$ for those closer to the screen. Here, the required K_1 , for the distance L_{drift} between magnet and screen, to focus the beam in one plane was used for each magnet. The initially determined transverse quadrupole offsets are listed in table 7.1 and visualized in fig. 7.2. The quadrupoles were then shifted according to the found positions. The process was repeated iteratively, by repositioning the magnets between measurement campaigns. Consequently, the beam line alignment was improved over time. The latest determined positions are shown in the same table 7.1 and fig. 7.2 for comparison.

Up to now the positional offset was reduced from the $100\,\mu\text{m}$ -level to the $10\,\mu\text{m}$ -level. Only a few are positioned at offsets larger than $10\,\mu\text{m}$. Any residual kicks originating from the quadrupole magnets are compensated with the installed corrector magnets.

7.2 Quadrupole Strength Calibration

A crucial step in the presented concept is the proper setting of the optimized beam optics and the focusing. To be able to apply it in the experiment, the strength of the quadrupole magnets has to be set accurately. Therefore, it is important to verify that the strengths of the magnets match the expected value when applying a current. This cannot be done by a focus scan on a profile screen, as the large energy spread would cause every energy-fraction to be of different size and consequently the full beam would be their (charge-weighted) average. The observable beam size would barely change, rendering this method not applicable. Instead, the beam is focused from the plasma source to the final spectrometer with only two quadrupoles, while all other quadrupoles in the transport are turned off. This way, the energy focused onto the spectrometer screen in the horizontal plane can be recorded.

arter the faces re positioning.												
Quad. No.		Initial position					Latest position					
		$\delta x \mu m$			δy μm			$\delta x \mu m$			$\delta y \mu m$	
1	-9	±	3	-34	±	3	-2	±	3	1	±	2
2	9	±	3	34	±	3	2	±	3	0	±	3
3	119	±	3	191	±	11	23	±	4	-2	±	11
4	125	±	4	199	±	9	0	±	5	-19	±	13
5	189	±	8	372	±	14	20	±	16	-13	±	11
6	182	±	8	471	±	18	8	±	14	3	±	14
7	100	±	9	110	±	49	-6	±	3	-11	±	7
8	122	±	10	94	±	43	-50	±	4	0	±	6
9	118	±	8	132	±	37	-36	±	2	2	±	5
10	121	±	8	27	±	41	39	±	2	-3	±	5
11	238	±	6	7	±	20	13	±	3	4	±	4

Table 7.1: Transverse position of quadrupole magnets at *LUX* after commissioning and after the latest re-positioning.

This is done for both combinations of polarities, where one of the quadrupole magnets is focusing in the horizontal plane and the other in the vertical. The deviation of the strengths of the magnets from the design value is found by comparing the recorded focused energies with the ones that were targeted.

An example for such a measurement is shown in figure fig. 7.3(a) and (b), performed with the second doublet set to focus an energy of 295 MeV. If the quadrupole strengths were correct, the waist positions for both polarizations of the quadrupole magnets were located at the position where 295 MeV hit the spectrometer screen. For this particular configuration the focused energy is lower than the targeted value for one polarity setting and larger for the other polarity setting. It was made sure that this is not caused by an angle or position offset at the electron spectrometer entrance. In fact, the average position in the BPMs (BPM3 and BPM4) between the quadrupole magnets and the spectrometer was close to zero, and the estimated impact on the energy measurement less than 0.1 %. The difference in focused energy indicates that the focusing strengths of these two quadrupole magnets do not match their assumed values, obtained from the mapping from applied current to field gradient.

An upper limit for the allowed deviation in focusing strength was estimated in section 4.5, by only allowing the focus size to deviate by about 5 μ m. The deviations in K_1 to still properly match into the undulator are estimated by using the mismatch parameter from eq. (3.43) and are approximately 0.5% for all quadrupole magnets, except for the second in the capturing doublet. The focus position is particularly sensitive to its strength due to the combination of a large K_1 , short magnet length and a large beam size in the vertical plane.

To find the deviation in the quadrupole strengths from their design value, the beam was focused with different combinations of quadrupoles onto the spectrometer. Here, the first doublet is excluded from the measurements. Its focusing properties are strongly affected by changes in distance to the plasma source. The position from which the electrons originate in the plasma is dependent on the drive laser

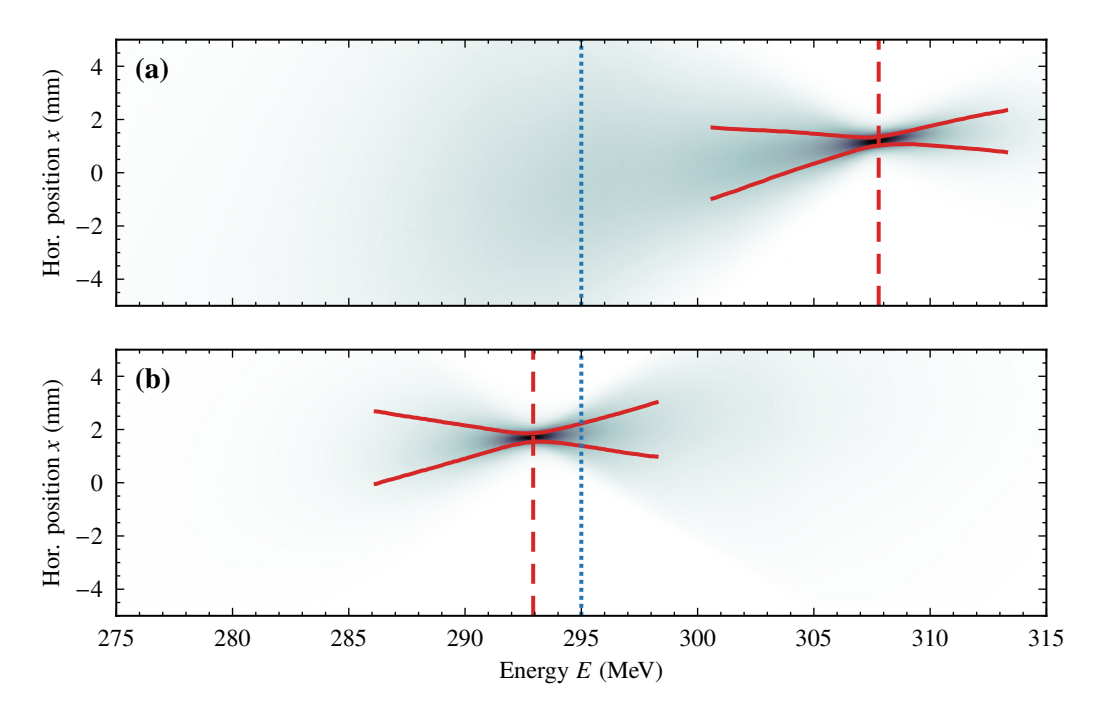


Figure 7.3: Electron beams focused on the second spectrometer with the second quadrupole doublet. The quadrupole magnets were set to focus the beam in both planes by (a) focus horizontally in quadrupole No.3 and defocus in quadrupole No. 4, resulting in (red, dashed) 307.8 MeV being focused on the spectrometer, and (b) vice versa, resulting in (red, dashed) 292.9 MeV being focused on the spectrometer. (Blue, dotted) The focused energy was set to 295 MeV. Camera counts are averaged over 100 shots to not be affected by shot-to-shot fluctuations. The waist position remains unaffected by averaging.

and plasma properties, which are tuned at the beginning of every operation of *LUX*. Therefore, to properly capture the beam, their strength, especially for the second quadrupole, has to be individually tuned in the experiment with the first spectrometer, before transmitting the beam towards the undulator and applying the focusing scheme.

During the first measurements, deviations of up to 4% were determined. Since this is a rather large discrepancy and above the obtained limit, the cause was investigated. The measurements were repeated over several measurement campaigns. The average electron energies in these measurements ranged from 270 MeV to 320 MeV. Their results are presented in figure fig. 7.4.

The exchange of two power supplies and two pole flippers of the quadrupole magnets had no effect and were ruled out as a cause for the deviation in magnet strength. However, the exchange of magnets, replacing the second doublet with spare quadrupole magnets from the same manufacturing batch, showed that the newly installed magnets had different strengths of approximately 1 % and 3 %. To verify the assumption, that the difference in magnet strength is a property inherit to the individual

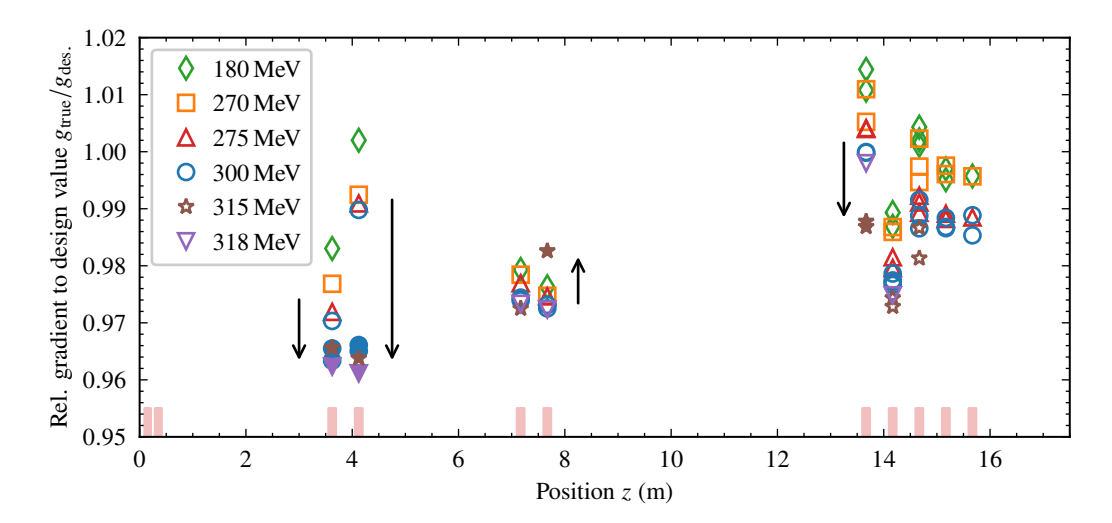


Figure 7.4: Quadrupole strengths relative to their design value, determined with beam based measurements at different energies, and therefore changing gradient. Required gradient to focus onto the spectrometer screen increases up to about 13 m and then decreases again. Markers show (green, diamond) 180 MeV, (orange, square) 270 MeV, (red, up triangle) 275 MeV, (blue, circle) 300 MeV, (brown, star) 315 MeV, and (purple, down triangle) 318 MeV. Arrow and filled markers show quadrupole magnets, that were replaced in between measurement campaigns.

magnets, one magnet from the third doublet and one of the quintet were interchanged. As a result, the deviation of the first magnet from the design value decreased by approximately 1 %, while the second magnet's deviation increased by a similar amount.

Additionally to the individual correction for each magnet, a dependence on the magnetic field gradient, and hence the applied current, was found. This is seen from two aspects in fig. 7.4. On the one hand, the deviation between expected to measured gradient is larger for the measurements, where beams with higher energy were used, which required higher gradients to focus the beam. On the other hand, the deviation decreases from the second doublet to the quintet, but then increases within the latter. Apparently, to focus into the spectrometer, the required gradients decrease towards the seventh quadrupole, which is close to the central point between plasma target and spectrometer, and increase again when going further downstream the beamline. Although not verified, a possible reason is that the measured hysteresis of peak gradient at the magnet center with respect to the applied current does not reflect all aspects of the magnet, for example changes in the shape and extent of the fringe field.

As a consequence, correction factors for each magnet are applied to compensate for the found deviations in gradient.

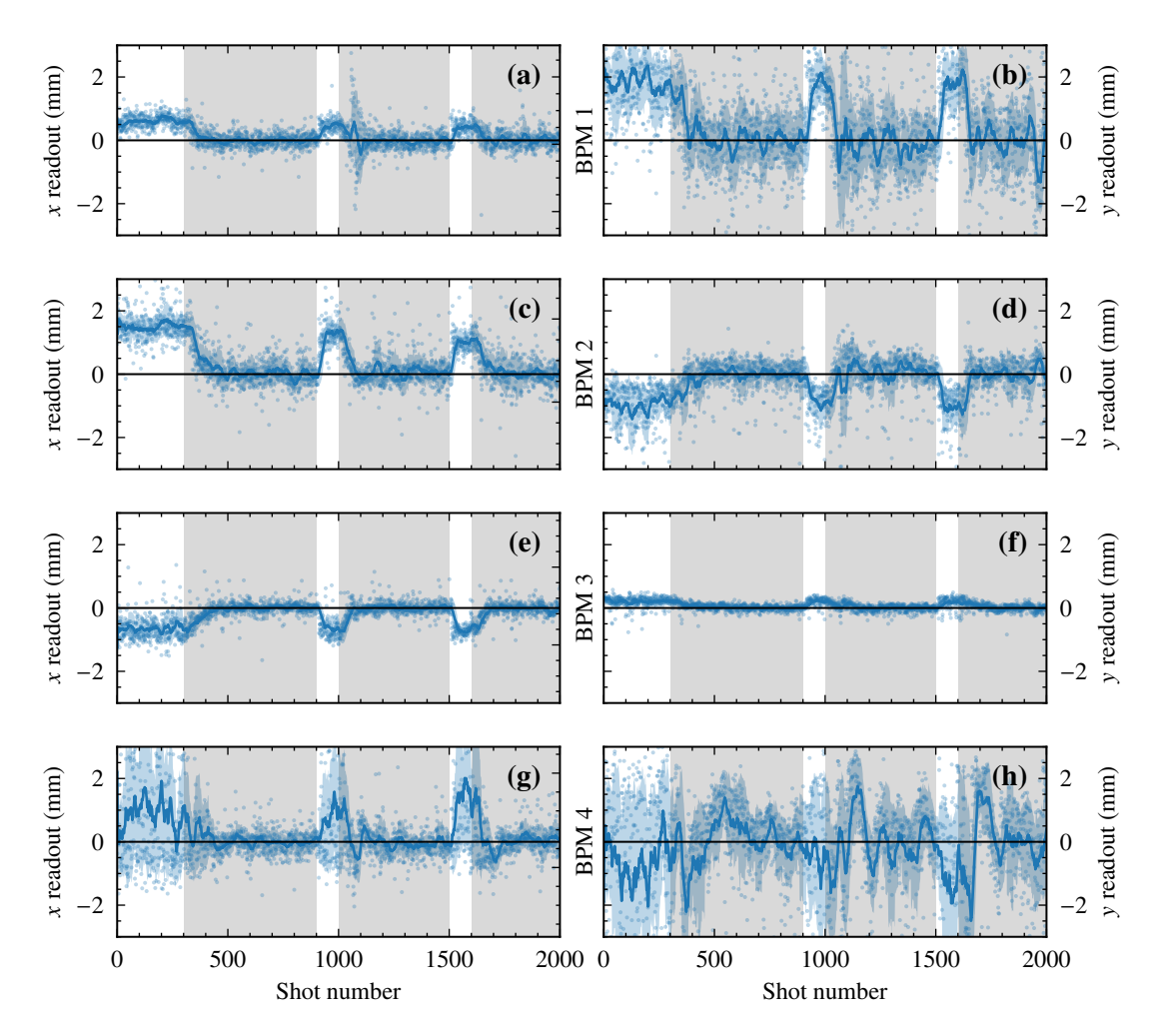


Figure 7.5: Beam position monitor readouts along the beamline with (white background) trajectory correction off and (gray background) trajectory correction on. From the top to the bottom panels, the individual BPM readouts are shown for BPM1 to BPM4, with the horizontal readouts shown in the left and the vertical readouts in the right panels, respectively. (Blue, solid) The rolling mean and (blue, shaded) corresponding rolling standard deviation over 30 shots. Individual shots going through the beamline and recorded in all 4 BPM are shown as dots in each panel. When the trajectory correction was not running, the corrector magnets were turned off.

7.3 Trajectory Correction

To remove the remaining trajectory offsets, either from residual positional offsets of the quadrupoles, or originating from initial beam position offset or pointing from the plasma source, a routine was implemented to steer the beam back on axis in the experiment. It aims to minimize the transverse offsets during the transport and to remove any beam pointing through the *FROSTY* undulator. The method utilizes the readings of the beam position monitors and sets the corrector dipole magnets accordingly to center the beam trajectory.

This is done by first correcting the position in the first two BPMs with the first 4 corrector dipoles. The newly imprinted offset and angle are considered when calculating the necessary steering. The corrector dipoles, located behind the chicane, are then used to adjust the position at the third BPM accordingly. Taking into account all offsets, angles and readings from the previous corrector dipoles and BPMs, the trajectory is then centered in the last BPM. This way, the electron beams travel on the axis defined by the last two BPMs through the undulator. Since there are shot-to-shot fluctuations from the plasma source, the correction works with the average of multiple shots (in the default configuration) and is continuously updating the corrector dipole strengths. The algorithm tunes the settings with a simulation of the trajectory through the beamline and applies all corrector dipole strengths simultaneously to the real machine, allowing for a fast convergence.

An example for running the trajectory correction, showing the BPM position readouts, is presented in fig. 7.5. The beam initially showed transverse position offsets of about 1 millimeter in all BPMs. The algorithm was then turned on and it tuned the correctors automatically to center the beam in the BPMs. In addition to centering the beams on average, the positional jitter was reduced by a factor of two. This improvement results from the presence of both energy and transverse jitters, and their coupling to each other. Variations in energy cause the beam to follow different trajectories through the beamline, if it has an offset or pointing relative to a quadrupole magnet's axes. Consequently, correcting the trajectory mitigates the combined effect of energy fluctuations and transverse positional and pointing jitters.

In this particular case, the initial jitter in the y plane originating from the plasma source, as seen in fig. 7.5(b), directly translates to a jitter behind the undulator, fig. 7.5(h). This corresponds to a beam pointing through the undulator, since the positional jitter in BPM3 is small. From the difference in position readings from BPM3 and BPM4 and their spacing of 4.2 m the beam pointing jitter of $\sigma_{\Delta y'} \simeq 0.3$ mrad is estimated. To achieve more consistent transport through the undulator, lower shot-to-shot fluctuations from the plasma source would be beneficial.

With this algorithm the beam trajectory offset is reduced throughout the beam line and aligns the beams on average to the design axis through the undulator.

7.4 Undulator Positioning

During the measurement campaigns, it was noticed, that the beam was steered in the vertical plane, when the undulator gap was changed. This indicates that the central axis between the upper and lower magnet arrays of *FROSTY* does not match the axis defined by the adjacent beam position monitors.

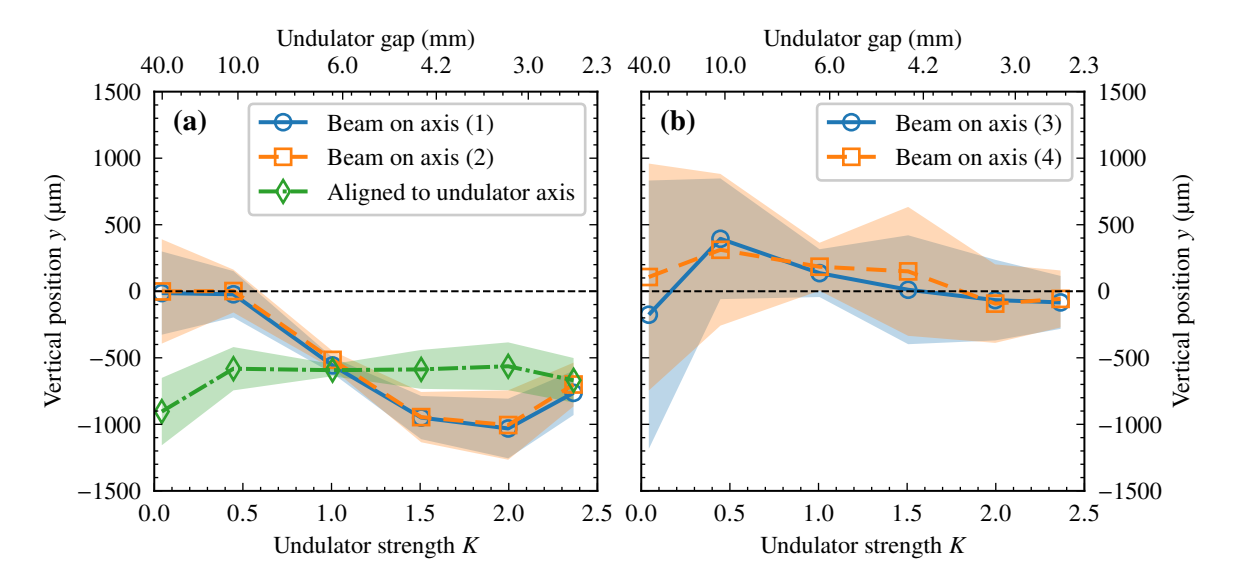


Figure 7.6: Steering of electron beam when closing the gap. Numbers (1)–(4) mark individual datasets where the undulator axis was measured. (a) Before the undulator was aligned to the design axis with (blue, circles) and (orange, squares) the beam being centered to the beam axis defined by BPM3 and BPM4 prior to closing the undulator gap, and (green, diamonds) after steering the beam to be aligned to the undulator axis instead of the design axis (b) After repositioning the undulator, the gap was again scanned twice with the beam being on the design trajectory defined by BPM3 and BPM4 prior to closing the gap.

This could be caused by either a positional offset, or a rotation, i.e. a tilt downwards or upwards along the beam trajectory, or a combination of both. In that case, the undulator focusing steers the beam away, whereas the steering depends on the undulator strength K, and consequently on the gap, and the amount of misalignment. Figure 7.6(a) shows the change of position in the BPM behind the undulator while changing the gap. The beam moves downwards when reducing the gap until reaching a gap of about 3 mm, indicating that the beam encountered a change in angle and position due to the natural undulator focusing. However, just from this, one cannot determine if the undulator is shifted or rotated to the design axis.

To determine the kind of misalignment, positional or rotational, and its amount, a procedure was performed that tunes two vertical corrector dipoles until a trajectory is found that does not change when changing the undulator gap. Before this procedure, the beam was centered through the undulator at fully opened gap to show zero readings on average in the BPMs in front and behind the undulator. Then the following steps were executed in a loop:

• The undulator gap is set to 6 mm, with a $K \simeq 1$, which changes the position in the BPM behind the undulator. The vertical position in the BPM behind the undulator is recorded.

- The undulator gap is fully opened again. A vertical corrector before the quintet is used to create a small offset and angle through the undulator. The strength is chosen such, that the beam has the same position in the BPM behind the undulator as found in the previous step. This way moving closer to the undulator axis.
- The undulator gap is closed again, but to a smaller value of 2.3 mm, with a $K \simeq 2.5$. The position is again recorded.
- Again the undulator is fully opened. This time a corrector dipole directly in front of the undulator is tuned to match the position in the BPM to correct only the angle, that might have been detuned at step 2.

This approach iteratively corrects position and angle through the undulator until a change in gap does not change the position in the BPM behind the undulator anymore. Two different gaps are used to avoid arriving at a state, where the positional offset and rotation of the undulator just cancel their contribution to a change in the vertical position at the BPM location. To confirm that the found trajectory matches the undulator axis, the gap was scanned and it was checked that the transverse position after the undulator is unaffected by the change in gap. This is also shown in fig. 7.6(a), where the trajectory through the undulator is such that the beam does not move vertically when closing the undulator gap. Using the BPM3 and BPM4 positional readouts of about $-50 \,\mu m$ and $-600 \,\mu m$, and the distance between BPM3 and BPM4 of about 4.2 m, the angle of the trajectory is found to be $-130 \,\mu rad$, coinciding with the rotation of the undulator. Since the undulator is longitudinally centered between these two BPM, its vertical positional offset is $-340 \,\mu m$.

It is assumed that the floor sank after positioning *FROSTY* in the accelerator tunnel, due to its weight of 6 tons.

Following the measurements, the undulator was shifted and rotated according to these values.

Finally, the measurement was repeated with the re-positioned undulator. As seen in fig. 7.6(b), the beam stays close to the central axis when closing the undulator gap. This confirms that the new position of the undulator matches the design axis more closely. However, the re-positioned undulator was not used for FEL experiments yet.

7.5 Undulator Radiation

The previous measures presented in this chapter were implemented one by one and improved over time. There were several measurement campaigns aiming to show free-electron lasing. However, up to the current date only spontaneous undulator radiation was observed at LUX. An exemplary image of recorded undulator radiation at a $K \simeq 2$ at an electron energy of $E \simeq 320$ MeV is shown in fig. 7.7(a). The corresponding spectrum, normalized to the signal at the fundamental wavelength for this setting, 57.7 nm, is shown in fig. 7.7(b). The steps in the spectrum match to the expected cut-off of the aluminum filter at 17 nm and its higher diffraction orders from the diffraction grating.

Here, the camera of the spectrometer was driven to different positions and recorded parts of the spectrum. The images were then individually calibrated and stitched to obtain the full spectrum.

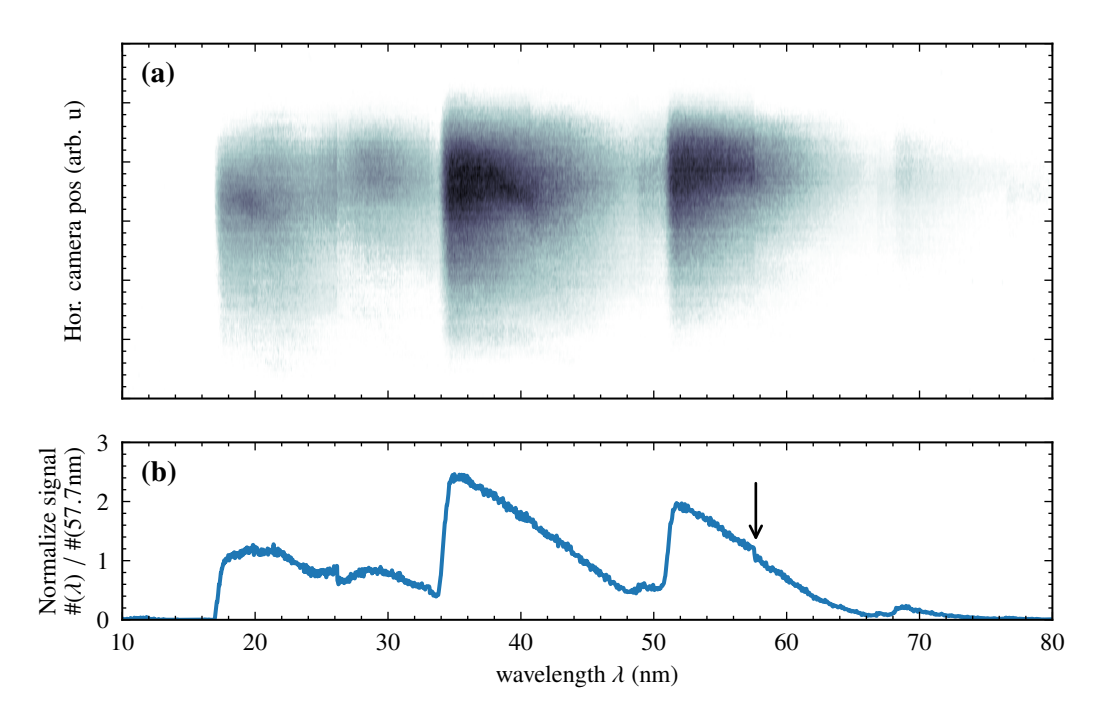
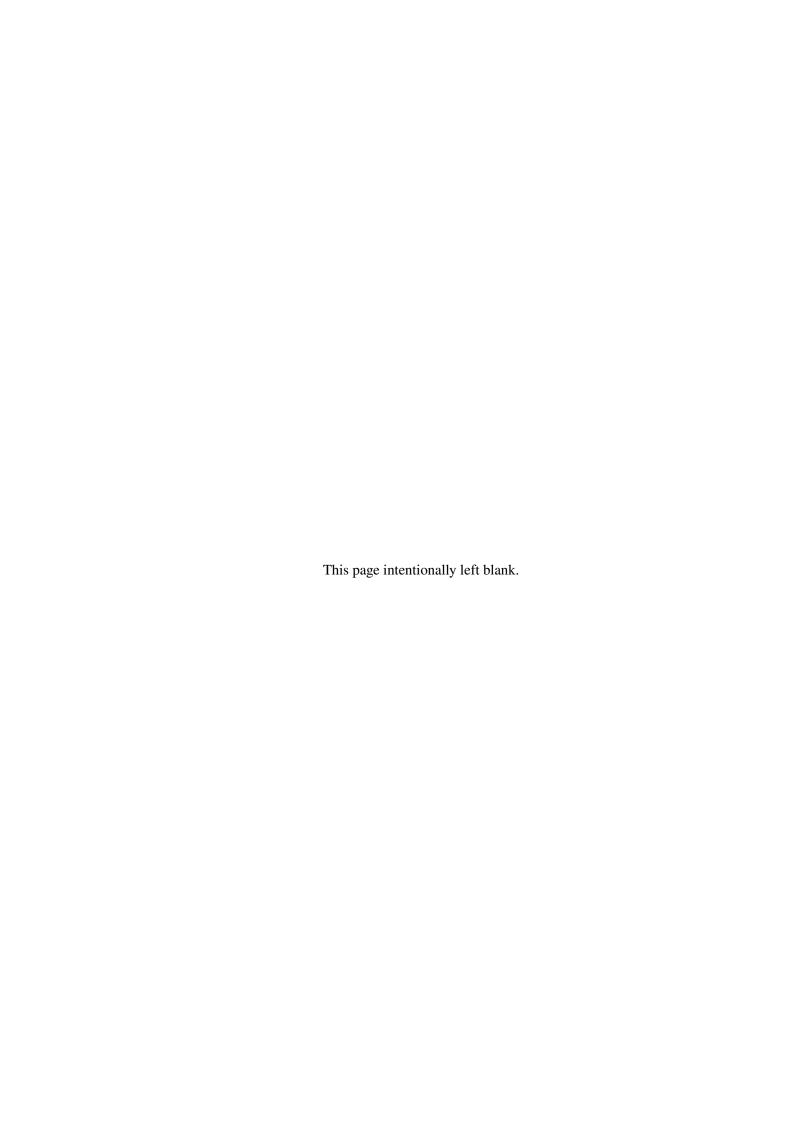


Figure 7.7: Undulator radiation recorded with the EUV spectrometer for a $K \simeq 2$ and electron energy of $E \simeq 320\,\text{MeV}$. (a) Images taken for the range of 10–80 nm. Edges of aluminum filter can be seen for multiple diffraction orders of the grating. (b) Spectrum normalized to the signal at the fundamental wavelength, which is marked by an arrow.

Still, all radiation measurements with the *FROSTY* undulator were done prior to the re-positioning of the undulator to the beamline design axis, shown in the previous section 5.4.

7.6 Conclusion

Over the course of several measurement campaigns, the beamline was characterized in terms of trajectory and beam optics. The positions and the strengths of the quadrupole magnets were determined by beam based measurements. Following this, they were iteratively aligned and re-calibrated to provide an improved trajectory and focusing. Additionally, a trajectory correction routine was implemented to align the beam to the design axis, going on a straight trajectory and centered through the undulator, and reduce positional jitters during transport. Lastly, the undulator was re-positioned to have its gap and magnetic axis aligned to the beam axis. It is still open for verification that these combined measures meet the strict requirements for free-electron lasing.



Conclusion and Outlook

Free-electron lasers (FELs) require high quality electron beams. As of today, operating an FEL with laser-plasma accelerated (LPA) electron beams remains challenging. Although providing kilo-amperes of current, the beams out of the plasma do not meet the stringent requirements for free-electron lasing. This is primarily due to the simultaneous presence of a percent-level energy spread, mrad-level divergences with transverse emittances on the order of mm mrad, and shot-to-shot instability in the beam quality of today's laser-plasma accelerators. Consequently, advanced beam manipulation and transport strategies are required to overcome current limitations and adapt state-of-the-art LPA beams for successful FEL operation. In addressing these challenges, a 25 m long beamline, capable of demonstrating free-electron lasing at the laser-plasma accelerator LUX, was designed, built and commissioned, based on the detailed conceptual layout developed in this thesis.

Challenges associated with preserving beam quality are analyzed, and strategies to limit degradation during beam transport are evaluated. This includes effects stemming from the beam itself, like chromatic emittance growth or coherent synchrotron radiation, and those introduced by beam optics, such as focusing and alignment errors.

The beam parameters were optimized to max out the number of gain lengths in the two meter short *FROSTY* undulator. By combining a magnetic decompression chicane and a tapered undulator, the slice energy spread in the beam is lowered to the level required by an FEL, while maintaining the resonance condition. This thesis extends this concept by implementing a chromatic focusing scheme that leverages the energy-dependent longitudinal position of electrons within a chirped bunch after decompression. It provides a constant transverse electron beam size at the position of the FEL radiation pulse by selectively focusing the portion of the beam that contributes to the FEL interaction. This effective beam size is not constrained by the emittance of the beam.

An algorithm was developed to optimize the full beamline for the chromatic focus slippage, which is required for an early startup in the short undulator. In contrast to previous methods, it includes the natural undulator focusing, thereby applying chromatic focusing in both transverse planes.

A beamline comprising a decompression chicane, consisting of 4 dipole magnets, and the necessary optics, provided by 11 quadrupole magnets, to implement the chromatic focusing scheme while limiting degrading effects was set up. It provides diagnostics to characterize the beam in terms of

transverse size, transverse position, and energy. The *FROSTY* undulator has been installed for studies of undulator radiation and free-electron lasing. The emitted radiation is recorded with a spectrometer that provides spectrally resolved measurements for wavelengths in the extreme ultraviolet.

A beam from particle-in-cell simulations, with properties as measured at *LUX*, was tracked through the optics lattice and then passed to the unaveraged free-electron laser code *Puffin* to investigate the FEL gain in the presence of a short bunch length, the longitudinal chirp with a percent-level projected energy spread, and the complex phase space provided by the focusing scheme. In an ideal case, it was shown that a signal two orders of magnitude larger than spontaneous undulator radiation is possible with the combination of the decompression and chromatic focusing schemes. Adding the chromatic focusing increases the gain from a factor of 5 for the decompression scheme alone to a factor of 100, and therefore greatly improves the detectability of first lasing. A spectrally resolved measurement improves the ratio of FEL to undulator radiation signal by an additional order of magnitude.

As a further step, *Puffin* was modified to handle undulator field profiles loaded from files, in particular measurement data. This enabled simulation of the influence of the real field errors of the 2 m *FROSTY* undulator on the FEL process. It was found that, although the growth rate is reduced toward the exit of the undulator due to a local field error, a power gain exceeding the spontaneous undulator radiation by a factor of 25 is possible with *FROSTY* when applying the chromatic focusing scheme. Further enhanced by the spectrally resolved measurement, such an FEL signal would be detectable in the experiment.

The individual beamline components were designed, assembled and commissioned within the frame of this thesis. The dipole magnets for the chicane were modified specifically to provide the required decompression for the *LUX* experiment. All magnets were measured and diagnostics calibrated. To reduce the impact of magnetic background fields on the beam trajectory and the beam quality, Helmholtz coils for their compensation were installed in the accelerator tunnel. An algorithm to calculate and apply the required currents to the accelerator magnets, as well as stabilization and feedback loops, was developed.

Using beam-based measurements, the transverse positional misalignments of the quadrupole magnets were determined and reduced, and their calibration, and hence the focusing, was refined using the obtained correction factors. An orbit correction routine was implemented to align the electron beam at runtime with the accelerator design trajectory when passing through the undulator. Finally, the natural undulator focusing was used to determine and correct the vertical displacement and rotation of the undulator. The experimental results indicate that the measures taken have remarkably improved beam transport and alignment, and demonstrate the critical role of precise beam control in achieving the stringent requirements of free-electron lasing.

In summary, this thesis addresses the multifaceted challenges of demonstrating free-electron lasing from laser-plasma accelerated beams by integrating advanced beam manipulation techniques, sophisticated beamline design, and rigorous simulation and experimental validation. Beginning with an in-depth exploration of the unique properties and limitations of LPA beams, the work methodically develops solutions to mitigate beam degradation during transport and to optimize the conditions for FEL operation. The combination of bunch decompression, undulator tapering, and the chromatic focusing scheme effectively counterbalances the intrinsic energy spread and emittance limitations, thereby

reducing the FEL gain length and enhancing the output signal. Furthermore, the conducted simulations underscore the feasibility of achieving and demonstrating FEL gain with the *LUX* setup and the *FROSTY* undulator.

Outlook

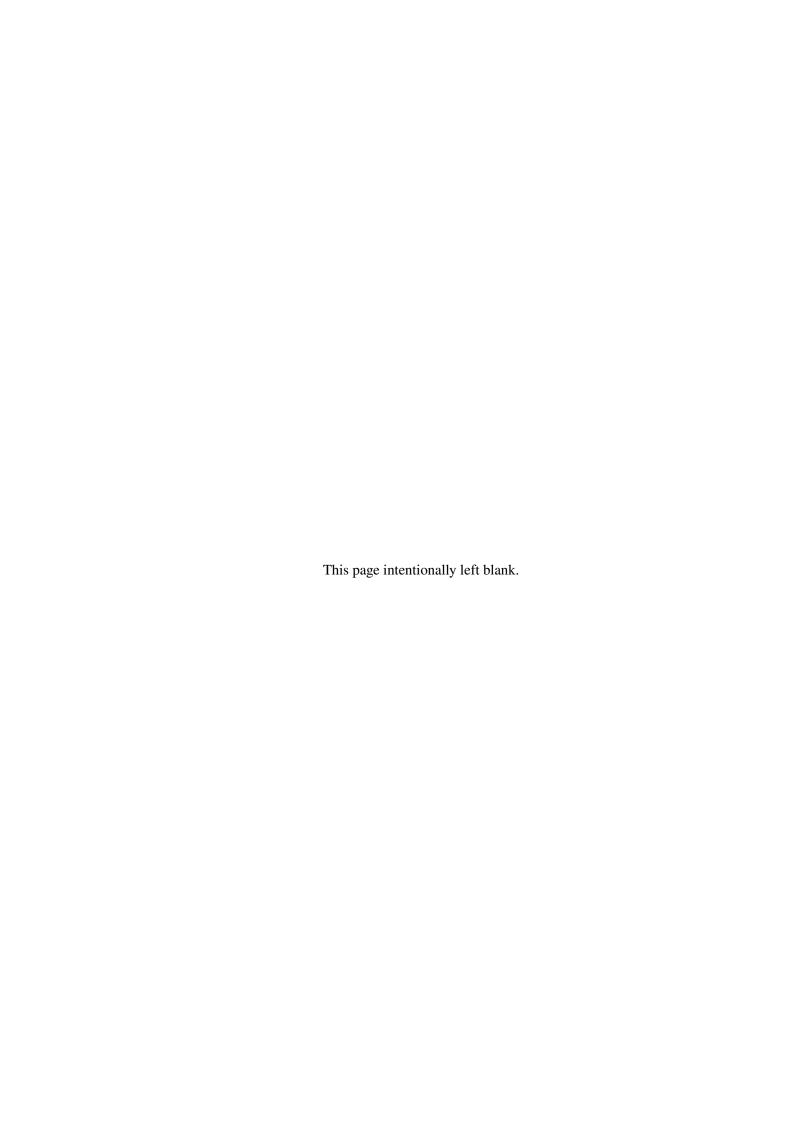
Following the characterization of the beamline and subsequent improvements to the positioning of components, the focusing strength of the quadrupole magnets, and the beam trajectory through the undulator, no dedicated FEL experiment has been conducted at *LUX* since the repositioning of the *FROSTY* undulator. Therefore, demonstrating FEL amplification with this setup, or a further optimized configuration, remains an open task for future experimental campaigns.

A straightforward improvement to the current system would be the installation of motorized linear stages to enable remote adjustment of beamline components during accelerator operation. In particular, real-time tuning of quadrupole magnet positions with immediate feedback on the electron beam trajectory would significantly reduce the time required for precise alignment. This approach would improve both the speed and accuracy of beamline adjustments compared to the current routine, which relies on dedicated measurement campaigns and manual repositioning.

A key long-term objective is not only to demonstrate the startup of FEL amplification but also to achieve saturation. Reaching this regime requires additional undulator length to accommodate more gain lengths, necessitating the installation of additional undulator modules. However, if the chromatic matching scheme presented in this thesis is to be implemented, the focus slippage would likely need to be adjusted to match the exponential gain regime rather than the startup phase. Consequently, such an extension would require modifications to the beamline design.

Ongoing advancements in laser systems and plasma sources may further improve the energy spread and emittance of laser-plasma accelerated electron beams, bringing them closer to the stringent requirements of FEL operation. These improvements could narrow or even eliminate the remaining gap between LPA-generated beams and the beam quality needed for lasing. Additionally, modern accelerator components, such as radially focusing plasma lenses, could facilitate early beam capture and enhance beam transport, potentially mitigating degrading effects while simplifying the beamline layout.

A substantial improvement could be achieved by reducing the delay between successive drive laser pulses at the plasma target. Increasing the repetition rate from the current 1 Hz operation to 100 Hz or even 1 kHz would allow for active stabilization of laser parameters, effectively suppressing both long-term drifts and pulse-to-pulse fluctuations. By minimizing temporal and spatial variations in the laser and the laser-plasma interaction, positional, pointing, and energy jitters in the electron beam would be significantly reduced, leading to enhanced stability and quality of the generated electron beams. *DESY*'s new flagship laser system *KALDERA*, a successor to the *ANGUS* laser system, has been designed precisely for this purpose and aims to operate at repetition rates on the 1 kHz-level. The *KALDERA* laser system is a prime candidate to demonstrate a laser-plasma based free-electron laser in saturation.



Bibliography

- [1] H. Winick, "Fourth generation light sources", Proceedings of the 1997 Particle Accelerator Conference (Cat. No.97CH36167), vol. 1, 1997, pp. 37–41, ISBN: 0-7803-4376-X, DOI: 10.1109/PAC.1997.749539 (cit. on pp. 1, 51).
- [2] R. Abela et al., "XFEL: The European X-Ray Free-Electron Laser - Technical Design Report", 2006, DOI: 10.3204/DESY_06-097 (cit. on pp. 1, 66).
- [3] S. Schreiber and B. Faatz, "The free-electron laser FLASH", High Power Laser Sci. Eng. 3 (2015), e20, DOI: 10.1017/hpl.2015.16 (cit. on p. 1).
- [4] P. Emma et al., "First lasing and operation of an ångstrom-wavelength free-electron laser", Nat. Photonics 4 (2010), pp. 641–647, DOI: 10.1038/nphoton.2010.176 (cit. on pp. 1, 66).
- [5] C. Bocchetta et al., "FERMI@Elettra Conceptual Design Report", ST/F-TN-07/12, 2007 (cit. on pp. 1, 66).
- [6] I. S. Ko et al., "Construction and Commissioning of PAL-XFEL Facility", Appl. Sci. 7 (2017), p. 479, DOI: 10.3390/app7050479 (cit. on p. 1).
- [7] T. Ishikawa et al., "A compact X-ray free-electron laser emitting in the sub-ångström region", Nat. Photonics 6 (2012), pp. 540–544, DOI: 10.1038/nphoton.2012.141 (cit. on p. 1).
- [8] T. Tajima and J. M. Dawson, "Laser Electron Accelerator", Phys. Rev. Lett. 43 (1979), pp. 267–270, DOI: 10.1103/PhysRevLett.43.267 (cit. on p. 2).
- [9] W. P. Leemans et al., "GeV electron beams from a centimetre-scale accelerator", Nat. Phys. 2 (2006), pp. 696–699, DOI: 10.1038/nphys418 (cit. on p. 2).
- [10] S. P. D. Mangles et al., "Monoenergetic beams of relativistic electrons from intense laser–plasma interactions", Nature 431 (2004), pp. 535–538, DOI: 10.1038/nature02939 (cit. on p. 2).
- [11] C. G. R. Geddes et al., "High-quality electron beams from a laser wakefield accelerator using plasma-channel guiding", Nature 431 (2004), pp. 538–541, DOI: 10.1038/nature02900 (cit. on p. 2).
- [12] J. Faure et al., "A laser–plasma accelerator producing monoenergetic electron beams", Nature 431 (2004), pp. 541–544, DOI: 10.1038/nature02963 (cit. on p. 2).

- [13] R. Weingartner et al., "Ultralow emittance electron beams from a laser-wakefield accelerator", Phys. Rev. ST Accel. Beams 15 (2012), p. 111302, DOI: 10.1103/PhysRevSTAB.15.111302 (cit. on pp. 2, 85).
- [14] A. R. Maier et al., "Decoding Sources of Energy Variability in a Laser-Plasma Accelerator", Phys. Rev. X 10 (2020), p. 031039, DOI: 10.1103/PhysRevX.10.031039 (cit. on pp. 2, 3, 11, 16).
- [15] D. A. Jaroszynski et al., "Radiation sources based on laser plasma interactions", Phil. Trans. Roy. Soc. Lond. A 364 (2006), pp. 689–710, DOI: 10.1098/rsta.2005.1732 (cit. on pp. 2, 35).
- [16] C. B. Schroeder et al., "Design of an XUV FEL driven by the laser-plasma accelerator at the LBNL LOASIS facility", *Proc. FEL'06*, JACoW, 2006, pp. 455–458 (cit. on p. 2).
- [17] F. Grüner et al., "Design considerations for table-top, laser-based VUV and X-ray free electron lasers", Appl. Phys. B 86 (2007), pp. 431–435, DOI: 10.1007/s00340-006-2565-7 (cit. on pp. 2, 35).
- [18] S. Hillenbrand et al., "Study of Laser Wakefield Accelerators as injectors for Synchrotron light sources", Nucl. Instrum. Methods Phys. Res. A 740 (2014), pp. 153–157, DOI: 10.1016/j.nima.2013.10.081 (cit. on p. 2).
- [19] S. A. Antipov et al., "Design of a prototype laser-plasma injector for an electron synchrotron", Phys. Rev. Accel. Beams 24 (2021), p. 111301, DOI: 10.1103/PhysRevAccelBeams.24.111301 (cit. on p. 2).
- [20] C. B. Schroeder et al., "Physics considerations for laser-plasma linear colliders", Phys. Rev. ST Accel. Beams 13 (2010), p. 101301, DOI: 10.1103/PhysRevSTAB.13.101301 (cit. on p. 2).
- [21] M. Kirchen et al., "Optimal Beam Loading in a Laser-Plasma Accelerator", Phys. Rev. Lett. 126 (2021), p. 174801, DOI: 10.1103/PhysRevLett.126.174801 (cit. on pp. 2, 10, 14, 15, 38).
- [22] W. Wang et al., "Free-electron lasing at 27 nanometres based on a laser wakefield accelerator", Nature 595 (2021), pp. 516–520, DOI: 10.1038/s41586-021-03678-x (cit. on p. 2).
- [23] A. R. Maier et al., "Demonstration Scheme for a Laser-Plasma-Driven Free-Electron Laser", Phys. Rev. X 2 (2012), p. 031019, DOI: 10.1103/PhysRevX.2.031019 (cit. on pp. 2, 27, 70, 75, 85, 87).
- [24] N. Delbos et al., "Lux A laser-plasma driven undulator beamline", Nucl. Instrum. Methods Phys. Res. A 909 (2018), pp. 318–322, DOI: 10.1016/j.nima.2018.01.082 (cit. on pp. 3, 93).

- [25] F. F. Chen, *Introduction to Plasma Physics and Controlled Fusion*, 3rd ed., vol. 1, Springer Cham, 2003, ISBN: 978-3-319-22309-4, DOI: 10.1007/978-3-319-22309-4 (cit. on p. 5).
- [26] P. Gibbon, "Introduction to Plasma Physics", *CAS Plasma Wake Acceleration*, CERN, 2016, pp. 51–65, doi: 10.5170/CERN-2016-001.51 (cit. on p. 6).
- [27] E. Esarey, C. B. Schroeder, and W. P. Leemans, "Physics of laser-driven plasma-based electron accelerators", Rev. Mod. Phys. 81 (2009), pp. 1229–1285, DOI: 10.1103/RevModPhys.81.1229 (cit. on pp. 8, 9).
- [28] J. M. Dawson, "Nonlinear Electron Oscillations in a Cold Plasma", Phys. Rev. 113 (1959), pp. 383–387, DOI: 10.1103/PhysRev.113.383 (cit. on p. 8).
- [29] P. Wilson, "Gradient limitation in accelerating structures imposed by surface melting", Proceedings of the 2003 Particle Accelerator Conference, vol. 2, IEEE, 2003, pp. 1282–1284, ISBN: 0-7803-7739-7, DOI: 10.1109/PAC.2003.1289679 (cit. on p. 8).
- [30] P. Gibbon, *Short Pulse Laser Interactions with Matter*, Imperial College Press, 2005, ISBN: 1-86094-135-4, DOI: 10.1142/p838 (cit. on p. 9).
- [31] J. Faure, "Plasma Injection Schemes for Laser-Plasma Accelerators", CERN Yellow Report (2016), pp. 143–157, DOI: 10.5170/CERN-2016-001.143 (cit. on p. 9).
- [32] W. P. Leemans et al., "Terahertz radiation from laser accelerated electron bunches", Phys. Plasmas 11 (2004), pp. 2899–2906, DOI: 10.1063/1.1652834 (cit. on p. 9).
- [33] J. van Tilborg et al., "Temporal Characterization of Femtosecond Laser-Plasma-Accelerated Electron Bunches Using Terahertz Radiation", Phys. Rev. Lett. 96 (2006), p. 014801, DOI: 10.1103/PhysRevLett.96.014801 (cit. on p. 9).
- [34] J. van Tilborg et al., "Single-shot spatiotemporal measurements of high-field terahertz pulses", Opt. Lett. 32 (2007), pp. 313–315, DOI: 10.1364/OL.32.000313 (cit. on p. 9).
- [35] M. Chen et al., "Theory of ionization-induced trapping in laser-plasma accelerators", Phys. Plasmas 19 (2012), p. 033101, poi: 10.1063/1.3689922 (cit. on p. 10).
- [36] M. Kirchen, "Novel Concepts for the Simulation and Experimental Demonstration of High-Quality Laser-Plasma Acceleration", PhD thesis: Universität Hamburg, 2021 (cit. on pp. 10, 13, 34, 93).
- [37] W. Lu et al., "Generating multi-GeV electron bunches using single stage laser wakefield acceleration in a 3D nonlinear regime", Phys. Rev. ST Accel. Beams 10 (2007), p. 061301, DOI: 10.1103/PhysRevSTAB.10.061301 (cit. on p. 10).
- [38] D. Strickland and G. Mourou, "Compression of amplified chirped optical pulses", Opt. Commun. 56 (1985), pp. 219–221, DOI: 10.1016/0030-4018(85)90120-8 (cit. on p. 11).

- [39] P. F. Moulton, "Spectroscopic and laser characteristics of Ti:Al₂O₃",
 J. Opt. Soc. Am. B 3 (1986), pp. 125–133, DOI: 10.1364/JOSAB.3.000125 (cit. on p. 11).
- [40] V. Leroux,"On the wavefront of ultrahigh intensity lasers: spatial contrast and gratings deformation",PhD thesis: Universität Hamburg, 2018 (cit. on p. 11).
- [41] T. F. J. Eichner, "Improved Pulse Characteristics and Power Scaling of Drive Lasers for Laser-Wakefield Acceleration", PhD thesis: Universität Hamburg, 2023, DOI: 10.3204/PUBDB-2023-06337 (cit. on pp. 11, 93).
- [42] P. Tournois, "Acousto-optic programmable dispersive filter for adaptive compensation of group delay time dispersion in laser systems", Opt. Commun. 140 (1997), pp. 245–249, poi: 10.1016/S0030-4018(97)00153-3 (cit. on p. 11).
- [43] S. Jalas, "Machine Learning Based Optimization of Laser-Plasma Accelerators", PhD thesis: Universität Hamburg, 2023, DOI: 10.3204/PUBDB-2024-01513 (cit. on p. 13).
- [44] T. Tajima, X. Q. Yan, and T. Ebisuzaki, "Wakefield acceleration", Rev. Mod. Phys. 4 (2020), p. 7, DOI: 10.1007/s41614-020-0043-z (cit. on p. 13).
- [45] A. J. Gonsalves et al., "Tunable laser plasma accelerator based on longitudinal density tailoring", Nature Phys. 7 (2011), pp. 862–866, DOI: 10.1038/nphys2071 (cit. on p. 13).
- [46] R. W. Hockney and J. W. Eastwood, *Computer simulation using particles*, Taylor & Francis, 1988, ISBN: 9780367806934, DOI: 10.1201/9780367806934 (cit. on p. 13).
- [47] R. Lehe et al., "A spectral, quasi-cylindrical and dispersion-free Particle-In-Cell algorithm", Comput. Phys. Commun. 203 (2016), pp. 66–82, DOI: 10.1016/j.cpc.2016.02.007 (cit. on p. 13).
- [48] L. Hübner, "Single Shot Emittance Measurements of Laser-Wakefield Accelerated Electron Beams at LUX", Master's Thesis: Universität Hamburg, 2018 (cit. on pp. 14, 15, 48, 93, 108).
- [49] P. Winkler, "Emittance Measurements at Laser-Wakefield Accelerators", PhD thesis: Universität Hamburg, 2019 (cit. on pp. 14, 15, 93).
- [50] S. Jalas et al., "Bayesian Optimization of a Laser-Plasma Accelerator", Phys. Rev. Lett. 126 (2021), p. 104801, DOI: 10.1103/PhysRevLett.126.104801 (cit. on pp. 14, 15, 38).
- [51] R. R. Wilcox, "Estimating Measures of Location and Scale", Introduction to Robust Estimation and Hypothesis Testing, ed. by R. R. Wilcox, 5th ed., Academic Press, 2022, pp. 45–106, ISBN: 978-0-12-820098-8, DOI: 10.1016/B978-0-12-820098-8.00009-9 (cit. on p. 14).
- [52] K. L. Brown, "A General First And Second Order Theory Of Beam Transport Optics And Its Application To The Design Of High-Energy Particle Spectrometers", *5th International Conference on High-Energy Accelerators*, 1965, pp. 507–514 (cit. on p. 18).

- [53] K. L. Brown, "First- and Second-Order Matrix Theory for the Design of Beam Transport Systems and Charged Particle Spectrometers." (1971), SLAC-75, Rev. 2, DOI: 10.2172/4742148 (cit. on p. 19).
- [54] J. Rossbach and P. Schmueser, "Basic course on accelerator optics", tech. rep. DESY-M-93-02, 1994, DOI: 10.5170/CERN-1994-001.17 (cit. on p. 20).
- [55] H. Wiedemann, *Particle Accelerator Physics*, Springer, Cham, 2015, ISBN: 978-3-319-18317-6, DOI: 10.1007/978-3-319-18317-6 (cit. on pp. 20, 42, 96).
- [56] P. M. Lapostolle, "Possible Emittance Increase through Filamentation Due to Space Charge in Continuous Beams", IEEE Trans. Nucl. Sci. 18 (1971), pp. 1101–1104, DOI: 10.1109/TNS.1971.4326292 (cit. on p. 24).
- [57] K. Floettmann, "Some basic features of the beam emittance", Phys. Rev. ST Accel. Beams 6 (2003), p. 034202, DOI: 10.1103/PhysRevSTAB.6.034202 (cit. on pp. 26, 37, 121).
- [58] E. D. Courant and H. S. Snyder, "Theory of the Alternating-Gradient Synchrotron", Ann. Physics 3 (1958), pp. 1–48, DOI: 10.1016/0003-4916(58)90012-5 (cit. on p. 26).
- [59] C. Pellegrini, "Free electron lasers: Development and applications", Part. Accel. 33 (1990), ed. by Y. Kimura et al., pp. 159–170 (cit. on pp. 27, 71).
- [60] C. Pellegrini, "Overview of Single Pass Free Electron Lasers", *Proc. EPAC'06* (Edinburgh, UK), European Particle Accelerator Conference 10, JACoW Publishing, Geneva, Switzerland, 2006, pp. 3636–3640 (cit. on p. 27).
- [61] M. Schreck and P. Wesolowski, "Analytical bunch compression studies for a linac-based electron accelerator", Phys. Rev. ST Accel. Beams 18 (2015), p. 100101, DOI: 10.1103/PhysRevSTAB.18.100101 (cit. on p. 31).
- [62] M. Sands, "A Beta mismatch parameter" (1991) (cit. on p. 34).
- [63] P. Emma and H.-D. Nuhn, "Quadrupole Magnet Error Sensitivities for FODO-Cell and Triplet Lattices in the LCLS Undulator", tech. rep. SLAC-TN-05-038, LCLS-TN-00-5, 2000, DOI: 10.2172/839698, URL: https://www.osti.gov/biblio/839698 (cit. on p. 34).
- [64] C. C. Finlay et al., "International Geomagnetic Reference Field: the eleventh generation", Geophys. J. Int. 183 (2010), pp. 1216–1230, DOI: 10.1111/j.1365-246X.2010.04804.x (cit. on p. 35).
- [65] F. J. Grüner et al., "Space-charge effects in ultrahigh current electron bunches generated by laser-plasma accelerators", Phys. Rev. ST Accel. Beams 12 (2009), p. 020701, DOI: 10.1103/PhysRevSTAB.12.020701 (cit. on p. 35).
- [66] A. Ashmore, R. Bartolini, and N. Delerue, "Numerical analysis of space charge effects in electron bunches at laser-driven plasma accelerators", Open Phys. 9 (2011), pp. 980–985, DOI: 10.2478/s11534-010-0142-5 (cit. on p. 35).

- [67] M. Migliorati et al.,
 "Intrinsic normalized emittance growth in laser-driven electron accelerators",
 Phys. Rev. ST Accel. Beams 16 (2013), p. 011302,
 DOI: 10.1103/PhysRevSTAB.16.011302 (cit. on p. 36).
- [68] C. A. Lindstrøm and E. Adli, "Design of general apochromatic drift-quadrupole beam lines", Phys. Rev. Accel. Beams 19 (2016), p. 071002, DOI: 10.1103/PhysRevAccelBeams.19.071002 (cit. on pp. 37, 96).
- [69] M. Ferrario, M. Migliorati, and L. Palumbo, "Space Charge Effects", CAS: Advanced Accelerator Physics 2013, ed. by W. Herr, CERN, 2014, pp. 331–356, DOI: 10.5170/CERN-2014-009.331 (cit. on pp. 39, 40).
- [70] G. Stupakov and G. Penn, *Classical Mechanics and Electromagnetism in Accelerator Physics*, 1st ed., Graduate texts in physics, Springer, ISBN: 978-3-319-90188-6, DOI: 10.1007/978-3-319-90188-6 (cit. on p. 42).
- [71] T. Ishikawa, "Accelerator-based X-ray sources: synchrotron radiation, X-ray free electron lasers and beyond", Philos. Trans. R. Soc. A 377 (2019), p. 20180231, DOI: 10.1098/rsta.2018.0231 (cit. on p. 42).
- [72] S. Heifets, G. Stupakov, and S. Krinsky, "Coherent synchrotron radiation instability in a bunch compressor", Phys. Rev. ST Accel. Beams 5 (6 2002), p. 064401, DOI: 10.1103/PhysRevSTAB.5.064401 (cit. on p. 42).
- [73] A. Novokhatski, "Coherent Synchrotron Radiation: Theory and Simulations.", 2012, pp. 127–144 (cit. on p. 44).
- [74] E. Saldin, E. Schneidmiller, and M. Yurkov, "On the coherent radiation of an electron bunch moving in an arc of a circle", Nucl. Instrum. Methods Phys. Res. A 398 (1997), pp. 373–394, DOI: 10.1016/S0168-9002(97)00822-X (cit. on p. 44).
- [75] Y. S. Derbenev et al., "Microbunch radiative tail head interaction", tech. rep. TESLA-FEL 1995-05, DESY, 1995, DOI: 10.3204/PUBDB-2018-04128 (cit. on p. 45).
- [76] A. D. Brynes et al., "Beyond the limits of 1D coherent synchrotron radiation", New J. Phys. 20 (2018), p. 073035, poi: 10.1088/1367-2630/aad21d (cit. on p. 45).
- [77] G. V. Stupakov, "Effect of centrifugal transverse wakefield for microbunch in bend", AIP Conf. Proc. 468 (1999), pp. 334–347, DOI: 10.1063/1.58423 (cit. on p. 46).
- [78] Y. Cai, "Coherent synchrotron radiation by electrons moving on circular orbits", Phys. Rev. Accel. Beams 20 (2017), p. 064402, DOI: 10.1103/PhysRevAccelBeams.20.064402 (cit. on p. 46).
- [79] Y. Cai and Y. Ding, "Three-dimensional effects of coherent synchrotron radiation by electrons in a bunch compressor", Phys. Rev. Accel. Beams 23 (2020), p. 014402, DOI: 10.1103/PhysRevAccelBeams.23.014402 (cit. on p. 46).

- [80] D. Z. Khan and T. O. Raubenheimer,
 "Novel bunch compressor chicane: The five-bend chicane",
 Phys. Rev. Accel. Beams 25 (2022), p. 090701,
 DOI: 10.1103/PhysRevAccelBeams.25.090701 (cit. on p. 46).
- [81] Y. Li and X. Huang, "Extraction of the Lie Map from Realistic 3D Magnetic Field Map", Proc. IPAC'12 (New Orleans, LA, USA, May 2012), JACoW Publishing, Geneva, Switzerland, pp. 1308–1310 (cit. on p. 47).
- [82] P. Mishra et al., "Transfer matrix calculation for ion optical elements using real fields", Nucl. Instrum. Methods Phys. Res. A 885 (2018), pp. 124–133, DOI: 10.1016/j.nima.2017.11.057 (cit. on p. 47).
- [83] M. Borland, "ELEGANT: A flexible SDDS-compliant code for accelerator simulation", tech. rep. LS-287, Argonne National Lab, IL, 2000, DOI: 10.2172/761286 (cit. on pp. 47, 48, 119).
- [84] K. G. Steffen, *High energy beam optics*, vol. 17, Interscience monographs and texts in physics and astronomy, Interscience Publishers, 1965 (cit. on pp. 47, 48).
- [85] R. Baartman and D. Kaltchev, "Short quadrupole parametrization", 2007 IEEE Particle Accelerator Conference (PAC), THPAN005, 2007, pp. 3229–3231, DOI: 10.1109/PAC.2007.4440381 (cit. on p. 48).
- [86] V. Balandin, W. Decking, and N. Golubeva, "Notes on Steffen Parameters of Extended Fringe-Field Quadrupoles", *Proc. of IPAC'16* (Busan, Korea), International Particle Accelerator Conference 7, JACoW, 2016, pp. 3226–3228, ISBN: 978-3-95450-147-2, DOI: 10.18429/JACoW-IPAC2016-THPMB005 (cit. on p. 48).
- [87] Y.-M. Peng and G. Xu, "Analytical transfer matrix of a quadrupole fringe", Chin. Phys. C 35 (2011), p. 1047, DOI: 10.1088/1674-1137/35/11/013 (cit. on p. 48).
- [88] H. Matsuda and H. Wollnik, "Third order transfer matrices for the fringing field of magnetic and electrostatic quadrupole lenses", Nucl. Instrum. and Methods 103 (1972), pp. 117–124, DOI: 10.1016/0029-554X(72)90468-5 (cit. on p. 48).
- [89] D. Zhou et al., "Explicit Maps for the Fringe Field of a Quadrupole", Conf. Proc. C 100523 (2010), THPD091 (cit. on p. 48).
- [90] N. Golubeva et al., "Steffen Hard-Edge Model for Quadrupoles with Extended Fringe-Fields at the European XFEL", *Proc. FEL'19* (Hamburg, Germany), Free Electron Laser Conference 39, JACoW Publishing, Geneva, Switzerland, 2019, pp. 588–591, ISBN: 978-3-95450-210-3, DOI: 10.18429/JACoW-FEL2019-THP001 (cit. on p. 48).
- [91] K. P. Blum, "Calibration of an Electro-Dipole Spectrometer for the LUX Laser-Plasma-Accelerator Beamline Upgrade", Bachelor's Thesis: Universität Hamburg, 2020 (cit. on pp. 48, 108).

- [92] K. Floettmann, "A Space Charge Tracking Algorithm", DESY, Hamburg, 1997, URL: https://www.desy.de/~mpyflo/ (visited on 2023-12-05) (cit. on p. 48).
- [93] P. J. Neyman et al., "Free Electron Lasers in 2017", Proc. 38th Int. Free Electron Laser Conf. (FEL'17) (Santa Fe, NM, USA), JACoW Publishing, pp. 204–209, DOI: 10.18429/JACoW-FEL2017-M0P066 (cit. on p. 51).
- [94] G. Ramian, "Free Electron Laser", 2019, URL: http://sbfel3.ucsb.edu/www/vl_fel.html (visited on 2023-11-20) (cit. on p. 51).
- [95] V. L. Ginsburg, "On the emission of microradiowaves and their absorption in the air", *Izv. AN USSR ser. phys.* Vol. 11, 2, USSR Academy of Sciences, 1947, pp. 165–182 (cit. on p. 51).
- [96] H. Motz, "Applications of the Radiation from Fast Electron Beams",J. Appl. Phys. 22 (1951), pp. 527–535, DOI: 10.1063/1.1700002 (cit. on p. 51).
- [97] H. Motz, W. Thon, and R. N. Whitehurst,
 "Experiments on Radiation by Fast Electron Beams", J. Appl. Phys. 24 (1953), pp. 826–833,
 DOI: 10.1063/1.1721389 (cit. on p. 51).
- [98] J. M. J. Madey, "Stimulated Emission of Bremsstrahlung in a Periodic Magnetic Field", J. Appl. Phys. 42 (1971), pp. 1906–1913, DOI: 10.1063/1.1660466 (cit. on p. 51).
- [99] J. M. J. Madey, H. A. Schwettman, and W. M. Fairbank, "A Free Electron Laser", IEEE Trans. Nucl. Sci. 20 (1973), pp. 980–983, DOI: 10.1109/TNS.1973.4327304 (cit. on p. 51).
- [100] L. R. Elias et al., "Observation of Stimulated Emission of Radiation by Relativistic Electrons in a Spatially Periodic Transverse Magnetic Field", Phys. Rev. Lett. 36 (1976), pp. 717–720, DOI: 10.1103/PhysRevLett.36.717 (cit. on p. 51).
- [101] D. A. G. Deacon et al., "First Operation of a Free-Electron Laser", Phys. Rev. Lett. 38 (1977), pp. 892–894, DOI: 10.1103/PhysRevLett.38.892 (cit. on p. 51).
- [102] A. M. Kondratenko and E. L. Saldin, "Generation of coherent radiation by relativistic electron beam in an ondulator", Dokl. AN USSR 249 (1979), pp. 843–847 (cit. on p. 51).
- [103] A. M. Kondratenko and E. L. Saldin, "Generation of coherent radiation by a relativistic electron beam in an ondulator", Part. Accel. 10 (1980), pp. 207–216 (cit. on p. 51).
- [104] R. Bonifacio, C. Pellegrini, and L. Narducci, "Collective instabilities and high-gain regime in a free electron laser", Opt. Commun. 50 (1984), pp. 373–378, DOI: 10.1016/0030-4018(84)90105-6 (cit. on pp. 51, 65).

- [105] P. Schmüser et al., *Free-Electron Lasers in the Ultraviolet and X-Ray Regime: Physical Principles, Experimental Results, Technical Realization*, 2nd ed., vol. 258, Springer Cham, 2014, ISBN: 978-3-319-04081-3, DOI: 10.1007/978-3-319-04081-3 (cit. on pp. 52, 62, 64, 65, 67–69, 73, 87, 88, 96).
- [106] J. A. Clarke, *The Science and Technology of Undulators and Wigglers*, Oxford Series on Synchrotron Radiation, Oxford University Press, 2004, ISBN: 9780198508557, DOI: 10.1093/acprof:oso/9780198508557.001.0001 (cit. on pp. 53, 54, 56, 58, 59, 61, 109).
- [107] N. V. Smolyakov and M. A. Galchenkova, "Electron Motion in the Three-Dimensional Field of Undulator", Phys. At. Nucl. 80 (2017), pp. 1580–1587, DOI: 10.1134/S106377881710009X (cit. on p. 54).
- [108] A. Loulergue et al., "Beam manipulation for compact laser wakefield accelerator based free-electron lasers", New J. Phys. 17 (2015), p. 023028, DOI: 10.1088/1367-2630/17/2/023028 (cit. on pp. 56, 84, 88, 95–97).
- [109] P. Elleaume, "Theory of undulators and wigglers",

 CAS CERN Accelerator School: Synchrotron Radiation and Free-electron Lasers: Chester,

 UK 6-13 Apr 1989. CAS CERN Accelerator School and Daresbury Laboratory: Course on

 Synchrotron Radiation and Free-electron Lasers, ed. by S. Turner, CERN. Geneva, 1990,

 pp. 142–157, DOI: 10.5170/CERN-1990-003.142 (cit. on p. 56).
- [110] K.-J. Kim, "Characteristics of synchrotron radiation", *AIP Conf. Proc.* Vol. 184, 1, 1989, pp. 565–632, DOI: 10.1063/1.38046 (cit. on pp. 58, 72).
- [111] ISO/TC 20/SC 14, "Space environment (natural and artificial) Process for determining solar irradiances", Standard, International Organization for Standardization, 2007 (cit. on p. 58).
- [112] B. Henke, E. Gullikson, and J. Davis, "X-Ray Interactions: Photoabsorption, Scattering, Transmission, and Reflection at E = 50-30,000 eV, Z = 1-92", At. Data Nucl. Data Tables 54 (1993), pp. 181–342, poi: 10.1006/adnd.1993.1013 (cit. on pp. 58, 112).
- [113] E. Gullikson, "X-Ray Interactions With Matter", 1995–2023, URL: https://henke.lbl.gov/optical_constants/ (visited on 2023-11-10) (cit. on p. 58).
- [114] M. Trunk, "Design, Construction and Commissioning of a Cryogenic Undulator for Laser-Plasma Based Free Electron Lasing at LUX", PhD thesis: Universität Hamburg, 2022 (cit. on pp. 58, 72, 93, 97, 109, 111, 112, 114, 115, 128).
- [115] K.-J. Kim, "Brightness, coherence and propagation characteristics of synchrotron radiation", Nucl. Instrum. Methods Phys. Res. A 246 (1986), pp. 71–76, DOI: 10.1016/0168-9002(86)90048-3 (cit. on p. 60).

- [116] D. Attwood and A. Sakdinawat, *X-rays and extreme ultraviolet radiation: principles and applications*, 2nd ed., Cambridge University Press, 2016, ISBN: 9781107062894 (cit. on p. 61).
- [117] T. Tanaka, "Major upgrade of the synchrotron radiation calculation code *SPECTRA*", J. Synchrotron Radiat. 28 (2021), pp. 1267–1272, DOI: 10.1107/S1600577521004100 (cit. on p. 61).
- [118] Z. Huang and K.-J. Kim, "Review of x-ray free-electron laser theory", Phys. Rev. ST Accel. Beams 10 (2007), p. 034801, DOI: 10.1103/PhysRevSTAB.10.034801 (cit. on pp. 65, 68, 72).
- [119] W. Ackermann et al., "Operation of a free-electron laser from the extreme ultraviolet to the water window", Nat. Photonics 1 (2007), pp. 336–342, DOI: 10.1038/nphoton.2007.76 (cit. on p. 66).
- [120] E. Saldin, E. Schneidmiller, and M. Yurkov, *The Physics of Free Electron Lasers*, Advanced Texts in Physics, Springer Berlin Heidelberg, 2000, ISBN: 978-3-540-66266-2, DOI: 10.1007/978-3-662-04066-9 (cit. on pp. 67, 70, 88).
- [121] A. He, L. Yang, and L. Yu, "High-Gain Free-Electron Laser Theory, Introduction", Synchrotron Light Sources and Free-Electron Lasers: Accelerator Physics, Instrumentation and Science Applications, ed. by E. J. Jaeschke et al., Springer International Publishing, 2016, pp. 119–160, ISBN: 978-3-319-14394-1, DOI: 10.1007/978-3-319-14394-1_2 (cit. on p. 67).
- [122] K.-J. Kim, "Three-Dimensional Analysis of Coherent Amplification and Self-Amplified Spontaneous Emission in Free-Electron Lasers", Phys. Rev. Lett. 57 (1986), pp. 1871–1874, DOI: 10.1103/PhysRevLett.57.1871 (cit. on p. 67).
- [123] C. Maroli, V. Petrillo, and M. Ferrario, "One-dimensional free-electron laser equations without the slowly varying envelope approximation",
 Phys. Rev. ST Accel. Beams 14 (2011), p. 070703,
 DOI: 10.1103/PhysRevSTAB.14.070703 (cit. on pp. 67, 79, 129).
- [124] N. Piovella and L. Volpe, "A Review of High-Gain Free-Electron Laser Theory", Atoms 9 (2021), p. 28, DOI: 10.3390/atoms9020028 (cit. on p. 68).
- [125] M. Rezvani Jalal and F. Aghamir, "Effect of energy spread on micro-bunching from shot noise in SASE FELs", Phys. Lett. A 375 (2011), pp. 1796–1802, DOI: https://doi.org/10.1016/j.physleta.2011.02.021 (cit. on p. 70).
- [126] T. Seggebrock et al.,
 "Bunch decompression for laser-plasma driven free-electron laser demonstration schemes",
 Phys. Rev. ST Accel. Beams 16 (2013), p. 070703,
 DOI: 10.1103/PhysRevSTAB.16.070703 (cit. on p. 70).
- [127] C. Schroeder et al., "Application of laser-plasma accelerator beams to free-electron lasers", FEL 2012 34th International Free Electron Laser Conference (2012), pp. 658–661 (cit. on p. 70).

- [128] J. Murphy and C. Pellegrini, "Introduction to the physics of the free electron laser", *Frontiers of Particle Beams*, ed. by M. Month and S. Turner, Springer Berlin Heidelberg, 1988, pp. 163–219, ISBN: 978-3-540-38935-4 (cit. on p. 71).
- [129] M. Xie, "Transverse coherence of self-amplified spontaneous emission", Nucl. Instrum. Methods Phys. Res. A 445 (2000), pp. 67–71, DOI: 10.1016/S0168-9002(00)00115-7 (cit. on p. 72).
- [130] M. Xie, D. A. G. Deacon, and J. M. J. Madey, "Eigenmode analysis of optical guiding in free-electron lasers", Phys. Rev. A 41 (1990), pp. 1662–1669, DOI: 10.1103/PhysRevA.41.1662 (cit. on p. 72).
- [131] E. Scharlemann, A. Sessler, and J. Wurtele, "Optical guiding in a free electron laser", Nucl. Instrum. Methods Phys. Res. A 239 (1985), pp. 29–35, DOI: https://doi.org/10.1016/0168-9002(85)90694-1 (cit. on p. 73).
- [132] M. Xie, "Design optimization for an X-ray free electron laser driven by SLAC linac", Proceedings Particle Accelerator Conference, vol. 1, 1995, pp. 183–185, DOI: 10.1109/PAC.1995.504603 (cit. on p. 74).
- [133] M. Xie, "Exact and variational solutions of 3D eigenmodes in high gain FELs", Nucl. Instrum. Methods Phys. Res. A 445 (2000), pp. 59–66, DOI: 10.1016/S0168-9002(00)00114-5 (cit. on p. 74).
- [134] R. Bonifacio and B. McNeil, "Slippage and superradiance in the high-gain FEL",
 Nucl. Instrum. Methods Phys. Res. A 272 (1988), pp. 280–288,
 DOI: 10.1016/0168-9002 (88) 90238-0 (cit. on p. 77).
- [135] R. Bonifacio et al., "Spectrum, temporal structure, and fluctuations in a high-gain free-electron laser starting from noise", Phys. Rev. Lett. 73 (1994), pp. 70–73, DOI: 10.1103/PhysRevLett.73.70 (cit. on pp. 77, 79).
- [136] R. Bonifacio et al., "A study of linewidth, noise and fluctuations in a FEL operating in SASE",
 Nucl. Instrum. Methods Phys. Res. A 341 (1994), pp. 181–185,
 DOI: 10.1016/0168-9002(94)90344-1 (cit. on pp. 77, 88).
- [137] R. Bonifacio et al., "Physics of the high-gain FEL and superradiance", Riv. Nuovo Cimento 13 (1990), pp. 1–69, DOI: 10.1007/BF02770850 (cit. on p. 78).
- [138] R. Bonifacio, C. Maroli, and N. Piovella, "Slippage and superradiance in the high-gain FEL: Linear theory", Opt. Commun. 68 (1988), pp. 369–374, DOI: 10.1016/0030-4018(88)90234-9 (cit. on p. 78).
- [139] S. Bajlekov, "Towards a free-electron laser driven by electrons from a laser-wakefield accelerator: simulations and bunch diagnostics", PhD thesis: Oxford University, UK, 2011 (cit. on pp. 78, 79).

- [140] L. Giannessi, P. Musumeci, and S. Spampinati, "Nonlinear pulse evolution in seeded free-electron laser amplifiers and in free-electron laser cascades",
 J. Appl. Phys. 98 (2005), p. 043110, DOI: 10.1063/1.2010624,
 URL: https://doi.org/10.1063/1.2010624 (cit. on p. 79).
- [141] B. McNeil, G. Robb, and D. Jaroszynski, "Self-amplification of coherent spontaneous emission in the free electron laser", Opt. Comm. 165 (1999), pp. 65–70, DOI: 10.1016/S0030-4018(99)00222-9 (cit. on p. 79).
- [142] D. A. Jaroszynski et al., "Coherent startup of an infrared free-electron laser", Phys. Rev. Lett. 71 (1993), pp. 3798–3801, DOI: 10.1103/PhysRevLett.71.3798 (cit. on p. 79).
- [143] R. Bonifacio et al., "New effects in the physics of high-gain free-electron lasers; a proposed experiment and possible applications", Riv. Nuovo Cimento 15 (1992), pp. 1–52, DOI: 10.1007/BF02845045 (cit. on p. 79).
- [144] N. Piovella, "High gain free electron laser amplifiers starting from coherent and incoherent spontaneous emission", Phys. Plasmas 6 (1999), pp. 3358–3368, DOI: 10.1063/1.873575 (cit. on pp. 79, 96).
- [145] Z. Huang and K.-J. Kim, "Effects of bunch density gradient in high-gain free-electron lasers", Nucl. Instrum. Methods Phys. Res. A 445 (2000), pp. 105–109, DOI: 10.1016/S0168-9002(00)00122-4 (cit. on pp. 79, 96).
- [146] R. Bonifacio, N. Piovella, and B. W. J. McNeil, "Superradiant evolution of radiation pulses in a free-electron laser", Phys. Rev. A 44 (1991), R3441–R3444, DOI: 10.1103/PhysRevA.44.R3441 (cit. on pp. 79, 129).
- [147] L. T. Campbell et al., "Analysis of ultra-short bunches in free-electron lasers",New J. Phys. 22 (2020), p. 073031, DOI: 10.1088/1367-2630/ab9850 (cit. on pp. 79, 129).
- [148] T. Tanaka, H. Kitamura, and T. Shintake, "Consideration on the BPM alignment tolerance in X-ray FELs", Nucl. Instrum. Methods Phys. Res. A 528 (2004), pp. 172–178, DOI: 10.1016/j.nima.2004.04.040 (cit. on p. 80).
- [149] B. Faatz, J. Pflüger, and Y. Nikitina, "Study of the undulator specification for the VUV-FEL at the TESLA test facility", Nucl. Instrum. Methods Phys. Res. A 393 (1997), pp. 380–384, DOI: 10.1016/S0168-9002(97)00517-2 (cit. on pp. 80, 81).
- [150] B. Faatz, J. Pflüger, and P. Pierini, "Dependence of the VUV-FEL performance at the TESLA Test Facility on magnetic field errors",
 Nucl. Instrum. Methods Phys. Res. A 375 (1996), pp. 441–444,
 DOI: 10.1016/0168-9002(95)01199-4 (cit. on pp. 80, 81).

- [151] K.-J. Kim, "Kick and phase errors in spontaneous and amplified radiation", Nucl. Instrum. Methods Phys. Res. A 445 (2000), pp. 24–27, DOI: 10.1016/S0168-9002(00)00107-8 (cit. on p. 81).
- [152] N. Kroll, P. Morton, and M. Rosenbluth, "Free-electron lasers with variable parameter wigglers", IEEE J. Quantum Electron. 17 (1981), pp. 1436–1468, poi: 10.1109/JQE.1981.1071285 (cit. on p. 85).
- [153] T. J. Orzechowski et al., "High-Efficiency Extraction of Microwave Radiation from a Tapered-Wiggler Free-Electron Laser", Phys. Rev. Lett. 57 (1986), pp. 2172–2175, DOI: 10.1103/PhysRevLett.57.2172 (cit. on p. 85).
- [154] E. A. Schneidmiller and M. V. Yurkov,
 "Optimization of a high efficiency free electron laser amplifier",
 Phys. Rev. ST Accel. Beams 18 (2015), p. 030705,
 DOI: 10.1103/PhysRevSTAB.18.030705 (cit. on p. 85).
- [155] E. A. Schneidmiller and M. V. Yurkov, "Obtaining high degree of circular polarization at x-ray free electron lasers via a reverse undulator taper",
 Phys. Rev. ST Accel. Beams 16 (11 2013), p. 110702,
 DOI: 10.1103/PhysRevSTAB.16.110702 (cit. on p. 85).
- [156] L. T. Campbell and A. R. Maier, "Velocity dispersion of correlated energy spread electron beams in the free electron laser", New J. Phys. 19 (2017), p. 033037, DOI: 10.1088/1367-2630/aa6205 (cit. on pp. 85, 86, 119).
- [157] E. L. Saldin, E. A. Schneidmiller, and V. Yurkov M., "Self-amplified spontaneous emission FEL with energy-chirped electron beam and its application for generation of attosecond x-ray pulses", Phys. Rev. ST Accel. Beams 9 (2006), p. 050702, DOI: 10.1103/PhysRevSTAB.9.050702 (cit. on p. 86).
- [158] W. M. Fawley et al., "Tapered undulators for SASE FELs",
 Nucl. Instrum. Methods Phys. Res. A 483 (2002), pp. 537–541,
 DOI: 10.1016/S0168-9002(02)00377-7 (cit. on p. 87).
- [159] Z. Huang and G. Stupakov, "Free electron lasers with slowly varying beam and undulator parameters", Phys. Rev. ST Accel. Beams 8 (2005), p. 040702, DOI: 10.1103/PhysRevSTAB.8.040702 (cit. on p. 87).
- [160] T. Tanaka, "SIMPLEX: simulator and postprocessor for free-electron laser experiments", Journal of Synchrotron Radiation 22 (2015), pp. 1319–1326, DOI: 10.1107/S1600577515012850 (cit. on p. 88).
- [161] C. M. Werle, "First Undulator Experiments at the LUX Beamline: Towards a Plasma-Based Accelerator as a Soft X-ray Source", PhD thesis: Universität Hamburg, 2019 (cit. on p. 93).

- [162] P. Messner, "Tunable Laser-Plasma Acceleration with Ionization Injection", PhD thesis: Universität Hamburg, 2020 (cit. on p. 93).
- [163] T. Hülsenbusch, "Optimizing White-light Generation for an Optical Parametric Chirped Pulse Amplifier used as a Titanium-Sapphire Seed Laser", Dissertation, Universität Hamburg, 2024, Dissertation: Universität Hamburg, 2024, p. 181, DOI: 10.3204/PUBDB-2024-07610 (cit. on p. 93).
- [164] K. Halbach, "Permanent Multipole Magnets with Adjustable Strength", IEEE Trans. Nucl. Sci. 30 (1983), pp. 3323–3325, DOI: 10.1109/TNS.1983.4336645 (cit. on p. 93).
- [165] F. Marteau et al., "Variable high gradient permanent magnet quadrupole (QUAPEVA)", Appl. Phys. Lett. 111 (2017), p. 253503, DOI: 10.1063/1.4986856 (cit. on p. 93).
- [166] P. Chen, "A possible final focusing mechanism for linear colliders", Part. Accel. 20 (1987), pp. 171–182 (cit. on p. 93).
- [167] R. Lehe et al., "Laser-plasma lens for laser-wakefield accelerators", Phys. Rev. ST Accel. Beams 17 (2014), p. 121301, DOI: 10.1103/PhysRevSTAB.17.121301 (cit. on p. 93).
- [168] D. Lipka et al., "Orthogonal Coupling in Cavity BPM with Slots", *Proc. DIPAC'09* (Basel, Switzerland, May 2009), JACoW Publishing, Geneva, Switzerland, pp. 44–46 (cit. on p. 108).
- [169] K. Corperation, *Keyence Optical Micrometers*, Available at https://www.keyence.de/products/measure/micrometer/ls-7000/models/ls-7070/ (accessed 2021-09-01), 2006 (cit. on p. 111).
- [170] T. L. Chow, *Introduction to Electromagnetic Theory: A Modern Perspective*, Jones and Bartlett Publishers, 2005, ISBN: 9780763738273 (cit. on p. 115).
- [171] L. T. Campbell and B. W. J. McNeil, "Puffin: A three dimensional, unaveraged free electron laser simulation code", Phys. Plasmas 19 (2012), p. 093119, DOI: 10.1063/1.4752743 (cit. on p. 119).
- [172] L. Campbell et al., "An Updated Description of the FEL Simulation Code Puffin", Proc. 9th International Particle Accelerator Conference (IPAC'18), Vancouver, BC, Canada, April 29-May 4, 2018 (Vancouver, BC, Canada), 9, JACoW Publishing, 2018, pp. 4579–4582, ISBN: 978-3-95450-184-7, DOI: 10.18429/JACoW-IPAC2018-THPMK112 (cit. on p. 119).
- [173] S. Biedron et al.,

 "Multi-dimensional free-electron laser simulation codes: a comparison study",

 Nucl. Instrum. Methods Phys. Res. A 445 (2000), pp. 110–115,

 DOI: 10.1016/S0168-9002(00)00124-8 (cit. on p. 119).
- [174] B. W. Garcia et al., "Comparing FEL Codes for Advanced Configurations", *Proc. FEL'17* (Santa Fe, NM, USA, Aug. 2017), JACoW Publishing, Geneva, Switzerland, pp. 60–63, DOI: 10.18429/JACoW-FEL2017-MOP016 (cit. on p. 119).

- [175] L. Campbell et al., "Unaveraged modelling of a LWFA driven FEL", FEL 2013: Proceedings of the 35th International Free-Electron Laser Conference (New York, NY, USA), ed. by C. Scholl and V. R. W. Schaa, JACoW, 2013, pp. 43–46 (cit. on pp. 119, 123).
- [176] T. Tanaka, "Accelerating the convergence of free electron laser simulations by retrieving a spatially coherent component of microbunching",
 Phys. Rev. Accel. Beams 27 (2024), p. 030703,
 DOI: 10.1103/PhysRevAccelBeams.27.030703 (cit. on p. 122).
- [177] C. Penman and B. McNeil, "Simulation of input electron noise in the free-electron laser", Opt. Commun. 90 (1992), pp. 82–84, DOI: 10.1016/0030-4018(92)90333-M (cit. on p. 123).
- [178] W. M. Fawley, "Algorithm for loading shot noise microbunching in multidimensional, free-electron laser simulation codes", Phys. Rev. ST Accel. Beams 5 (2002), p. 070701, DOI: 10.1103/PhysRevSTAB.5.070701 (cit. on p. 123).
- [179] B. W. J. McNeil, M. W. Poole, and G. R. M. Robb, "Unified model of electron beam shot noise and coherent spontaneous emission in the helical wiggler free electron laser", Phys. Rev. ST Accel. Beams 6 (2003), p. 070701, DOI: 10.1103/PhysRevSTAB.6.070701 (cit. on p. 123).
- [180] P. Traczykowski, L. Campbell, and B. MNeil, "Up-sampling of electron beam simulation particles with addition of shot-noise", Comput. Phys. Commun. 286 (2023), p. 108661, DOI: 10.1016/j.cpc.2023.108661, URL: https://www.sciencedirect.com/science/article/pii/S0010465523000061 (cit. on p. 123).
- [181] L. T. Campbell, *Puffin Manual*, Available at https://github.com/UKFELs/Puffin, 2018 (cit. on p. 123).

List of Figures

 2.4 Illustration of (a) showing gas inlets at the bottom, an outlet at the top (in the experiment on the side), and the laser envelope propagating to the right, and (b) the longitudinal plasma density profile. Shown are pure hydrogen gas H₂ (blue), mixed gas doped with nitrogen N₂ + H₂ (orange) and resulting plasma density (grey) 2.5 Transverse and longitudinal distributions from a particle-in-cell simulation with laser and plasma properties matching those used at <i>LUX</i>. (a) Horizontal position and angle, (b) Vertical position and angle, (c) Longitudinal position and total energy. Raw data from simulation was provided by S. Jalas. The beam distribution was rescaled to match experimentally observed parameters. The curves represent the projected 1<i>D</i> 			
 2.2 Illustration of laser-plasma acceleration. Electrons of the plasma are expelled from high intensity regions of the laser pulse. In response to this expulsion, the electrons oscillate about the propagation axis with a frequency approximately equal to ~ ω_p, generating a density modulation in the plasma with a corresponding electric field trailing the laser pulse. Possible trajectories for electrons getting accelerated in the plasma wake are illustrated for (a) self-injection and (b) ionization injection 2.3 Overview of the ANGUS amplifier stages from top to bottom. Pump laser energies are indicated in green on the left. The temporal shape of the laser pulse is schematically depicted on the right. The color gradient should illustrate the temporal chirp of the pulse. The pulse is provided by the optical parametric chirped pulse amplification (OPCPA) frontend and stretched in time before being amplified to higher energy levels in the subsequent amplifier stages. Finally, before the beam is sent to LUX and the plasma source, it is recompressed to achieve the targeted power levels and short pulse duration	2.1	pulse in the $1d$ limit. The laser pulse propagates to the right and is centered at $\zeta=0$. The spatial scale is normalized to the plasma wavelength λ_p . Displayed are the electric potential ϕ , the electron density modulation $n-1$, the normalized longitudinal electric field E_z/E_0 and the normalized laser intensity $\langle a^2 \rangle$ for two cases: (a) Non-relativistic	6
 plasma wake are illustrated for (a) self-injection and (b) ionization injection 2.3 Overview of the <i>ANGUS</i> amplifier stages from top to bottom. Pump laser energies are indicated in green on the left. The temporal shape of the laser pulse is schematically depicted on the right. The color gradient should illustrate the temporal chirp of the pulse. The pulse is provided by the optical parametric chirped pulse amplification (OPCPA) frontend and stretched in time before being amplified to higher energy levels in the subsequent amplifier stages. Finally, before the beam is sent to <i>LUX</i> and the plasma source, it is recompressed to achieve the targeted power levels and short pulse duration	2.2	Illustration of laser-plasma acceleration. Electrons of the plasma are expelled from high intensity regions of the laser pulse. In response to this expulsion, the electrons oscillate about the propagation axis with a frequency approximately equal to $\sim \omega_p$,	
 Overview of the <i>ANGUS</i> amplifier stages from top to bottom. Pump laser energies are indicated in green on the left. The temporal shape of the laser pulse is schematically depicted on the right. The color gradient should illustrate the temporal chirp of the pulse. The pulse is provided by the optical parametric chirped pulse amplification (OPCPA) frontend and stretched in time before being amplified to higher energy levels in the subsequent amplifier stages. Finally, before the beam is sent to <i>LUX</i> and the plasma source, it is recompressed to achieve the targeted power levels and short pulse duration. 2.4 Illustration of (a) showing gas inlets at the bottom, an outlet at the top (in the experiment on the side), and the laser envelope propagating to the right, and (b) the longitudinal plasma density profile. Shown are pure hydrogen gas H₂ (blue), mixed gas doped with nitrogen N₂ + H₂ (orange) and resulting plasma density (grey). 2.5 Transverse and longitudinal distributions from a particle-in-cell simulation with laser and plasma properties matching those used at <i>LUX</i>. (a) Horizontal position and angle, (b) Vertical position and angle, (c) Longitudinal position and total energy. Raw data from simulation was provided by S. Jalas. The beam distribution was rescaled to match experimentally observed parameters. The curves represent the projected 1<i>D</i> 			_
pulse. The pulse is provided by the optical parametric chirped pulse amplification (OPCPA) frontend and stretched in time before being amplified to higher energy levels in the subsequent amplifier stages. Finally, before the beam is sent to <i>LUX</i> and the plasma source, it is recompressed to achieve the targeted power levels and short pulse duration	2.3	Overview of the <i>ANGUS</i> amplifier stages from top to bottom. Pump laser energies are indicated in green on the left. The temporal shape of the laser pulse is schematically	7
 plasma source, it is recompressed to achieve the targeted power levels and short pulse duration. 2.4 Illustration of (a) showing gas inlets at the bottom, an outlet at the top (in the experiment on the side), and the laser envelope propagating to the right, and (b) the longitudinal plasma density profile. Shown are pure hydrogen gas H₂ (blue), mixed gas doped with nitrogen N₂ + H₂ (orange) and resulting plasma density (grey). 2.5 Transverse and longitudinal distributions from a particle-in-cell simulation with laser and plasma properties matching those used at <i>LUX</i>. (a) Horizontal position and angle, (b) Vertical position and angle, (c) Longitudinal position and total energy. Raw data from simulation was provided by S. Jalas. The beam distribution was rescaled to match experimentally observed parameters. The curves represent the projected 1<i>D</i> 		pulse. The pulse is provided by the optical parametric chirped pulse amplification (OPCPA) frontend and stretched in time before being amplified to higher energy levels	
 2.4 Illustration of (a) showing gas inlets at the bottom, an outlet at the top (in the experiment on the side), and the laser envelope propagating to the right, and (b) the longitudinal plasma density profile. Shown are pure hydrogen gas H₂ (blue), mixed gas doped with nitrogen N₂ + H₂ (orange) and resulting plasma density (grey) 2.5 Transverse and longitudinal distributions from a particle-in-cell simulation with laser and plasma properties matching those used at <i>LUX</i>. (a) Horizontal position and angle, (b) Vertical position and angle, (c) Longitudinal position and total energy. Raw data from simulation was provided by S. Jalas. The beam distribution was rescaled to match experimentally observed parameters. The curves represent the projected 1<i>D</i> 			
nitrogen N ₂ + H ₂ (orange) and resulting plasma density (grey)	2.4	Illustration of (a) showing gas inlets at the bottom, an outlet at the top (in the experiment on the side), and the laser envelope propagating to the right, and (b) the longitudinal	12
2.5 Transverse and longitudinal distributions from a particle-in-cell simulation with laser and plasma properties matching those used at LUX. (a) Horizontal position and angle, (b) Vertical position and angle, (c) Longitudinal position and total energy. Raw data from simulation was provided by S. Jalas. The beam distribution was rescaled to match experimentally observed parameters. The curves represent the projected 1D			14
	2.5	Transverse and longitudinal distributions from a particle-in-cell simulation with laser and plasma properties matching those used at <i>LUX</i> . (a) Horizontal position and angle, (b) Vertical position and angle, (c) Longitudinal position and total energy. Raw data from simulation was provided by S. Jalas. The beam distribution was rescaled to	14
			15
3.1 Illustration of a curved reference orbit with local bending radius ρ (not to scale for better visualization). The position of a partials is given relative to a local reference	3.1	Illustration of a curved reference orbit with local bending radius ρ (not to scale for	
better visualization). The position of a particle is given relative to a local reference frame moving along with the reference orbit			18

3.2	Illustration of (red, solid) the equivalent ellipse with area proportional to the emittance $\pi \epsilon_x$ of (blue, circles) a particle distribution in $(x - x')$ space. (Red, dashed) Extent of the ellipse is $\sigma_x = \sqrt{\epsilon_x \check{\beta}}$ and $\sigma_{x'} = \sqrt{\epsilon_x \check{\gamma}}$. (Red, dotted) The slope is given by $m = \langle xx' \rangle / \sigma_x^2$ and connects the points of horizontal extent	25
3.3	Schematic layout of a C-chicane showing trajectories of different energies. Reference energy (black solid) is deflected by an angle θ . Lower energy particles (red, dotted) have a larger detour and higher energy particles (blue, dashed) a shorter one. In the symmetric case, all magnets have same length $L_{\rm mag}$ and kick angle θ , and the spacing from first to second and third to fourth dipole are equal $L_{\rm space}$	27
3.4	Longitudinal $(\zeta - \delta)$ space of a bunch with length $\sigma_{\zeta} = 2 \mu m$ and energy spread of $\sigma_{\delta} 1 \%$. Shown are (a) the initially uncorrelated bunch and (b) after stretching the bunch to $5 \times$ its initial length. The (blue, solid) projected energy distribution and therefore the energy spread do not change, but (orange, dotted) a single slice can have (orange, solid) lower local energy spread.	28
3.5	Change of longitudinal beam parameters with varying R_{56}^{ζ} for a beam with initially $\sigma_{\zeta} = 2 \mu m$, $\sigma_{\delta} = 1 \%$, and no chirp $\langle \zeta \delta \rangle = m = 0$. Results obtained from (blue, solid) the full formulas eqs. (3.32) to (3.34) and (orange, dashed) approximations for expanding about $R_{56}^{\zeta} \to \infty$ are shown for (a) bunch length, (b) linear energy chirp, and (c) slice energy spread	29
3.6	Example of emittance increase after the plasma source for (a) horizontal plane and (b) vertical plane. Beam is captured with two quadrupoles of 10 cm length each (grey boxes). The first quadrupole focuses and the second defocuses in the horizontal plane. Shown are the (blue solid) projected normalized emittance without chromatic contribution eq. (3.25), (orange dashed) exact projected normalized emittance eq. (3.45), and (red dotted, diamonds) the approximation including a chromatic contribution eq. (3.46) yielding an upper limit and evaluated before and after drift spaces. Beam simulated with <i>ASTRA</i>	36
3.7	Gaussian distributed chirped bunch with 1,5 mrad divergence in both transverse directions, $\sigma_{\delta} = 1,5$ % projected energy spread, and an initially $\sigma_{\Delta} = 1$ % uncorrelated energy spread. (a) Local energy spread σ_{Δ} of 1 µm long slices for (orange dashed) the initial bunch and (solid blue) the bunch propagated by 50 cm in a free drift. The region for calculating the slice parameters was shifted by 0,1 µm for individual data points. (b) Longitudinal $(\zeta - \delta)$ space, overlaid for (orange) the initial position $s = 0$ and (blue) after propagating the beam to $s = 50$ cm	38

3.8	Strength and impact of transverse space charge forces expected for a gaussian shaped beam with LUX parameters $I_{\text{peak}} = 2.5 \text{kA}$ and $\gamma \approx 600$. Beam radii are $\sigma_r = 3.5 \mu \text{m}$ (blue) and $\sigma_r = 100 \mu \text{m}$ (orange, scaled ×100 for better visual representation). Dashed lines represent the linear approximations of the force. (a) Normalized space charge force at the bunch center directly after the plasma source, alongside the corresponding linear defocusing strength. The linear model holds for $r/\sigma_r \approx 1$. (b) Evolution of transverse beam size in free drift, assuming linear space charge force. For typical divergences of 0,5 mrad, transverse space charge effects are negligible. An effect becomes visible only if the divergence is reduced by approximately an order of magnitude.	40
3.9	Rate of change in energy due to longitudinal space charge forces per unit length propagated in the beam transport. Amplitude depends on a particle's position within the bunch, illustrated for a gaussian beam with LUX parameters: (blue solid) $\gamma \simeq 600$ after the source with $I_{\rm peak} = 2.5$ kA, $\sigma_r = 3.5$ µm, (orange dashed) after transverse expansion $I_{\rm peak} = 2.5$ kA, $\sigma_r = 100$ µm, (green dash-dotted, magnified ×10 for visual representation) and after being stretched with a chicane by a factor of 5 to $I_{\rm peak} = 500$ kA, $\sigma_r = 100$ µm.	41
3.10	Illustration of an (blue ellipses) electron beam following a curved trajectory through a dipole magnet. (Red dashed line) Synchrotron radiation emitted early in the bend from the tail of the bunch (position (1)) overtakes the electron bunch as it progresses along the bend. Parts of this radiation then interact with particles at the head of the bunch at a later position in the bend (position(2))	43
3.11	Rate of change in energy along the beam due to coherent synchrotron radiation as predicted by eq. (3.53). The beam has a charge of 45 pC. Particles at the bunch tail and center are decelerated and particles at the head accelerated. (a) Influence of bunch length with (blue solid) $\sigma_{\zeta,0}=2\mu\mathrm{m}$, (orange dashed) $2.5\times\sigma_{\zeta,0}$, and (green dash-dotted) $5\times\sigma_{\zeta,0}$. The deflection angle $\theta_0=25\mathrm{mrad}$ corresponds to a bending radius of 13,7 m for a 35 cm long dipole magnet. (b) Variations in the rate of energy change at different kick angles for an initially short bunch of $\sigma_{\zeta,0}=2\mu\mathrm{m}$, ranging from (orange short-dashed) $0.5\theta_0$ to (purple long-dashed) $1.5\theta_0$. The blue solid line represents the same parameters across both plots	43
3.12	Relative increase in horizontal normalized emittance from CSR for a beam with $\gamma_0=587$ and a kick angle of $\theta_0=25$ mrad dependent on horizontal and longitudinal beam size, calculated according to eqs. (3.55) to (3.57). The markers highlight specific transverse beam sizes for a bunch length of $\sigma_{\zeta}=2~\mu\text{m}$, where the emittance growth is limited to (green circle) 20 %, (black diamond) 50 %, and to (blue triangle) 100 %.	44
3.13	Comparison of (black solid) a realistic quadrupole field profile with models for simplification, which include (blue box) the usual hard-edge model, (orange box) a modified hard-edge-model to improve accuracy of the matrix elements, and (green dotted) a step-wise approximation with 20 subdivisions	47

Schematic view of an undulator structure with alternating polarity of the magnets, guided by iron pole shoes towards the gap and creating a periodic vertical magnetic field along (green line) the central axis. The electron beam moves on a (red line) sine trajectory in the horizontal plane about this central axis. Figure adapted from [105].	52
(a) Fundamental wavelength of undulator radiation for different electron energies dependent on undulator strength given by eq. (4.20) . Gray shaded area indicates transmission window of an aluminum filter ≈ 17 to 80 nm in the reasonably accessible range for the undulator strength of $0.5 < K < 2.55$. (b) Transmission of a 250 nm aluminum filter	57
Illustration of the coherence condition for undulator radiation. An electron travels one undulator period λ_u from A to B in $t = \lambda_u/(\overline{\beta_z}c)$, therefore radiation of wavelength λ_l emitted at A under an angle θ is traveling a distance $\lambda_u/(\overline{\beta_z}$ in the same time. Radiation emitted at B in the same direction interferes constructively if the wavefront is shifted by an integer multiple of λ_l . Figure adapted from [106]	59
(a) Finite wave train of $N_u = 10$ cycles and (b) corresponding spectrum with minima at $\Delta\omega/\omega_l = \pm 1/N_u$	60
Gain curve obtained from eqs. (4.37a) to (4.37c) starting from a small initial field. Insets (a)-(d) show the microbunching process at different stages of the amplification process up to saturation, where the average energy transfer between electrons balances and the power level starts to oscillate	63
Gain power curve according to (blue solid) eq. (4.43) and (orange dashed) the approximation for $z \gg L_g$ for the first 12 gain lengths	65
(a) Change of growth parameter $-\text{Im}(\hat{\alpha})$ for Gaussian distributed energy spread, obtained from eq. (4.49). Only the root that corresponds to an increase in \tilde{E}_x is shown for (orange) being on resonance and (blue) at optimal energy detuning. Different space charge parameter \hat{k}_p are (solid) 0,0, (dotted) 0,2, and (dashed) 0,5. Values are normalized to the growth rate of a monoenergetic beam and no space charge. An approximation for the growth rate at optimum detuning is also shown (black, solid). (b) Optimal detuning at which largest growth rate is achieved	68
Increase in gain length relative to the initial 1D gain length as a function of applied (de)compression, considering different initial scaled uncorrelated energy spreads: $\Delta_0 = \sigma_{\Delta,0}/\rho_{\rm FEL}$ (blue, solid) 0.2, (green, dash-dotted) 1.0, and (purple, long dashed) 2.0. The case where neither compression nor decompression improves the gain length is indicated by (orange, dashed) $1/\sqrt{3} \simeq 0.6$. The <i>LUX</i> parameters (red, dotted) correspond to $\Delta_0 \simeq 1.4$, suggesting a benefit from decompression. Additionally, (black, solid) the locations of minima is indicated, representing the optimal stretching factor $n_{B,\rm opt}$. Note that the scaling of the n_B -axis changes depending on whether n_B is greater or smaller than 1, reflecting that compression and decompression are reciprocal operations.	69
	guided by iron pole shoes towards the gap and creating a periodic vertical magnetic field along (green line) the central axis. The electron beam moves on a (red line) sine trajectory in the horizontal plane about this central axis. Figure adapted from [105]. (a) Fundamental wavelength of undulator radiation for different electron energies dependent on undulator strength given by eq. (4.20). Gray shaded area indicates transmission window of an aluminum filter ≈ 17 to 80 nm in the reasonably accessible range for the undulator strength of $0.5 < K < 2.55$. (b) Transmission of a 250 nm aluminum filter

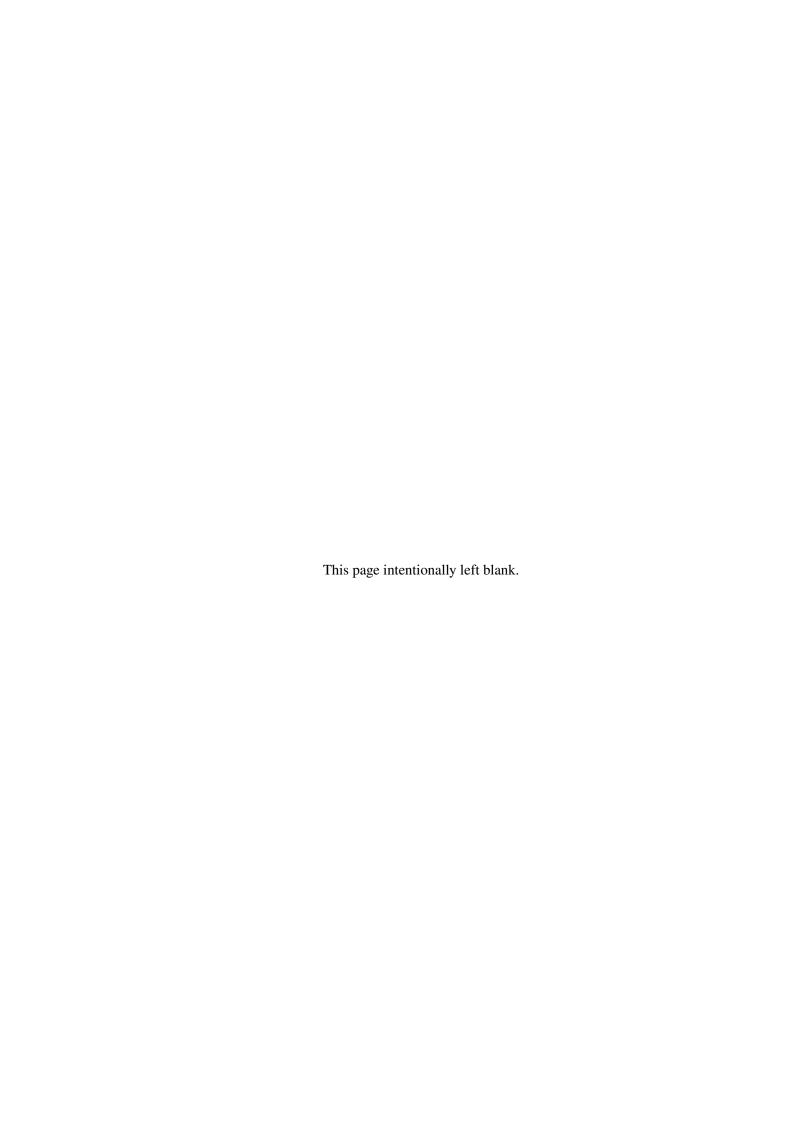
4.9	Change of scaling parameters for 3D gain length at LUX parameters with varying decompression n_B . (a) Values of (blue, solid) η_d , (orange, dashed) η_ϵ , and (green, dash dotted) η_γ related to the change in $L_{g,1D}$ and slice energy spread σ_Δ . (b) Total change of $\Lambda_{\rm Xie}$	76
4.10	Scaling of $3D$ gain length for LUX parameters at varying decompression n_B . The $1D$ gain length (purple, long dashed) increases due to $3D$ effects (blue, solid). Neglecting either contributions from emittance (orange dashed), diffraction (green, dash dotted), or energy spread (red, dotted) reveals, that a combination of the latter two have largest impact	76
4.11	(a) Increase in gain length due to short electron bunch lengths σ_{ζ} compared to the steady state cooperation length $L_{c,0}$. (Blue triangle) In the $3D$ case the gain length is expected to be almost increased by 200% while (orange square) in the $1D$ case the influence of the short bunch would be insignificant for LUX parameters. (b) With decompression the ratio $\sigma_{\zeta}/L_{c,0}$ is shifted to more favorable values and therefore reducing the impact from short bunches on the gain length	77
4.12	Scaling of the gain length L_g from Xie fit and including bunch length effects dependent on the bunch stretching factor n_B for LUX beam parameters. Different lines represent different spot sizes σ_r in the undulator from (blue, solid) 7,5 μ m to (purple, long dashed) 75 μ m. The average achievable beam size in the undulator coincides with the curve for (red, dotted) 45 μ m and is the same as given before in fig. 4.10	82
4.13	Scaling of (a) the gain length L_g from Xie fit and including bunch length effects, and (b) the corresponding optimum bunch stretching $n_{B,\text{opt}}$ dependent on the transverse beam spot size σ_r for LUX beam parameters. Different lines represent differences in the normalized emittance ϵ_n in the undulator for (blue, solid) 1 mm mrad, (orange, dashed) 1,5 mm mrad, and (green, dash dotted) 2 mm mrad. Additionally the gain length for (red, dotted) zero emittance is shown, corresponding to a beam of constant size	83
4.14	(a) Minimum gain length L_g from Xie fit and including bunch length effects. (b) The corresponding (blue, solid) optimum bunch stretching $n_{B,\mathrm{opt}}$ and (orange, dashed) beam spot size σ_r dependent on the normalized emittance ϵ_n for LUX beam parameters.	83
4.15	Schematic illustration for the use of a tapered undulator to keep the radiation resonant. From left to right: The (green, circle) initially short and unchirped bunch passes a (blue, triangles) decompression chicane and is stretched and chirped afterwards. The taper of the (white and blue) undulator is set to have (yellow parts) different fractions of the electron bunch emit at the same wavelength. As the (orange, waves) radiation passes through the bunch it is amplified	86
	Parties and content to amphines.	50

4.16	Emitted power from SVEA FEL simulations for (a) the power emitted to all frequencies and (b) the power filtered about $\pm 2\%$ relative bandwidth about the fundamental. Power is shown for (blue, solid) initial <i>LUX</i> parameters, focus at the undulator center in the horizontal and matched to natural focusing in the vertical plane, (orange, dashed) energyspread as after decompression with $R_{56}^{\zeta}=500\mu\text{m}$, but no chirp or taper, (green, dash-dotted) same as before, but with constant beam size of 35 μ m, and (red, dotted), constant beam size, but with chirp and taper included	89
5.1	Schematic illustration of chromatic matching scheme showing transverse beam sizes σ_x for (red, dashed) a lower energy E than (black, solid) the central energy E_0 focused in the front, and (blue, dotted) a higher energy E_+ focused in the back of (position indicated by grey box) the undulator. A radiation pulse is shown below, starting with an initial group velocity $v_g \simeq c$. It slows down in the exponential gain regime at later positions in the undulator, slipping by $\lambda_l/(3\lambda_u)$ relative to the electron bunch.	94
5.2	Optimized beamline layout for LUX with beam sizes for the (a) horizontal plane and (b) vertical plane. Energies are focused along the undulator according to a chromatic matching with about 1 %/m focus slippage over the undulator. The reference energy (black, solid) is focused at the center of the undulator, whereas (red, dash-dotted) -1 % lower energies are focused at the undulator entrance and (blue, dashed) 1 % higher energies are focused at its exit. Initial beam size and divergence are 3,5 μ m and 0,5 mrad in both planes. Colored boxes indicate (red) quadrupole magnets with $K > 0$, (green) quadrupole magnets with $K > 0$, (blue) chicane dipole magnets, and	
5.3	(grey) the undulator	99
5.4	figure, original by P. Winkler	102
5.5		103
5.6	used at LUX	103
5.7	second and last two, and (c) first, all other quadrupole magnets used at LUX (a) Peak magnetic field g_0 of chicane dipole magnets dependent on the applied current	104
3.1	and (b) field profile of chicane dipole magnets. \dots	105
5.8	(a) R_{56} dependent on the applied current for a 300 MeV beam. The quadratic increase is reduced by saturation effects in the magnets toward higher currents. (b) Maximum (absolute) R_{56} in the chicane. Magnet pole width and apertures limit the value at energies below 180 MeV. Maximum value of the left plot is indicated by a red square.	105
5.9	(a) Measured dependence of peak field on applied current and (b) field profiles for the corrector dipole magnets: (blue, solid) correctors 1, 3, 4, (orange dashed) corrector 2, (green dash-dotted) correctors 5–8, and (red dotted) 10 and 11	

5.10	spectrometer and (orange, dashed) the second spectrometer. (b) $2D$ field map of central $(y-z)$ -plane for the second spectrometer with trajectories of (orange, dashed) 100 MeV, (blue, solid) 300 MeV, and (green, dash-dotted) 500 MeV leaving the spectrometer magnet through the fringe field at the bottom or rear edge 107
5.11	Strength parameter <i>K</i> for the <i>FROSTY</i> undulator dependent on the gap. (red, square) A <i>K</i> of 2 is achieved with a gap of 3 mm
5.12	(a) Second field integral of the measured horizontal magnetic field of the <i>FROSTY</i> undulator. (b) Corresponding average horizontal electron movement for an energy of 300 MeV. A pointing of –80 μrad at the undulator entrance was chosen such that the average motion up to the local kick at 1,3 m is about the central axis of the undulator. (c) Root mean square beam wander along the undulator
5.13	Efficiencies of the EUV spectrometer components dependent on the wavelength. (a) Reflectivity of the gold mirror. (b) Transmission of 250 nm aluminum filter [112]. (c) Grating reflectivity to the (blue, solid) first, (orange, dashed) second, and (green, dash-dotted) third diffraction order $G1-G3$. (d) CCD camera spectral responsivity. Figures (a),(b),(d) adapted from [114]
5.14	Signal on CCD including the effects of the components in the EUV spectrometer at LUX . Wavelength corresponds to the position in the image plane of the first diffraction order of the grating. Signal is normalized to the counts of the total spontaneous radiation in the first three diffraction orders of the grating at 65 nm (a) Spontaneous undulator radiation for (orange, dashed) first, (green, dash-dotted) second, and (red, dotted) third diffraction order $G1-G3$. (Black, solid) their combined signal. (b) Total signal for undulator radiation (same is in (a)) and FEL signal for the (red, solid) highest signal and (blue, dotted) lowest signal from 5 simulations. Raw spectrum shows same photon count for wavelength ranges of only spontaneous undulator radiation. Lower signal level in the FEL case comes from the absence of lower wavelengths in the simulation and their higher diffraction orders
5.15	Magnetic background field along the accelerator for (a) the horizontal, (b) vertical, and (c) longitudinal field components. The horizontal and vertical field component are compensated with correction coils spanning the range 0,5 m to 17 m to minimize the (d) (blue, solid) horizontal and (orange, dashed) vertical second field integral at the last corrector before the undulator. Beamline lattice shown for (red) quadrupole magnets, (green) corrector magnets, (purple) electron spectrometer, and (blue) chicane dipoles
6.1	(a) Longitudinal phase space of the LUX reference beam after transport to the undulator entrance with a bunch stretching of $R_{56}^{\zeta} = 550 \mu\text{m}$. The bunch is stretched to a bunch length of 5,3 μ m. The (red line) current profile peaks at about 1,1 kA and shows a slight asymmetry with higher currents towards the bunch tail compared to (blue, dotted) a gaussian fit. (b) Slice energy spread along the beam evaluated over a slice length of 1 μ m, matching the estimated cooperation length

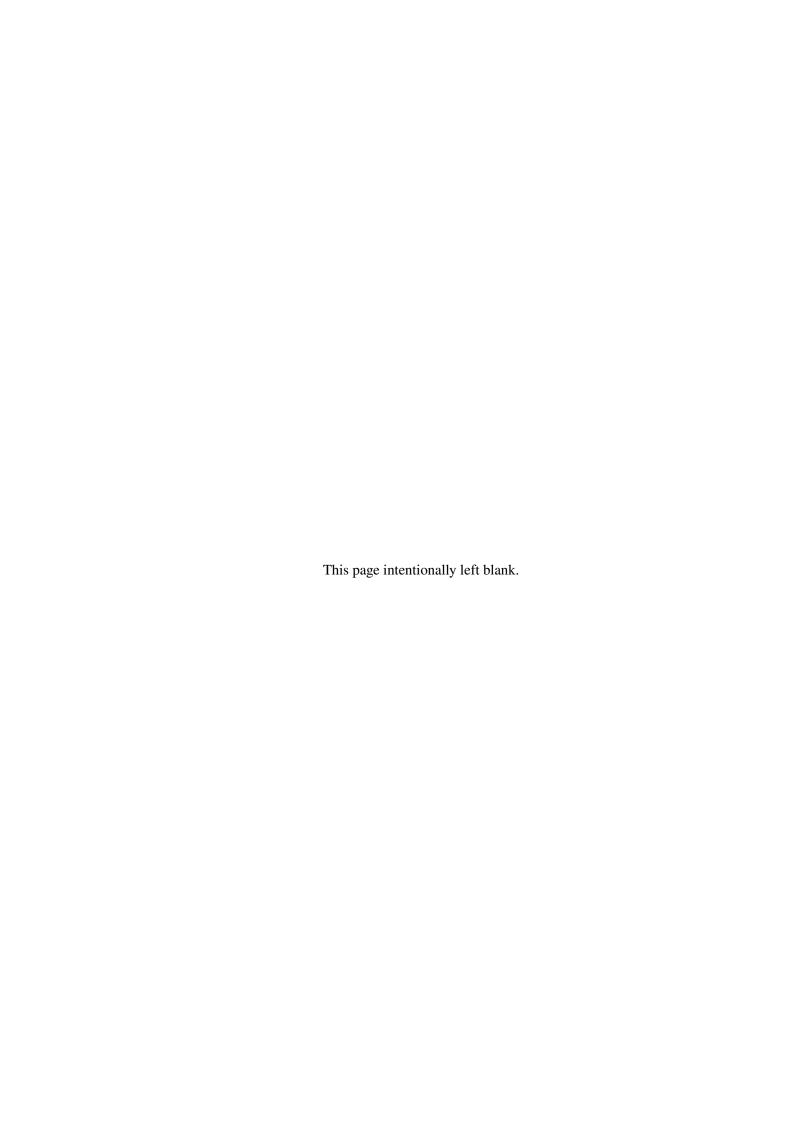
6.2	Transverse particle distribution along the bunch for (a)-(c) the horizontal plane and (d)-(f) the vertical plane. The focus position shifts towards the head in both planes from (a)+(d) undulator entrance, via the (b)+(e) undulator center to (c)+(f) undulator end. Additionally, the (red dashed) $\pm 1\sigma$ beam sizes about the mean values $\langle \cdot \rangle$ are
	shown. Asymmetries that originate from the initial beam and effects in tracking primarily affect particles at the head and tail $ \sigma_{\zeta} \gtrsim 6 \mu \text{m}$, outside the core region 121
6.3	Normalized slice emittances along the bunch for the (a) horizontal and (b) vertical plane. It changes from (blue, solid) the undulator entrance, via (orange, dashed) the undulator center to (green, dash-dotted) the undulator end. Each slice is about the estimated cooperation length of 1 µm
6.4	Emitted Power from simulation with LUX beam parameters after transport and perfect undulator field with $K=2$ and a taper of 1 %/m. It is shown for (blue, solid) mean value with (blue, filled) 1σ standard deviation calculated over 10 simulations with different shot noise seed values. In comparison (orange, dashed and filled) the spontaneous undulator radiation is shown for the same seed values. The power level reaches about 2,5 GW at the end of the undulator
6.5	Ratio of total emitted power to spontaneous undulator radiation only, averaged over 10 simulations with different shot-noise seeds for (blue, solid) an ideal sinusoidal undulator field and (orange, dashed) the measured $FROSTY$ field profile with (filled) 1σ standard deviation calculated over 10 simulations. To cover the extent of the full $FROSTY$ field, the z axis is slightly longer and the undulator centered within this
	range
6.6	(a) Temporal profile of normalized power of one simulation. (Red, solid) Envelope of the maximum and minimum instantaneous power and (Red, Dashed) the average power. (Blue) The instantaneous power shows oscillations twice as fast as the electric
67	field with frequency $f = 2c/\lambda_l$. (b) Corresponding normalized power spectral density. 126
6.7	(a) Radiation intensity profile. (b) Projected transverse profiles to the horizontal and vertical axes
6.8	Ratio of total emitted power to spontaneous undulator radiation only, (blue solid) averaged over 10 simulations with different shot-noise seeds for (a) an ideal sinusoidal undulator field and (b) the measured $FROSTY$ field profile. (solid) represents 1σ standard deviation. Additionally, (orange, dashed) a Gaussian fit is applied to the central region to estimate the best taper
6.9	(a) Ratio of total emitted power to spontaneous undulator radiation only filtered within a window about ±2 % of the fundamental, (blue solid) averaged over 10 simulations with different shot-noise seeds and (orange, dashed) a gaussian fit applied of the central region to estimate the best taper. (b) Averaged spectra about the fundamental for (blue, solid) a taper of 1 %/m, close to the optimum, and detuned tapers of (orange, dashed) -1 %/m and (green, dash dotted) 3 %/m
7.1	Line foci with single quadrupole magnet. Unprocessed camera image. (a) Focus in the horizontal axis and (b) focus in the vertical axis only

7.2	Transverse positions of quadrupole magnets at <i>LUX</i> for (a) the horizontal and (b) the vertical axis. (Red) Initial position after commissioning and (blue) after measuring	
	the magnetic axes and re-positioning. Lines between the measured data points for the	
	offset positions are added for better visualization.	132
7.3	Electron beams focused on the second spectrometer with the second quadrupole	1 52
1.5	doublet. The quadrupole magnets were set to focus the beam in both planes by (a)	
	focus horizontally in quadrupole No.3 and defocus in quadrupole No. 4, resulting	
	in (red, dashed) 307,8 MeV being focused on the spectrometer, and (b) vice versa,	
	resulting in (red, dashed) 292,9 MeV being focused on the spectrometer. (Blue, dotted)	
	The focused energy was set to 295 MeV. Camera counts are averaged over 100 shots	
	to not be affected by shot-to-shot fluctuations. The waist position remains unaffected	
	by averaging.	135
7.4	Quadrupole strengths relative to their design value, determined with beam based	100
,	measurements at different energies, and therefore changing gradient. Required gradient	
	to focus onto the spectrometer screen increases up to about 13 m and then decreases	
	again. Markers show (green, diamond) 180 MeV, (orange, square) 270 MeV, (red, up	
	triangle) 275 MeV, (blue, circle) 300 MeV, (brown, star) 315 MeV, and (purple, down	
	triangle) 318 MeV. Arrow and filled markers show quadrupole magnets, that were	
	replaced in between measurement campaigns	136
7.5	Beam position monitor readouts along the beamline with (white background) trajectory	
	correction off and (gray background) trajectory correction on. From the top to the	
	bottom panels, the individual BPM readouts are shown for BPM1 to BPM4, with the	
	horizontal readouts shown in the left and the vertical readouts in the right panels,	
	respectively. (Blue, solid) The rolling mean and (blue, shaded) corresponding rolling	
	standard deviation over 30 shots. Individual shots going through the beamline and	
	recorded in all 4 BPM are shown as dots in each panel. When the trajectory correction	
	was not running, the corrector magnets were turned off.	137
7.6	Steering of electron beam when closing the gap. Numbers (1)–(4) mark individual	
	datasets where the undulator axis was measured. (a) Before the undulator was aligned	
	to the design axis with (blue, circles) and (orange, squares) the beam being centered	
	to the beam axis defined by BPM3 and BPM4 prior to closing the undulator gap, and	
	(green, diamonds) after steering the beam to be aligned to the undulator axis instead	
	of the design axis (b) After repositioning the undulator, the gap was again scanned	
	twice with the beam being on the design trajectory defined by BPM3 and BPM4 prior	139
7.7	to closing the gap	139
1.1	energy of $E \simeq 320 \text{MeV}$. (a) Images taken for the range of 10–80 nm. Edges of	
	aluminum filter can be seen for multiple diffraction orders of the grating. (b) Spectrum	
	normalized to the signal at the fundamental wavelength, which is marked by an arrow.	141
	normanzea to the signal at the randamental wavelength, which is marked by all allow.	1 T I



List of Tables

2.1	LUX beam reference parameters. Values were obtained from measurements, if possible and else taken from simulations
4.1	Xie fitting parameters for formula eq. (4.66)
5.1 5.2	Magnet strength for optimized LUX lattice with chromatic focusing into the undulator. 98 Installed components at LUX and their center positions in the beamline. Based on their position the components are categorized in one of three sections: The capturing section from the plasma target to the first electron spectrometer, the chicane section from the quadrupoles after the first spectrometer to the profile screen behind the chicane, and the undulator section from the quintet to the end of the beamline. Used abbreviations: Quad. = quadrupole, Cor. H. = horizontal corrector, Cor. V. = vertical corrector, e^- -Spec. = Electron Spectrometer, Dip. = Chicane Dipole.
5.3	Properties of quadrupole magnets used at <i>LUX</i>
5.4	Properties of chicane dipole magnets used at <i>LUX</i>
5.5	Properties of corrector dipoles at <i>LUX</i>
5.6	Properties of spectrometer dipoles at <i>LUX</i>
7.1	Transverse position of quadrupole magnets at <i>LUX</i> after commissioning and after the latest re-positioning



Acknowledgements

I would like to thank Andreas R. Maier, my primary supervisor, and the leader of the *LUX* team and the MPL group. His guidance and leadership have been invaluable throughout the course of my thesis. I am also grateful to Wolfgang Hillert for serving as my second supervisor.

A special thanks goes to Bernhard Schmidt, whose lectures on accelerator physics were truly inspiring and initially sparked my fascination with the field. I have fond memories of his lectures, the exercise groups, and the excursions. His unique approach to teaching accelerator physics and igniting my interest played a significant role in shaping my academic path, which might have been quite different otherwise.

I am deeply appreciative of all the members of MPL, and especially the *LUX* and *ANGUS* operators, including Paul Winkler, Max Trunk, Manuel Kirchen, Sören Jalas, Philipp Messner, Matthias Schnepp, Timo Eichner, Cora Braun, Thomas Hülsenbusch, and Christian Werle. The experiments at *LUX* would not have been possible without their work and dedication. Although not individually mentioned, I thank all other group members for the exciting and enjoyable times we shared, and especially making the beam times even more enjoyable by adding the most important ingredients to science: fun and social glue. Thank you all for the wonderful years!

Special thanks go to Paul Winkler and Max Trunk for their numerous and constructive comments, helpful tips, and valuable feedback on this thesis.

I would also like to acknowledge the work of and thank the technical groups, whose support was a major contribution in constructing the LUX experiment in its current form. I particularly want to highlight the commitment of the entire MEA and MKK/MPC groups for their constant support and assistance. Jörg Ludwig deserves special recognition for his efforts and support with magnetic measurements at Building 27.

To my dear friends Jan, Timo, Finn, Vanessa, and Tanja, thank you for being yourselves and for the wonderful times we've shared for 20+ years.

My deepest gratitude goes to my family – my parents, Andrea and Wolfgang, and my brother Nils – for their unwavering support, not just during my PhD, but throughout my entire life. I also want to express my deepest appreciation to my grandparents, Brunhilde and Klaus. Although I can no longer share my experiences with them, I believe they played a major role in fostering my early curiosity about the world and encouraging me not just to ask questions, but to seek answers.

To Claudia, thank you for your love and support. You encourage me to pursue my goals while also knowing when I need to slow down and take a break. Thank you for being a part of my life and for your understanding during these demanding times.

Curriculum Vitae

Personal Details

Name Lars Hübner

Date of Birth 29.03.1993

Email lars.huebner@studium.uni-hamburg.de

lars.huebner@desy.de

mail-lars.huebner@web.de

Education

2005–2011	Abitur, Gymnysium Neu Wulmstorf, Germany
2011–2015	BSc student in Physics, Universität Hamburg, Hamburg, Germany. Thesis Title: Tests and measurements with a thermal VXD mock-up for BELLE-II
2015–2018	MSc student in Physics, Universität Hamburg, Hamburg, Germany. Thesis Title: Single shot emittance measurements of laser-wakefield accelerated electron beams at LUX
2019–2025	Doctoral student in Physics, Universität Hamburg, Hamburg, Germany Thesis title: Beam Transport for a Laser-Plasma Driven Free-Electron Laser at

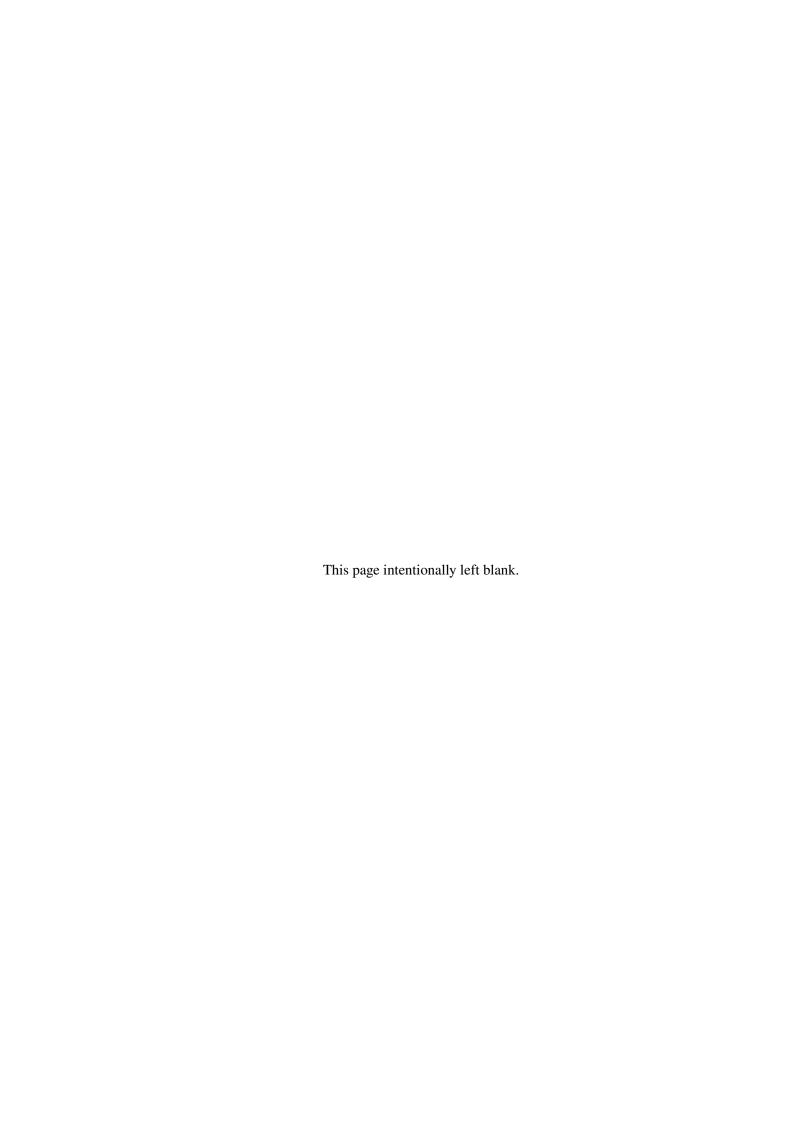
Professional Experience

2019– Deutsches Elektronen-Synchrotron DESY, Hamburg

the LUX Experiment

Languages

German Mother tongue English Fluent



List of Publications

N. Delbos, C. Werle, I. Dornmair, T. Eichner, L. Hübner, S. Jalas, S.W. Jolly, M. Kirchen, V. Leroux, P. Messner, M. Schnepp, M. Trunk, P.A. Walker, P. Winkler, A.R. Maier,

Lux - A laser-plasma driven undulator beamline,

Nucl. Instrum. Methods Phys. Res. A 909, 318–322 (2018)

A. R. Maier, N. M. Delbos, T. Eichner, L. Hübner, S. Jalas, L. Jeppe, S. W. Jolly, M. Kirchen, V. Leroux, P. Messner, M. Schnepp, M. Trunk, P. A. Walker, C. Werle, P. Winkler, *Decoding Sources of Energy Variability in a Laser-Plasma Accelerator*, Phys. Rev. X 10, 031039 (2020)

S. Jalas, M. Kirchen, P. Messner, P. Winkler, **L. Hübner**, J. Dirkwinkel, M. Schnepp, R. Lehe, A. R. Maier, *Bayesian optimization of a laser-plasma accelerator*,

Phys. Rev. Lett. 126, 104801 (2021)

M. Kirchen, S. Jalas, P. Messner, P. Winkler, T. Eichner, L. Hübner, T. Hülsenbusch, L. Jeppe, T. Parikh, M. Schnepp, A. R. Maier,

Optimal beam loading in a laser-plasma accelerator,

Phys. Rev. Lett. 126, 174801 (2021)

S. Jalas, M. Kirchen, C. Braun, T. Eichner, J. B. Gonzalez, **L. Hübner**, T. Hülsenbusch, P. Messner, G. Palmer, M. Schnepp, C. Werle, P. Winkler, W. P. Leemans, A. R. Maier, *Tuning curves for a laser-plasma accelerator*,

Phys. Rev. Accel. Beams 26, 071302 (2023)

P. Winkler, M. Trunk, **L. Hübner**, A. Martinez de la Ossa, S. Jalas, M. Kirchen, I. Agapov, S. A. Antipov, R. Brinkmann, T. Eichner, A. Ferran Pousa, T. Hülsenbusch, G. Palmer, M. Schnepp, K. Schubert, M. Thévenet, P. A. Walker, C. Werle, W. P. Leemans, A. R. Maier, *Active energy compression of a laser-plasma electron beam*, Nature 640, 907–910 (2025)